

THE UNIVERSITY OF CHICAGO

ORDER AND DISORDER IN VISUAL CORTEX: SPONTANEOUS SYMMETRY
BREAKING AND STATISTICAL MECHANICS OF PATTERN FORMATION IN
VECTOR MODELS OF CORTICAL DEVELOPMENT

A DISSERTATION SUBMITTED TO
THE FACULTY OF THE DIVISION OF THE PHYSICAL SCIENCES
IN CANDIDACY FOR THE DEGREE OF
DOCTOR OF PHILOSOPHY

DEPARTMENT OF MATHEMATICS

BY
PETER J. THOMAS

CHICAGO, ILLINOIS

AUGUST 2000

To Timothy Farragut Thomas and Marian Horton McCaa Thomas, who taught me
curiosity, generosity and persistence.

ABSTRACT

Stimulus-response properties of neurons in primary visual cortex exhibit intriguing spatial organization. Models for the development of ocular-dominance stripes, stimulus orientation preference, the retinotopic map, cytochrome oxidase distribution and spatial frequency-preference maps fall into two families: “feature” models, which treat the map properties abstractly, divorced from direct connection to biological structures, and “synaptic” models, which capture important biological detail but give little analytical insight into the nature of pattern formation in the cortex. In this work I derive a feature model for cortical pattern formation from a detailed synaptic model and show how to apply analytical techniques developed for the study of pattern formation in condensed-matter physics to cortical maps. First, I examine the pattern-forming properties of several of the common cortical-feature models. Then I explore the properties of an alternative model adapted from Heisenberg’s XY magnetic spin model. The statistical-physics framework is used to quantify the disorder measured in the orientation map, which is shown to lie at the edge of a continuous phase-transition to a disordered state. I derive this spin model from a biologically detailed synaptic model first in a simplified case and then in a general setting. The receptive field properties fan-in weight, retinotopy, orientation tuning and receptive-field width, are encoded in the geometry of the thalamocortical synaptic weights. I show that adding a soft constraint on the feedforward fan-out from the thalamus induces coupling between different components of the cortical map. Finally I show how to apply the techniques of equivariant bifurcation theory and group-representation theory to study the patterns formed by the generalized XY model. The symmetry structure of the cortical-map problem forces the coupling of certain map elements and not others: for instance the orientation preference couples to the direction of retinotopic shear. In addition, I predict a relationship between the orientation gradient and local anisotropy in retinocortical magnification.

ACKNOWLEDGEMENTS

I wish to thank Professor Jack Cowan for his encouragement, his endless inspirations and his commitment to his students. Thanks also to my student colleagues Trevor Mundel, Alex Dimitrov, Misha Belkin, Anindya Sen and Iris Chen, for contributing to a vibrant research atmosphere. Thanks to Marty Golubitsky, Rick Jensen, Paul Bressloff, Gary Blasdel, Jenny Lund and Terry Sejnowski for their encouragement. Special thanks to Phil Ulinski and the National Institutes of Health for financial support under training grant T-32-MH20029.

Thanks to Nathan Dunfield, Bryan Claire and Martin Pergler for developing and maintaining the \LaTeX macro `easychthesis`. Thanks to International House, Qumbya housing cooperative, the Covenantal Community of University Church, Bill and Madeleine Hamblin, and Andy Carter and Diane Herrmann, for providing places I could live and work. Thanks to my parents Tim and Marian Thomas, and also to Donna and Larry Steele and Don Levine sensei, for support and encouragement.

Most of all, thanks to Diana Steele for her unwavering faith and support.

TABLE OF CONTENTS

ABSTRACT		iii
ACKNOWLEDGEMENTS		iv
1 INTRODUCTION		1
1.1 Overview		1
1.2 Biology of Cortical Maps		4
1.2.1 Anatomy and Physiology of the Mammalian Visual System		5
1.2.2 Physiology: Cortical Maps		9
1.2.3 Development of the Mammalian Visual System		16
1.3 Correlation-Based Models of Cortical-Map Formation		19
1.3.1 Hebb's Rule		19
1.3.2 Turing Mechanism for Pattern Formation		20
1.3.3 Turing Analysis of Competitive Hebbian Learning		23
1.3.4 Feature Models		28
2 MONTE CARLO SIMULATIONS OF THE XY FEATURE MODEL		36
2.1 The Classical Ising and XY Models		36
2.1.1 Definitions of the Classical Models		36
2.1.2 Dynamical Monte Carlo Simulation		38
2.2 Extension of the Classical Models to Cortico-Cortical Interaction		41
2.2.1 Continuous Phase Transition		49
2.2.2 Comparison with Cortical Data		52
2.2.3 Higher-Dimensional Maps		57
3 DERIVATION OF A GENERALIZED XY-MODEL FROM COMPETITIVE HEBBIAN LEARNING		65
3.1 Geometry of Geniculo-Cortical Weights		65
3.2 The Hebbian Model		68
3.3 Orientation and Retinotopy		74
4 THE GENERALIZED XY MODEL: MONOCULAR CASE		79
4.1 The Cortical-Map Vector		80
4.2 Dynamical Equation for $w(x, r)$		81
4.2.1 Constrained Hebb Rule		81
4.2.2 Existence of an Homogeneous Steady State		82
4.3 Derivation of Linear Interactions Between Cortical-Map Components		87

5	SYMMETRY ANALYSIS OF CORTICAL-MAP FORMATION: MONOCULAR CASE	101
5.1	Equivariance	103
5.2	Restriction to Plane-Periodic Solutions	115
5.3	Pattern Formation on a Square Lattice	118
5.3.1	Irreducible Representations	120
5.3.2	Symmetry-Adapted Basis Vectors	125
5.3.3	Axial Subgroups	130
5.4	Numerical Isolation of a Bifurcating Planform on the Square Lattice .	133
5.5	Pattern Formation on a Hexagonal Lattice	135
6	SUMMARY AND CONCLUSION	141
6.1	Predictions	142
6.2	Discussion	142
6.2.1	Noise in Cortical Maps	142
6.2.2	Alternative Models for Cortical Feature-Map Development . .	142
6.2.3	Ocular Dominance and the Orientation Map	144
	APPENDIX A: QUADRATIC FORMS	147
A.1	Degenerate Quadratic Forms	147
A.2	Nondegenerate Quadratic Forms	148
A.3	Measuring Anisotropy in a Map from $\mathbb{R}^2 \rightarrow \mathbb{R}^2$	152
	APPENDIX B: GAUSSIAN IDENTITIES	156
	APPENDIX C: STATISTICS FOR ANGULAR VARIABLES	160
	APPENDIX D: EQUIVARIANT BIFURCATION THEORY	164
D.4	Introduction	164
D.5	Equivariant Bifurcation Problems	164
D.6	Representation Theory and Isotypic Decomposition	166
D.7	Symmetry-Adapted Basis Methods: Example	170
D.8	Spontaneous Symmetry Breaking in the n -Box Brusselator	175
D.9	Spontaneous Symmetry Breaking in the Bénard Problem	180
	APPENDIX E: MATLAB CODES	184
E.10	Simulated Annealing Codes	184
E.11	Visualization Codes	192
E.12	Pattern Formation Analysis	196
E.13	General Utilities	213
	BIBLIOGRAPHY	219

LIST OF FIGURES

1.1	Orientation-Preference Map via Differential Optical Imaging.	4
1.2	Visual Pathway from Eye to Thalamus to V1.	6
1.3	Columnar Organization of Orientation Preference.	8
1.4	Retino-Cortical Map Visualized by Deoxyglucose Autoradiograph. . .	10
1.5	Ocular-Dominance Maps in Cat and Monkey.	13
1.6	Spatial-Frequency Preference Map.	15
1.7	Animal Coat Patterns	21
1.8	Schematic Turing Mechanism for Pattern Formation	23
1.9	Illustration of One-dimensional Retinotectal Map Formation.	25
1.10	Kohonen’s Self Organizing Map	31
2.1	Topological Point Defects in Orientation.	38
2.2	Sigmoid Acceptance Function for Different Inverse Temperatures β . .	41
2.3	Examples of Ising and XY Patterns.	43
2.4	Locally Optimal Orientation Pattern.	44
2.5	Globally Optimal Orientation Roll Pattern.	46
2.6	Energy as a Function of Defect Spacing: Vortex-Antivortex Pair. . . .	47
2.7	Simplest Stable Defect Configuration, XY model.	48
2.8	Energy as a Function of Defect Spacing: Vortex Lattice.	49
2.9	Orientation Scatter at Different Inverse Temperatures β	53
2.10	Phase Transition in Center-Surround XY Model.	54
2.11	XY Configurations Near the Phase Transition.	55
2.12	Vector Field Generated by XYZ model	59
2.13	Spin Model for Orientation and Ocular Dominance	60
2.14	Orientation and Directional Motion Maps	61
2.15	Orientation and Magnitude Interpreted as Spatial Frequency.	63
2.16	Preference for High <i>vs.</i> Low Spatial Frequency.	63
3.1	Feed-forward Weights from the LGN to Cortex.	69
3.2	Orientation Map Auto-correlation Function.	70
3.3	Sample Retinotopic Distortion Pattern.	76
3.4	Effect of Retinotopic Distortion on Orientation Map.	78
4.1	Constrained Receptive-Field Dynamics and Steady-State.	87
4.2	Convolution Kernels for the First-Order Interactions in Equations 4.31–	
	4.35 Induced by Dependence of Higher Moments on Lower Moments.	93

5.1	Euclidean Group Action on Retinotopic Distortion and Orientation Vector.	109
5.2	Splitting the Retinotopic Distortion Subspace.	121
5.3	Symmetry-Adapted Basis Vectors, Square Lattice Even Irrep.	128
5.4	Symmetry-Adapted Basis Vectors, Square Lattice Odd Irrep.	129
5.5	An Even Square Planform.	132
5.6	Lattice Vectors and Wave Vectors for the Hexagonal Lattice.	135
5.7	Odd Axial Planforms on the Hexagonal Lattice.	139
6.1	Correlation of Ocular Dominance and Orientation Maps	145
6.2	Ocular Dominance and Orientation Patterns	146
A.3	Eccentricity and Magnitude of Orientation Preference.	151
A.4	Shear from the Singular Value Decomposition.	155
C.5	Resultant Sum of von Mises Functions.	163
D.6	3×3 discretized membrane	170
D.7	Discrete Laplacian	171
D.8	Lowest frequency; $\sin(\pi x) \sin(\pi y)$	175
D.9	Highest frequency; $\sin(3\pi x) \sin(3\pi y)$	176
D.10	Hexagonal Lattice \mathcal{L}	181
D.11	Four planforms for bifurcation subgroups of $(T_2 \times D_6) \oplus \mathbb{Z}_2$: Rolls, Hexagons, Triangles, and Patchwork	183

LIST OF TABLES

3.1	Geometrical Reduction of Synaptic Weight $w(x, r)$	67
4.1	Cortical map vector components.	81
4.2	Integrals of Fan-Out Constraint Terms.	96
4.3	First-Order Influence K_{ij} of Fan-Out on Cortical-Map Vector.	97
4.4	First-Order Influence K_{ij} of Retinotopic Distortion on Cortical-Map Vector.	98
4.5	First-Order Influence K_{ij} of Orientation Components on Cortical-Map Vector.	99
4.6	First-Order Influence K_{ij} of Receptive-Field Width Deviation on Cortical-Map Vector.	100
5.1	Components of the Cortical-Map Vector.	102
5.2	Action of Rotation and Reflection Elements of Γ_{sq} on V_{sq}	119
5.3	Action of Translation Elements of Γ_{sq} on V_{sq}	120
5.4	Action of the Group Generators on $V_j, j = 1, 4$	122
5.5	Mass Representation: 4×4 Matrices.	122
5.6	First Orientation Representation: 4×4 Matrices.	123
5.7	Absolute Irreducibility of ρ_{M} and ρ_{O1} , Respectively.	124
5.8	The Character Function.	125
5.9	Symmetry-Adapted Basis Vectors, Square Lattice Even Irrep.	127
5.10	Symmetry-Adapted Basis Vectors, Square Lattice Odd Irrep.	127
5.11	Symmetry-Adapted Basis Vectors, Hexagonal Lattice Even Irrep.	137
5.12	Symmetry-Adapted Basis Vectors, Hexagonal Lattice Odd Irrep.	137
5.13	Axial Planforms on the Hexagonal Lattice.	137

CHAPTER 1

INTRODUCTION

1.1 Overview

The architecture of the visual cortex exhibits intriguing spatial organization. Neurons in primary visual cortex respond selectively to a variety of features of visual stimuli, including orientation, ocularity, retinotopic position, direction of motion and spatial frequency. For most of these features, nearby neurons are organized into *columns*: cell populations extending perpendicular to the cortical surface and exhibiting similar response preferences, for example, for vertical over horizontal contour orientations. At the same time any local region of cortex of the size of a *hypercolumn* (about 2 square mm in humans) contains columns representing all stimulus features: all orientations, right and left eye input, high and low spatial frequency. The resulting cortical architecture is a superposition of quasi-regular mosaics showing short-range order and long-range disorder.

The study of the nature and origin of these *topographic cortical maps* serves three purposes. Whereas topographic maps are ubiquitous throughout sensory and motor structures of the central nervous system, mechanisms underlying their formation should be generally applicable to understanding the interplay of genetic regulation and spontaneous pattern formation in development. Whereas map formation emerges as a collective property formed by many interacting parts of a complex system, the effort to build biologically realistic models of the underlying mechanism provides a test bed for our understanding of the neurobiological basis of learning and development in the visual system. Finally, whereas the map-formation problems constitute a many-dimensional dynamical system with complex interactions, nontrivial symmetry-effects, and noise-driven phenomena, they pose a challenge arena for the application

of the methods of applied mathematics and statistical physics as well as theoretical biology.

Models of cortical-map formation fall into two classes: *synaptic models* and *feature models*. The former describe explicitly the development of synaptic weights underlying cortical-stimulus preferences. Rich in biological detail, they are typically difficult to analyze and yield only modest theoretical insight. Feature models, on the other hand, dispense with biological realism and approach cortical maps as abstract vector fields over the plane. These abstract models concoct heuristic update rules to account for the organization of cortical features. A principal innovation in this work is to construct a realistic synaptic model from which a corresponding feature-level dynamical system may be derived. I thereby justify the analytically more tractable cortical-feature map.

I model the inter-related cortical-feature maps as resulting from a spontaneous symmetry-breaking process in which a uniform, isotropic geniculo-cortical architecture loses stability under the influence of lateral cortical competition and correlation-based weight modification. The cortical-map features jointly comprise a vector derived from various moments of the receptive field profiles. The center-surround lateral architecture influences all cortical-map vectors in the same way, providing a common wavelength for pattern formation in the different features. The geometrical nature of the features—total input weight, center-of-mass, covariance matrix—mean that departures from uniformity in the lower moments influence the subsequent formation of patterns in the higher moments. Conversely, smooth nonlinear constraints on the total synaptic weight projecting from geniculate loci determine additional influences of each feature on the others.

The entire feature-development dynamics may be captured, to first order, in a linear integro-differential equation that possesses the symmetries of the Euclidean planar motions under a novel group action. I prove equivariance of the model system under this action. After restricting the search for solutions to plane-periodic functions I calculate the reduction of the restricted group action to a sum of irreducible representations. The isotypic components of the solution space provide a classification of interacting features in cortical maps that has been previously overlooked. The analysis of these symmetries leads to the identification of certain patterns of

interaction between the features. For example, because they exhibit different types of symmetry, *compression waves* of retinotopic distortion (including those running perpendicular to the ocular dominance stripes) and *transverse waves* of retinotopic distortion couple to *different* kinds of orientation-preference patterns. As a result of symmetry-forced interactions, local anisotropies in magnification should couple with local orientation-preference.

By representing the cortical-map features as moments of the receptive fields, I obtain, in a completely natural way, a derivation of a *vector model* for map development. This vector model is in the same family as the XY and Ising models familiar from the physics of magnetic spin lattices. In particular, for the orientation map there is a direct connection to the XY model with a mixed ferro-antiferromagnetic Hamiltonian. The statistical-physics framework affords a natural treatment of *disorder* in cortical maps, lacking in other feature models. Using dynamical Monte-Carlo techniques to simulate the finite-temperature Gibbs ensemble of a vector model connects it to statistical measures of disorder in the architecture of visual cortex. I find that the distribution of orientation preference in the cortex lies at the edge of a continuous phase-transition to a disordered state.

Situated at the interface of neurobiology, applied mathematics and statistical physics, this work draws on Hebb's theory of synaptic modification [32], Turing's biological pattern-formation mechanism [77], the symmetry analysis pioneered by Busse [10] and the magnetic spin models introduced by Heisenberg [11, 61]. Other models of cortical-map formation beginning from some form of explicit synaptic learning-rule have been developed by von der Malsburg [83] and Miller [56] and are reviewed in section 1.3. The application of spontaneous symmetry-breaking to cortical pattern-formation was pioneered by Cowan and Ermentrout [22], in the context of geometric visual hallucinations, and remains an active research topic in parallel with these studies in cortical-map formation [7, 8, 9].

1.2 Biology of Cortical Maps

The vertebrate nervous system shows a striking combination of orderly and disorderly architectures. The image below shows the averaged activity of local neuron populations in a 3x4 mm region of primary visual cortex, color-coded for the angle at which a moving grating elicits the maximal response. It appears that nearby neu-

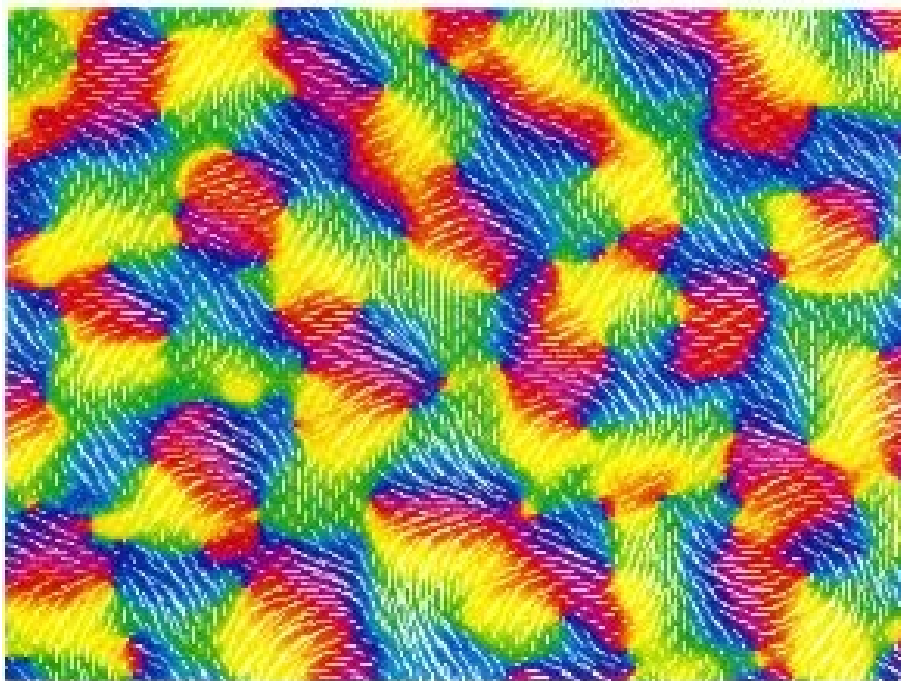


Figure 1.1: Orientation-preference map obtained by differential imaging with voltage-sensitive dyes [3]. Colorbar runs from 0 to π . Courtesy G. Blasdel.

rons (100-200 μ distant) have highly correlated orientation preferences while no order persists at longer scales (500-1000 μ)¹ At the same time, the preferred orientations of individual cells may vary widely within an apparent iso-orientation region, indicating short-range disorder [49].

To understand the origin and functional significance of this and other spatial structures in the visual system it is necessary to develop mathematical models constrained by the known anatomy and physiology. To orient the reader I will sketch biological

¹For the auto-correlation function see Figure 3.2.

background pertaining to the mammalian visual system from the eye to the primary visual cortex (V1). I will then describe in more detail the patterns of orientation preference, ocular dominance and retinotopic organization manifest in V1.

1.2.1 Anatomy and Physiology of the Mammalian Visual System

Visual System Anatomy: Eye and Thalamus

The visual system is the most thoroughly studied sensory system in vertebrates. It has an obvious spatial structure, with the two-dimensional organization of each level in the eye, thalamus and cortex corresponding to the two-dimensional projection of the visual field. Visual stimuli lend themselves to ready manipulation, more so than tactile, olfactory or even auditory stimuli, and the visual cortex—located at the back of the mammalian brain (the rostral end of the occipital lobe, see Figure 1.2)—allows easy access for imaging and electrophysiology studies.

Visual stimuli affect the nervous system through the light-sensitive pigments in the rods and cones of the retina. The rods and cones activate a network of neurons with a center-surround architecture that suppresses the response to areas of uniform luminosity and enhances the response to high-contrast features such as a dark spot on a light background or a light spot on a dark background.

The mammalian thalamus, part of the midbrain, is a composite organ through which sensory signals of all modalities pass before entering the cortex. Afferent nerve fibers from the retinae contact neurons in the *lateral geniculate nucleus* (LGN) of the thalamus, forming layers segregated by eye of origin and response properties. “ON” cells in the LGN respond selectively to bright spots on dark backgrounds, and also to sudden uniform increases in light intensity. “OFF” cells respond to dark spots on light backgrounds and to sudden decreases in uniform light intensity. Both types of cells have very weak or no tuning for oriented stimuli. Although the thalamus plays a major role in regulating alertness and attention to signals from different sense organs, and may play a significant role in integrating the animal’s representation of the outside world, it has frequently been viewed as a passive transmitter of the visual image—coded in terms of spike rate—along the way to the cortex.

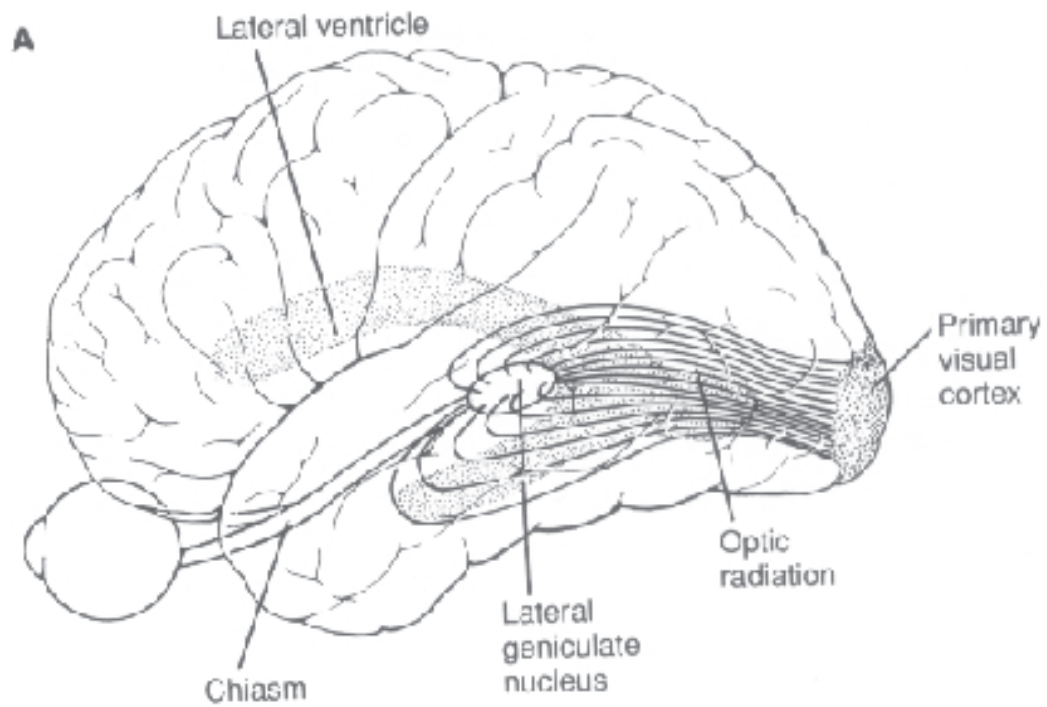


Figure 1.2: Visual pathway from the eye to the dorsal lateral geniculate of the thalamus to striate cortex, also known as V1, primary visual cortex or area 17. From Kandel *et al.*, [42].

Visual Anatomy: Primary Visual Cortex

In an attempt to discover the primary building blocks of sensory perception, neurophysiologists have recorded the selective responses of cortical cells to a collection of “elementary” visual stimuli. These stimuli may, up to a point, be ranked in order of salience.

Neurons of primary visual cortex lie in a multi-layered sheet, covering an area roughly 36 mm by 54 mm in the adult human brain, which corresponds to a distorted topographic representation of two-dimensional visual space. The *location* of a stimulus in the visual field determines most strongly a cell’s response or lack of response. For example, an arbitrarily bright point stimulus on a blank screen will illicit no statistically reliable response above the background firing rate unless it lies within a localized region of visual space, the cell’s *classical receptive field*.

Afferent fibers driven by the two eyes remain segregated in the thalamus and converge for the first time in V1. “Monocular” cells respond significantly to point stimuli only if they fall within the classical receptive field *and* impinge on a given eye. Hubel and Wiesel introduced an index for binocularity ranging from one (completely driven by the ipsilateral eye) through four (binocular) to seven (completely driven by the contralateral eye [34]).

In 1962 Hubel and Wiesel discovered the third principal determinant of V1 neuron response: *orientation tuning* [35]. While measuring the receptive-field properties of cortical neurons in area 17 of cat, they found many cells that responded only to bar or edge stimuli oriented within a roughly thirty-degree range, centered on a preferred orientation that elicited maximal response. In contrast to the geniculate cells that immediately preceded them in the visual pathway, the typical cortical cells had very weak responses to circularly symmetric high-contrast stimuli. Furthermore, Hubel and Wiesel discovered that the cells’ response characteristics had a *columnar organization* [40]. Penetrating the cortex with an electrode perpendicular to the surface, they found cells in all layers that responded to roughly the same preferred orientation, and also to the roughly the same position in visual space. When penetrating the cortex laterally, they observed that the preferred orientation changed gradually,

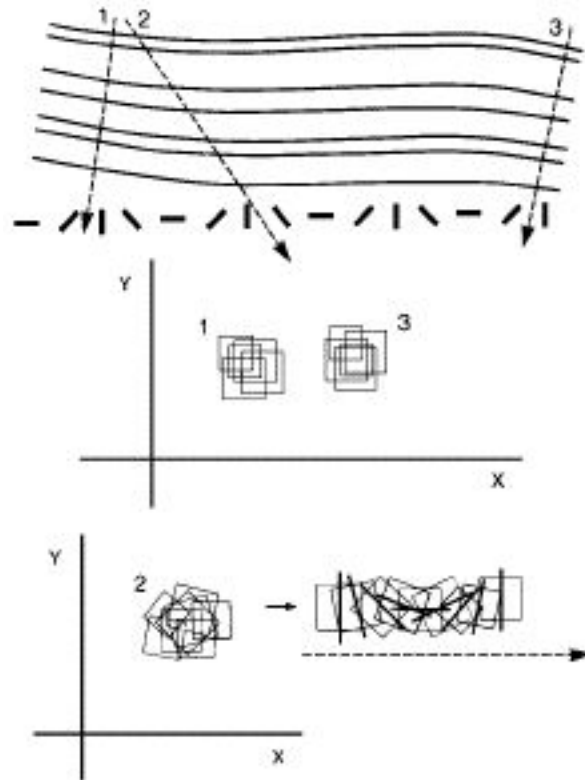


Figure 1.3: Columnar organization of orientation preference. Using microelectrode penetrations, Hubel and Wiesel found that receptive fields in a vertical penetration tended to align along the same axis, giving all the cells in a column of cortical tissue a similar preference for oriented bars. Cells in a column also responded to the same position in visual space, with some scatter. Moving tangentially along the surface the orientation varies, changing roughly by π every millimeter, with occasional sudden jumps (not shown). From Gilbert 1992 [29].

at a rate of roughly a full period π every mm, with occasional sudden jumps by as much as $\pi/2$ (see Figure 1.3).

Hubel and Wiesel proposed a mechanism for the origin of cortical orientation selectivity that continues to motivate theoretical and experimental efforts [28, 35]. Their *feedforward model* for orientation tuning supposes that cortical cells receive synaptic input from elongated subregions within their receptive fields, alternating between ON-center and OFF-center geniculate cells. A moving light (or dark) bar aligned with the direction of elongation will excite the cortical cell as it simultaneously triggers all the ON-center (or OFF-center) cells, and stops inhibiting the adjoining region of

opposite polarity. A moving bar oriented in the wrong direction will simultaneously excite some of the cells of one polarity while inhibiting others of the opposite, and the cortical cell will not receive enough input from its receptive field to cross its threshold. Evidence for anisotropic patterns of feedforward input has accumulated, although a role for lateral cortico-cortical interactions in orientation selectivity have not been ruled out [28].

1.2.2 *Physiology: Cortical Maps*

The primary determinants of neural response within the classical receptive field—topography (or retinotopy), ocular dominance and orientation preference—have well-characterized spatial organization across the cortical surface.

The efferent fibers from the LGN converge on the visual cortex in a topographically ordered fashion, preserving neighborhood relations originating in the retina. The topography of the cortical representation of space, defined as the map from the location of a cell in the cortex to the center of its classical receptive field in visual-field or retinal coordinates, is determined in part by the decrease in the packing density of retinal ganglion cells with eccentricity in the visual field. Taking (r, θ) as polar coordinates in the retina, the packing density decreases as roughly ²:

$$\rho \propto \frac{k_1}{(1 + k_2 r)^2}.$$

Meanwhile, the cell density is very nearly constant across V1. Rays extending from the center of the visual field correspond to medial-to-lateral (horizontal) lines in V1 away from the foveal area, and concentric circles in the visual field correspond to dorso-ventral (vertical) lines in the cortex. Assuming that each retinal ganglion maps to the same number of cortical cells, the differential packing density determines a magnification factor $\mu = 1/\rho$ from which we can infer the coarse retino-cortical map. Near the foveal representation this map approximates the identity $x_1 = r \cos \theta; x_2 =$

²This approach to deducing the retinotopic map was introduced by Schwartz [65].

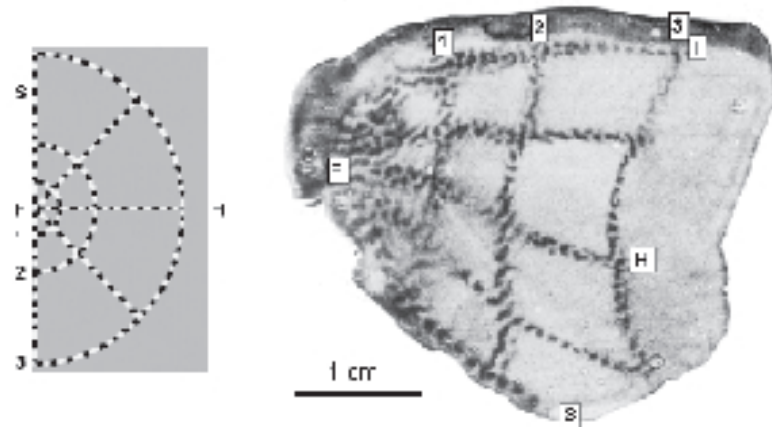


Figure 1.4: Retino-cortical map visualized by deoxyglucose autoradiograph. After injection of the metabolic indicator, the animal viewed the pattern on the left as it was inverted (black-to-white) at full contrast. From Tootell [75], as modified by Swindale [72]. ‘S’ indicates superior visual field, ‘I’ indicates inferior. ‘F’ indicates foveal region, ‘H’ indicates horizontal meridian. The concentric circles were located at 1° (‘1’), 2.3° (‘2’) and 5.4° (‘3’) eccentric to the fovea, respectively.

$r \sin \theta$, to first order; in the periphery it approximates the complex logarithm ³:

$$x_1 = \log r$$

$$x_2 = \theta$$

This map may be visualized using metabolic markers such as cytochrome oxidase immunoreactive stains or deoxyglucose autoradiograph techniques (see Figure 1.4). On a smaller scale, say a two or three mm-square region of cortical surface, the topography may be taken to be a linear map of retinotopic coordinates. On this scale

³See [15].

we may approximate the cortical sheet as a plane with coordinates⁴

$$x := [x_1, x_2]^{\text{tr}} \in \mathcal{X}.$$

Similarly a small region of the LGN may be represented by its retinotopic coordinates

$$r := [r_1, r_2]^{\text{tr}} \in \mathcal{R}$$

The retinotopic map of the cortex, $R : \mathcal{X} \rightarrow \mathcal{R}$ is smooth and 1 : 1 on this scale and so we can impose coordinate systems on \mathcal{X} and \mathcal{R} such that the Jacobian of the map is always positive. Therefore we may locally approximate the retino-cortical map as a linear mapping from \mathbb{R}^2 to itself.

Given a linear map from \mathbb{R}^2 to \mathbb{R}^2 , we can represent the local anisotropy in the map as a vector, the magnitude of which represents the ratio of the eigenvalues of $J = \partial R / \partial x$, and the direction of which indicates the cortical direction corresponding to the greatest retinotopic stretching. This direction parallels the first principal eigenvector of J (see Appendix A.3). The determinant of J is the retinocortical magnification, the retinal (or thalamic) area represented per unit cortical area. On a sufficiently coarse scale the curvature of the cortical surface and of the complex logarithmic map invalidate the affine linear description of the mapping.

The retinotopic position map assigns nearby cortical cells to nearby points in the visual field—it is *topographically organized*. The ocular-dominance characteristic of a cortical cell, a scalar quantity, is also topographically mapped. Experiments with dyes that trace the anatomical connectivity from the right or left eye, metabolic tracers that are taken up selectively by some cortical cells when one eye is closed, and electrophysiological recordings all indicate a topographic arrangement of ocular

⁴Vectors in the idealized cortical, thalamic and/or retinal plane will be implied by x , r , etc. Consistent with MATLAB conventions, I take vectors to be *column vectors*, $x = \begin{bmatrix} x_1 \\ x_2 \end{bmatrix}$, unless indicated otherwise. The *transpose* of a matrix or a vector will be denoted by superscript “tr”. Hence $x^{\text{tr}} := [x_1, x_2]$, and $\begin{pmatrix} a & b \\ c & d \end{pmatrix}^{\text{tr}} = \begin{pmatrix} a & c \\ b & d \end{pmatrix}$. Cortical map vectors will occasionally be denoted via bold face, such as $\mathbf{v}(x)$.

dominance in V1 [40]. Nearby cells tend to be driven by the same eye (continuity) while both eyes are present within any 800-micron-wide region. The underlying pattern resembles zebra stripe in some species, or spot patterns in others (see Figure 1.5).

The local shear in the retinotopic map of Macaque monkeys, at the scale of ocular dominance columns, has been estimated at $\eta \approx \sqrt{2}$. It is believed that this anisotropy may reflect the interaction of the retinocortical map with the arrangement of ocular dominance stripes on the cortical surface⁵. In addition to this locally uniform shear, there is finer-scale distortion of the retinotopic map at the hypercolumn and sub-hypercolumn level.

On a sub-millimeter scale, Das and Gilbert have recently succeeded in measuring distortions and discontinuities in the retinotopic map that seem to coincide with locations of rapid variation of preferred stimulus orientation[18]. The mapping properties of the cortex require attention at different scales, from tens of millimeters to a hundred microns. At each scale it is of interest what the shape of the coarse map is and what the deviations of the average retinotopy are on one scale from the average retinotopy on a larger scale. In principle we can represent the deviation from the mean retinotopy as the difference between the local retinotopy $R(\underline{x})$ and a mean retinotopy averaged over an appropriate scale, $(g_\sigma * R)(\underline{x})$, i.e.⁶

$$\begin{aligned} \underline{s}(\underline{x}) &= R(\underline{x}) - \int_{\underline{x}'} g_\sigma(\underline{x} - \underline{x}') R(\underline{x}') \underline{d}x' \\ g_\sigma(\underline{x}) &= \frac{1}{2\pi\sigma^2} \exp(-\|\underline{x}\|^2/2\sigma^2) \end{aligned}$$

In 1986, Blasdel and Salama pioneered the measurement of orientation and ocular-dominance maps by direct observation of the cortical surface during stimulation of the visual system [5]. First with voltage-sensitive dyes, and later through imaging of intrinsic metabolism-related optical signals, researchers were able to construct

⁵G. Blasdel, personal communication.

⁶Recall that x and x' are planar vectors, so we are convolving with the product of two one-dimensional Gaussians.

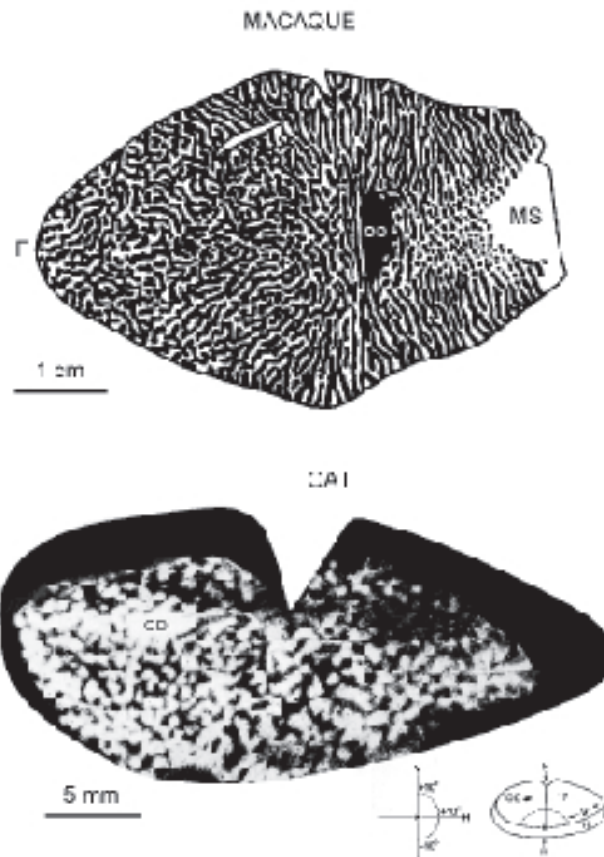


Figure 1.5: Ocular dominance maps in cat and monkey. Cytochrome oxidase techniques reveal the pronounced spatial structure for ocular dominance. Marker injected into one eye was carried up the visual pathway to the cortex where it stained cells predominantly driven by that eye but not the other. The resulting patterns show irregular stripes at a typical wavelength of 300-400 microns in macaque monkey, and blobs with a similar spacing in cat. From Swindale 1996 [72].

vector maps of orientation preference and selectivity over cortical regions many hypercolumns in extent [2, 3, 6] (see Figure 1.1). These maps showed quasi-regular lattices of *orientation singularities* separated by *linear zones* where orientation varied continuously, and *fractures* where orientation changed suddenly.

The differential imaging techniques for boosting the optical signals above noise require smoothing the data by spatial and temporal averaging. Therefore, while the resulting image appears quite smooth and the centers of the pinwheels seem precisely defined, the underlying distribution of individual cellular responses could in principle be quite heterogeneous. The magnitude of the vector field obtained by optical methods, representing the sharpness of the orientation tuning at a given position, drops smoothly to zero orientation preference at the centers of the singularities. From this data it is impossible to infer the variance of the local distribution of individual cells' peak orientation preferences. Because of these statistical ambiguities it is essential that a model for the organization of the system be flexible enough to incorporate a variable amount of local scatter in orientation preference (or ocular dominance, topography, etc.) as part of the descriptive parameters.

Studies by Maldonado and Gray attempted to quantify the typical amount of nearest-neighbor scatter in preferred orientation by simultaneous recording of the responses of nearby cells. They confirmed that significantly more scatter might be present than suggested by the smooth appearance of the optical imaging maps. Unfortunately they could not give decisive bounds on the variance of the local distributions of preferences.

Spatial-Frequency Preference

In 1997 Hübener and colleagues reported using optical imaging to identify the spatial distribution of *spatial-frequency preference* [41]. After recording the optical images generated when cats viewed grating patterns of different orientations and different stripe widths, Hübener *et al.* pooled the response magnitudes to higher and lower sets of spatial frequencies and compared the differences in response, averaging over all orientations. They reported finding isolated regions of V1, roughly the size of

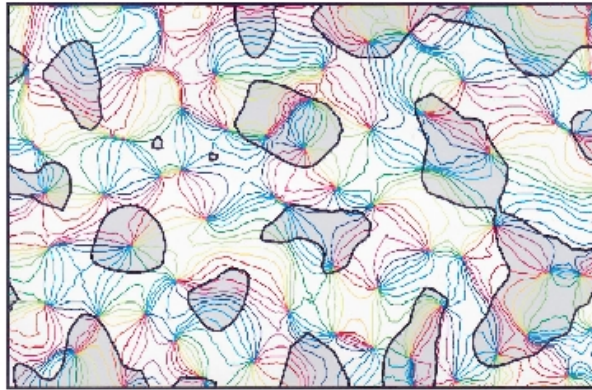


Figure 1.6: Spatial-frequency preference map: from Hübener *et al.*, [41].

orientation columns, that were more responsive to low spatial frequencies. Moreover, roughly half the orientation singularities measured were located inside these low-spatial-frequency zones, while the other half were in the connected region more responsive to higher spatial frequencies⁷. The distribution of orientation preference and high-*vs.*-low s.f. regions measured by Hübener *et al.* are shown in Figure 1.6.

Interactions between map components

Perhaps the most striking characteristic of these cortical maps is the degree of *co-ordination* between them. In monkeys the ocular-dominance bands are elongated and “stripelike”, and the orientation pinwheels show a strong tendency to lie at the centers of these stripes [60]. In cats, the ocular dominance bands are more compact and “bloblike”, and the orientation pinwheels are typically located near the extremal points of the ocular dominance [17]. Consistent with this arrangement, the gradient of the ocular dominance tends to lie orthogonal to the gradient of the preferred orientation[25]. The orientation pinwheels are reported to coincide with the fine-scale retinotopic dislocations reported by Das and Gilbert, and while spatial maps of chromatic preference have not yet been published, the color-sensitive cells are thought to

⁷The connectedness of the high-sf population is of course dependent on the spatial frequency chosen to distinguish “low” from “high”.

be concentrated in regions of higher metabolic activity which also coincide with the pinwheels (cytochrome oxidase “blobs”).

1.2.3 Development of the Mammalian Visual System

Time-Course of Development

As the animal develops embryologically, nerve fibers from the contralateral (opposite-side) eye project to the LGN, and then to the cortex, before the corresponding fibers from the ipsilateral (same-side) eye. In cats, orientation-selective cells can be observed as early as the eighth day after birth, and orientation maps can be obtained from optical imaging as early as the twelfth postnatal day. If stimuli are presented through the ipsilateral eye, the optical imaging reveals a very disordered map [16]. At the same time, the response to stimuli presented to the ipsilateral eye is weak overall—that is, the entire V1 is approximately monocular. Under normal developmental circumstances, the ipsilateral fibers become established between postnatal days 7 and 21, with the second eye’s orientation map matching the already extant map. Gradually the influence of the two eyes evens out until there are ocular dominance regions of equal size for each eye. If the eyelids are sutured so that no patterned visual experience occurs through the second eye, the orientation preferences develop normally until sometime in the third week after birth at which point they decay until the ipsilateral eye has no recognizable orientation pattern. Simultaneously the net input weight from the deprived eye appears to decay as well.

Correlation-Based Learning

The functional interaction of different parts of the brain depend in large part on the extent and arrangement of synaptic connections between them. A given synapse between an axon and a dendrite or cell body may be more or less potent, as the amount of neurotransmitter typically released for every action potential in the axon is not a fixed quantity. Furthermore, a given axon may make multiple synapses onto the dendritic arbor and soma of the postsynaptic cell. These two sources of variability lend

a continuous nature to the synaptic efficacy with which one cell influences another, represented in models as the *synaptic weight*. In much of theoretical neuroscience the problems of learning, memory, computation and development may be cast as problems of the variation of synaptic weights appropriate to some task between different neural tissues. The patterns of ocular dominance, orientation preference and topography have their origin in patterns of the distribution of synaptic weights between the LGN and the cortex, or within and between different cortical layers, although they may also arise in part through dynamical effects which have more to do with spatiotemporal patterns of spiking than with quasi-static synaptic weights. In the case of ocular dominance it is especially clear that the phenomenon involves inhomogeneous distribution of synaptic weight, preferentially coming from one eye or the other; metabolic labeling and biocytin injection experiments which trace out connectivity patterns come close to measuring the synaptic weights – as in the number and size of synapses—directly.

The synaptic weights may vary in the organism by the growth of new synapses, expansion and reinforcement of existing ones, and weakening or elimination of synapses. Such a rule could be based for example on strengthening or weakening the synaptic strength from a particular cell when that cell's incoming action potentials are more strongly correlated with the recipient cell's firing than those of the other synapses. Alternatively the cell could weaken correlated synapses and strengthen uncorrelated ones, or strengthen both the most highly correlated excitatory synapses and the most highly anti-correlated inhibitory synapses. All these variants amount to *correlation-based learning*, first clearly stated by Donald Hebb in his 1949 book *The Organization of Behavior*.

When an axon of cell A is near enough to excite a cell B and repeatedly or persistently takes part in firing it, some growth process or metabolic change takes place in one or both cells such that A 's efficiency, as one of the cells firing B , is increased. [32, page 62]

This reasoning leads naturally to the hypothesis that the synaptic strength between two cells should be affected by cross-correlations in their firing. If impulses from

a presynaptic cell regularly participate in firing a postsynaptic cell, then the strength of that synapse should tend to increase; negative correlations in firing should force a synapse to lose strength. Thus a network of interacting neurons could “learn” the correlation structure of an ensemble of inputs by following some variant of a Hebbian developmental rule. With various modifications, Hebb’s rule has remained a centerpiece of our understanding of the physiology of learning and self-organization, and remains the basis of the models to be discussed in the next section.

1.3 Correlation-Based Models of Cortical-Map Formation

1.3.1 Hebb's Rule

In its simplest incarnation, Hebb's rule sets the adjustment of weights proportional to the correlation over a learning interval

$$\Delta w(x, r) \propto \langle I(r)a(x) \rangle . \quad (1.1)$$

Here r denotes the location of a cell sending out ascending fibers, such as retina or LGN, which then synapse on tectum or cortex at x . $I(r)$ is the activity in the lower level (or the *input*) and $a(x)$ is the activity in the higher level. In this form the rule may be unstable: once the synaptic weights find an optimal pattern so that $\langle I(r)a(x) \rangle$ is everywhere positive, they are liable to grow without bound. To remedy this instability, various means of constraining the synaptic weights have been introduced. It is also common to construct some form of competition for synaptic weight between cells in a given neural network layer.

Synaptic Models *vs.* Feature Models

Models based on competitive Hebbian learning generally take two forms: *Synaptic models* treat the formation of cortical maps in terms of developmental rules for the synaptic weights that underlie a cortical cell's receptive field properties. *Feature models* use heuristically derived rules to treat the development of cortical maps directly in terms of abstracted quantities such as orientation and ocular dominance. These models barter realism for complexity, with the synaptic model making explicit use of correlated thalamic and cortical activity and dynamics based directly on Hebbian mechanisms. In order to prevent the unbounded growth of a rule such as 3.3, synaptic models must incorporate explicit constraints on the growth or decline of synaptic weights. Most modeling efforts have used hard saturations in which the weight dynamics are discontinuous at an upper or lower boundary. In these cases the analysis of pattern formation, as spontaneous destabilization of a rapidly grow-

ing mode, may only be applied in a small neighborhood of some initial homogeneous configuration (such as unoriented receptive fields). A more thorough analysis of the systems's behavior is usually possible for abstract models that dispense with detailed constructions of cortical cell properties from synaptic weight distributions. But while pattern formation may be more readily studied in feature models, their biological interpretations can be unconvincing [54, p. 69].

Comprehensive reviews of modeling approaches to cortical maps are presented in [25] and [72].

1.3.2 Turing Mechanism for Pattern Formation

Mathematically, both the feature and synaptic models exploit a simple mechanism for spatial pattern formation. A homogeneous initial state—be it unoriented receptive fields, uniform input from both eyes, or a zero vector field in some abstract space—loses stability to an eigenmode of the linearized correlation-based dynamics. In some models, nonlinearities serve to select between different modes or combinations of modes and stabilize an inhomogeneous steady state, but in most, this stabilization is either implicit or forced by nonanalytic constraints.

The visual cortex is not the first biological tissue to attract attention to its spot and stripe patterns (see Figure 1.7). In 1952, Turing introduced a theory for the formation of spatially inhomogeneous patterns by a spatially homogeneous system of equations [77, 59]. Turing proposed a reaction between two morphogens in the embryonic skin, one of which would serve as a precursor for local pigmentation. If both morphogens were autocatalytic and one inhibited the production of the other—which in turn promoted the production of the first—then a steady-state uniform admixture of the two could lose stability if the inhibitor diffused more quickly than the promoter. The basic mechanism was a linear instability favoring a particular wavelength, determining the size of the ensuing stripe or spot periodicity.

The essence of the mechanism may be illustrated in the neural context with a



Figure 1.7: Animal Coat Patterns. **Top:** Zebra. **Middle:** Leopard. **Bottom:** Cattle.

single-variable integral equation:

$$\frac{\partial a(x, t)}{\partial t} = f(a) + \int_{x'} A(x - x') a(x', t) dx' \quad (1.2)$$

Here $a(x, t)$ represents the time-varying activity at cortical location x , $A(|y|)$ is an intracortical interaction between cortical units separated by distance $|y|$, presumed to be an even function, and $f(a)$ is a local cortical dynamics in the absence of lateral influence. For example, $f(a)$ may have the form $a(a - a_u)(a - a_s)$, $a_u < a_s$. For this function $a = 0$ and $a = a_s$ are stable fixed-points, while $a = a_u$ is unstable. Suppose that we begin with initial conditions smooth enough to expand a in a Taylor series in x . Integrating by parts, we may write

$$\frac{\partial a(x, t)}{\partial t} = f(a) + a(x, t) \int_y A(y) dy + \frac{\partial^2 a(x, t)}{\partial x^2} \int_y \frac{y^2}{2!} A(y) dy + \quad (1.3)$$

$$\frac{\partial^4 a(x, t)}{\partial x^4} \int_y \frac{y^4}{4!} A(y) dy + \dots \quad (1.4)$$

$$= f(a) + A_0 a(x, t) + A_2 \frac{\partial^2 a(x, t)}{\partial x^2} + A_4 \frac{\partial^4 a(x, t)}{\partial x^4} + \dots \quad (1.5)$$

If the lateral interaction has a nonzero sum it can be incorporated into $f(a)$, so we can assume that $A_0 = 0$. Now make the ansatz that there is a mode of inhomogeneity about the steady state described by $a(x, t) - a_s \approx \varepsilon e^{\sigma t} e^{ikx}$, where k is a wave-vector and $0 < \varepsilon \ll 1$. Substituting into equation 1.3 gives

$$\sigma = -f'(a_s) + |k|^2 A_2 - |k|^4 A_4 + \dots$$

Positive σ for a given k indicates decay of that mode toward the steady state. If A_2 and A_4 are both negative, the dispersion curve $\sigma(|k|^2)$ has a minimum at a nonzero value of $|k|^2$. When the local dynamics has a sufficiently robust steady state, *i.e.* $f'(a_s) \ll 0$, all modes decay and the homogeneous state is stable. Should $f'(a_s)$ weaken, there is a critical mode k_* at which the homogeneous state first loses stability, as shown in Figure 1.8.

For a typical center-surround lateral interaction such as a difference of Gaussians

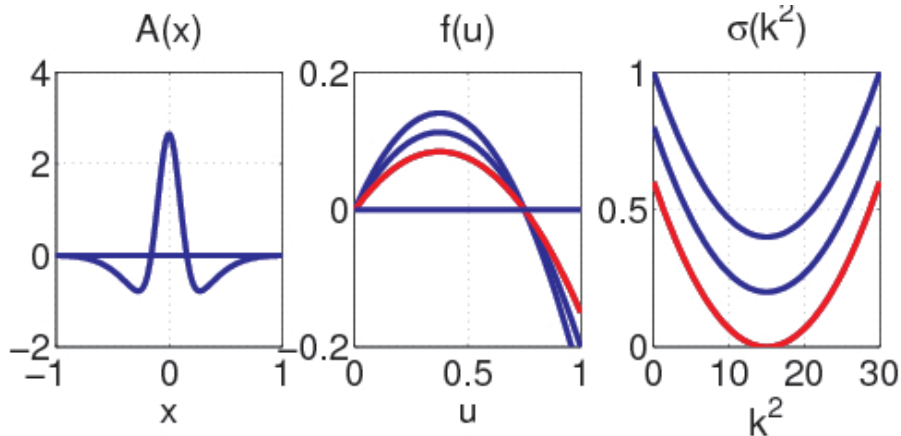


Figure 1.8: Schematic Turing mechanism for pattern formation.

Left: Lateral cortico-cortical interaction $A(x)$, modeled as a broad Gaussian subtracted from a narrow one.

Center: Local steady-state dynamics $f(a)$. When the derivative of f at the steady state is not sufficiently negative to damp all modes, instability sets in (lower curve).

Right: Dispersion curve $\sigma(|k|^2)$. The critical wavelength occurs at the minimum of the curve.

(see Figure 1.8) all the even moments are negative except A_0 . The instability of the homogeneous state arises because of the “anti-diffusion” term $A_2 < 0$, while the wavelength is determined by both A_2 and A_4 .

1.3.3 Turing Analysis of Competitive Hebbian Learning

Tea-Trade Model

In 1977 Willshaw and von der Malsburg introduced the “tea-trade” model for the establishment of a globally ordered topographic map from the eye to the brain, based on an analogy to Hebbian learning and chemical markers [78]. Imagine local tea growers in India each with a slightly different blend of flavors than her neighbors. The concentrations of the different ingredients of tea we suppose vary continuously across the face of the subcontinent. Traders from Britain buy the local teas and distribute them around England. Local tastes in tea we also suppose vary topographically across the island so that nearby towns prefer flavors from nearby towns in India. Further assuming that each trader can carry only a limited tonnage of tea, we suppose that

each will tend to strengthen contacts with the best customers while weakening ties with the rest. Gradually each trader gets more specialized both in collecting and distributing according to local flavors and local tastes, and eventually the network of traders establishes a topographic reproduction of India within the borders of Britain, and vice versa.

Replacing the teas by (unidentified) chemical markers which diffuse across the retina, and traders by fibers synapsing on various parts of the tectum, this heuristic model suggests how a topographic map of the retina may be established [78, 83].

Häussler and von der Malsburg's Analysis

Expanding on the tea-trade model, Häussler and von der Malsburg analyzed the development of a one-to-one retinotopic mapping between a one-dimensional retina and tectum [31]. Their model incorporates local correlation or smoothing and competition mediated by saturating the net input or output weight at a point. Beginning from diffuse initial weights Häussler and von der Malsburg model the retinotectal map as a spontaneous symmetry-breaking phenomenon. An ordered map forms due to the selection of an appropriate mode in a Turing-like pattern-forming process (Figure 1.9).

Häussler and von der Malsburg's system obeys the differential equation

$$\frac{d}{dt}w(x, r) = \alpha(1 - w(x, r)) + \beta w(x, r) \left\{ \begin{array}{l} \int_{x' \in X} \int_{r' \in \Omega} C_x(x - x') C_r(r - r') w(x', r') dx' dr' \\ - \frac{1}{2} \left(\begin{array}{l} c_x \int_{r' \in \Omega} C_r(r - r') \int_{x' \in X} w(x', r') dx' dr' + \\ c_r \int_{x' \in X} C_x(x - x') \int_{r' \in \Omega} w(x', r') dr' dx' \end{array} \right) \end{array} \right\} \quad (1.6)$$

where $c_r = \int_{r \in \Omega} C_r(r) dr$, $c_x = \int_{x \in X} C_x(x) dx$, and $\Omega = [0, 1)$ and $X = [0, 1)$ are the retinal and tectal domains, respectively. They impose periodic boundary conditions for both x and r , and assume a Gaussian form for both the correlation-based terms $C_r(r)$ and $C_x(x)$. The double convolution in x and r smooths the existing map locally,

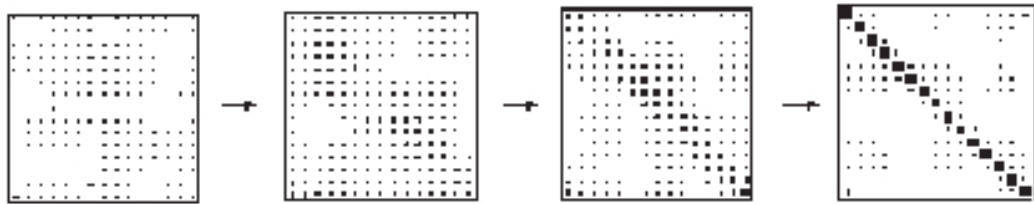


Figure 1.9: Illustration of one-dimensional retinotectal map formation. Figure from Häussler and von der Malsburg, “Development of Retinotopic Projections: an Analytical Treatment” [31]. The synaptic strengths connecting a one-dimensional retina and tectum form a matrix whose entries are represented by the size of the small squares. The initial conditions were biased to select the “correct” diagonal. Abcissa: retinal position. Ordinate: tectal position.

effecting local cooperation in forming connections. The subtraction of the two single convolution terms guarantees that neither the net fan-in weight to any tectal point x

$$\lambda(x) = \int_{r \in \Omega} w(x, r) dr$$

nor the net fan-out weight from any retinal point r

$$\gamma(r) = \int_{x \in X} w(x, r), dx$$

can grow without bound. These saturation terms effect a lateral competition between different points on the retina and tectum. This combination of local facilitation and lateral competition is the heart of the Turing pattern-formation mechanism.

For $\alpha \gg \beta$ the homogeneous state $w(x, r) \equiv 1$ is stable. At a critical value of β/α this homogeneous state loses stability and a critical mode appears. Nonlinear stability analysis of small plane-wave perturbations of the steady state,

$$w(x, r) = 1 + \varepsilon (\exp(i2\pi(k_r r + k_x x)) + \text{c.c.}), (k_r, k_x) \in \mathbb{Z}^2, \quad (1.7)$$

shows that the higher-order terms select the modes $k_r = \pm k_x = \pm 1$, corresponding to a one-to-one retinotectal map. The selection of the +1 orientation over -1 requires an additional mechanism such as a chemical marker or bias in the initial conditions.

Miller's Model for Receptive-Field Formation

The most comprehensive approach to cortical-map formation through synaptic models has been the work of Miller and colleagues [55, 54, 86, 87, 24, 52, 56, 53]. As in the work of Willshaw, Häussler and von der Malsburg, the map of cortical selectivity is determined by the pattern of thalamocortical afferents. Miller assumes a linear dynamics, derived from the linearization of a nonlinear Hebb rule about a homogeneous steady state, with hard upper and lower-bound synaptic limits to the growth or decay of synaptic weights. Weight development is determined by a fixed pattern of lateral cortical interactions $I(x - x')$, typically with a center-surround architecture, a

distance-dependent correlation function $C(r - r')$ describing the statistics of geniculate activity, and a proscribed *arbor function* $\text{Arb}(x - r)$. The arbor function defines a rough retinotopic map on the cortex by restricting the total synaptic weight to lie under a Gaussian-like envelope⁸. This retinotopic map is assumed to be linear and isotropic.

Miller achieves pattern formation by setting up competition between different thalamic (input) cell types j distinguished by their mutual correlation functions. In modeling ocular dominance, the cell types represent the right and left eyes, with cross-eye correlations $C_{RL}(r - r')$ weaker than same eye $C_{RR}(r - r') = C_{LL}(r - r')$ or even negative. In modeling orientation, the cell types represent inputs from ON-center and OFF-center cells. In modeling the emergence of directional-selective cells, the eye classes include lagged and non-lagged geniculate cells.

The dynamics are typically given by an equation such as:

$$\frac{d}{dt}w_j(x, r) = \eta \text{Arb}(x - r) \left(F_j^U[\mathbf{w}](x, r) - \frac{\sum_j \int_r F_j^U[w](x, r) dr}{4|\text{Arb}|} \right) \quad (1.8)$$

$$F_j^U[w](x, r) = \int_{x'} I(x - x') \sum_{j'} \int_{r'} C_{jj'}(r - r') w_j(r', x') dr' dx' \quad (1.9)$$

Here j runs through the different eye classes. The unconstrained update rule 1.9 reflects a fixed retinotopy imposed by the arbor function, which also provides hard upper bounds for the synaptic weight from r to x .

The formation of orientation-selective cortical cells is achieved as the receptive field selectively boosts synapses from elongated ON-center and OFF-center subregions, just as in the Hubel-Wiesel feedforward model. A dispersion curve determined by $I(x - x')$, the intracortical interaction function, determines a length scale for the fastest-growing orientation-tuning mode. The selection of a most-unstable wavelength gives spatial frequency selection in the ON/OFF-center competition case; in the Right/Left-eye case wavelength selection determines the periodicity of the ocular dominance stripes.

⁸Miller's $I(x - x')$ corresponds to the center-surround convolution kernel $A(x - x')$ I will use in the following Chapters to denote the intracortical interaction. To avoid confusion I will substitute "Arb($x - r$)" for Miller's $A(x - r)$.

For certain parameter values it is possible to model the development of ocular dominance and orientation simultaneously by including both Right/Left and ON/OFF-center eye classes. The maps developed in this fashion do not quite reproduce the observed relationship between ocular dominance and orientation. Because the model uses a fixed arbor shape, within which individual synaptic units may be relatively stronger or weaker, it is inflexible with respect to retinotopic distortions or anisotropy. In simulations the orthogonality of iso-orientation and ocular dominance contours emerges as a consequence of the hard constraints, and cannot be investigated analytically.

1.3.4 *Feature Models*

Feature models seek to avoid the analytical limitations inherent in explicit modeling of intricate biological phenomena such as the sculpting of receptive fields by Hebbian modification of each individual synapse. Instead, these more abstract models deal with map variables such as orientation or spatial frequency directly, and attempt to formulate *heuristic* update rules reflecting the underlying mechanisms of local cooperation and lateral competition. A good example is Swindale's model for the joint formation of orientation and ocular dominance.

Swindale's Model for the Joint Development of Ocular Dominance and Orientation Preference

In 1980, Swindale [68] derived a dynamical system for the organization of ocular dominance columns from a set of heuristic rules. Whatever mechanism might underlie the establishment of ocular dominance, he reasoned that nearby neurons should develop similar eye preferences while those further apart should develop opposite. By following such guidelines, the cortex could achieve the competing goals of continuity of representation and local coverage of all stimulus attributes. Swindale studied the

behavior of the integro-differential equation

$$\frac{\partial n(x, t)}{\partial t} = \left(\int_{x'} A(x - x') n(x', t) dx' + K \right) (1 - n^2(x, t)) \quad (1.10)$$

as a model for ocular dominance development. $A(y)$ is the effective lateral cortical interaction between cells of the same eye class (typically a difference of Gaussians), $-1 \leq n(x) \leq 1$ represents the ocular dominance, and K represents possible asymmetry in the interaction between the different eye classes. The term $(1 - n^2)$ is a multiplicative constraint that effectively shuts down the development at x when $n(x)$ reaches ± 1 . For $K = 0$ this system forms striplike patterns from random initial conditions, and for $K \neq 0$ it can form blob or spot patterns.

Motivated by the observation that 2-deoxyglucose labeling experiments revealed striplike organization of vertical orientation preference in the striate cortex of the tree shrew, Swindale investigated the possibility that similar heuristic rules might underlie the formation of spatial patterns of orientation preference [70]. He derived another dynamical equation for an orientation vector

$$\chi(x) = \begin{bmatrix} q(x) \cos(2\phi(x)) \\ q(x) \sin(2\phi(x)) \end{bmatrix}$$

in which the π -periodic orientation preference at cortical location x is $\phi(x)$, and the strength (alternatively, the sharpness) of the orientation response is $q(x)$:

$$\frac{\partial \chi(x, t)}{\partial t} = \left(\int_{x'} A(x - x') \chi(x') dx' \right) (q_M - q(x)). \quad (1.11)$$

The multiplicative constraint prevents $q(x)$ from exceeding a maximum value q_M . This system forms pinwheel singularity patterns when started from random initial conditions, and successfully mimics the development of the orientation maps.

Finally, it is possible to knit together the orientation and ocular-dominance maps with such an abstract model more readily than in the synaptic models. By weighting the growth weight of $\chi(x)$ with a term involving a pre-established ocular dominance, Swindale showed that the orientation map could be made to locate its pinwheels

generally at the centers of the ocular dominance columns, as observed *in vivo* [74]:

$$\frac{\partial \chi(x, t)}{\partial t} = \left(\int_{x'} A(x - x') \chi(x') dx' \right) \left(1 - \left| \int_{x'} A(x - x') n(x') dx' \right| \right)^\alpha (q_M - q(x)). \quad (1.12)$$

The positive constant α slows the growth of orientation selectivity at the centers of the ocular dominance regions, allowing the surrounding regions to form without pinwheels, and forcing the pinwheel defects into the central regions.

Kohonen's Self-Organizing Map

In 1982 Teuvo Kohonen pioneered a *Self-Organizing Map* [43, 44], abstracted from competitive Hebbian learning, which learned to approximate a density function on one space by a lattice on another (in a way that could be efficiently implemented on a serial computer). When one views one space as representing the “world” or the presynaptic sheet, and the approximating lattice as a discrete “representation” or postsynaptic sheet, one recovers the sort of topographic representation achieved by the Hebbian rule. What is important for my purposes here is that Kohonen's algorithm can produce stripes or spirals in a two-dimensional geometry. As Kohonen puts it:

Stripes occur whenever a two-dimensional map tries to approximate a higher-dimensional signal distribution which has significant variance in more than two dimensions. [44, page 00]

Kohonen's algorithm uses a stochastic sampling of the feature space X ; this space is “represented” by a map $\{y_j\}$ from the vertices of a lattice $\{j\} \subset \mathbb{Z}^n$ to points y_j in the feature space X . For the retino-tectal application we take X to comprise points the visual field and y_j the visual field location represented by the tectal location $j \in \mathbb{Z}^2$. Of course in practice we only consider finite subsets of the lattice, i.e. finitely many representing cells or nodes.

Over time, the learning rule varies from coarse- to fine-grained. A neighborhood function $h_{cj}(t)$ modulates the effect of each node on its neighbors, narrowing, as time



Figure 1.10: Kohonen’s self-organizing map. The feature space X is the triangular region from which points are randomly drawn. The representing map takes points on the line to points on the plane. As the neighborhood function narrows (left to right) the map becomes more convoluted.

advances, to a delta function. A Gaussian in $|c - j|$ with decreasing variance is a typical choice. Figure 1.10 shows the evolution of a map with $n = 1$ and X a subset of the plane. As the neighborhood function contracts, the mapping becomes more convoluted and the region covered by the map becomes a better representation of the triangular region, given the limits of the topological mismatch.

The feature space X will carry a probability distribution $p(x)$ which we are to capture as faithfully as possible with $\{y_j\}$. Starting from arbitrary initial conditions on the $\{y_j\}$ (either scattered over X or lumped together), a topographic map will form if the variance in $h_{cj}(t)$ is reduced slowly enough (width $\propto 1/t$). At each timestep the algorithm reads:

1. Draw $x \in X$ from the distribution $p(x)$.
2. Find a closest node given the current map $\{y_j\}$. I.e., set $c = \operatorname{argmin}\{j; \|x - y_j\|\}$.
3. Learning step: update $\Delta y_j = (x - y_j)h_{cj}(t)$
4. Advance t (shrink h_{cj}) and repeat.

Given sufficiently slow schedule for shrinking h_{cj} this formula can be shown to converge to a topographic representation of the density $p(x)$, with a magnification factor at corresponding j given by $M(j) = 1/|\det(\partial y_j / \partial j)| \propto p(x)^{2/3}$ [63]. Lin recently showed how a modification of the update rule leads to a correct faithful representation of $p(x)$ [46].

The algorithm can be implemented efficiently on a serial computer, which is its greatest advantage over explicit Hebbian learning. The biological motivation is thus: a stimulus drawn from the ensemble $p(x)$ excites all cells to some degree but due to lateral competition in the postsynaptic sheet a single winner cell y_c —chosen as the best current approximation of the stimulus – dominates the response. This cell⁹ adjusts its representation of the outside world by unspecified means. Likewise its neighbors, to greater or lesser degree as specified by the interaction term h_{cj} , adjust their representations of the outside world accordingly.

The algorithm lacks a plausible biological scheme for the representation of the outside world and must be preassigned both the “right” dimension and topology. In addition, the analysis of the stripe-formation mechanism is complicated by the nonlinearity of the system.

Ritter and Schulten write a Markov-model description of the algorithm and derive a Fokker-Planck equation for fluctuations about the homogeneous steady state. The formation of stripes in a two-dimensional medium, which could represent *e.g.* ocular dominance, high- vs. low- spatial frequency, color preferences or orientation etc. corresponds to taking for example, a square grid of n^2 nodes indexed as $j \in \mathbb{Z}_n^2$ and the input distribution to be uniform on a rectangular solid $X = [0, 1] \times [0, 1] \times [-s, s]$. With periodic boundary conditions in the plane, there is an homogeneous state in which the nodes j regularly tile the square $[0, 1] \times [0, 1]$ at zero vertical displacement. This configuration is a steady-state solution of the Markov process in the sense that its mean displacement under the algorithm is zero, by symmetry. Ritter and Schulten showed through a linear stability analysis that this steady state is unstable to long-wavelength perturbations that are confined to the plane. These may be either transverse or longitudinal.

For sufficiently small s , however, the planar solution is stable to normal perturbations. There is a dispersion curve for the decay of perturbations perpendicular to the

⁹Throughout, references to a “cell” may generally be replaced by “local cell collective” or “unit” at the reader’s discretion. Due to individual variability in cell behavior it may be a matter of sound design to have local redundancy in the microstructure of the circuit, i.e. several cells together forming an ensemble representation as more or less one unit. See for comparison [14].

plane, which varies with s and which has a peak at a wavenumber proportional to the width of the neighborhood function. If one were to increase s to a critical value s_{cr} the steady state would lose stability to oscillations at a particular wavelength λ_{cr} . As the width of the neighborhood function goes to zero, the instability occurs at smaller and smaller wavelengths; the critical value of s , however, is independent of the neighborhood function's width in the linearized system.

Elastic-Net Algorithm

Another model based on competitive Hebbian learning was introduced in 1987 by Richard Durbin and David Willshaw. Their *elastic net* is a deterministic algorithm for establishing a topographic mapping between spaces. Instead of Kohonen's continuous space X discretely sampled according to $p(x)$ the elastic net takes N points in X to be fixed. In their original application [21] these points are the N cities which the traveling salesman must each visit once on his route. For the traveling salesman problem (TSP) the "route" comprises the M nodes $\{y_0, \dots, y_{M-1}\}$ endowed with the topology of the circle ($y_0 \equiv y_M$). To make it possible to visit each city, assume $M > N$.¹⁰

The configuration of the $\{y_j\}$ evolves down the gradient of an energy function with terms representing forces pulling each node toward each city, and internal elasticity of the network.

$$E = -\alpha K \sum_i \log \sum_j h(|x_i - y_j|, K) + \frac{\beta}{2} \sum_j |y_{j+1} - y_j|^2 \quad (1.13)$$

Durbin and Willshaw choose the neighborhood function to be a Gaussian of width K :

¹⁰The salesman must visit every city following the shortest possible route. This problem belongs the class of NP-complete computations, which is to say that the computational complexity of every known algorithm for finding the globally optimal solution grows faster with increasing N than N^p for all p .

$h(d, K) = \exp(-d^2/2K^2)$, which gives an update rule $\Delta y_j = -K\partial E\partial y_j$

$$\begin{aligned}\Delta y_j &= \alpha \sum_i w_{ij}(K) (x_i - y_j) + \beta K (y_{j+1} - 2y_j + y_{j-1}) \\ w_{ij}(K) &= \frac{1}{Z_i(K)} \exp[-|x_i - y_j|^2/2K^2] \\ Z_i(K) &= \sum_j \exp[-|x_i - y_j|^2/2K^2].\end{aligned}$$

The first term in Δy_j is an elastic force, which obeys Hooke's law with a coefficient of "fitting" elasticity αw_{ij} , which depends on the width parameter K and on the configurations of all the N cities and M nodes. In the context of the tea-trade model for synaptic plasticity we recognize w_{ij} as the synaptic weights between N presynaptic and M postsynaptic cells. The second term in Δy_j represents a "smoothing elasticity" with coefficient βK , pulling adjacent nodes along the route towards each other.

When K is sufficiently large, the smoothing energy dominates and all nodes collapse onto the centroid of the cities. As K decreases, this equilibrium becomes unstable to a series of bifurcations [20]. First, the chain begins to stretch out along the direction of the first principal component of the distribution of cities. As K diminishes, there is a second bifurcation in which the chain opens up into a loop. As K is gradually decreased, subsequent bifurcations occur until the loop passes near each city, and as $K \rightarrow 0$ each city comes to coincide with (at least) one of the nodes y_j . The tours derived in this manner were not more than about 1% longer than tours derived by other heuristic methods for identical sets of cities.

Durbin, Yuille and Szeliski also show that the energy function 1.13 has a probabilistic interpretation [20]. They take the energy function to define a Gibbs distribution

$$\begin{aligned}L(\{y_j\}, K) &= \frac{1}{(2\pi)^N K^{2N} M^N} \exp\left[-\frac{E}{\alpha K}\right] \\ &= \prod_{i=1}^N \frac{1}{M} \left\{ \sum_{j=1}^M \frac{1}{2\pi K^2} \exp\left[-\frac{|x_i - y_j|^2}{2K^2}\right] \right\} \prod_{j=1}^M \exp\left[-\frac{\beta(y_j - y_{j+1})^2}{\alpha K}\right],\end{aligned}$$

which is the product of a conditional likelihood of the positions of the cities given a particular tour, or $P(\{x_i\}|\{y_j\})$, with an *a priori* estimate of the likelihood of a tour, $P(\{y_j\})$. The *a priori* distribution for the tours favors shorter total tour lengths. The conditional probability $P(\{x_i\}|\{y_j\})$ arises if one infers the location of each city x_i independently from the set of tour points—not knowing which tour point corresponds to which city—with an assumed Gaussian error in the representations of positions of variance K^2 . It is the product of N independent conditional probabilities

$$P(x_i|\{y_j\}) = \frac{1}{M} \left\{ \sum_{j=1}^M \frac{1}{2\pi K^2} \exp \left[-\frac{|x_i - y_j|^2}{2K^2} \right] \right\} \prod_{j=1}^M$$

[20].

From Bayes' Theorem we know the conditional probability of a tour given a set of cities, $P(\{y_j\}|\{x_i\})$ is proportional to the product $P(\{x_i\}|\{y_j\})P(\{y_j\})$. Minimizing E corresponds to maximizing L , or finding the most likely tours given the city configuration. Lowering K corresponds to lowering the temperature governing the Gibbs distribution.

Spin Models

Another class of feature models, derived from the magnetic models of classical condensed-matter physics, are the “XY” models described in the next chapter. Because they provide a bridge between the biological detail of the synaptic models and the analytic insight of the feature models, they will form the subject of the rest of the thesis. Spin models are closely related to Swindale’s heuristic feature model, which may be regarded as a gradient-descent version of the mean-field of the XY-type models. Chapter 2 will introduce the XY and Ising spin models and their adaptations to modeling cortical maps. Chapter 3 will illustrate how such spin models arise naturally from the reduction of a Hebbian synaptic model. Chapters 4 and 5 extend the XY models to capture the interactions between multiple cortical-map features and analyse the pattern-formation properties of the resulting systems.

CHAPTER 2

MONTE CARLO SIMULATIONS OF THE XY FEATURE MODEL

Cowan and Friedman [13] demonstrated that a simple Hamiltonian model for a lattice of interacting magnetic spins could be adapted to capture the phenomenology of the ocular dominance and orientation maps. Within the spin lattice framework it is also possible to model, phenomenologically, interactions between maps, the critical time windows in map development and the local variation of orientation between adjacent neurons. The spin model framework may also be extended to multidimensional pattern formation.

2.1 The Classical Ising and XY Models

2.1.1 Definitions of the Classical Models

The Ising model for a lattice of interacting magnetic spins is the paradigmatic condensed-matter system for the study of critical phenomena (phase transitions). Each site of a lattice $\{i \in \mathbb{Z}_N^2\}$ has a spin that can be “up” ($z_i = +1$) or “down” ($z_i = -1$). Each pair of neighboring sites $\langle i, j \rangle$ makes a contribution to the total energy of $z_i z_j$. In addition, an external magnetic field h_i may be applied to site i . The total energy is given by the Hamiltonian function

$$H[\mathbf{z}] = -\frac{1}{2} \sum_{ij} J_{ij} z_i z_j + \sum_i h_i z_i. \quad (2.1)$$

Here J_{ij} is one when i and j are adjacent neighbors and zero otherwise, and \mathbf{z} denotes a particular configuration of all the z_i . The interaction J_{ij} wraps around the edges

of the lattice to give periodic boundary conditions. As an alternative to nearest-neighbor coupling J_{ij} may be taken to have the form of a Gaussian in the distance between sites i and j :

$$J_{ij} = Jg(|i - j|, \sigma_J^2). \quad (2.2)$$

(See A.3 for notational conventions regarding Gaussians.)

In thermal equilibrium at a given inverse temperature $\beta = 1/kT$, any one of the $2^{(N^2)}$ possible spin configurations \mathbf{z} has probability given by the Gibbs distribution

$$P(\mathbf{z}) = \frac{\exp(-\beta H[\mathbf{z}])}{\sum_{\mathbf{z}} \exp(-\beta H[\mathbf{z}])}. \quad (2.3)$$

The denominator in equation 2.3 is the partition function $Z(\beta)$.

At low temperature ($\beta \gg 1$) the system approaches a ground state in which all spins are coaligned (for $h_i \equiv 0$), corresponding to maximal magnetization. For large β , the partition function sum is dominated by the lowest energy states. As the temperature increases, nearly optimal energy states—those with relatively small numbers of misaligned spins—grow in probability relative to the pure $+1$ or -1 state. Although the pure state is always more likely than any other single configuration, the larger numbers of energetically equivalent possible disorderly states makes them more and more likely to appear at nonzero temperatures.

At high temperature ($\beta \ll 1$) the highly disordered states, with no correlation between neighboring spins, dominate. At the extreme of $\beta \rightarrow 0$, all configurations have the same probability $1/N^2$. As β increases from zero, correlations begin to appear between nearby spins. At a critical temperature β_c there is a phase transition at which the correlation length diverges and beyond which the spontaneous magnetization is nonzero.

In the closely related XY model, the binary spins z_i are replaced by planar unit vectors

$$\chi_i = \begin{pmatrix} \cos \theta_i \\ \sin \theta_i \end{pmatrix}$$

that interact according to the Hamiltonian

$$H[\underline{\chi}] = \sum_{ij} J_{ij} \chi_i \cdot \chi_j \quad (2.4)$$

$$= \sum_{ij} J_{ij} \cos(\theta_i - \theta_j). \quad (2.5)$$

Unlike the Ising model, the XY model does not exhibit spontaneous magnetization (alignment of the spins) even as $\beta \rightarrow 0$ because the θ_i are continuously variable [11, 45, 51]. A point about which path integration of $\nabla\theta(x)$ gives $\pm 2\pi$ is a *vortex* or a *spin singularity* (see Figure 2.1). The system develops vortex-antivortex pairs which are stable even at low temperatures. As the temperature increases, the phase transition occurs through the unbinding of vortex pairs; at high temperature the correlation length drops as in the Ising model.

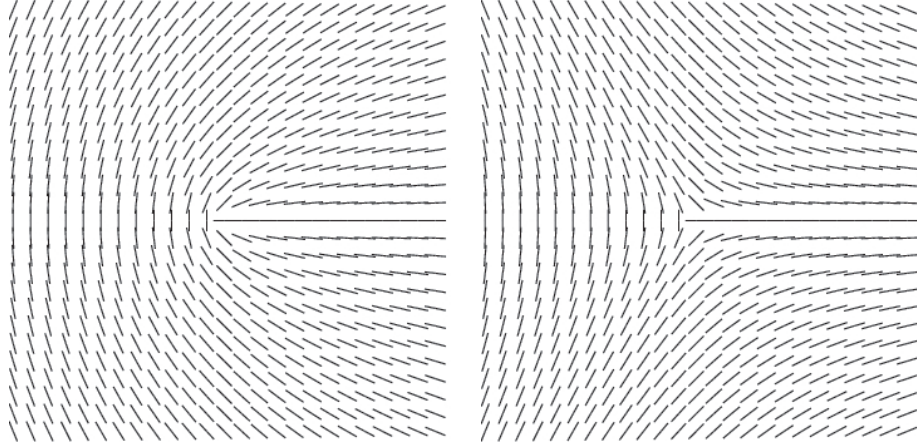


Figure 2.1: Topological point defects in the π -periodic orientation variable $\phi(x)$. **Left:** +1. **Right:** -1. Both defect patterns approach local constancy as $|x| \rightarrow \infty$.

2.1.2 Dynamical Monte Carlo Simulation

Monte Carlo simulation techniques are commonly used to generate sample spin configurations from the equilibrium distribution of a Hamiltonian system at a given temperature [1]. Beginning with some initial configuration of planar spins on an $N \times N$ lattice $\underline{\theta} = \{\theta_j | j \in \mathbb{Z}_N^2\}$, a single spin θ_i is given a chance to change its value

by choosing an alternative θ'_i according to a sampling probability conditional on θ_i , $P_{\text{samp}}(\theta'_i|\theta_i)$. In simulations, I used a wrapped Gaussian distribution on the circle (see Appendix A.3):

$$P_{\text{samp}}(\theta'|\theta) = g_{\text{wr}}(|\theta - \theta'|, \sigma_\theta^2) \quad (2.6)$$

The change in energy, should the new value be accepted, would be $\Delta H = H[\underline{\theta}'] - H[\underline{\theta}]$. The change will be accepted with probability $P_{\text{acc}}(\underline{\theta}'|\underline{\theta})$ given by Glauber's function:

$$\begin{aligned} P_{\text{acc}}(\underline{\theta}'|\underline{\theta}) &= S_\beta(\Delta H) \\ &= \frac{1}{1 + \exp(\beta\Delta H)}. \end{aligned} \quad (2.7)$$

Thus a change in configuration that yields the same total energy is accepted with probability 1/2; unfavorable (energy-increasing) alterations are accepted less often and favorable (energy-decreasing) ones more often. The acceptance criteria become stricter at lower temperatures (see figure 2.2).

The transition probability is given by the product

$$P_{\text{trans}}(\underline{\theta} \rightarrow \underline{\theta}') = P_{\text{samp}}(\theta'|\theta)P_{\text{acc}}(\underline{\theta}'|\underline{\theta}). \quad (2.8)$$

Executing this scheme yields a random walk in $\underline{\theta}$ that is ergodic in the hypertorus $\Theta = \{0 \leq \theta_j < 2\pi | j \in \mathbb{Z}_N^2\}$, meaning that every state $\underline{\theta}$ is reachable from every other state $\underline{\theta}'$ with a finite probability by some path in the random walk. Furthermore, the steady-state probability distribution of this Monte Carlo process is the Gibbs distribution

$$P(\underline{\theta}) = \frac{\exp(-\beta H[\underline{\theta}])}{\int_{\Theta} \exp(-\beta H[\underline{\theta}]) d\underline{\theta}}. \quad (2.9)$$

Let $P(\theta)$ be a steady-state probability distribution for the Monte Carlo algorithm. At equilibrium, the net probability of transition from θ to θ' must equal the net probability of the reverse transition (the ‘‘detailed balance’’ condition), i.e.

$$P(\underline{\theta})P_{\text{trans}}(\underline{\theta} \rightarrow \underline{\theta}') = P(\underline{\theta}')P_{\text{trans}}(\underline{\theta}' \rightarrow \underline{\theta}). \quad (2.10)$$

Substituting 2.6–2.8 into 2.10 yields

$$\begin{aligned}
 P(\underline{\theta})g_{\text{wr}}(|\theta - \theta'|, \sigma_{\theta}^2) \frac{1}{1 + \exp(\beta\Delta H)} &= P(\underline{\theta}')g_{\text{wr}}(|\theta' - \theta|, \sigma_{\theta}^2) \frac{1}{1 + \exp(-\beta\Delta H)} \\
 \frac{P(\underline{\theta})}{P(\underline{\theta}')} &= \frac{1 + \exp(+\beta\Delta H)}{1 + \exp(-\beta\Delta H)} \\
 &= \frac{\exp(-\beta(H[\underline{\theta}]))}{\exp(-\beta(H[\underline{\theta}']))}.
 \end{aligned} \tag{2.11}$$

Normalization of the probability distribution ensures that 2.9 holds.

In practice, it is preferable to execute the Monte Carlo algorithm "in parallel": at a given time step t a candidate new spin θ'_j is selected at each site $j \in \mathbb{Z}_N^2$ and all the transitions are decided simultaneously and independently by evaluating the change against the existing configuration $\underline{\theta}$. The new configuration is given by

$$(\underline{\theta})^{t+1} = \underline{\alpha}(\underline{\theta}')^t + (\underline{1} - \underline{\alpha})(\underline{\theta})^t$$

where α_j is 1 with probability $P_{\text{trans}}(\theta'_j|\theta_j)$ and 0 otherwise.

The algorithm converges to the Gibbs distribution in the infinite time limit, but for short time intervals it produces highly correlated states. Especially at low temperatures, it may take an extremely long time to wander through the phase space Θ . If $H[\underline{\theta}]$ has suboptimal local minima the algorithm may become "trapped" for times longer than the time available for computation, yielding metastable states. It is these states which are of interest for the cortical modeling as described below. In the low-temperature regime, the sigmoid acceptance function $S_{\beta}(\Delta H)$ approaches Heaviside's step function (see figure 2.2) so that sample points achieving a lower energy are almost invariably chosen, while those raising the energy are almost all discarded. In this extreme the algorithm's random walk is strongly biased down the energy gradient, yielding the approximate update rule

$$\Delta\theta_k \approx -\eta \frac{\partial H[\underline{\theta}]}{\partial \theta_k} = -\eta \frac{\partial}{\partial \theta_k} \frac{-1}{2} \sum_{ij} J_{ij} \cos(\theta_i - \theta_j) \tag{2.12}$$

$$= -\eta \sum_j J_{kj} \sin(\theta_k - \theta_j) \tag{2.13}$$

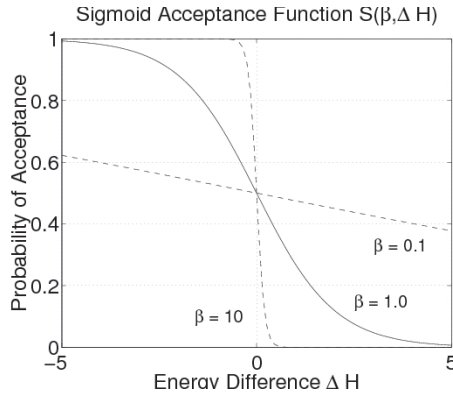


Figure 2.2: Sigmoid acceptance function for different inverse temperatures β . Increases in energy are less likely to be accepted than decreases.

where the effective rate constant η depends on σ_θ and other parameters of the simulation. Thus the metastable states are characterized by

$$\sum_j J_{ij} \sin(\theta_i - \theta_j) = 0, \forall i \in \mathbb{Z}_N^2. \quad (2.14)$$

2.2 Extension of the Classical Models to Cortico-Cortical Interaction

Two considerations make the XY model interesting for modeling the cortical maps. The available data on the structure of these maps is inherently statistical. Optical imaging data gives bulk behavior of local populations of cells, averaged together both under the optical and temporal resolution of the experimental devices. Microelectrode recordings give detailed information on the behavior of individual cells but cannot determine the spatial organization of the behavior, except along one-dimensional penetrations. As Maldonado and Gray wrote in their 1996 paper, "the variance of receptive-field properties within local clusters of cells is largely unknown" [49]. Unlike the Kohonen map and elastic net models, Monte Carlo simulations of the XY model naturally incorporate a variable degree of disorder in local receptive field properties under the guise of the thermodynamic temperature. Stretching the analogy a bit, one

may even speculate that the critical period in development corresponds to a phase transition occurring in the model as an effective temperature falls.

In addition to the advantages of a statistical model, the existence of vortices in the XY model makes it an interesting candidate for modeling the orientation map in primary visual cortex: the orientations of cells $\phi_i \in [0, \pi)$ may be mapped onto spin vectors

$$\chi_i = \begin{pmatrix} \cos 2\phi_i \\ \sin 2\phi_i \end{pmatrix}$$

and the lateral interaction J_{ij} may represent lateral interactions between neurons in the cortical network. The orientation maps observed *in vivo* exhibit a particular length scale related to the typical spacing of the orientation singularities. As confirmed by computing the autocorrelation of one of Blasdel's maps, in addition to local correlation there is lateral *anticorrelation* in preferred orientation peaking at approximately 300 microns [25].

Lateral connectivity within the cortical network involves different populations of cells with both excitatory and inhibitory interactions on different length scales. Pioneering modeling work by Wilson and Cowan [84, 85] showed how biologically plausible cortical circuits could exhibit effective lateral interactions that were locally excitatory but laterally inhibitory. Replacing the standard XY model interaction J_{ij} with a circularly-symmetric difference of Gaussians¹

$$A_{ij} = g(i - j, \sigma_+^2) - g(|i - j|, \sigma_-^2),$$

where $\sigma_- \approx 3\sigma_+$, Cowan and Friedman generated orientation maps that bore good qualitative resemblance to the Blasdel maps [13]. Using this same A_{ij} in place of J_{ij} in the Ising and XY models generate reasonable simulations of ocular dominance and orientation maps. Examples are shown in figure 2.3.

¹Gaussian notation defined in appendix A.3. For $u \in \mathbb{R}^2$, $g(u, \sigma^2) := \frac{1}{2\pi\sigma^2} \exp\left(-\frac{\|u\|^2}{2\sigma^2}\right)$.

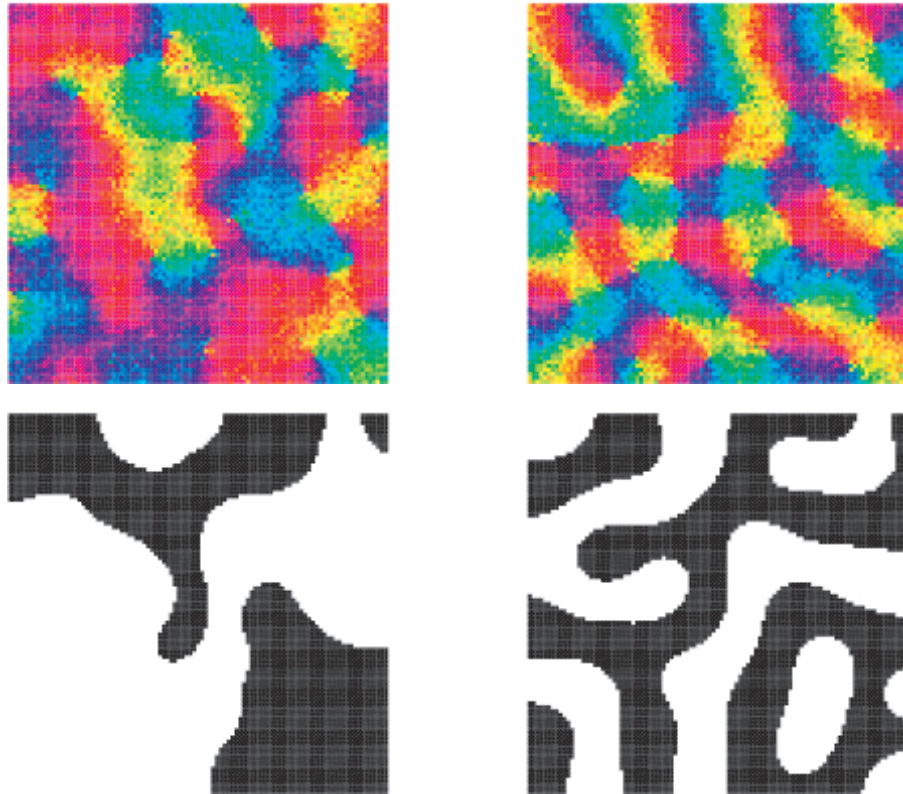


Figure 2.3: Examples of Ising and XY patterns. Sample patterns generated by the Ising and XY Models with ferromagnetic interaction J_{ij} and center-surround interaction A_{ij} . **Top:** XY models. **Bottom:** Ising models. **Left:** $J_{ij} = g(|i - j|, (60\mu)^2)$. **Right:** $A_{ij} = g(|i - j|, (100\mu)^2) - g(|i - j|, (300\mu)^2)$. Box size: 2mm.

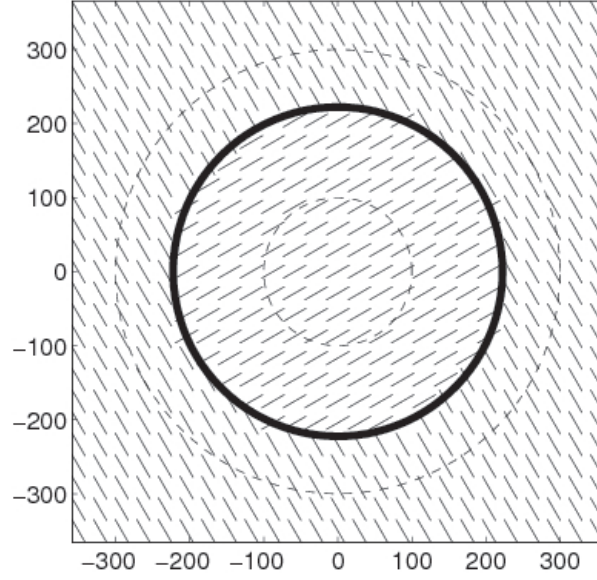


Figure 2.4: Locally optimal orientation pattern. Optimal configuration of spins surrounding a single spin in the difference-of-Gaussians XY model. The inner circle has radius σ_+ , the outer has radius σ_- , and the heavy circle indicates where $A(x) \equiv 0$. Scale units in microns.

Energy Analysis

Whereas the ground state of the classical XY model in the absence of an applied field is $\phi_i \equiv \phi_0$, for arbitrary ϕ_0 , this state has zero total energy when

$$\int_x A(x) dx = 0.$$

In the former case, a spin coaligned with its neighbors contributes as much as $-\int_x J(x) dx$ to the energy. In the latter case, the greatest possible contribution from a single spin $\phi(x)$ is $H_0 = -J \int_x |A(x)| dx$, which occurs only if all spins $\phi(x')$ within the ferromagnetic range $|x - x'| < r_+$ coalign with the spin at x , and all those in the antiferromagnetic range $|x - x'| > r_+$ anti-align, as shown in figure 2.4. For $A(x) = g(x, \sigma_+^2) - g(x, \sigma_-^2)$ with $\sigma_- = \alpha\sigma_+$, r_+ is found to be

$$r_+ = 2\sigma_+ \sqrt{\alpha^2 \log(\alpha) / (\alpha^2 - 1)} \approx \begin{cases} 0.96, & \alpha = 2 \\ 1.11, & \alpha = 3. \end{cases}$$

The maximum possible energy contributed by one spin is then found to be

$$H_0 = -J \left(\frac{\alpha^2 - 1}{\alpha^2} \right) \exp \left(\frac{-2 \log \alpha}{\alpha^2 - 1} \right).$$

The arrangement in figure 2.4 is optimal only for the central cell. A better global configuration is given by the stripe or roll pattern

$$\phi(x) = k \cdot x \pmod{\pi}$$

in which every unit contributes the same energy

$$H(k) = -\frac{J}{2} \left(\exp \left(-\frac{|k|^2 \sigma_+^2}{2} \right) - \exp \left(-\frac{|k|^2 \sigma_-^2}{2} \right) \right).$$

The lowest-energy stripe configuration occurs when

$$|k| = \frac{2}{\sigma_+} \sqrt{\frac{\log \alpha}{\alpha^2 - 1}},$$

corresponding to an optimal stripe width d_{opt} of

$$d_{\text{opt}} = \frac{\pi}{2} \sqrt{\frac{\alpha^2 - 1}{\log \alpha}} \sigma_+ \approx \begin{cases} 3.27\sigma_+, & \alpha = 2 \\ 4.24\sigma_+, & \alpha = 3 \end{cases}$$

and energy

$$H[\phi_{\text{opt}}] \equiv \frac{1}{2} H_0 \approx \begin{cases} -0.473J/2, & \alpha = 2 \\ -0.675J/2, & \alpha = 3. \end{cases}$$

See figure 2.5.

Topological Defects

In the classical XY model, a single vortex defect is energetically unfavorable, and this is again the case with the center-surround interaction. A *pair* of defects with opposite polarity may be superimposed on a roll pattern background as in figure 2.6. This con-

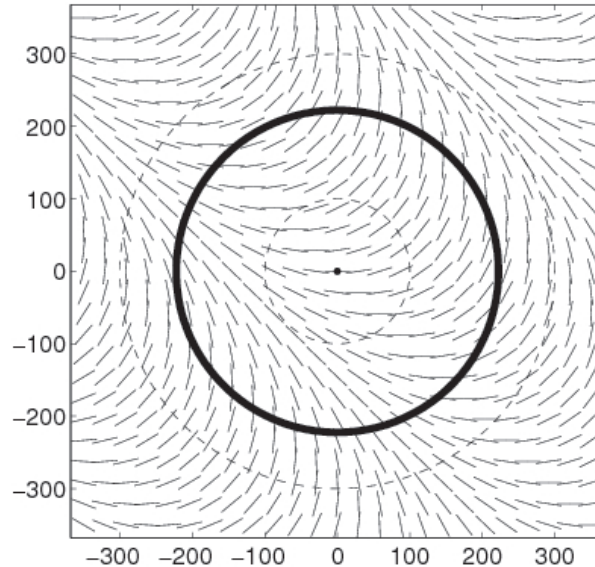


Figure 2.5: Globally optimal orientation roll pattern. Optimal roll pattern for the XY model with difference-of-Gaussians interaction. In this configuration each spin contributes $H_0/2$ to the total energy, where H_0 is the maximal possible contribution of a single spin. Scale units in microns.

figuration is not stable, however. Generating a series of defect patterns with different spacing shows that defect energy grows monotonically with increasing separation between the defects (see figure 2.6). Under a low-temperature dynamical Monte Carlo simulation, the two defects approach one another and annihilate, returning $\phi(x)$ to the optimal stripe pattern. In case the initial defect spacing is too large, the inverted strip between the singularities will break down into a string of vortex pairs, each of which collapses and annihilates.

The dynamics governing the interaction of vortex defects is more complicated than a simple Coulomb-type attraction: a combination of four defects in a rectangular configuration with two positive defects on one side and two negative on the other, superimposed on a roll-pattern background, is stable under the low-temperature Monte Carlo dynamics. Figure 2.7 shows such a configuration. This pattern of four defects occurs commonly in the biological maps, and comprises an area of cortex roughly corresponding to a single hypercolumn.

Another simple configuration is a periodic lattice of defects alternating as on a

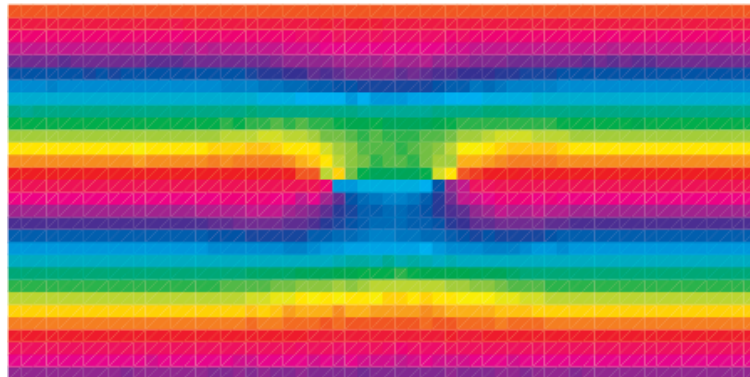
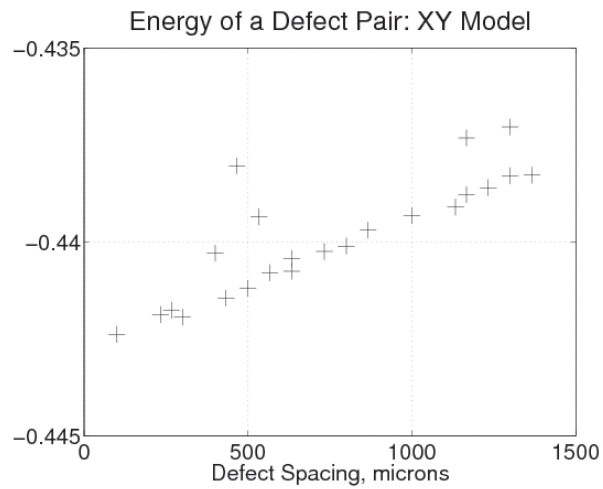


Figure 2.6: Energy as a function of defect spacing: vortex-antivortex pair.

Top: Energy as a function of separation distance for sample XY configurations with two pinwheel defects superimposed on an optimal stripe pattern. Configurations were generated inverting the direction of increasing ϕ in a rectangle one half-wavelength wide, followed by Monte Carlo relaxation at low temperature.

Bottom: A sample two-pinwheel orientation defect pattern.

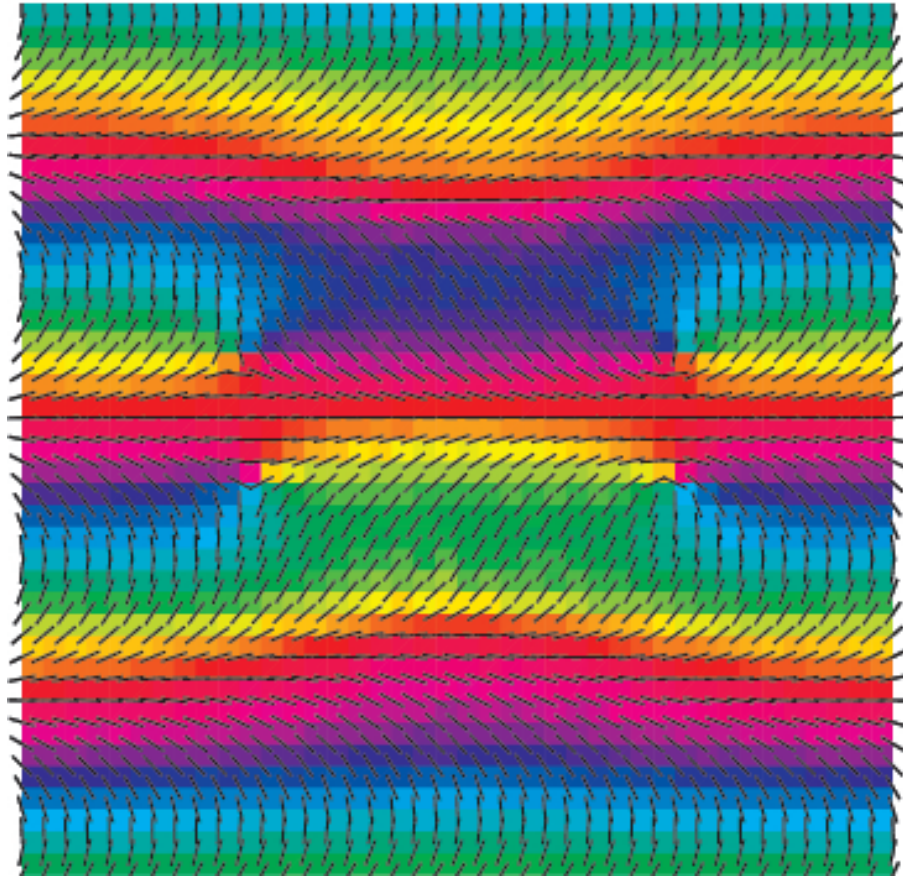


Figure 2.7: Simplest stable defect configuration, XY model. Note the configuration of singularities: $\begin{pmatrix} -\pi & +\pi \\ -\pi & +\pi \end{pmatrix}$.

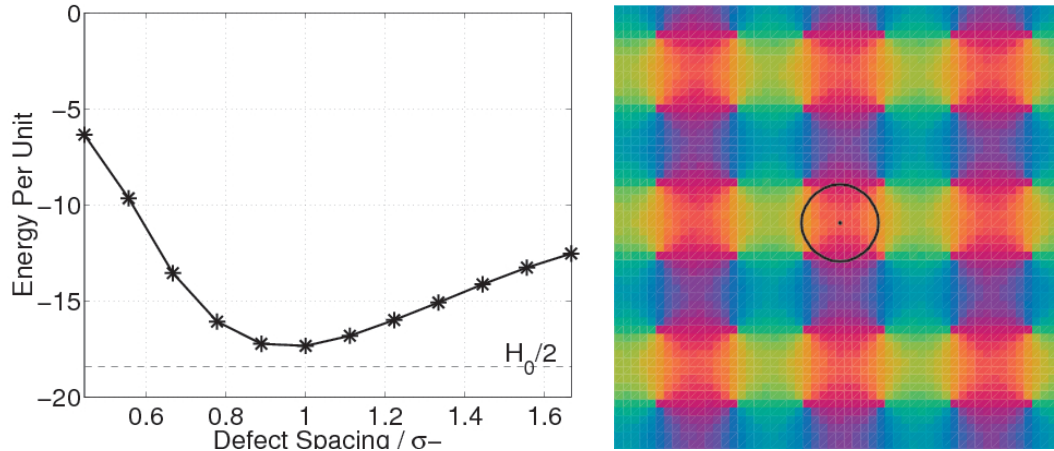


Figure 2.8: Energy as a function of defect spacing: vortex lattice. Optimal checkerboard orientation defect lattice for difference-of-Gaussians XY model.

Left: Average energy per unit of checkerboard configurations as a function of defect spacing. Orientation configuration was relaxed at low temperature with difference-of-Gaussians interaction, $\sigma_- = 3\sigma_+$.

Right: Zero contour of interaction superimposed on the optimally spaced defect lattice for size comparison.

checkerboard:

$$\begin{bmatrix} + & - & + & - \\ - & + & - & + \\ + & - & + & - \\ - & + & - & + \end{bmatrix}.$$

Figure 2.8 shows the energy of this defect lattice configuration as a function of defect separation, and the optimal checkerboard pattern with the zero contour of A superimposed for scale reference.

2.2.1 Continuous Phase Transition

Like its pure ferro-magnetic cousin, our mixed ferro-antiferromagnetic XY model exhibits a continuous phase transition as the temperature decreases. However because of the center-surround interaction structure, when local order begins to set in, it does so at an intermediate length-scale corresponding to the optimal roll-pattern wavelength. On this scale the attraction of local roll patterns is strongest, leading to the

formation of “linear zones”. But because the orientation and phase of neighboring linear zones is random, as they form they generate topological defects at their intersections. As this pattern of linear zones and pinwheels takes shape, a complicated dynamics governs the collision and annihilation of some pinwheel configurations and the stabilization of those that remain. At the same time that the pattern forms on the center-surround length scale d_{opt} , there remains a significant *lack* of order on both the smaller (nearest-neighbor) and larger scales. As in the purely ferromagnetic XY model, at finite temperature there is no long-range order, no global magnetization. But there is *local* magnetization that grows or decreases with the inverse temperature β .

Local Order and Disorder

To assess the degree of *local* order we may choose one of several measuring sticks, such as the average deviation of χ_i from the local field at site i , or else the average difference between nearest neighbor spins.

Given a particular configuration of spins surround a site i ,

$$\{\phi_j | j \neq i\},$$

we may calculate the local field χ_i^{loc} , which has magnitude q_i^{loc} and orientation ϕ_i^{loc} :

$$\begin{aligned} \chi_i^{\text{loc}} &:= \sum_{j \neq i} A_{ij} \begin{bmatrix} \cos 2\phi_j \\ \sin 2\phi_j \end{bmatrix} \\ &= \sum_{j \neq i} A_{ij} \chi_j \\ &=: q_i^{\text{loc}} \begin{bmatrix} \cos 2\phi_i^{\text{loc}} \\ \sin 2\phi_i^{\text{loc}} \end{bmatrix} \end{aligned} \tag{2.15}$$

Were these surrounding spins $\{\phi_{j \neq i}\}$ fixed in place, the distribution of ϕ_i in thermal

equilibrium would be given by

$$P_i(\phi_i|\{\phi_{j\neq i}\}) = \frac{\exp(\beta \frac{J}{2} q_i^{\text{loc}} \cos(2(\phi_i - \phi_i^{\text{loc}})))}{I_0(\beta \frac{J}{2} q_i^{\text{loc}})}$$

where J is a constant determining the units of conversion from energy to temperature, generally taken to be unity. $I_0(\kappa)$ is the modified Bessel function of order zero, the integral of $\exp(\kappa \cos 2\phi)$ (see Appendix A.3 for a discussion of statistical measures for functions taking on angular values). The strength of the field, which indicates the degree of local order, may be determined by taking the circular variance of ϕ_i , the expectation of $|\exp(2i\phi_i)|$. By symmetry the circular mean of $P_i(\phi_i|\{\phi_{j\neq i}\})$ is just ϕ_i^{loc} , so the circular variance is:

$$\begin{aligned} E[|e^{2i\phi_i}|] &= \int_{\phi_i} \cos(2(\phi_i - \phi_i^{\text{loc}})) P_i(\phi_i|\{\phi_{j\neq i}\}) d\phi_i \\ &= \frac{I_1(\beta \frac{J}{2} q_i^{\text{loc}})}{I_0(\beta \frac{J}{2} q_i^{\text{loc}})} \\ &=: \mathcal{S}(\beta \frac{J}{2} q_i^{\text{loc}}) \end{aligned}$$

The population response function $\mathcal{S}(\kappa)$ is sigmoidal on a log scale, going to 0 as $\kappa \rightarrow 0$ and going to 1 as $\kappa \rightarrow \infty$ (see Appendix A.3). Given a sample configuration from a Monte Carlo simulation at a given temperature β we can find $E[|e^{2i\phi_i}|]$ by averaging $\chi_i \cdot \chi_i^{\text{loc}}$ over the entire population, and numerically inverting \mathcal{S} .

Another natural measure of local order at thermal equilibrium is given by the circular variance of the distribution of nearest-neighbor angle differences,

$$E_{\{\|i-j\|=1\}}[\cos(2(\phi_i - \phi_j))].$$

This measure does not go to one as β approaches ∞ , because the low-temperature metastable steady states have a finite rate of change of orientation between neighbors, corresponding roughly to the rate of change in the optimal roll pattern.

In their paper on the local scatter of orientation tuning properties, Maldonado

and Gray use a third measure, the average of the absolute difference in angle between pairs of nearby neurons.

Monte Carlo Simulation

The three measures given above behave similarly for model data generated by the Monte Carlo simulation. Figure 2.9 shows the “average angle difference” corresponding to each of the three measures at thermal equilibrium for a range of inverse temperatures β . At high temperatures (small β) all three measures give an expected angle difference of $\pi/4$ —there is no expected correlation, either between nearest neighbors or between spins and the local field. At low temperature, the nearest-neighbor differences asymptotically approach the roll-pattern minimum difference while the expected difference between ϕ_i and ϕ_i^{loc} drops to zero.

Figure 2.10 shows the effective local field strength κ (determined from the circular variance of $\phi_i - \phi_i^{\text{loc}}$) as a function of inverse temperature β , and the logarithmic rate of change of κ with respect to β . The two are roughly proportional at the extremes of temperature, with $\kappa \approx 0.0010\beta$ for $\beta \ll 1$ (high temperature equilibrium) and $\kappa \approx 0.012\beta$ for $\beta \gg 1$ (low temperature equilibrium). In between these ranges there is a sharp spike in $\partial \log(\kappa)/\partial \log(\beta)$, indicating the existence of a phase transition.

Figure 2.11 shows equilibrium steady states generated from random initial conditions at various values of β . Note that at the higher-temperature samples, the underlying pattern (on the length scale d_{opt}) has fewer latent topological defects than those “annealed” more quickly, i.e. held at lower temperatures throughout the simulation.

2.2.2 Comparison with Cortical Data

Orientation Map at the Edge of Disorder

Maldonado and Gray and Maldonado *et al.* investigated the variance of orientation preferences in cat V1. In contrast to the uniform map produced by the optical imaging techniques, they found significant amounts of scatter even in linear zones. Near

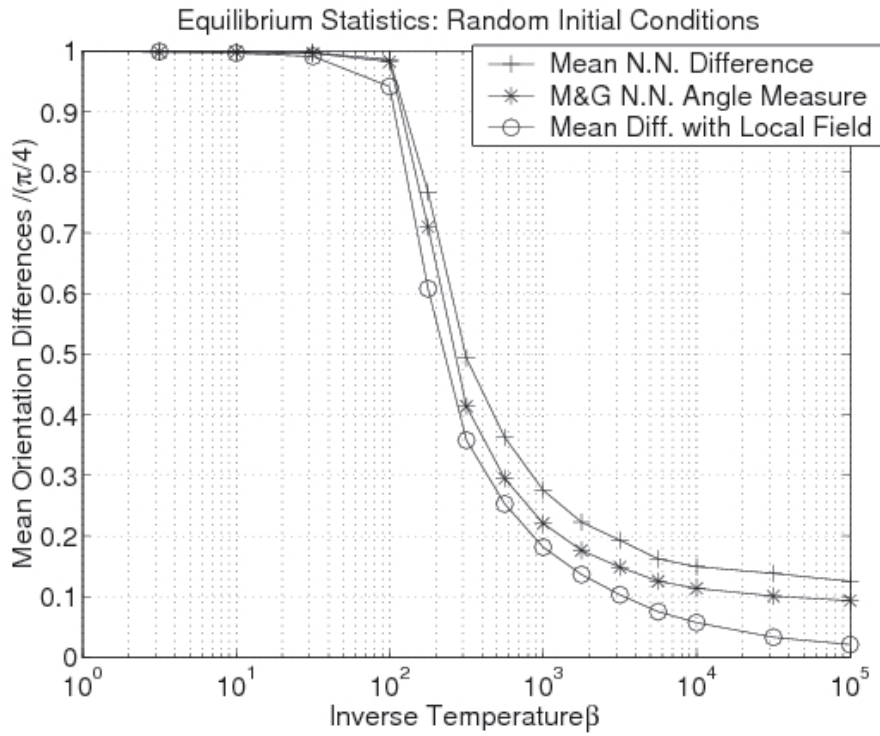


Figure 2.9: Orientation scatter at different inverse temperatures β . Variability of orientation in equilibrium steady-state at different temperatures β . Shown is the average of $\cos 2(\phi_i - \phi_j)$ where i, j are adjacent neighbors (+) at equilibrium; and the average of $\cos 2(\phi_j - \phi'_j)$ where ϕ_j is the orientation and ϕ'_j is the local orientation calculated as the field average with interaction A_{ij} , (o).

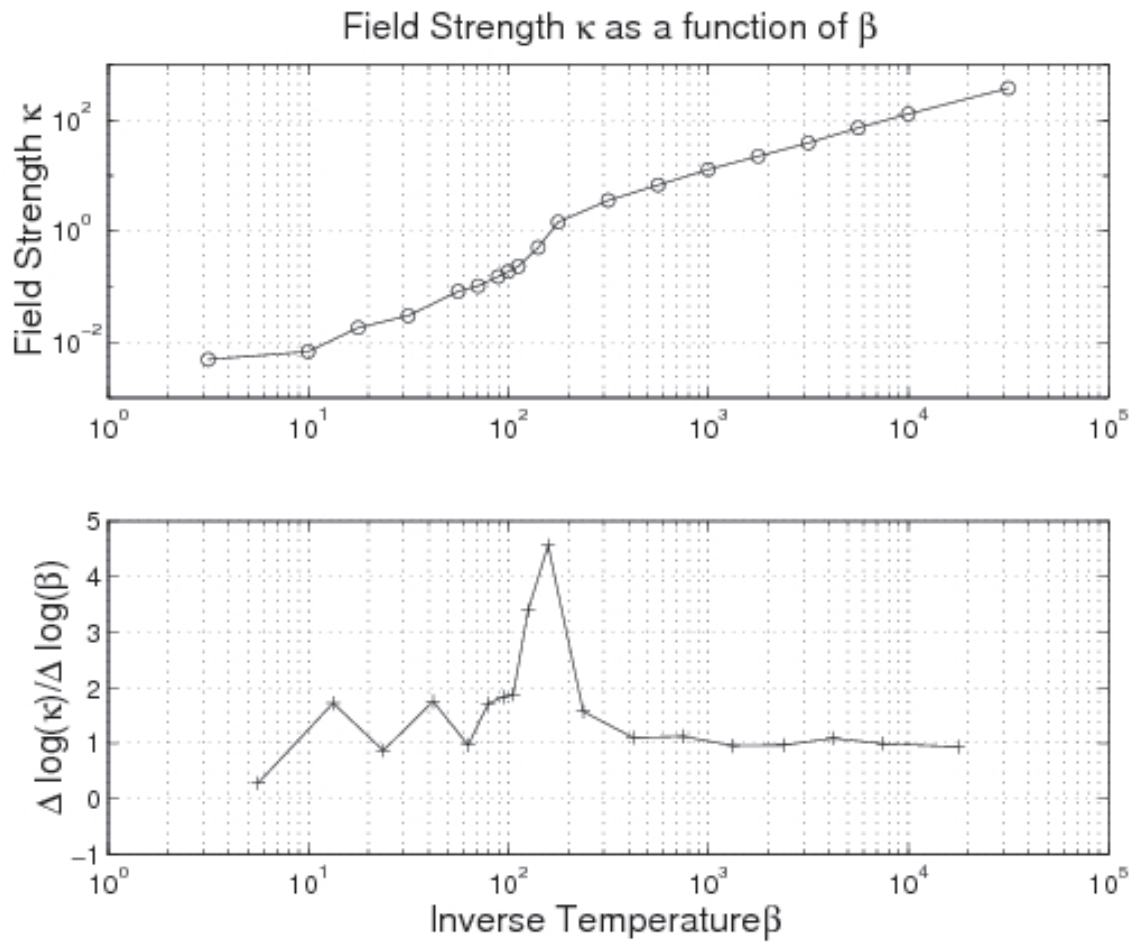


Figure 2.10: Phase transition in center-surround XY model.

Top: Effective local field strength κ versus inverse temperature β . Data from Monte Carlo simulations with random initial conditions.

Bottom: Rate of change of $\log \kappa$ with respect to $\log \beta$. The sharp peak in $\frac{\partial \log \kappa}{\partial \log \beta}$ indicates the phase transition.

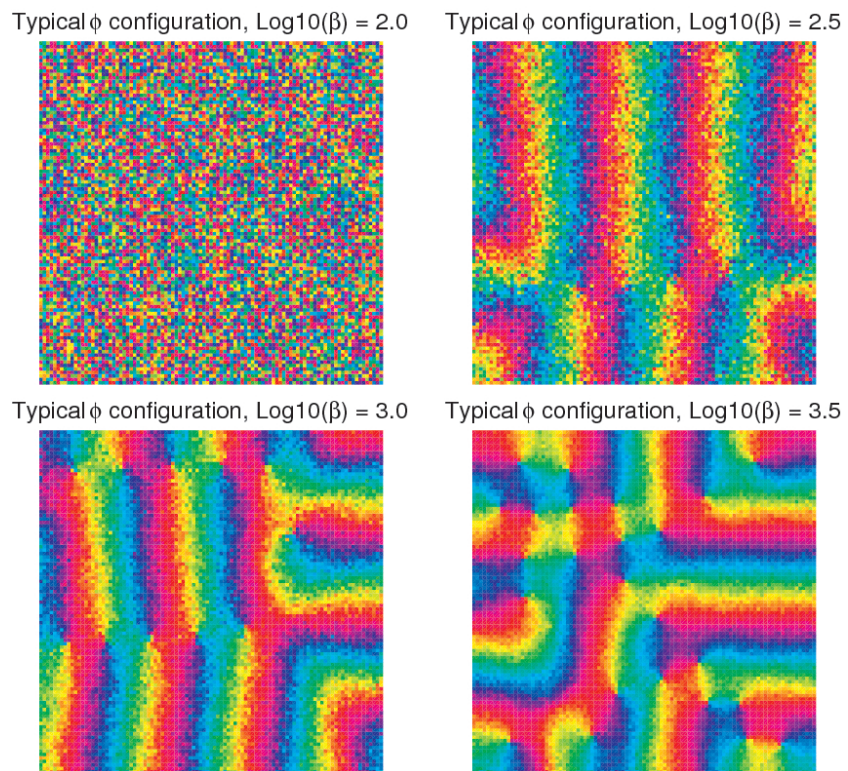


Figure 2.11: XY Configurations near the phase transition. Sample configurations drawn from the XY equilibria at different inverse temperatures β . Simulations began from random initial conditions.

pinwheel sites they found an even larger scatter of orientation preferences between nearby cells. They estimate that their tetrode technique picks up neighboring cells within a 65-micron seeing radius of the electrode tip.

Ignoring the finite volume taken up by each cell, if pairs of points are chosen from a uniform distribution inside a sphere of radius 65μ , the expected distance between the points is $66.9 \pm 0.1\mu$ (estimated with a simple Monte Carlo sampling scheme). For computational convenience the simulations reported here are designed so that one pixel corresponds to roughly 50 microns distance in the model cortex, so the nearest-neighbor results should be comparable.

Maldonado and Gray report a mean absolute angle difference between simultaneously recorded cells of 19.7° , or $0.438\pi/4$. Consulting Figure 2.10, we see this mean absolute nearest-neighbor difference corresponds closely to the simulation value at $\log_{10}(\beta) \approx 2.2$. This temperature, from Figure 2.11, lies *just below* the critical temperature marking the phase transition. *Thus the organization of the cortical orientation map appears to lie just outside the threshold of disorder.*

Orientation Scatter and Optical Imaging

In light of the disorder in V1 it is worth noting a potentially misleading artifact of the *differential imaging of intrinsic optical signals* used by Blasdel and others to generate the orientation maps. Each pixel in the CCD camera used to collect optical signals combines signals resulting from the activities of perhaps dozens of cortical cells. To improve the signal-to-noise ratio, Blasdel and coworkers digitally average together 4×4 blocks of adjacent pixels. If the orientation preferences of *single cells* is given by $\phi(x)$, and the individual response of each cell to a grating stimulus with orientation ϕ_0 is modeled to be $q_0 \cos 2(\phi_0 - \phi(x))$, and the network interaction is given by convolution with a center-surround kernel A , and the spatial averaging in the experiment amounts to filtering with a Gaussian $g(x, \sigma_0^2)$, then the recorded responses

will be given by ²

$$q_0 \int_{x'} g(x - x', \sigma_0^2) \int_{x''} A(x' - x'') \cos 2(\phi_0 - \phi(x'')) dx'' dx' = \langle q \rangle \cos 2(\phi_0 - \langle \phi \rangle). \quad (2.16)$$

The signal strength $\langle q \rangle(x)$ will be larger or smaller depending on the amount of scatter in ϕ , except at the pinwheel centers where it will go smoothly to zero, but there is no independent way to determine its strength relative to a standard measure. The optically obtained orientation preference, $\langle \phi \rangle(x)$, will vary smoothly with sharply defined pinwheel singularities regardless of the disorder of the underlying distribution. Points that appear as highly localized singularities in the orientation map may in fact be broad regions with salt-and-pepper admixtures of all orientations. This intuition may be checked by taking the noisy maps derived above and processing them in a simulated reproduction of Blasdel's differential imaging method (see the MATLAB function `diffim.m` in Appendix D.9). Recently, Maldonado, Gödecke, Gray and Bonhoeffer have measured the scatter in orientation tuning in pinwheel *vs.* linear zones, as well as individual cells' tuning characteristics in these different regions. They concluded that indeed the situation of cells near pinwheel centers does not dictate that they have broader tuning than their linear-zone counterparts, and they found no strong indication that the local variability against the background pattern is larger in one kind of region than another [48].

2.2.3 Higher-Dimensional Maps

The generalized XY model may be extended in an *ad hoc* fashion to higher dimensional maps such as orientation and ocular dominance, orientation and directional preference, or orientation and spatial frequency.

The simplest extension of the XY model is to replace the XY vector confined to a plane with an n-vector mapping points on the cortical surface to vectors in \mathbb{R}^n . The

²c.f. Appendix A.3

XY Hamiltonian is replaced by

$$H = -\frac{J}{2} \sum_{i,j} A_{ij} \left(x_i^{(1)} x_j^{(1)} + x_i^{(2)} x_j^{(2)} + \cdots + x_i^{(n)} x_j^{(n)} \right) \quad (2.17)$$

where A_{ij} is the usual difference-of-Gaussians interaction in the plane and $\sum_{k=1}^n \left(x_i^{(k)} \right)^2 = 1$.

In contrast to the case in which the spin vector is confined to the plane, no topological defects develop in the n -vector case for $n \geq 3$. The projection into the plane of two of the components will show singularities while the full vector field courses smoothly “over” or “under” the singularity, as shown in Figure 2.12. In sufficiently high dimensions, the pattern loses coherence as the volume “close” to a given vector expands.

Orientation and Ocular Dominance

For a model of the joint development of ocular dominance and orientation, the spin vector may be taken to lie on the surface of a sphere in \mathbb{R}^3 —the “XYZ model”. We may interpret x_i, y_i as the coordinates of an orientation vector and z_i as the ocular dominance. We obtain patterns in which the orientation singularities predominantly lie near the extrema of the ocular dominance pattern (see Figure 2.13), out of geometric necessity. This model is biologically opaque, however.

Directional Preference and the Orientation Map

Visual area 18 of the cat exhibit a map not only for stimulus orientation but also for direction-of-motion preference [73, 66]. The familiar orientation map in this area couples to the map for stimulus motion in such a way that the preferred direction of motion lay perpendicular to the preferred orientation. Direction forms a 2π -periodic quantity while orientation is only π -periodic. Therefore, if the orientation-preference map only forms singularities of topological charge ± 1 , then there will necessarily be line-singularities or fractures in the direction-preference map. These line singularities

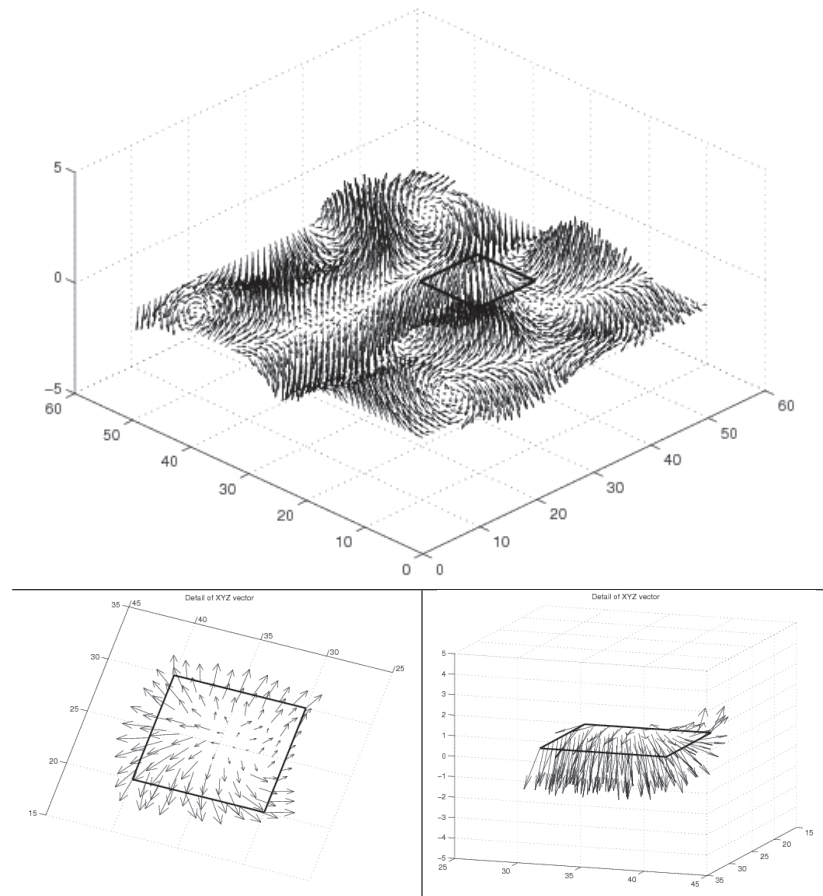


Figure 2.12: Vector field generated by XYZ model.

Top: Vector field generated with difference-of-Gaussians interaction. All arrows have approximately uniform length. The vector field is smooth—there are no singularities comparable to the topological defects in the XY model. Note the small square accented on the plane.

Bottom Left: Vectors over the small square region viewed in a projection in which there appears to be a singularity at the center of the region.

Bottom Right: Vectors over the same region viewed in a different projection. Rather than exhibiting a singularity, the vectors at the center of the square are normal to the plane of the first projection.

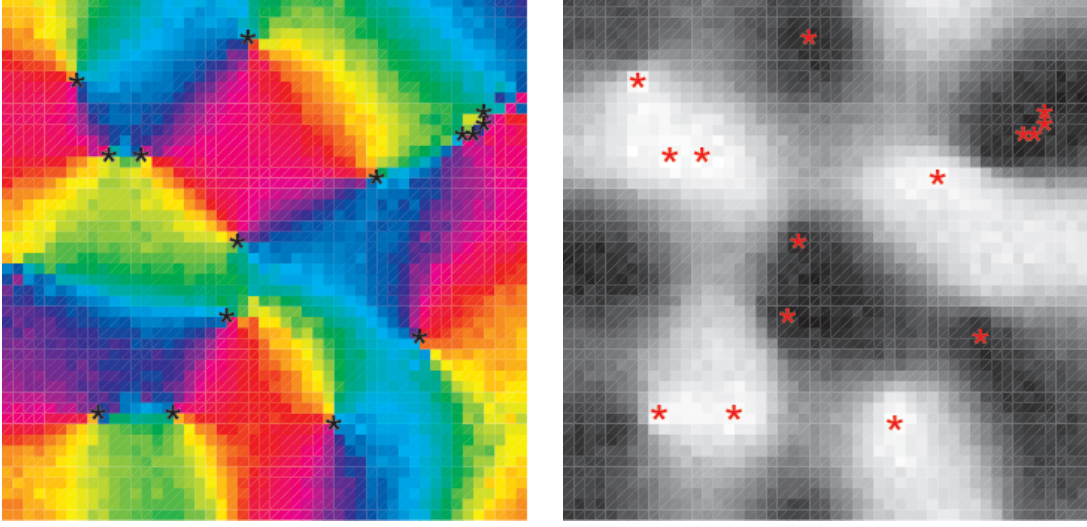


Figure 2.13: Spin model for orientation and ocular dominance.

Left: Orientation-Preference Map, taken from the first two components of the 3-vector. Stars mark orientation singularities.

Right: Ocular Dominance Map, taken from the third component of the 3-vector. Stars mark the same orientation singularities as on the Left. Diagram 1 mm x 1 mm.

end in half-charge point singularities in the direction field that coincide with the full singularities in the orientation field, and were observed experimentally.

If the directional-preference map dominated the pattern formation process we would expect to see double singularities in the orientation map and single singularities in directional preference, without line singularities. It is straightforward to model the development of a directional-preference vector $[p, \theta]$ under the influence of a pre-established orientation map $[q, \phi]$ by using the Hamiltonian

$$H[\theta|\phi] = -\frac{1}{2} \sum_{ij} A_{ij} \{ J_1 p_i p_j \cos(\theta_i - \theta_j) + J_2 q_i p_j \cos 2(\phi_i - \theta_j) \}$$

with $[q_i, \phi_i]$ in a fixed pattern. When the self-coupling of the directional vector is sufficiently strong, $J_1 \gg J_2$, the directional map forms unit singularities (charge $\pm 2\pi$) in locations only weakly correlated with the orientation singularities. For sufficiently strong $J_2 \gg J_1$, the orientation map forces the directional map to form line singularities such as those shown in Figure 2.14.

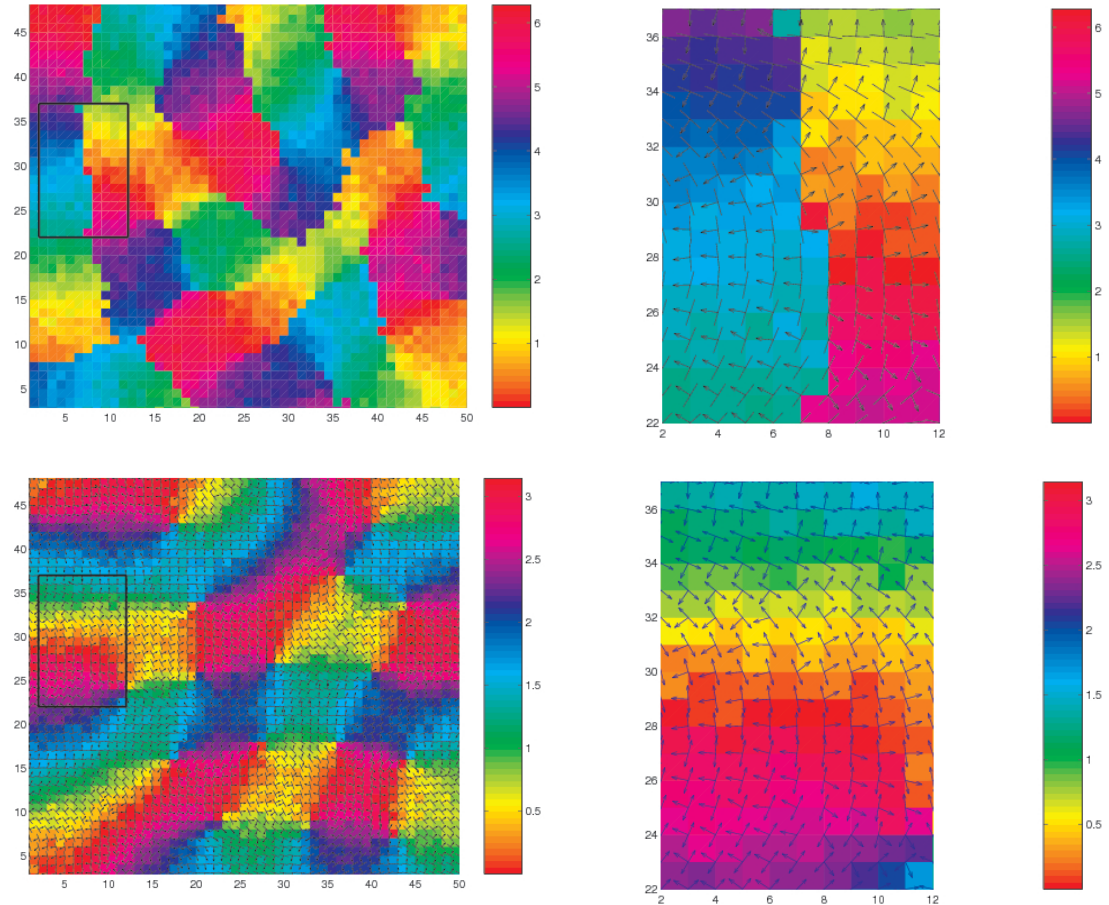


Figure 2.14: Orientation and directional motion maps.

Top Left: Directional Motion-Preference Map generated by coupling a 360° vector both to itself and to an established orientation field. The box intersects a line singularity running vertically down the left side of the pattern.

Top Right: Close-up view of the box from the top left image. The color indicates the directional preference, as do the arrow heads. The arrow-less line segments indicate the underlying orientation preference, which varies continuously across the line singularity in directional preference.

Bottom Left: Orientation Preference Map, fixed during development of the directional field.

Bottom Right: Close-up of boxed area. Note continuity of the orientation map, in contrast to the fracture in the direction map.

Spatial Frequency Distribution

Given a vector map over the plane, we may choose to interpret the scalar magnitude of the map as the preferred spatial frequency rather than the strength of the orientation-tuning preference. We may then represent cortical cells as Gabor filters with spatial frequency vector \underline{k} acting on the feedforward signal:

$$f_{\underline{k}}(\underline{y}) = \cos(\underline{k} \cdot \underline{y}) \exp(-\|\underline{B}\underline{y}\|^2). \quad (2.18)$$

We will take the Gaussian envelope to be circularly symmetric, i.e. $B = \begin{pmatrix} 1/d & \\ & 1/d \end{pmatrix}$.

The response to an input signal with luminosity profile $\cos(\underline{k}' \cdot \underline{y})$ is then the inner product of this function with the filter 2.18:

$$R(\underline{k}, \underline{k}', \underline{B}) = \int_{\underline{y}} f_{\underline{k}}(\underline{y}) \cos(\underline{k}' \cdot \underline{y}) \underline{d}\underline{y} \quad (2.19)$$

$$\begin{aligned} &= \frac{d^2\pi}{2} \left[\exp\left(\frac{-d^2\|\underline{k} + \underline{k}'\|^2}{4}\right) + \exp\left(\frac{-d^2\|\underline{k} - \underline{k}'\|^2}{4}\right) \right] \\ &= d^2\pi \exp\left[-\frac{d^2}{4} (\|\underline{k}\|^2 + \|\underline{k}'\|^2)\right] \cosh\left[\frac{d^2}{2} \underline{k} \cdot \underline{k}'\right]. \end{aligned} \quad (2.20)$$

For a fixed window size d , the response falls off rapidly if either \underline{k} or \underline{k}' are too large, or if the angle difference $\phi - \phi'$ is too large. Also, the response falls off more quickly with angle difference if the spatial frequency is large.

I recreate the algorithm used by Hübener *et al.* to determine spatial-frequency preference as follows. Taking a sample distribution of orientation and accompanying scalar (Figure 2.15), I “present” stimuli with either “high” spatial frequency (5 on the scale of 0 to 5.5 given by the extrema of the magnitude) and “low” spatial frequency (3 on the same scale). The orientations of the stimuli are $k\pi/4$, $k \in \{0, 1, 2, 3\}$. I sum the responses to all orientations at each point and take the difference between “high” and “low”. This “raw data” I then convolve with a Gaussian of four-pixel radius to simulate the optical and/or digital averaging used. The resulting quantity varies within ± 6 in arbitrary units. By placing a contour line at the level -5, I reproduce

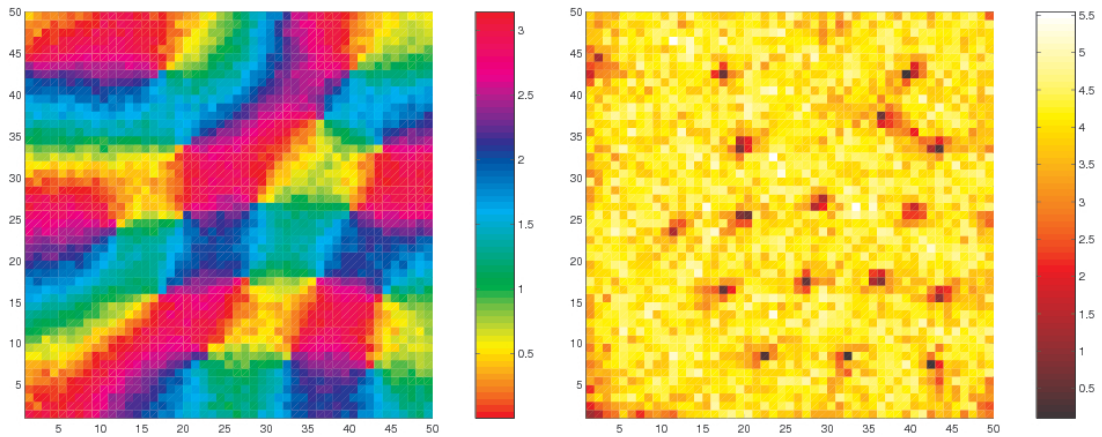


Figure 2.15: Orientation and magnitude interpreted as spatial frequency.
Left: Orientation-preference map generated on a 50×50 grid with cylindrical interaction function (6 pixels positive radius, 12 pixels negative radius).
Right: Magnitude for same simulation, which used magnitude decay rate of 10%. Dark indicates lower magnitude; the color scale runs roughly from 0 to 5.5.

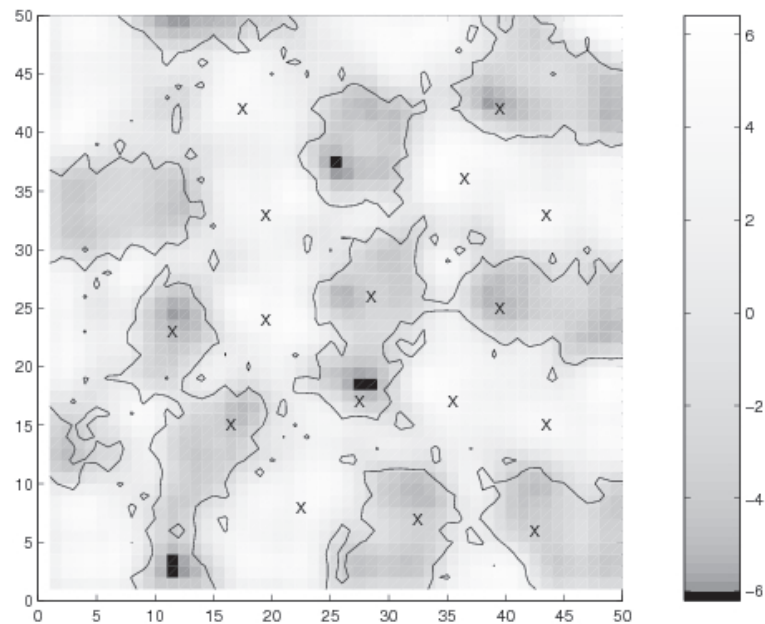


Figure 2.16: Preference for high *vs.* low spatial frequency. Interpreting the scalar magnitude in Figure 2.15 as local spatial frequency–preference, the averaging scheme described in the text resulted in this distribution of preference for higher over lower spatial frequencies, averaged over all orientations. Small “X”s indicate the positions of the singularities in Figure 2.15. See text for details.

Hübener’s result that low spatial frequency–preference cells reside in isolated “islands” in a “sea” of high spatial–frequency preference.

The desire to justify such seemingly artificial extensions of the XY model motivated the search for a reduction from a synaptic to a feature-level learning rule, the results of which are presented in the next Chapter.

CHAPTER 3

DERIVATION OF A GENERALIZED XY-MODEL FROM COMPETITIVE HEBBIAN LEARNING

Chapter 2 described an application of the XY model to the study of cortical map structure. In the form presented it is merely a phenomenological model like other feature models: orientation is treated as an abstraction bearing little direct relation to cortical architecture. To remedy this lack of biological significance it is desirable to develop a model that does more justice to the biological underpinnings of these maps, insofar as they have been characterized. To this end I introduce a model for the development of the synaptic connections carrying visual information to V1 from the thalamus, and show that under a biologically appropriate developmental dynamics the synaptic weights embody the XY rule defined abstractly in Chapter 2:

$$\dot{\phi}(x) = \eta' \int_{x'} A(x - x') \sin 2(\phi(x') - \phi(x)) dx' \quad (3.1)$$

where $A(x)$ is the center-surround lateral cortical interaction, $\phi(x)$ is the π -periodic orientation variable, and η' is a rate constant.

3.1 Geometry of Geniculo-Cortical Weights

The fundamental conceptual issue for the biological justification of the XY-type models is finding the appropriate reduction from a high-dimensional description of the synaptic weights to a low-dimensional feature description such as preferred orientation. The synaptic-weight function from geniculate locations r to cortical locations x , denoted $w(x, r)$, specifies an L^2 (square integrable) function of r for each point x corresponding to the classical *receptive field* of the neuron at x . That is, for fixed x , geniculate activity at points r in the support of $w(x, r)$ affect the cortical activity

at $a(x)$ while those at points r outside the support of $w(x, r)$ do not. Conversely we can also define the *projective field* of a geniculate neuron at location r as the support (in x) of $w(x, r)$. For convenience it is common to represent $w(x, r)$ as a Gaussian in r with mean varying as a function of x , in which case the support would strictly be unbounded; in this case there is an implicit threshold weight below which single units could not excite any activity, so the receptive fields are actually finite. I will assume that at each point x the receptive field profile $w(x, r)$ is bounded, L^2 , and has defined first and second moments. These moments provide the reduction from the infinite-dimensional to the finite-dimensional description because they are the quantities of primary interest. I define the net fan-in $\lambda(x)$ or input mass of the receptive field, the retinotopy $R(x)$ or center of mass of the receptive field, the receptive field size $\sigma(x)$, the preferred orientation $\phi(x)$ and tuning strength $q(x)$ in terms of the first two moments, as given in table 3.1. I will refer to the net input mass interchangeably as $\lambda(x)$ or as $m(x)$. (In Chapter 4 I will introduce the complementary term, the net fan-out $\gamma(r)$ from a geniculate site r .) The covariance matrix $Q(x)$ is defined by integrating the outer product uu^{tr} , where $u = r - R(x)$ is the displacement from the center of mass.

$$Q(x) = \begin{pmatrix} Q_{11} & Q_{12} \\ Q_{21} & Q_{22} \end{pmatrix} = \frac{\int_u w(x, u + R(x)) \begin{pmatrix} u_1^2 & u_1 u_2 \\ u_2 u_1 & u_2^2 \end{pmatrix} du}{m(x)}$$

Define $\tilde{w}(x, r)$ as the Gaussian with the same zeroth, first and second moments as $w(x, r)$:

$$\tilde{w}(x, r) = \frac{m(x)}{2\pi\sqrt{\det Q(x)}} \exp\left(-\frac{1}{2}u^{\text{tr}} Q(x)^{-1}u\right).$$

Quantity	Definition	Interpretation	Restriction
$m(x)$	$\int_r w(x, r) dr$	Fan-In (input mass)	m_0
$R(x)$	$\frac{\int_r w(x, r)r dr}{m(x)}$	Retinotopy	μx
$Q(x)$	$\frac{\int_u w(x, u+R(x))uu^{\text{tr}} du}{m(x)}$	Covariance Matrix	$\frac{\sigma_0^2}{2}I_2 + \frac{q_0}{2}\Phi_2(\phi)$
$\sigma(x)$	$\text{Tr}Q(x)$	Receptive Field Width	σ_0
$q(x)$	$\sqrt{(Q_{11} - Q_{22})^2 + (2Q_{12})^2}$	Orientation Selectivity	q_0
$\phi(x)$	$\frac{1}{2} \tan^{-1} \left(\frac{2Q_{12}}{Q_{11} - Q_{22}} \right)$	Preferred Orientation	(free)

Table 3.1: Geometrical reduction of synaptic weight $w(x, r)$. The zeroth and first moments of the receptive field at x , $w(x, r)$, define the input mass (fan-in) and the retinotopy (center-of-mass). The 2×2 symmetric matrix of second moments $Q(x)$ defines the receptive field width, preferred orientation and orientation tuning strength.

I_2 denotes the 2×2 identity matrix, and $\Phi_2(\phi)$ is the matrix $\begin{pmatrix} \cos 2\phi & \sin 2\phi \\ \sin 2\phi & -\cos 2\phi \end{pmatrix}$.

In the simplest case I restrict m, R, Q, σ and q to constant values as indicated, allowing only the orientation preference $\phi(x)$ to vary freely.

As shown in Appendix 6.2.3, the level curves of \tilde{w} in the r -plane form ellipses with major axis oriented along the direction $\phi(x)$ given by

$$\begin{aligned} 2Q_{12}(x) &= q(x) \sin 2(\phi(x) + \frac{\pi}{2}) \\ Q_{11}(x) - Q_{22}(x) &= q(x) \cos 2(\phi(x) + \frac{\pi}{2}) \\ \frac{2Q_{12}(x)}{Q_{11}(x) - Q_{22}(x)} &= \tan 2(\phi(x) + \frac{\pi}{2}) \end{aligned} \quad (3.2)$$

The $\phi(x)$ direction is the principal axis of the weight distribution of the receptive field afferent to x . Hence to the extent that the direction of orientation preference is determined by the geometry of feedforward connections (as in the Hubel-Wiesel scheme) $\phi(x)$ will also determine the preferred orientation of the unit at x . The quantity $q(x)$ is closely related to the eccentricity of the receptive field profile, with $q = 0$ indicating circularly symmetric or nonselective receptive fields, so I will consider it as the *magnitude* of the orientation tuning vector $\chi(x) = q(x) (\cos 2\phi(x), \sin 2\phi(x))^{\text{tr}}$. The *width* of the receptive field $\sigma(x)$ is given by the trace of the covariance matrix: $\sigma(x) = \sqrt{\text{Tr}Q(x)/2}$. The quantities of net input $m(x)$, retinotopy $R(x)$, width $\sigma(x)$, orientation and magnitude $\phi(x), q(x)$ determine the shape of the receptive field profile up through the second moments, as illustrated in Figure 3.1.

3.2 The Hebbian Model

The mechanism of Hebbian learning specifies a rule for modifying synaptic weights based on the correlation of pre- and post-synaptic activity. In its simplest form, the changes in the weights are directly proportional to the correlations:

$$\Delta w(x, r) = \eta \langle I(r) a(x) \rangle. \quad (3.3)$$

I will assume that an input pattern at the LGN, $I(r)$, gives rise to activity $a(x)$ in the cortex given by filtering the feedforward signal $\int_r w(x, r) I(r) dr$ by a difference-

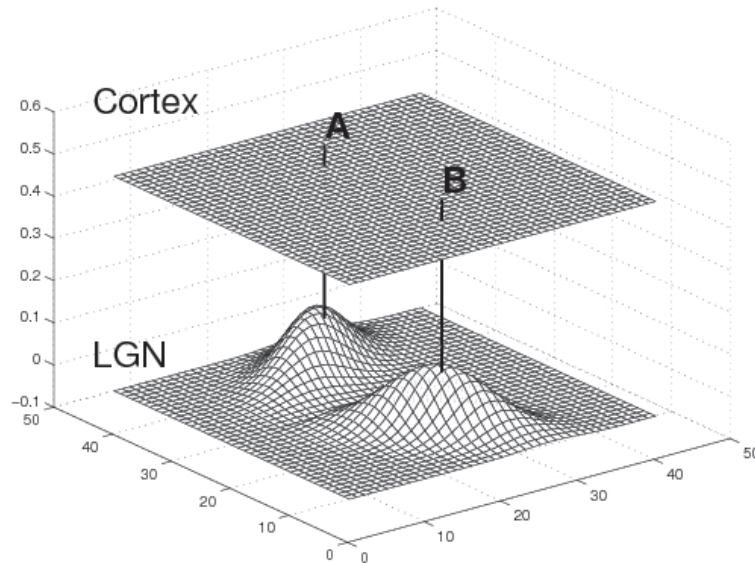


Figure 3.1: Feed-forward weights from the LGN to the cortex. Shown are $w(x, r)$ for two different locations in the cortex, $x = A$ and $x = B$. We can approximate the weights from the LGN to x as an ellipsoidal Gaussian with major axis aligned along the preferred orientation $\phi(x)$. Here $\phi(A) = \pi/6$ while $\phi(B) = 3\pi/4$. The vertical bars denote the centers of the receptive fields for A and B , respectively. Both Gaussians have the same input mass, width and orientation magnitude.

of-Gaussians center-surround function $A(x) = g(x, \sigma_+^2) - g(x, \sigma_-^2)$:

$$a(x) = \int_{x'} A(x - x') \int_r I(r) w(x', r) dr dx'. \quad (3.4)$$

The center-surround filter approximately represents the effects of competition mediated by lateral inhibition in the cortex. From studies of tracer dye injections, the lateral connectivity in cortex is known to be roughly isotropic on the hypercolumn length scale (below 1000 microns). Excitatory pyramidal neurons in V1 are believed to project further within the hypercolumn than inhibitory basket cells, but depending on delays, threshold levels and disynaptic connections these longer-range connections may be effectively inhibitory under normal cortical conditions. Solutions to the two-population Wilson-Cowan equations also indicate center-surround-type behavior is possible in regimes in which inhibitory self-interaction is shorter than excitatory self-interaction, provided crossover interactions between the excitatory and inhibitory

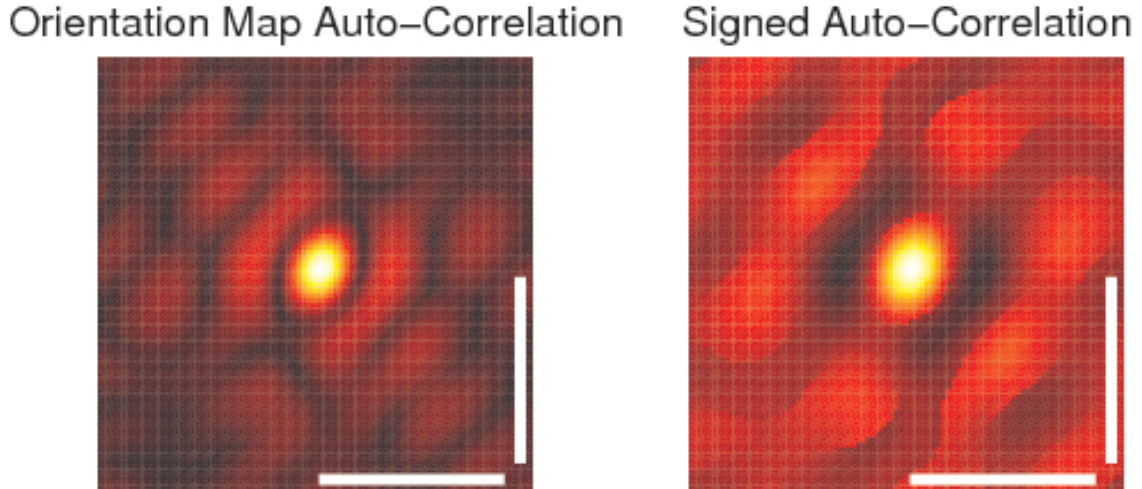


Figure 3.2: Orientation map auto-correlation function. Data provided courtesy of G. Blasdel. The auto-correlation function of the orientation map was calculated using matlab's `xcorr2` function with the map represented as a complex field $z = qe^{2i\phi}$. **Left:** Magnitude of $c(x)$, where $c(x) = \int_{x'} z(x' + x)\bar{z}(x) dx$. **Right:** *Signed auto-correlation function*, the magnitude of $c(x)$ times the sign of the real part of $c(x)$. This function illustrates that the first ring of correlation outside the central region represents *anticorrelation*. Scale bars, one mm.

populations is strong enough [85]. Finally, an effective lateral circuit that imposes short-range correlation and lateral anti-correlation matches the correlation structure seen in Blasdel's orientation-map data (see Figure 3.2).

The Hebb rule update of $w(x, r)$ depends on the correlation function $\langle I(r)a(x) \rangle$, which is given by

$$\langle I(r)a(x) \rangle = \int_{x'} A(x - x') \int_{r'} \langle I(r)I(r') \rangle w(x', r') dr' dx'.$$

It is natural to assume that the auto-correlation function $G(r, r')$ of the inputs is invariant under translations $r \rightarrow r + r_0$, reflections $r \rightarrow -r$ and rotations $r \rightarrow \text{Rot}_\theta r$. Let $G(r - r') = \langle I(r)I(r') \rangle$ denote such a correlation function. Then the update rule (3.3) becomes a double convolution

$$\Delta w(x, r) = \eta \int_{x'} A(x - x') \int_{r'} G(r - r') w(x', r') dr' dx'. \quad (3.5)$$

The learning rate η is taken to be small enough that the weight changes are based on the entire ensemble of input patterns $I(r)$ rather than being driven by a small number of them. While the Hebbian update rule specifies the change in every geniculocortical connection, I will restrict consideration to the changes occurring in the reduced variables $m, RandQ$. In this way I reduce the dynamical problem from the high-dimensional synaptic-weight space to the low-dimensional “feature” space. Because the moment variables and the update rule are all linear in w , the derivation of update rules for the reduced quantities is straightforward. (In Chapter 4, I will consider some effects of nonlinear constraints.) In order to derive the XY model for the orientation map, assume that the input mass and retinotopy are uniform, i.e.

$$m(x) = m_0 \quad (3.6)$$

$$R(x) = R_0 + (x - x_0)/\mu. \quad (3.7)$$

The effect of a small change Δw in the weights on the orientation at x is felt through the changes in the elements of the covariance matrix ΔQ_{ij} . Differentiating 3.2 gives

$$2\Delta\phi(x) = \left(\frac{\cos(2(\phi(x) + \frac{\pi}{2}))2\Delta Q_{12}(x) - \sin(2(\phi(x) + \frac{\pi}{2}))(\Delta Q_{11} - \Delta Q_{22})}{q(x)} \right). \quad (3.8)$$

The changes induced in Q by Δw are found by taking the second moments of equation 3.5.

$$\begin{aligned} \Delta Q(x) &= \frac{1}{m_0} \int_u uu^{\text{tr}} \Delta w(x, u + R(x)) du \\ &= \frac{\eta}{m_0} \int_u uu^{\text{tr}} \int_{x'} A(x - x') \int_{r'} G(u + R(x) - r') w(x', r') dr' dx' du \\ &= \frac{\eta}{m_0} \int_{x'} A(x - x') \int_{r'} w(x', r') \int_u uu^{\text{tr}} G(u + R(x) - r') du dr' dx' \end{aligned}$$

In addition to the symmetry properties of G , I take G to be normalized, i.e. $\int_r G(r) dr = 1$. This may be arranged by changing the constant η if necessary. Together with the

symmetry of G this condition guarantees the center-of-mass of G is at 0:

$$\int_u G(u + v) du = -v. \quad (3.9)$$

Exploiting 3.9 we can calculate the inner integral:

$$\begin{aligned} & \int_u uu^{\text{tr}} G(u + R(x) - r') du \\ &= \int_u \left((u + R(x) - r')(u + R(x) - r')^{\text{tr}} - u(R(x) - r')^{\text{tr}} \right. \\ & \quad \left. - (R(x) - r')u^{\text{tr}} - (R(x) - r')(R(x) - r')^{\text{tr}} \right) G(u + R(x) - r') du \\ &= \sigma_G^2 I_2 + (R(x) - r')(R(x) - r')^{\text{tr}} \end{aligned}$$

where σ_G is the width of G . Similarly, the center of mass of $w(x', r')$ is $R(x')$.

Denoting the difference in retinotopy $R(x) - R(x')$ by ΔR , we find

$$\begin{aligned} & \int_{r'} w(x', r') \int_u uu^{\text{tr}} G(u + R(x) - r') du dr' \\ &= \int_{r'} \frac{w(x', r')}{m_0} \left(\sigma_G^2 I_2 + (R(x) - r')(R(x) - r')^{\text{tr}} \right) dr' \\ &= \sigma_G^2 I_2 + \int_{r'} \frac{w(x', r')}{m_0} (\Delta R + R(x') - r') (\Delta R + R(x') - r')^{\text{tr}} dr' \\ &= \sigma_G^2 I_2 + \int_{r'} \frac{w(x', r')}{m_0} \left(\Delta R \Delta R^{\text{tr}} + \Delta R (R(x') - r')^{\text{tr}} \right. \\ & \quad \left. + (R(x') - r') \Delta R^{\text{tr}} + (R(x') - r')(R(x') - r')^{\text{tr}} \right) dr' \\ &= \sigma_G^2 I_2 + \Delta R \Delta R^{\text{tr}} + Q(x') \\ &= \sigma_G^2 I_2 + \frac{1}{\mu^2} (x - x')(x - x')^{\text{tr}} + Q(x') \end{aligned} \quad (3.10)$$

We can now finish the outer integral in 3.9:

$$\begin{aligned}
& \int_{x'} A(x-x') \int_{r'} w(x', r') \int_u uu^{\text{tr}} G(u+R(x)-r') du dr' dx' \\
&= m_0 \int_{x'} A(x-x') \left(\sigma_G^2 I_2 + \frac{1}{\mu^2} (x-x')(x-x')^{\text{tr}} + Q(x') \right) dx' \\
&= m_0 \left(\frac{1}{\mu^2} \int_y yy^{\text{tr}} A(y) dy + \int_{x'} A(x-x') Q(x') dx' \right) \\
&= \frac{m_0}{\mu^2} (\sigma_+^2 - \sigma_-^2) I_2 + m_0 \int_{x'} A(x-x') Q(x') dx'.
\end{aligned}$$

Thus the update rule for the elements of $Q(x)$ is given by

$$\Delta Q(x) = \eta \left(\frac{\sigma_+^2 - \sigma_-^2}{\mu^2} I_2 + \int_{x'} A(x-x') Q(x') dx' \right). \quad (3.11)$$

In terms of the quantities in equation 3.8 we can write

$$\begin{aligned}
\Delta(Q_{11} - Q_{12})(x) &= \eta A * (Q_{11} - Q_{22}) = \eta A * (q(x) \cos 2(\phi(x) + \frac{\pi}{2})) \\
2\Delta Q_{12}(x) &= \eta A * (2Q_{12}) = \eta A * (q(x) \sin 2(\phi(x) + \frac{\pi}{2}))
\end{aligned}$$

were we use the notation $(f * g)(x) = \int_{x'} f(x-x')g(x') dx'$ to denote convolution. If we take our orientation “spin” vectors to have uniform magnitude $q(x) = q_0$ as in the classical XY model, we have

$$\begin{aligned}
& 2\Delta\phi(x) \\
&= \eta \frac{q_0 (\cos 2(\phi(x) + \frac{\pi}{2}) A * \sin 2(\phi(x) + \frac{\pi}{2}) - \sin 2(\phi(x) + \frac{\pi}{2}) A * \cos 2(\phi(x) + \frac{\pi}{2}))}{q_0} \\
&= \eta \int_{x'} A(x-x') \\
&\quad \left(\cos 2(\phi(x) + \frac{\pi}{2}) \sin 2(\phi(x') + \frac{\pi}{2}) - \sin 2(\phi(x) + \frac{\pi}{2}) \cos 2(\phi(x') + \frac{\pi}{2}) \right) dx' \\
&= \eta \int_{x'} A(x-x') \sin(\phi(x') - \phi(x)) dx'
\end{aligned}$$

which is the low-temperature XY update rule 3.1. This derivation exemplifies the extreme case of reduction of a full synaptic model to a model for the develop-

ment of a single feature map, $\phi(x)$. We may instead choose to let both $\phi(x)$ and $q(x)$ vary, in which case the update rule specifies a change in the vector $\chi(x) = q(x)(\cos 2\phi(x), \sin 2\phi(x))^{\text{tr}}$:

$$\Delta\chi(x) = \eta \int_{x'} A(x - x')\chi(x') dx'. \quad (3.12)$$

3.3 Orientation and Retinotopy

Observations by Das and Gilbert demonstrated strong correlations between the orientation map and the pattern of retinotopic distortion in cat V1 [18]. If we relax the uniform retinotopy condition 3.7 then we can study the influence that retinotopic distortions have on the orientation vector χ . We assume a uniform “background” or “average local” retinotopy with respect to which the fine-grained retinotopic distortion may be defined. On the scale of a few hypercolumns, this background retinotopy is approximately uniform [4] and may be taken to be the identity map (up to rotation and translation) if binocular effects are neglected. Therefore we take the local retinotopic distortion $s(x)$ to be defined as:

$$s(x) = R(x) - R_0 - \frac{x - x_0}{\mu}. \quad (3.13)$$

Introducing $s(x) \neq 0$ modifies the consequences of equation 3.5. In place of equation 3.10 we now have

$$\begin{aligned} & \int_{r'} w(x', r') \int_u uu^{\text{tr}} G(u + R(x) - r') du dr' \\ &= \sigma_G^2 I_2 + \frac{1}{\mu^2} (x - x' + \Delta s)(x - x' + \Delta s)^{\text{tr}} + Q(x') \end{aligned} \quad (3.14)$$

where $\Delta s = s(x) - s(x')$. The update rule for Q , equation 3.9, is modified by the addition of several terms that depend on the pattern of retinotopic distortion $s(x)$.

$$\begin{aligned} \Delta Q &= \eta \left(\frac{\sigma_+^2 - \sigma_-^2}{\mu^2} I_2 + \int_{x'} A(x - x') \frac{x - x'}{\mu} (s(x) - s(x'))^{\text{tr}} dx' \right. \\ &\quad + \int_{x'} A(x - x') (s(x) - s(x')) \left(\frac{x - x'}{\mu} \right)^{\text{tr}} dx' \\ &\quad \left. + \int_{x'} A(x - x') (s(x) - s(x')) (s(x) - s(x'))^{\text{tr}} dx' + A * Q \right) \end{aligned} \quad (3.15)$$

The new terms are independent of $Q(x)$, so they act as forcing terms driving the orientation vector pattern away from what would otherwise be a steady state pattern. Extracting the components of change of the orientation vector

$$\begin{aligned} \chi_1 &= Q_{11} - Q_{22} \\ \chi_2 &= 2Q_{12} \end{aligned}$$

gives the expression:

$$\Delta \chi_j = A * \chi_j + 2 \left(A \frac{x}{\mu} \right)^{\text{tr}} * S_j s - 2 s^{\text{tr}} S_j (A * s) + A * \left(s^{\text{tr}} S_j s \right) \quad (3.16)$$

for $j = 1, 2$. Equation 3.16 uses the notation

$$S_1 = \begin{pmatrix} 1 & 0 \\ 0 & -1 \end{pmatrix} \quad (3.17)$$

$$S_2 = \begin{pmatrix} 0 & 1 \\ 1 & 0 \end{pmatrix} \quad (3.18)$$

$$\left(A x^{\text{tr}} \right) * v = \int_{x'} A(x - x') \{ (x_1 - x'_1) v_1(x') + (x_2 - x'_2) v_2(x') \} dx'$$

To see the effects of the extra terms in equation 3.16, consider the arbitrary pattern of retinotopic distortion shown in Figure 3.3. Recall that $s(x)$ is the deviation of the retinotopic position from a uniform background grid. It is a vector field with a 2π

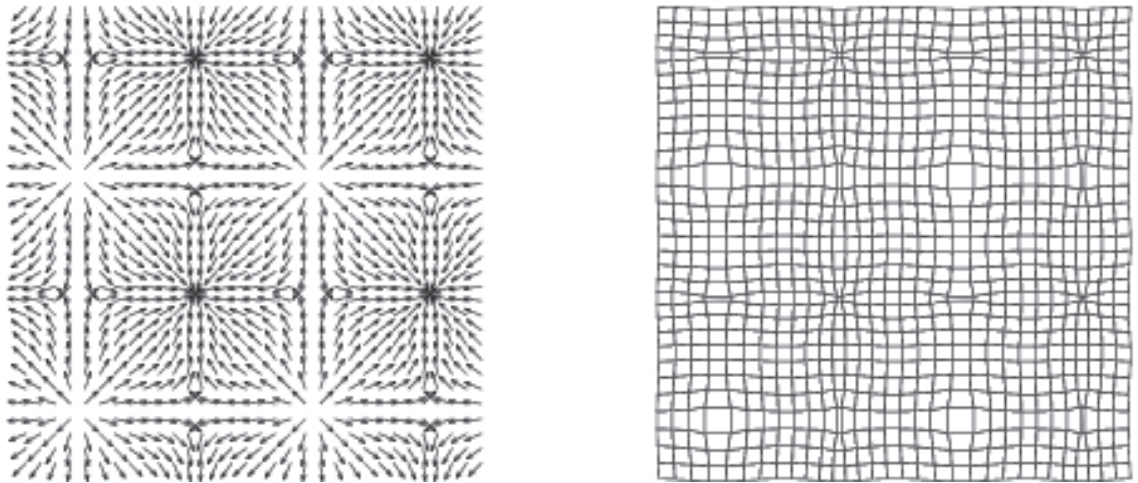


Figure 3.3: Sample retinotopic distortion pattern. A periodic pattern of retinotopic distortion.

Left: The retinotopic distortion vector field $s(x)$ with a lattice of positive and negative singularities.

Right: The distorted retinotopic map $R(x)$. Note the negative singularities corresponding to both horizontal shear (upper left) and vertical shear (lower right).

rotation symmetry, unlike the π -periodic orientation vector. Figure 3.3 shows a lattice of positive and negative singularities in $s(x)$. Note that a positive singularity (angle of $s(x)$ changes in the same sense as position about singularity) may correspond either to a dilation, a contraction or a local twist (twist not shown). A negative singularity in $s(x)$ corresponds to a *shear* in the retinotopic map. The value of $\Delta\chi_j - A*\chi_j$ for each component $j = 1, 2$ is depicted in Figure 3.4. Recall that the first component χ_1 gives the excess elongation of the receptive field in the horizontal direction, or equivalently the preference for a horizontal contour over a vertical one. The second component χ_2 gives the preference for $+\pi/4$ oblique over $-\pi/4$ oblique. The $s(x)$ -singularities giving isotropic dilation or contraction do not contribute substantially to either component. The singularities giving *horizontal* shear drive χ_1 *positive* while those giving *vertical* shear drive χ_1 *negative*—these singularities force the receptive fields to lie along the direction of the shear. Since this particular distortion pattern has little oblique shear there is almost no effect on χ_2 . Hence the model predicts a relationship between the direction of shear in the retinotopic map in V1 and the preferred orientation. (See section A.3 for further discussion of retinotopic shear.) We shall see in Chapter 5 that this relation between retinotopic shear and the orientation vector persist in a more complete model for interaction between cortical map components, and may be understood in terms of the symmetry properties of the different feature components.

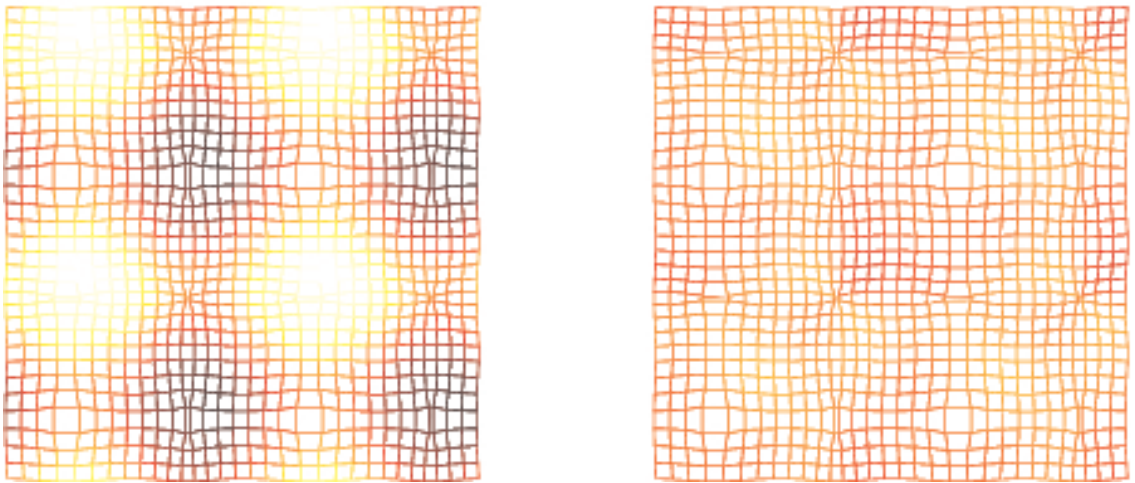


Figure 3.4: Effect of retinotopic distortion on the orientation map.

Left: Contribution of distortion terms to $\Delta\chi_1$. Positive (light) indicates forcing orientation vector towards the horizontal. Negative (dark) indicates forcing χ towards vertical. Compare Figure 3.3.

Right: Contribution of distortion terms to $\Delta\chi_2$. Note the largest effects come from regions with pronounced vertical and horizontal retinotopic shear, and most of the effect is on χ_1 .

CHAPTER 4

THE GENERALIZED XY MODEL: MONOCULAR CASE

The last chapter derived the XY rule for the orientation map from a Hebbian synaptic model with difference-of-Gaussians lateral interaction, assuming regular retinotopy $R(x) = \frac{x}{\mu}$ and uniform input weight $\lambda(x) \equiv 1$. In striate cortex, the input weight to any layer is not necessarily uniform. It has been suggested, for example, that the cytochrome oxidase “blob” regions, which have higher levels of activity than the surrounding regions, represent loci of greater-than-average net input [47]. Some researchers report that the blob patterns obtained histologically coincide with the centers of the orientation singularities obtained optically, indicating that net input weight may be linked to the orientation map. The retinotopic map is also not uniform on a fine scale, but has deviations from the coarse background retinotopy. Although globally the retinotopy obeys an approximate complex logarithmic mapping from visual-field to cortical coordinates, on the scale of a few hypercolumns this map is approximately the identity (up to a locally uniform rotation and translation). But on a finer-grained scale, within a single hypercolumn, neighboring cells’ retinotopic positions deviate from this identity map by small displacements that I will represent with the (small) planar vector $s(x)$. Das and Gilbert showed in 1997 that this retinotopic distortion vector is significantly correlated with the orientation map [18]. In addition, the ocular dominance map, which arises from differences in the net input weight from the two eyes, is strongly related to the orientation map, with the orientation singularities situated centrally within the OD stripes (or OD blobs, in the case of cats [17]). In order to study the joint development of different cortical maps it is necessary to relax the constraint on uniform input weight and retinotopy. In this chapter, I derive a model for the linear interactions of different cortical-map features (in the monocular case). To do this I modify the Turing-kernel equation that motivated Chapter 3 to include constraints on the net fan-in weight to any cortical site

and the net fan-out weight from any geniculate site. I posit an homogeneous initial state with uniform fan-in and fan-out weights, uniform retinotopy and no orientation preference. The cortical map appears through spontaneous breaking of the symmetry of this homogeneous state. The coupling between different map features arises in two ways: because lower moments of the receptive field profiles appear in the definitions of the higher moments, nonuniformities in retinotopy (the first moment) directly affect the development of the orientation vector (a second moment), while nonuniformities in the input weight affect all higher moments. Additionally, all quantities are coupled through the fan-out constraint, which thus plays a crucial role in determining the joint feature maps. The importance of this constraint has been overlooked in earlier, less geometrically motivated models.

4.1 The Cortical-Map Vector

The rough background retinotopy with globally correct orientation assumed in Chapter 3, $R(x) = \frac{x}{\mu}$, can arise from a combination of correlation-based learning and chemical markers. The former was shown in a one-dimensional model analyzed by Häussler and von der Malsburg [31] (see Chapter 1.3). In the absence of an additional selection mechanism such as a chemical marker biasing the location of retinotectal connections, the Häussler-von der Malsburg model will form either a right-to-left or a left-to-right map with equal probability. In the two-dimensional case, the map formation process is neutrally stable to any rotation or reflection of the respective coordinate axes

$$R(x) = \begin{pmatrix} \cos(\theta) & -\sin(\theta) \\ \pm \sin(\theta) & \pm \cos(\theta) \end{pmatrix} \cdot \frac{x}{\mu}.$$

Hence unless the initial conditions are somehow biased toward forming a global map of the correct orientation, one may expect continuous deformations in the cardinal directions by θ for different locations x . In order to establish a map of the correct orientation, it is necessary to include a term describing some sort of location- or axis-specific marker [82, 79]. Such a marker need only be present long enough to add a slight asymmetry to random initial conditions, and removed after a brief initial

Map Component	Definition	Name
$\hat{\lambda}(x)$	$\lambda(x) - \lambda_0$	Input Weight Deviation
$s(x)$	$R(x) - \frac{x}{\mu}$	Retinotopic Distortion Vector
$\chi(x)$	$\begin{pmatrix} Q_{11}(x) - Q_{22}(x) \\ 2Q_{12}(x) \end{pmatrix}$	Orientation Tuning Vector
$\rho(x)$	$\sigma^2(x) - \sigma_0^2$	R.F. Width Deviation

Table 4.1: Components of the cortical-map vector. See Table 3.1 for definitions of λ, R, Q .

period [33]. I will assume for the remainder a uniform coarse retinotopy given by $R(x) = \frac{x}{\mu} + s(x), |s(x)| \ll 1$. All spatial quantities such as R, s and x are taken to represent vectors in the plane. The retinocortical magnification μ has units of either (cortical) millimeters per degree of visual angle or (cortical) millimeters per (geniculate) millimeters, as appropriate. Against this background, I define the following quantities geometrically given the feedforward weights $w(x, r)$: The net deviation in input mass, $\hat{\lambda}(x)/\lambda_0 = (\lambda(x) - \lambda_0)/\lambda_0$, the retinotopic distortion vector $s(x)$, the orientation tuning vector $\chi(x)$ (from the axes and elongation of the covariance matrix, see Appendix 6.2.3) and $\rho(x)$, the deviation of the receptive field width (trace of the covariance matrix) from its uniform value (see Table 4.1).

4.2 Dynamical Equation for $w(x, r)$

4.2.1 Constrained Hebb Rule

The basic pattern-forming mechanism for cortical-map development in the orientation-XY model was the difference-of-Gaussians convolution kernel in equation 3.4. By modifying this equation in order to constrain the total cortical input and geniculate output weights at each location, I derive a dynamical equation that couples together the patterns formed by different components (for example, orientation and retinotopy). The unconstrained dynamics will be given by

$$\mathbf{F}_{\text{uncon}}[w](x, r) = \lambda \int_{x'} A(x - x') \int_{r'} G(r - r') w(x', r') dr' dx' - \alpha w(x, r) + \mathcal{C}h(x, r) \quad (4.1)$$

where α is a decay constant, λ determines the strength of the pattern-forming mechanism and $\mathcal{Ch}(x, r)$ is a small term biasing the retinotopic map to the correct orientation, representing chemical markers. Limits to the physical size of dendritic arbors and the packing density of afferent fibers, and limitations to the amount of stimulation a cell can tolerate, prevent the net feedforward input to a given cortical location $\lambda(x)$ from growing without bound. I assume an equilibrium level of input λ_0 to which each cortical cell tends. Similarly, physiological and geometric constraints limit the amount of outgoing synaptic weight that a given geniculate cell can project to the cortex. The net output weight or *fan-out*, given by

$$\Upsilon(r) = \int_x w(x, r) dx, \quad (4.2)$$

also tends toward a preferred level $\Upsilon_0 = \mu\lambda_0$. I model this soft uniformity constraint in both $\lambda(x)$ and $\Upsilon(r)$ with logistic growth terms:

$$\mathbf{F}_{\text{con}}[w](x, r) = w(x, r) \{K_\lambda(\lambda(x) - \lambda_0) + K_\Upsilon(\Upsilon(r) - \Upsilon_0)\}. \quad (4.3)$$

These constraint terms are just in balance when every geniculate cell has the same representation in the cortex and every cortical cell has the same average input activity.

4.2.2 Existence of an Homogeneous Steady State

I will assume that the dynamical system

$$\begin{aligned} \frac{1}{\eta} \frac{d}{dt} w(x, r) &= \mathbf{F}[w](x, r) := \mathbf{F}_{\text{uncon}}[w](x, r) + \mathbf{F}_{\text{con}}[w](x, r) \\ &= \lambda \int_{x'} A(x - x') \int_{r'} G(r - r') w(x', r') dr' dx' \\ &\quad - \alpha w(x, r) + \mathcal{Ch}(x, r) \\ &\quad + w(x, r) \{K_\lambda(\lambda(x) - \lambda_0) + K_\Upsilon(\Upsilon(r) - \Upsilon_0)\} \\ w(x, r) &\geq 0 \end{aligned} \quad (4.4)$$

has a homogeneous steady state of the form

$$w_0(x, r) = \lambda_0 f\left(\left|\frac{x}{\mu} - r\right|\right) \quad (4.5)$$

where $f(|u|) \lesssim \exp(-k||u||^2)$ as $|u| \rightarrow \infty$, and the moments of f satisfy $\int_u f(u) du = 1$, $\int_u f(u)u du = 0$, and $\int_u f(u)uu^{\text{tr}} du = \sigma_0^2 I_2$. This steady-state receptive-field profile $f(u)$ is circularly symmetric, so the orientation tuning vector $\chi(x) \equiv 0$. It represents an undistorted retinotopy, $s(x) \equiv 0$, and uniform input mass $\hat{\lambda}(x)/\lambda_0 \equiv 0$ and output $\Upsilon(r)/\Upsilon_0 \equiv 1$. I will further assume that at a critical value of λ this homogeneous steady state loses stability to an inhomogeneous patterned state, representing the initial development of a cortical map. The patterns of orientation, retinotopy, etc., that emerge through such symmetry-breaking bifurcations may be analyzed using techniques from group-representation theory in Chapter 5. To argue that a steady state of the form described exists for equation 4.4, I will show explicitly a steady state for a generalized dynamical system of similar form. Consider the generalized equations

$$\frac{1}{\eta} \frac{d}{dt} w(x, r) = \kappa \left\{ \begin{array}{l} \lambda w(x, r)^p \int_{x'} A(x - x') \int_{r'} G(r - r') w(x', r') dr' dx' \\ -\alpha w(x, r) + \mathcal{C}h(x, r) \end{array} \right\} \\ + w(x, r) \{K_\lambda(\lambda(x) - \lambda_0) + K_\Upsilon(\Upsilon(r) - \Upsilon_0)\}, \quad (4.6)$$

$$0 \leq p \leq 1$$

This form is very close to the Häussler-von der Malsburg equations, for which $p = 1$ (see section 1.3.3). By choosing particular forms for A , G and $\mathcal{C}h$ it is possible to tailor-make a steady state $w_0(x, r) = f\left(\frac{x}{\mu} - r\right)$ that is a circularly symmetric Gaussian with receptive field width σ_0 :

$$f(u) = g(u, \sigma_0^2) := \frac{1}{2\pi\sigma_0^2} \exp\left(-\frac{||u||^2}{2\sigma_0^2}\right). \quad (4.7)$$

For analytical tractability I take each of the quantities to be composed of Gaussians:

$$A(x) = g(x, \sigma_+^2) - g(x, \sigma_-^2) \quad (4.8)$$

$$G(r) = g(r, \sigma_r^2) \quad (4.9)$$

$$\mathcal{Ch}(x, r) = K_{\mathcal{Ch}} g\left(\frac{x}{\mu} - r, \sigma_{\mathcal{Ch}}\right), \quad (4.10)$$

where $\sigma_+ < \sigma_-$. Substituting these forms into equation 4.6, I calculate (see identities for Gaussians in appendix A.3):

$$A *_x G *_r w_0 = \int_{x'} A(x - x') \int_{r'} G(r - r') w_0(x', r') \quad (4.11)$$

$$= \lambda_0 \mu^2 \left\{ g\left(\frac{x}{\mu} - r, \sigma_0^2 + \sigma_r^2 + \frac{\sigma_+^2}{\mu^2}\right) - g\left(\frac{x}{\mu} - r, \sigma_0^2 + \sigma_r^2 + \frac{\sigma_-^2}{\mu^2}\right) \right\}$$

$$\lambda w_0^p A *_x G *_r w_0 = \frac{\lambda \mu^2 \lambda_0^{1+p} (2\pi \sigma_0^2)^{1-p}}{2\pi} \left\{ \begin{array}{l} \frac{g\left(\frac{x}{\mu} - r, \frac{\sigma_0^2(\sigma_0^2 + \sigma_r^2 + (\sigma_+/\mu)^2)}{(1+p)\sigma_0^2 + \sigma_r^2 + (\sigma_+/\mu)^2}\right)}{(1+p)\sigma_0^2 + \sigma_r^2 + (\sigma_+/\mu)^2} \\ - \frac{g\left(\frac{x}{\mu} - r, \frac{\sigma_0^2(\sigma_0^2 + \sigma_r^2 + (\sigma_-/\mu)^2)}{(1+p)\sigma_0^2 + \sigma_r^2 + (\sigma_-/\mu)^2}\right)}{(1+p)\sigma_0^2 + \sigma_r^2 + (\sigma_-/\mu)^2} \end{array} \right\} \quad (4.12)$$

By choosing σ_0 and p to satisfy

$$\sigma_0^2 = \frac{1-p}{p} \left(\sigma_r^2 + \left(\frac{\sigma_+}{\mu}\right)^2 \right), \quad (4.13)$$

I make σ_0 equal the width of the Gaussian in the first (positive) term of equation 4.12. For reasonable choices of σ_r (100 microns) and σ_+/μ (100 microns—this is the spread of local cortical excitation converted to geniculate distances by the magnification factor) and the convenient value of $p = 0.5$ I obtain the reasonable value $\sigma_0 \approx 140$ microns for the steady-state geniculate receptive-field width. If I now set the decay constant α appropriately then the decay term will just cancel the positive term

from equation 4.12:

$$\alpha = \frac{\mu^2}{2\sigma_0^2} \sqrt{\frac{\lambda_0}{2\pi}}. \quad (4.14)$$

I now choose $K_{\mathcal{Ch}}$ and $\sigma_{\mathcal{Ch}}$ to match the remaining negative term from equation 4.12:

$$\sigma_{\mathcal{Ch}}^2 = \frac{2\sigma_0^2 \left(\sigma_0^2 + \sigma_r^2 + \frac{\sigma_-^2}{\mu^2} \right)}{3\sigma_0^2 + \sigma_r^2 + \frac{\sigma_-^2}{\mu^2}} \quad (4.15)$$

$$K_{\mathcal{Ch}} = \frac{1}{2\pi \left(3\sigma_0^2 + \sigma_r^2 + \frac{\sigma_-^2}{\mu^2} \right)}. \quad (4.16)$$

With these *ad hoc* choices for the terms in the modified dynamical equation 4.6 the weight profile $w_0(x, r) = \lambda_0 g\left(\frac{x}{\mu} - r, \sigma_0^2\right)$ exactly cancels the “unconstrained” terms. At the same time the constraint terms are balanced because $\lambda(x) \equiv \lambda_0$ and $\gamma(r) \equiv \gamma_0 = \mu\lambda_0$. The Gaussian form for $\mathcal{Ch}(x, r)$ is not unrealistic for a chemical marker subject to diffusion, although the tightness of its distribution may be unreasonable (given the widths stated above for σ_r, σ_+ and $\sigma_- = 3\sigma_+$, I have $\sigma_{\mathcal{Ch}} \approx 170$ microns). The purpose of this construction is merely to make plausible a localized isotropic, homogeneous steady-state receptive-field distribution for equation 4.4. To obtain the dynamical equation (4.4) of interest we decrease p from 0.5 to 0. Note that the steady-state Gaussian distribution w_0 narrows to Dirac’s delta function as $p \rightarrow 1$. As $p \rightarrow 0$ with $\kappa = 0$ the steady-state receptive field width $\sigma_0 \rightarrow \infty$, according to equation 4.13. But the Mexican hat tends to contract the receptive-field width. The receptive field width is taken to be the variance of the receptive field distribution,

$$\sigma^2 = \frac{1}{2} \text{Tr} \left(\int_u w(x, u + R(x)) u u^{\text{tr}} du \right) \quad (4.17)$$

$$= \frac{1}{2} \int_u w(x, u + R(x)) \|u\|^2 du. \quad (4.18)$$

Because σ^2 is a linear functional of w , a dynamical expression for σ may be derived directly from the full dynamical system for w . Taking $w(x, r)$ to be of the form

$\lambda_0 g(r - x/\mu, \sigma^2)$ for a time-dependent σ^2 , I calculate:

$$\begin{aligned}
\frac{d}{dt}\sigma^2 &= \frac{1}{2} \int_u \left(\frac{d}{dt} w(x, u + R(x)) \right) ||u||^2 du & (4.19) \\
&= \frac{1}{2} \int_u \eta \mathbf{F}_{\text{uncon}}[w](x, u + R(x)) ||u||^2 du \\
&= \frac{\eta}{2} \int_u \left(\begin{array}{c} \lambda \int_{x'} A(x - x') \int_{r'} G(u + R(x) - r') w(x', r') dr' dx' \\ -\alpha w(x, u + R(x)) + \mathcal{C}h(x, u + R(x)) \end{array} \right) ||u||^2 du \\
&= \frac{\eta}{2} \int_u \left(\begin{array}{c} \lambda (\lambda_0 g(u, \sigma^2 + \sigma_r^2 + \sigma_+^2) - \lambda_0 g(u, \sigma^2 + \sigma_r^2 + \sigma_-^2)) \\ -\alpha \lambda_0 g(u, \sigma^2) + K_{\mathcal{C}h} g(u, \sigma_{\mathcal{C}h}^2) \end{array} \right) ||u||^2 du \\
&= \eta \left(\lambda \lambda_0 (\sigma_+^2 - \sigma_-^2) - \alpha \lambda_0 \sigma^2 + K_{\mathcal{C}h} \sigma_{\mathcal{C}h}^2 \right).
\end{aligned}$$

For reasonable parameter values and $K_{\mathcal{C}h} \approx 1$, $\frac{d}{dt}\sigma^2 < 0$ for $\lambda \gtrsim 0.4$, even if $\alpha = 0$. For $\alpha > 0$ and large initial receptive field size, σ^2 decreases rapidly. Indeed it is even possible to have $\frac{d}{dt}\sigma^2 < 0$ when σ^2 reaches zero! This conclusion renders irrelevant the existence of a $\sigma = \infty$ steady state. It is the $w \geq 0$ constraint that prevents the collapse of the receptive fields to zero width distributions: as σ decreases, the inhibitory surround in equation 4.4 would drive w negative away from the central region. Because w is not allowed below zero weight, there is a net increase in the fan-in weight λ above λ_0 (see Figure 4.1). With the constraint in effect, the central area of greatest interest for my purposes remains well approximated by a Gaussian, while the periphery has a sharp edge at $w = 0$. Because the shape of this steady-state receptive field cannot be determined analytically, I will approximate the homogeneous state with the Gaussian w_0 defined in equation 4.7. In the following, I will ignore the small difference between λ_0 and λ_{SS} , which can be incorporated with a change in scale.

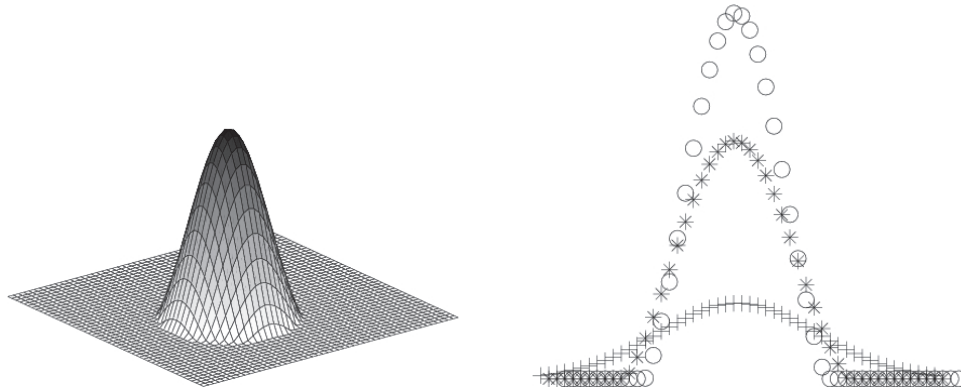


Figure 4.1: Constrained receptive-field dynamics and steady-state.

Left: Steady-state shape of a single receptive field under a simplified dynamics, involving only convolution with A and G , and the logistic constraint.

Right: Development of receptive field shape from initial Gaussian.

Initial receptive field profile: $+++$. Intermediate r.f. profile: $***$. Final r.f. profile: ooo . The nonnegativity constraint forces the total fan-in mass λ_{SS} higher than λ_0 . For this simulation $\lambda_{SS} \approx 1.189\lambda_0$.

4.3 Derivation of Linear Interactions Between Cortical-Map Components

In the homogeneous steady state

$$w_0(x, r) = \lambda_0 g\left(\frac{x}{\mu} - r, \sigma_0^2\right) := \frac{\lambda_0}{2\pi\sigma_0^2} \exp\left(-\frac{|\frac{x}{\mu} - r|^2}{2\sigma_0^2}\right)$$

the receptive fields are assumed to have uniform fan-in weight

$$\frac{\hat{\lambda}(x)}{\lambda_0} = \frac{\lambda(x) - \lambda_0}{\lambda_0} = 0,$$

regular retinotopy

$$s(x) = R(x) - \frac{x}{\mu} = 0,$$

circularly symmetrical profiles

$$\chi(x) = \begin{pmatrix} Q_{11} - Q_{22} \\ 2Q_{12} \end{pmatrix} = 0$$

and uniform widths

$$\rho(x) = \sigma^2(x) - \sigma_0^2 = 0.$$

Thus the cortical-map vector for the homogeneous Gaussian state is identically zero:

$$\mathbf{v} = \begin{pmatrix} \hat{\lambda}(x)/\lambda_0 \\ \begin{pmatrix} s_1(x) \\ s_2(x) \end{pmatrix} \\ \begin{pmatrix} \chi_1(x) \\ \chi_2(x) \end{pmatrix} \\ \rho(x) \end{pmatrix} \equiv \mathbf{0}. \quad (4.20)$$

Rather than study the linearization of equation 4.4 about $w_0(x, r)$ with respect to arbitrary perturbations $w_0(x, r) + \varepsilon h(x, r)$, I will restrict attention to the geometrical properties of a perturbation $h(x, r)$ corresponding to the cortical maps of interest. As an inhomogeneous pattern in w develops from the homogeneous state, I will study interactions between the components of \mathbf{v} when all are of order ε :

$$|v_i(x)| \ll 1, \forall i = 1, \dots, 6, \forall x \in X. \quad (4.21)$$

Each cortical-map “feature” $v_i(x)$ is a linear functional of $w(x, r)$, hence of $h(x, r) = (w(x, r) - w_0(x, r))/\varepsilon$ corresponding to a component of one of the zeroth, first or second vector moments of w with respect to r at cortical location x . Therefore the dynamical behavior of each is described by the corresponding “moment” of equation 4.4 (see Table 3.1 for the moment definitions):

$$\frac{d}{dt} \hat{\lambda}(x) = \int_{r \in \mathbb{R}^2} \eta \mathbf{F}[w](x, r) dr \quad (4.22)$$

$$\frac{d}{dt} (\lambda(x) s(x)) = \int_{r \in \mathbb{R}^2} \eta \mathbf{F}[w](x, r) \left(r - \frac{x}{\mu} \right) dr \quad (4.23)$$

$$\frac{d}{dt} (\lambda(x) \chi(x)) = \int_{u \in \mathbb{R}^2} \eta \mathbf{F}[w](x, u + R(x)) \begin{pmatrix} u_1^2 - u_2^2 \\ 2u_1 u_2 \end{pmatrix} du \quad (4.24)$$

$$\frac{d}{dt} (\lambda(x) \rho(x)) = \int_{u \in \mathbb{R}^2} \eta \mathbf{F}[w](x, u + R(x)) \frac{\|u\|^2}{2} du \quad (4.25)$$

Recall that the retinotopy $R(x) = s(x) + x/\mu$ includes the order ε retinotopic distortion. There is a cascade of perturbation effects from lower moments to higher moments. Inhomogeneities in $\lambda(x)$ affect all the higher moment, as evident in equation 4.22. Inhomogeneities in the retinotopy vector $s(x)$ affect the dynamics of the orientation vector and the receptive field width. The dynamical constraints on weight evolution (equation 4.3) include a logistic constraint on the net fan-out weight $\Upsilon(r)$ from each geniculate location r . In the homogeneous state the fan-out has a uniform value $\Upsilon_0 = \mu^2 \lambda_0$, where μ is the geniculocortical magnification factor. Variation of the fan-in weight, the centers of the receptive fields or their elongation in various directions spoil the uniformity of the fan-out, inducing a perturbation $\hat{\Upsilon}(r) = \Upsilon(r) - \Upsilon_0$. For example, if the receptive fields of two nearby cortical cells move their centers closer together than would be dictated by the homogeneous spacing $|\Delta r| = |\Delta x|/\mu$, the geniculate locations in the region of increased overlap gain net fan-out weight while those just beyond the original cell centers lose fan-out weight. In this way the uniform representation of all geniculate locations becomes compromised, so the logistic Υ -term provides reinforcement of the homogeneous state. In order to account for the mutual interactions of perturbations in vector components arising from different moments of the synaptic-weight profile, I develop a Taylor expansion of $w(x, r)$ about $w_0(x, r) = \lambda_0 g\left(r - \frac{x}{\mu}, \sigma_0^2\right)$ given $\mathbf{v} \neq \mathbf{0}$. In order to express deviations of the Gaussian profile from circular symmetry I introduce the bivariate Gaussian notation:

$$g(u, Q) = \frac{1}{2\pi\sqrt{\det(Q)}} \exp\left(-\frac{1}{2}u^{\text{tr}}Q^{-1}u\right), \quad (4.26)$$

where $Q(x) = \begin{pmatrix} Q_{11}(x) & Q_{12}(x) \\ Q_{12}(x) & Q_{22}(x) \end{pmatrix}$ is the (symmetric) covariance matrix of the receptive field profile for w at x . When Q is a multiple of the identity matrix, $Q = \sigma^2 I_2$, the two notations $g(u, \sigma^2)$ and $g(u, \sigma^2 I_2)$ coincide. I also remind the reader of the following notation: two matrices that arise frequently in calculations

with the orientation vector are

$$S_1 = \begin{pmatrix} 1 & \\ & -1 \end{pmatrix} \quad (4.27)$$

$$S_2 = \begin{pmatrix} & 1 \\ 1 & \end{pmatrix}. \quad (4.28)$$

Thus $u^{\text{tr}} S_1 u$ and $u^{\text{tr}} S_2 u$ are shorthand for $u_1^2 - u_2^2$ and $2u_1 u_2$, respectively. To first order in $\hat{\lambda}/\lambda_0, s, \chi$ and ρ , a perturbed receptive field profile for cortical location x is given by:

$$\begin{aligned} w(x, r) &= (\lambda_0 + \hat{\lambda}(x)) \cdot \\ &g \left(r - \frac{x}{\mu} - s(x), (\sigma_0^2 + \rho(x)) I_2 + \frac{1}{2} \begin{pmatrix} \chi_1(x) & \chi_2(x) \\ \chi_2(x) & -\chi_1(x) \end{pmatrix} \right) \\ &= \lambda_0 g \left(r - \frac{x}{\mu}, \sigma_0^2 \right) \cdot \\ &\left\{ 1 + \frac{\hat{\lambda}(x)}{\lambda_0} + \frac{(r - x/\mu) \cdot s(x)}{\sigma_0^2} + \frac{\rho(x)}{\sigma_0^2} \left(\frac{\|r - x/\mu\|^2}{2\sigma_0^2} - 1 \right) + \right. \\ &\left. \frac{1}{4\sigma_0^4} \left(\chi_1(x)(r - x/\mu)^{\text{tr}} S_1 (r - x/\mu) + \chi_2(x)(r - x/\mu)^{\text{tr}} S_2 (r - x/\mu) \right) \right\} \\ &+ O((\hat{\lambda}, s, \chi, \rho)^2) \end{aligned} \quad (4.29)$$

(4.30)

Substituting the first-order perturbed weights 4.29 and 4.38 into the dynamical systems 4.4 and calculating the moments as in equation 4.22 yields equations for the interactions mediated by the direct “geometrical” effects of lower moments on higher.

For Gaussian identities used in calculating the moment integrals see Appendix A.3.

$$\begin{aligned} \frac{1}{\eta} \frac{d}{dt} \frac{\hat{\lambda}(x)}{\lambda_0} &= \lambda A * \left(\frac{\hat{\lambda}}{\lambda_0} \right) - \alpha \left(\frac{\hat{\lambda}}{\lambda_0} \right) - K_\lambda \hat{\lambda} \\ &\quad - K_\gamma \int_u \hat{\gamma}(u + R(x)) g(u, \sigma_0^2) du \end{aligned} \quad (4.31)$$

$$\begin{aligned} \frac{1}{\eta} \frac{d}{dt} s(x) &= \lambda A * s - \alpha s - \lambda \left(A \frac{x}{\mu} \right) * \left(\frac{\hat{\lambda}}{\lambda_0} \right) \\ &\quad - K_\gamma \int_u \hat{\gamma}(u + R(x)) g(u, \sigma_0^2) u du \end{aligned} \quad (4.32)$$

$$\begin{aligned} \frac{1}{\eta} \frac{d}{dt} \chi_1(x) &= \lambda A * \chi_1 - \alpha \chi_1 + \lambda \left(A \frac{x^{\text{tr}} S_1 x}{\mu^2} \right) * \left(\frac{\hat{\lambda}}{\lambda_0} \right) + 2\lambda \left(A \frac{x^{\text{tr}}}{\mu} \right) * (S_1 s) \\ &\quad - K_\gamma \int_u \hat{\gamma}(u + R(x)) g(u, \sigma_0^2) \left(u^{\text{tr}} S_1 u \right) du \end{aligned} \quad (4.33)$$

$$\begin{aligned} \frac{1}{\eta} \frac{d}{dt} \chi_2(x) &= \lambda A * \chi_2 - \alpha \chi_2 + \lambda \left(A \frac{x^{\text{tr}} S_2 x}{\mu^2} \right) * \left(\frac{\hat{\lambda}}{\lambda_0} \right) + 2\lambda \left(A \frac{x^{\text{tr}}}{\mu} \right) * (S_2 s) \\ &\quad - K_\gamma \int_u \hat{\gamma}(u + R(x)) g(u, \sigma_0^2) \left(u^{\text{tr}} S_2 u \right) du \end{aligned} \quad (4.34)$$

$$\begin{aligned} \frac{1}{\eta} \frac{d}{dt} \rho(x) &= \lambda A * \rho - \alpha \rho + \left(A \left(\lambda \frac{\|x\|^2}{\mu^2} + \sigma_r^2 \right) \right) * \left(\frac{\hat{\lambda}}{\lambda_0} \right) + 2\lambda \left(A \frac{x^{\text{tr}}}{\mu} \right) * s \\ &\quad - K_\gamma \int_u \hat{\gamma}(u + R(x)) g(u, \sigma_0^2) \left(\|u\|^2 - \sigma_0^2 \right) du \end{aligned} \quad (4.35)$$

Each quantity \dot{v}_i/η has a term $\lambda A * v_i - \alpha v_i$ pitting Turing-type pattern growth due to the difference-of-Gaussians lateral interaction A against the decay rate α . Here $*$ denotes convolution in the x variable:

$$((f) * (g))(x) := \int_{x' \in \mathbb{R}^2} f(x - x') g(x') dx'.$$

Therefore each component of the vector separately obeys dynamics that can form patterns when λ increases beyond a critical value—although this value may be different for different components v_i . Because each of these self-interaction terms arises from the same underlying pattern-forming mechanism $A*$, *each component of the cortical map will become unstable to patterns at a common wavelength*. This common length scale allows the assumption in Chapter 5 of plane-periodic solutions in all compo-

nents at once, and thus simplifies the search for bifurcating solutions considerably. The logistic fan-in constraint makes the fan-in deviation $\hat{\lambda}(x)$ decay at a rate K_λ . If there is a finite deviation of the net input weight from its uniform equilibrium value λ_0 , then each of the other \dot{v}_i is influenced by a convolution term of the form

$$\lambda \left(A f'_i \left(\frac{x}{\mu} \right) \right) * \left(\frac{\hat{\lambda}}{\lambda_0} \right) := \lambda \int_{x' \in \mathbb{R}^2} A(x - x') f'_i \left(\frac{(x - x')}{\mu} \right) \left(\frac{\hat{\lambda}(x')}{\lambda_0} \right) dx'$$

where $f'_i(u)$ generates a vector moment:

$$f'_i(u) = \begin{cases} u_1, & i = 2 \\ u_2, & i = 3 \\ u^{\text{tr}} S_1 u, & i = 4 \\ u^{\text{tr}} S_2 u, & i = 5 \\ \|u\|^2 + \sigma_r^2/\lambda, & i = 6 \end{cases} . \quad (4.36)$$

The various convolution kernels $A(x)f'_i(x/\mu)$ are pictured in Figure 4.2. Also shown is $A(x)$, corresponding to $f'_1(x) := \mathbf{1}$. Just as deviations in the zeroth moment or fan-in weight affect the evolution of all higher moments, so do deviations in the first moment, $s(x)$, affect the second-order moment components $\chi_1(x)$, $\chi_2(x)$ and $\rho(x)$. The fourth terms in equations 4.33, 4.34 and 4.35 combine convolution with an inner product. For example, the 4th term for the $\dot{\rho}$ expression is interpreted as

$$\left(A \frac{x^{\text{tr}}}{\mu} \right) * s = \int_{x' \in \mathbb{R}^2} A(x - x') ((x_1 - x'_1)s_1(x') + (x_2 - x'_2)s_2(x')) dx'.$$

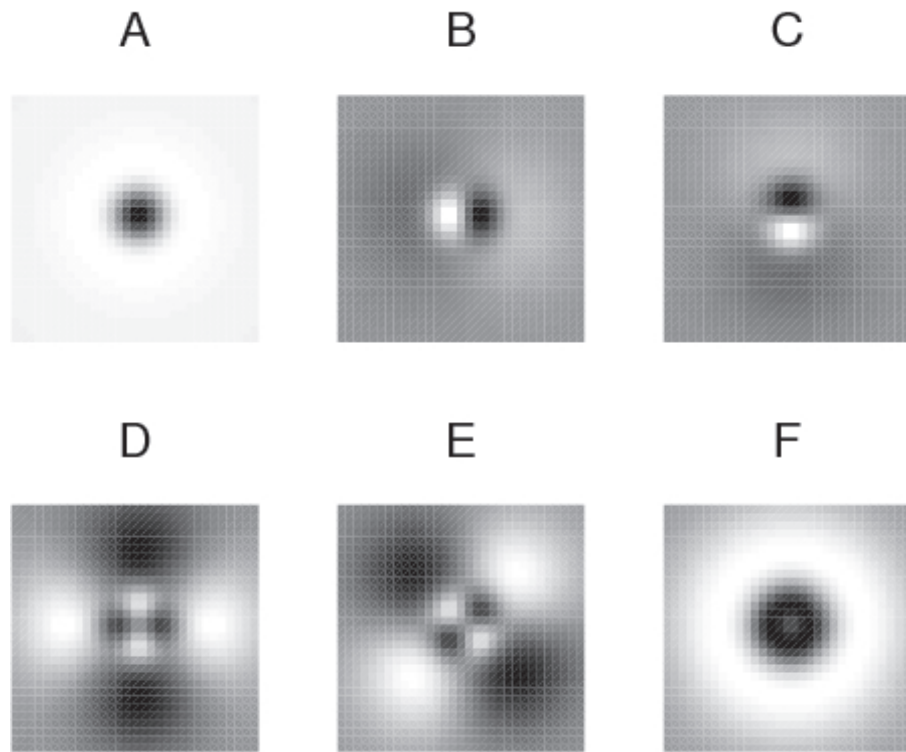


Figure 4.2: Convolution kernels for the first-order interactions in equations 4.31–4.35 induced by dependence of higher moments on lower moments. **A:** $A(x)$. **B:** $A(x) \frac{x_1}{\mu}$. **C:** $A(x) \frac{x_2}{\mu}$. **D:** $A(x) \frac{x^{\text{tr}} S_1 x}{\mu^2}$. **E:** $A(x) \frac{x^{\text{tr}} S_2 x}{\mu^2}$. **F:** $A(x) \left(\lambda \frac{\|x\|^2}{\mu^2} + \sigma_r^2 \right)$. Dark indicates positive values.

The terms for the two χ components are interpreted similarly. Each expression for \dot{v}_i ends with a term, resulting from the fan-out constraint, of the form

$$-K_\gamma \int_u \hat{\gamma}(u + R(x))g(u, \sigma_0^2)f_i(u) du, \quad f_i(u) = \begin{cases} 1, & i = 1 \\ u_1, & i = 2 \\ u_2, & i = 3 \\ u^{\text{tr}}S_1u, & i = 4 \\ u^{\text{tr}}S_2u, & i = 5 \\ \|u\|^2 - \sigma_0^2, & i = 6 \end{cases}. \quad (4.37)$$

With the exception of f_6 these functions are identical to the f'_i that arose from the fan-in constraint term. To obtain the full interactions I eliminate the fan-out terms by rewriting the fan-out explicitly in terms of cortical-map components \mathbf{v} . The fan-out deviation $\hat{\gamma}(r)$ induced by $\hat{\lambda}/\lambda_0, s, \chi$ and ρ is found by integrating the first-order Taylor expansion of the perturbed weight profile $w(x, r)$, equation 4.29, in the x variable. Once $\hat{\gamma}(r)$ is obtained the integrals in 4.37 may be computed, via the Gaussian identities in appendix A.3. Substituting these integrals back into equations 4.31—4.35 completes the calculation. To first order in $\hat{\lambda}/\lambda_0, s, \chi$ and ρ the perturbed fan-out is given by:

$$\begin{aligned} \hat{\gamma}(r) = & \int_{x'} g(r - x'/\mu, \sigma_0^2) \hat{\lambda}(x') dx' + \\ & \frac{\lambda_0}{\sigma_0^2} \int_{x'} g(r - x'/\mu, \sigma_0^2) (r - x'/\mu) \cdot s(x') dx' + \\ & \frac{\lambda_0}{4\sigma_0^4} \int_{x'} g(r - x'/\mu, \sigma_0^2) (r - x'/\mu)^{\text{tr}} S_1 (r - x'/\mu) \chi_1(x') dx' + \\ & \frac{\lambda_0}{4\sigma_0^4} \int_{x'} g(r - x'/\mu, \sigma_0^2) (r - x'/\mu)^{\text{tr}} S_2 (r - x'/\mu) \chi_2(x') dx' + \\ & \frac{\lambda_0}{\sigma_0^2} \int_{x'} g(r - x'/\mu, \sigma_0^2) \left(\frac{\|r - x'/\mu\|^2}{2\sigma_0^2} - 1 \right) \rho(x') dx' \\ & + O((\hat{\lambda}/\lambda_0, s, \chi, \rho)^2). \end{aligned} \quad (4.38)$$

The integrals arising from the fan-out perturbation terms in 4.37 are given in Table 4.2. For convenience I adopt the following shorthand:

$$G(x) := g\left(\frac{x}{\mu}, 2\sigma_0^2\right)$$

where $g(u, \sigma_0^2)$ is the normal distribution with width σ_0 as defined by equation 4.7. Also, given planar vectors \mathbf{a} , \mathbf{b} and \mathbf{c} I will adopt the notation

$$\begin{aligned} \left(\begin{bmatrix} \mathbf{a}_1 \\ \mathbf{a}_2 \end{bmatrix}, \begin{bmatrix} \mathbf{b}_1 \\ \mathbf{b}_2 \end{bmatrix} \right) * \begin{bmatrix} \mathbf{c}_1 \\ \mathbf{c}_2 \end{bmatrix} &= \begin{bmatrix} [\mathbf{a}_1, \mathbf{b}_1] * \begin{bmatrix} \mathbf{c}_1 \\ \mathbf{c}_2 \end{bmatrix} \\ [\mathbf{a}_2, \mathbf{b}_2] * \begin{bmatrix} \mathbf{c}_1 \\ \mathbf{c}_2 \end{bmatrix} \end{bmatrix} \\ &= \begin{bmatrix} (\mathbf{a}_1 * \mathbf{c}_1 + \mathbf{b}_1 * \mathbf{c}_2) \\ (\mathbf{a}_2 * \mathbf{c}_1 + \mathbf{b}_2 * \mathbf{c}_2) \end{bmatrix} \end{aligned} \quad (4.39)$$

This combination of vectors and convolution appears in the last term for the $\hat{\Upsilon}$ -integral of $f(u) = u$. Combining Table 4.2 and equations 4.31–4.35 gives the full interactions, to first order in $\hat{\lambda}/\lambda_0$, s , χ and ρ . The resulting expressions take the following form:

$$\frac{1}{\eta} \frac{d}{dt} \mathbf{v} = -\alpha \mathbf{v} + \lambda A * \mathbf{v} + \mathbf{K} * \mathbf{v} \quad (4.40)$$

where \mathbf{K} is a six-by-six matrix of convolution kernels and

$$(\mathbf{K} * \mathbf{v})_i := \sum_{j=1}^6 \left(\int_{x' \in \mathbb{R}^2} \mathbf{K}_{ij}(x - x') \mathbf{v}_j(x') dx' \right).$$

The convolution kernels composing \mathbf{K} are given in Tables 4.3, 4.5 and 4.6. Each convolution kernel K_{ij} gives the first-order influence of the j^{th} component of the cortical-map vector $v_j(x)$ on the development of the i^{th} component $v_i(x)$. The influence of the two retinotopic-distortion components on the two-vector representing the

$f(u)$	$\int_u \hat{\gamma}(u + R(x))g(u, \sigma_0^2)f(u) du$
1	$\lambda_0 G * \left(\frac{\hat{\lambda}}{\lambda_0} \right) + \frac{\lambda_0}{\sigma_0^2} \left(\frac{x^{\text{tr}}}{2\mu} G \right) * s$ $+ \frac{\lambda_0}{4\sigma_0^4} \left(\left[\frac{x^{\text{tr}} S_1 x}{4\mu^2}, \frac{x^{\text{tr}} S_2 x}{4\mu^2} \right] G \right) * \chi$ $+ \frac{\lambda_0}{2\sigma_0^4} \left(\left(\frac{\ x\ ^2}{4\mu^2} + \frac{\sigma_0^2}{2} \right) G \right) * \rho$
u	$\lambda_0 \left(\frac{x}{2\mu} G \right) * \left(\frac{\hat{\lambda}}{\lambda_0} \right) + \frac{\lambda_0}{\sigma_0^2} \left(\left(\frac{\sigma_0^2}{2} I_2 - \frac{xx^{\text{tr}}}{4\mu^2} \right) G \right) * s$ $+ \frac{\lambda_0}{4\sigma_0^4} \left(\left[\left(\sigma_0^2 I_2 - \frac{xx^{\text{tr}}}{4\mu^2} \right) S_1 \frac{x}{2\mu}, \left(\sigma_0^2 I_2 - \frac{xx^{\text{tr}}}{4\mu^2} \right) S_2 \frac{x}{2\mu} \right] G \right) * \chi$ $+ \frac{\lambda_0}{2\sigma_0^4} \left(\left(2\sigma_0^2 - \frac{\ x\ ^2}{4\mu^2} \right) \frac{x}{2\mu} G \right) * \rho$
$u^{\text{tr}} S_i u$ $(i = 1, 2)$	$\lambda_0 \left(\frac{x^{\text{tr}} S_i x}{4\mu^2} G \right) * \left(\frac{\hat{\lambda}}{\lambda_0} \right) + \frac{\lambda_0}{\sigma_0^2} \left(\left(\frac{x^{\text{tr}} S_i x x^{\text{tr}}}{8\mu^3} - \sigma_0^2 \frac{x^{\text{tr}}}{2\mu} S_i \right) G \right) * s$ $+ \frac{\lambda_0}{4\sigma_0^4} \left\{ \left(\left[\frac{x^{\text{tr}} S_i x x^{\text{tr}} S_1 x}{16\mu^4}, \frac{x^{\text{tr}} S_i x x^{\text{tr}} S_2 x}{16\mu^4} \right] G \right) * \chi \right.$ $\left. - \left(\left(2\sigma_0^2 \frac{\ x\ ^2}{4\mu^2} - \sigma_0^4 \right) G \right) * \chi_i \right\}$ $+ \frac{\lambda_0}{2\sigma_0^4} \left(\frac{x^{\text{tr}} S_i x}{4\mu^2} \left(\frac{\ x\ ^2}{4\mu^2} - 3\sigma_0^2 \right) G \right) * \rho$
$\ u\ ^2$	$\lambda_0 \left(\left(\frac{\ x\ ^2}{4\mu^2} + \sigma_0^2 \right) G \right) * \left(\frac{\hat{\lambda}}{\lambda_0} \right) + \frac{\lambda_0}{\sigma_0^2} \left(\frac{\ x\ ^2 x^{\text{tr}}}{8\mu^3} G \right) * s$ $+ \frac{\lambda_0}{4\sigma_0^4} \left(\left[\frac{x^{\text{tr}} S_1 x}{4\mu^2}, \frac{x^{\text{tr}} S_2 x}{4\mu^2} \right] \left(\frac{\ x\ ^2}{4\mu^2} - \sigma_0^2 \right) G \right) * \chi$ $+ \frac{\lambda_0}{2\sigma_0^4} \left(\left(\frac{\ x\ ^2}{4\mu^2} - 2\sigma_0^2 \right) G \frac{\ x\ ^2}{4\mu^2} \right) * \rho$

Table 4.2: Integrals of fan-out constraint terms, monocular model.

K_{ij}	$j = 1$
$i = 1$	$-\lambda_0 (K_\gamma G + K_\lambda \delta)$
$\begin{pmatrix} i = 2 \\ i = 3 \end{pmatrix}$	$-\lambda \left(\frac{x}{\mu} A \right) - \lambda_0 K_\gamma \left(\frac{x}{2\mu} G \right)$
$i = 4$	$\lambda \frac{x^{\text{tr}} S_1 x}{\mu^2} A - \lambda_0 K_\gamma \frac{x^{\text{tr}} S_1 x}{4\mu^2} G$
$i = 5$	$\lambda \frac{x^{\text{tr}} S_2 x}{\mu^2} A - \lambda_0 K_\gamma \frac{x^{\text{tr}} S_2 x}{4\mu^2} G$
$i = 6$	$\left(\lambda \frac{\ x\ ^2}{\mu^2} + \sigma_r^2 \right) A - \lambda_0 K_\gamma \frac{\ x\ ^2}{4\mu^2} G$

Table 4.3: First-order influence K_{ij} of fan-out on cortical-map vector. Monocular model.

orientation map, for example, is given by the four convolution kernels

$$\begin{pmatrix} K_{42} & K_{43} \\ K_{52} & K_{53} \end{pmatrix}$$

in Table 4.5. Each component also interacts with itself through convolution with the difference-of-Gaussians λA , as well as obeying intrinsic decay at rate α .

Euclidean symmetry of the linear system and the steady state leads to degeneracy of the eigenvalues at a symmetry-breaking bifurcation. The analysis of solutions of the pattern-formation problem depends on the techniques of equivariant bifurcation theory, developed in the next chapter.

K_{ij}	$(j = 2, j = 3)$
$i = 1$	$-K_{\gamma} \frac{\lambda_0}{\sigma_0^2} \left(\frac{x^{\text{tr}}}{2\mu} G \right)$
$\begin{pmatrix} i = 2 \\ i = 3 \end{pmatrix}$	$-K_{\gamma} \frac{\lambda_0}{\sigma_0^2} \left(\left(\frac{\sigma_0^2}{2} I_2 - \frac{xx^{\text{tr}}}{4\mu^2} \right) G \right)$
$i = 4$	$2\lambda \frac{x^{\text{tr}}}{\mu} AS_1 - \frac{\lambda_0 K_{\gamma}}{\sigma_0^2} \frac{x^{\text{tr}}}{2\mu} S_1 \left(\frac{xx^{\text{tr}}}{4\mu^2} - \sigma_0^2 I_2 \right) G$
$i = 5$	$2\lambda \frac{x^{\text{tr}}}{\mu} AS_2 - \frac{\lambda_0 K_{\gamma}}{\sigma_0^2} \frac{x^{\text{tr}}}{2\mu} S_2 \left(\frac{xx^{\text{tr}}}{4\mu^2} - \sigma_0^2 I_2 \right) G$
$i = 6$	$2\lambda \frac{x^{\text{tr}}}{\mu} A - \frac{\lambda_0 K_{\gamma}}{\sigma_0^2} \left(\frac{\ x\ ^2}{4\mu^2} - \sigma_0^2 \right) \frac{x^{\text{tr}}}{2\mu} G$

Table 4.4: First-order influence K_{ij} of retinotopic distortion on cortical-map vector. Monocular model.

K_{ij}	$j = 4$	$j = 5$
$i = 1$	$-K_{\gamma} \frac{\lambda_0}{4\sigma_0^4} \frac{x^{\text{tr}} S_1 x}{4\mu^2} G$	$-K_{\gamma} \frac{\lambda_0}{4\sigma_0^4} \frac{x^{\text{tr}} S_2 x}{4\mu^2} G$
$\begin{pmatrix} i = 2 \\ i = 3 \end{pmatrix}$	$-K_{\gamma} \frac{\lambda_0}{4\sigma_0^4} \left(\left(\sigma_0^2 - \frac{xx^{\text{tr}}}{4\mu^2} \right) S_1 \frac{x}{2\mu} G \right)$	$-K_{\gamma} \frac{\lambda_0}{4\sigma_0^4} \left(\left(\sigma_0^2 - \frac{xx^{\text{tr}}}{4\mu^2} \right) S_2 \frac{x}{2\mu} G \right)$
$i = 4$	$-K_{\gamma} \frac{\lambda_0}{4\sigma_0^4} \left(\frac{(x^{\text{tr}} S_1 x)^2}{16\mu^4} - 2\sigma_0^2 \frac{\ x\ ^2}{4\mu^2} + \sigma_0^4 \right) G$	$-K_{\gamma} \frac{\lambda_0}{4\sigma_0^4} \frac{x^{\text{tr}} S_1 x x^{\text{tr}} S_2 x}{16\mu^4} G$
$i = 5$	$-K_{\gamma} \frac{\lambda_0}{4\sigma_0^4} \frac{x^{\text{tr}} S_1 x x^{\text{tr}} S_2 x}{16\mu^4} G$	$-K_{\gamma} \frac{\lambda_0}{4\sigma_0^4} \left(\frac{(x^{\text{tr}} S_2 x)^2}{16\mu^4} - 2\sigma_0^2 \frac{\ x\ ^2}{4\mu^2} + \sigma_0^4 \right) G$
$i = 6$	$-K_{\gamma} \frac{\lambda_0}{4\sigma_0^4} \frac{x^{\text{tr}} S_1 x}{4\mu^2} \left(\frac{\ x\ ^2}{4\mu^2} - 2\sigma_0^2 \right) G$	$-K_{\gamma} \frac{\lambda_0}{4\sigma_0^4} \frac{x^{\text{tr}} S_2 x}{4\mu^2} \left(\frac{\ x\ ^2}{4\mu^2} - 2\sigma_0^2 \right) G$

Table 4.5: First-order influence K_{ij} of orientation components on cortical-map vector. Monocular model.

K_{ij}	$j = 6$
$i = 1$	$-K_{\gamma} \frac{\lambda_0}{2\sigma_0^4} \left(\left(\frac{\ x\ ^2}{4\mu^2} + \frac{\sigma_0^2}{2} \right) G \right)$
$\left(\begin{array}{c} i = 2 \\ i = 3 \end{array} \right)$	$-K_{\gamma} \frac{\lambda_0}{2\sigma_0^4} \left(\left(2\sigma_0^2 - \frac{\ x\ ^2}{4\mu^2} \right) \frac{x}{2\mu} G \right)$
$i = 4$	$-K_{\gamma} \frac{\lambda_0}{2\sigma_0^4} \left(\frac{x^{\text{tr}} S_1 x}{4\mu^2} \left(\frac{\ x\ ^2}{4\mu^2} - 3\sigma_0^2 \right) G \right)$
$i = 5$	$-K_{\gamma} \frac{\lambda_0}{2\sigma_0^4} \left(\frac{x^{\text{tr}} S_2 x}{4\mu^2} \left(\frac{\ x\ ^2}{4\mu^2} - 3\sigma_0^2 \right) G \right)$
$i = 6$	$-K_{\gamma} \frac{\lambda_0}{2\sigma_0^4} \left(\frac{\ x\ ^4}{16\mu^4} - 3\sigma_0^2 \frac{\ x\ ^2}{4\mu^2} - \frac{\sigma_0^4}{2} \right) G$

Table 4.6: First-order influence K_{ij} of receptive-field width deviation on cortical-map vector. Monocular model.

CHAPTER 5
SYMMETRY ANALYSIS OF CORTICAL-MAP
FORMATION: MONOCULAR CASE

Chapter 4 presented a nonlinear developmental dynamics for geniculo-cortical weights derived from a Hebbian learning rule for feed-forward connections and a center-surround lateral interaction within cortex:

$$\begin{aligned}
 \frac{1}{\eta} \frac{d}{dt} w(x, r) &= \mathbf{F}_0[w](x, r) \\
 &= -\alpha w(x, r) \\
 &\quad + \lambda \int_{x'} A(x - x') \int_{r'} G(r - r') w(x', r') dr' dx' + \mathcal{C}h(x, r) \\
 &\quad + w(x, r) \{K_\lambda(\lambda(x) - \lambda_0) + K_\gamma(\gamma(r) - \gamma_0)\} \\
 w(x, r) &\geq 0
 \end{aligned} \tag{5.1}$$

This equation has a steady state of the form

$$w_{\text{SS}}(x, r) = \lambda_0 f\left(\left|r - \frac{x}{\mu}\right|\right) \tag{5.2}$$

which is stable for sufficiently small values of λ/α . When a critical eigenvalue crosses the imaginary axis, either as the decay α decreases or the pattern-forming feedback λ increases, we have the growth of a pattern of deviations from the steady-state receptive field profiles w_{SS} . The zeroth, first and second moments of the deviation of $w(x, r)$ from the isotropic, homogeneous steady-state profile forms the cortical-map vector with components v_1, \dots, v_6 as defined in Table 5.1.

From the underlying dynamical system 5.1, Chapter 4 shows how to derive a reduced dynamical system governing the development of the cortical-map vector,

Vector Component	Model Variable	Description
$v_1(x)$	$\frac{\hat{\lambda}(x)}{\lambda_0}$	Deviation of the total input mass from the homogeneous steady state value.
$\begin{bmatrix} v_2 \\ v_3 \end{bmatrix}$	$s(x)$	Deviation of the retinotopy from the average background $R(x) = \frac{x}{\mu}$.
$\begin{bmatrix} v_4 \\ v_5 \end{bmatrix}$	$\chi(x)$	Orientation preference vector: deviation of receptive field profile from circular symmetry.
$v_6(x)$	$\rho(x)$	Deviation of receptive field size from uniform steady state value.

Table 5.1: Components of the cortical-map vector.

including interactions between its components, through first order in $|\mathbf{v}|$:

$$\frac{1}{\eta} \frac{d}{dt} \mathbf{v} = \mathbf{F}[\mathbf{v}] = -\alpha \mathbf{v} + \lambda A * \mathbf{v} + \mathbf{K} * \mathbf{v} \quad (5.3)$$

It is then possible to study the formation of cortical-map patterns as a bifurcation from the homogeneous steady state 5.2 in terms of the dynamical system 5.3.

The bifurcation picture is complicated by the high degree of symmetry in the system. As described in Appendix A.3, when a dynamical system commutes with a set of symmetries, the bifurcation problem becomes degenerate and the symmetry group of the system must be exploited to find bifurcating solution branches. The “spontaneous” appearance of solutions with symmetry less than that of the underlying dynamical system (i.e. the symmetry of a proper subgroup of the group of symmetries of the dynamical system) is called *spontaneous symmetry breaking* and provides the mechanism for creating structured solutions in an otherwise structureless system—such as the creation of an anisotropic cortical map from an initially isotropic

architecture.

The first task in bringing to bear group-theoretic methods for the identification of solutions of equations 5.3 is to sort out their symmetries. The symmetry relations between different components of the cortical-map vector, such as orientation and retinotopy, will govern the interactions between these components in the bifurcating patterns.

The underlying system from which 5.3 derives already has significant symmetry which is preserved by the reduction process. I will first describe these symmetries, describe the symmetry relations of orientation, mass and retinotopy, and then show the group action under which 5.3 is *equivariant* (section 5.1). Then I will impose certain periodicity assumptions on the solutions to 5.3 in order to study fundamental properties of the solutions, in 5.2. In section 5.3.1, I will use the irreducible representations of the group of symmetries of the restricted solutions to simplify the eigenvalue problem associated with 5.3, and classify the kinds of bifurcating patterns that may be expected generically. Finally, in section 5.4, I will display samples of the kinds of cortical-map patterns formed by this system for the particular convolution kernels used earlier (those derived in Chapter 4). Background material on equivariant bifurcation theory with tutorial examples may be found in Appendix A.3.

5.1 Equivariance

To a first approximation, the local architecture of V1 is invariant under the group of rotations, translations and reflections of the plane—or \mathbf{E}_2 , the Euclidean symmetries of the plane. \mathbf{E}_2 is the semi-direct product of the circle group \mathbf{O}_2 (the rotations and reflections of the plane about the origin) with the translation group \mathbf{T}_2 . These groups act on functions $f(x, r)$, $f : \mathbb{R}^2 \times \mathbb{R}^2 \rightarrow \mathbb{R}$ as follows:

$$\begin{aligned} \text{Translation: } \mathcal{T}_{(\delta x, \delta r)}[f] &= f(x - \delta x, r - \delta r) \\ \text{Rotation: } \mathcal{Rot}_\psi[f] &= f(R_{-\psi}x, R_{-\psi}r) \\ \text{Reflection: } \mathcal{Ref}[f] &= f(S_1x, S_1r) \end{aligned}$$

where $R_\psi = \begin{pmatrix} \cos \psi & -\sin \psi \\ \sin \psi & \cos \psi \end{pmatrix}$ is a 2×2 rotation matrix and $S_1 = \begin{pmatrix} 1 & 0 \\ 0 & -1 \end{pmatrix}$ reflects about the horizontal axis. The translation operator has two indices $\delta x, \delta r$. The uniform background retinotopic map that we assume will have a magnification μ , in which case the dynamical system 5.1 should be invariant under the translation action when the translations have the form $\mathcal{T}_{(\mu\delta r, \delta r)}$.

For each operator γ I demonstrate equivariance, *i.e.*

$$\gamma[\mathbf{F}_0[w]] = \mathbf{F}_0[\gamma[w]] \quad (5.4)$$

Translation Invariance

Translation invariance follows from the convolution structure of the second term of equation 5.1, the form of the chemical marker term $\mathcal{Ch}(x, r) = \mathcal{Ch}(\|r - x/\mu\|)$, and the other terms' linear dependence on w or integrals of w . Note that without the chemical marker term the system is invariant under both translations in x and in r separately.

To be shown:

$$\mathcal{T}_{(\mu\delta r, \delta r)}[\mathbf{F}_0[w]] = \mathbf{F}_0[\mathcal{T}_{(\mu\delta r, \delta r)}[w]]$$

$$\begin{aligned}
& T_{(\delta x, \delta r)} [\mathbf{F}_0[w]] \\
&= -\alpha w(x - \delta x, r - \delta r) \\
&\quad + \lambda \int_{x'} A(x - \delta x - x') \int_{r'} G(r - \delta r - r') w(x', r') dr' dx' \\
&\quad + \mathcal{Ch}(x - \delta x, r - \delta r) \\
&\quad + w(x - \delta x, r - \delta r) K_\lambda \left(\lambda_0 - \int_r w(x - \delta x, r) dr \right) \\
&\quad + w(x - \delta x, r - \delta r) K_\gamma \left(\gamma_0 - \int_x w(x, r - \delta r) dx \right) \\
&= -\alpha w(x - \delta x, r - \delta r) \\
&\quad + \lambda \int_{x'} A(x - x') \int_{r'} G(r - r') w(x' - \delta x, r' - \delta r) dr' dx' \\
&\quad + \mathcal{Ch}(\| \frac{x - \delta x}{\mu} - (r - \delta r) \|) \\
&\quad + w(x - \delta x, r - \delta r) K_\lambda \left(\lambda_0 - \int_r w(x - \delta x, r - \delta r) dr \right) \\
&\quad + w(x - \delta x, r - \delta r) K_\gamma \left(\gamma_0 - \int_x w(x - \delta x, r - \delta r) dx \right) \\
&= \mathbf{F}_0 \left[\mathcal{T}_{(\delta x, \delta r)}[w] \right] \quad - \text{when } \delta r = \mu \delta x.
\end{aligned}$$

□

Rotation and Reflection Invariance

To be shown:

$$\mathcal{Rot}_\psi [\mathbf{F}_0[w]] = \mathbf{F}_0 [\mathcal{Rot}_\psi[w]]$$

$$\mathcal{Ref} [\mathbf{F}_0[w]] = \mathbf{F}_0 [\mathcal{Ref}[w]]$$

Let M be a 2×2 matrix representing either a rotation $M = R_\psi$, or a reflection $M = S_1 R_\psi$. In either case $|\det M| = 1$. Invariance follows from the \mathbf{O}_2 -invariance of the convolution kernels A and G and the chemical marker term \mathcal{Ch} , and from the

rotational invariance of integration:

$$\int_{x \in \mathbb{R}^2} f(Mx) dx = \int_{x \in \mathbb{R}^2} f(x) |\det M| dx$$

For $\gamma \in \mathbf{O}_2$,

$$\begin{aligned} & \gamma [\mathbf{F}_0[w]] \\ &= -\alpha w(Mx, Mr) \\ & \quad + \lambda \int_{x'} A(Mx - x') \int_{r'} G(Mr - r') w(x', r') dr' dx' \\ & \quad + \mathcal{Ch}(Mx, Mr) \\ & \quad + w(Mx, Mr) \left(\lambda_0 - \int_r w(Mx, r) dr \right) \\ & \quad + w(Mx, Mr) \left(\gamma_0 - \int_x w(x, Mr) dx \right) \\ &= -\alpha w(Mx, Mr) \\ & \quad + \lambda \int_{x'} A(x - M^{-1}x') \int_{r'} G(r - M^{-1}r') w(x', r') dr' dx' \\ & \quad + \mathcal{Ch}(\|M \left(r - \frac{x}{\mu} \right)\|) \\ & \quad + w(Mx, Mr) \left(\lambda_0 - \int_r w(Mx, Mr) \frac{dr}{|\det M|} \right) \\ & \quad + w(Mx, Mr) \left(\gamma_0 - \int_x w(Mx, Mr) \frac{dx}{|\det M|} \right) \\ &= -\alpha w(Mx, Mr) \\ & \quad + \lambda \int_{x'} A(x - x') \int_{r'} G(r - r') w(Mx', Mr') \frac{dr'}{|\det M|} \frac{dx'}{|\det M|} \\ & \quad + \mathcal{Ch}(x, r) \\ & \quad + w(Mx, Mr) \left(\lambda_0 - \int_r w(Mx, Mr) dr \right) \\ & \quad + w(Mx, Mr) \left(\gamma_0 - \int_x w(Mx, Mr) dx \right) \\ &= \mathbf{F}_0[\gamma[w]] \end{aligned}$$

□

Not only is the dynamical system for the synaptic weights invariant under the

Euclidean group, the steady state solution w_{SS} is as well (see equation 5.2). Because the dynamics for the cortical-map vector, equation 5.3, derive from linearization of \mathbf{E}_2 -invariant dynamics about an \mathbf{E}_2 -invariant steady state, we expect that equation 5.3 should also be Euclidean-invariant. However its invariance is not immediately obvious: for example, the convolution kernels involved are not rotationally invariant (see Figure 4.2). Furthermore, we now have an n -dimensional vector field over the plane $\mathbf{f} : \mathbb{R}^2 \rightarrow \mathbb{R}^n$ rather than a synaptic weight-type function $f : \mathbb{R}^2 \times \mathbb{R}^2 \rightarrow \mathbb{R}$. We must identify the action of \mathbf{E}_2 appropriate to this new setting and show the equivariance of equation 5.3 directly.

Consider the components of the cortical-map vector $\mathbf{v}(x)$ in turn. The fan-in mass is a scalar function of cortical position $\lambda(x)$, so its transformation is simply governed by changing coordinates in the underlying plane:

$$\mathcal{T}_{\delta x}[\lambda](x) = \lambda(x - \delta x) \quad (5.5)$$

$$\mathcal{Rot}_{\psi}[\lambda](x) = \lambda(R_{-\psi}x) \quad (5.6)$$

$$\mathcal{Ref}[\lambda](x) = \lambda(S_1x) \quad (5.7)$$

The retinotopic distortion vector $s(x)$ transforms under rotations not only due to the rotation of the planar coordinates x but also by rotating with respect to its own axes:

$$\mathcal{T}_{\delta x}[s](x) = s(x - \delta x) \quad (5.8)$$

$$\mathcal{Rot}_{\psi}[s](x) = R_{+\psi}s(R_{-\psi}x) \quad (5.9)$$

$$\mathcal{Ref}[s](x) = S_1s(S_1x) \quad (5.10)$$

The orientation preference vector $\chi(x)$ also transforms both through the change of x -coordinates and through the direct action of rotation on χ . But while a rotation through π reverses the direction of the retinotopic distortion vector, it leaves the preferred orientations (principal axes of the receptive fields) unchanged. Recall that

χ is a π -periodic quantity:

$$\chi(x) = \begin{pmatrix} \cos 2\phi(x) \\ \sin 2\phi(x) \end{pmatrix}.$$

Whereas rotating space through an angle ψ rotates $s(x)$ also by ψ , this action “rotates” χ by 2ψ .

Finally, reflection sends 2ϕ to -2ϕ , so it acts on $\chi(x)$ and $s(x)$ in the same way. Therefore the action of \mathbf{E}_2 on $\chi(x)$ is given by:

$$\mathcal{T}_{\delta x}[\chi](x) = \chi(x - \delta x) \quad (5.11)$$

$$\mathcal{Rot}_{\psi}[\chi](x) = R_{2\psi}\chi(R_{-\psi}x) \quad (5.12)$$

$$\mathcal{Ref}[\chi](x) = S_1\chi(S_1x) \quad (5.13)$$

Figure 5.1 illustrates the transformation of $s(x)$ and $\chi(x)$ under rotation and reflection. If we include a sixth component in the cortical-map vector denoting the deviation of the receptive field widths from their equilibrium values, $\rho(x) = \sigma^2(x) - \sigma_0^2$, it transforms in the same manner as the fan-in $\lambda(x)$.

Altogether, the action of \mathbf{E}_2 on $\mathbf{v}(x)$ may be expressed as follows:

$$\mathcal{T}_{\delta x}[\mathbf{v}](x) = \mathbf{v}(x - \delta x) \quad (5.14)$$

$$\mathcal{Rot}_{\psi}[\mathbf{v}](x) = \begin{pmatrix} 1 & & & \\ & R_{\psi} & & \\ & & R_{2\psi} & \\ & & & 1 \end{pmatrix} \mathbf{v}(R_{-\psi}x) \quad (5.15)$$

$$\mathcal{Ref}[\mathbf{v}](x) = \begin{pmatrix} 1 & & & \\ & S_1 & & \\ & & S_1 & \\ & & & 1 \end{pmatrix} \mathbf{v}(S_1x). \quad (5.16)$$

The difference in action on the two quantities $s(x)$ and $\chi(x)$ will determine the kinds of patterns that can be formed when they are coupled together.

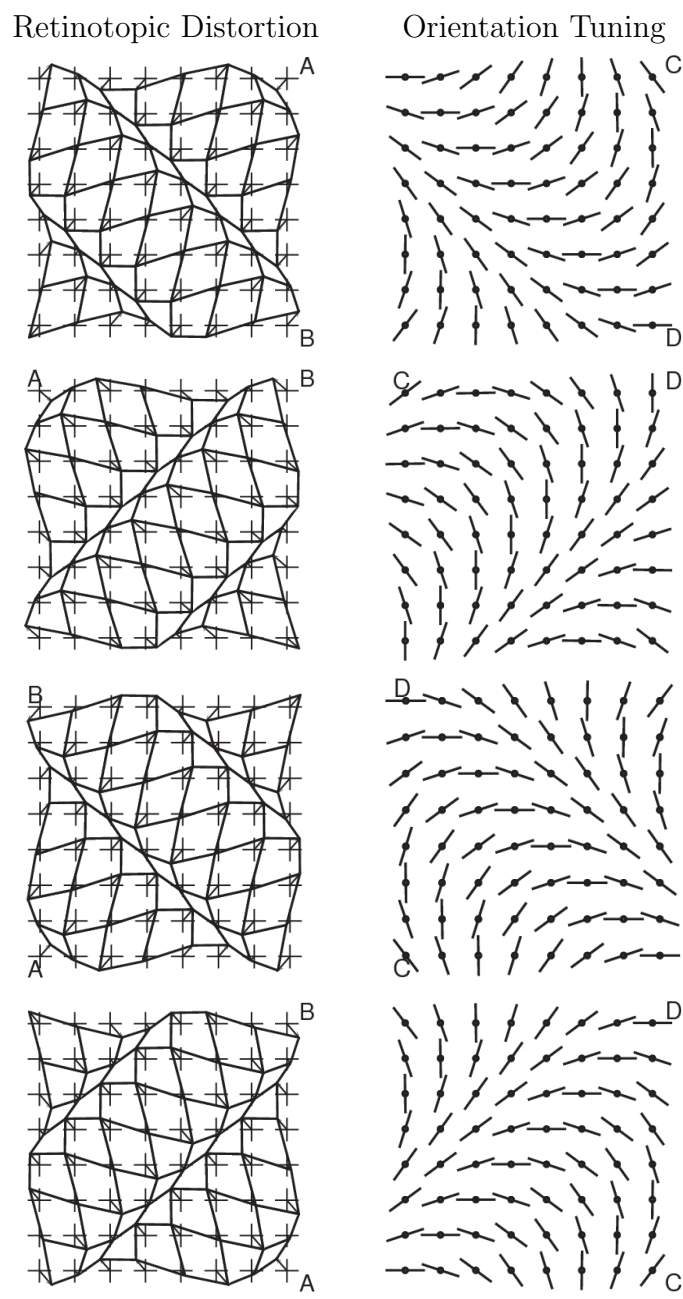


Figure 5.1: \mathbf{E}_2 action on $s(x)$ and $\chi(x)$. **Top:** Initial patterns. **Second Row:** Rotation by $\pi/2$. **Third Row:** Rotation by π . Note the retinotopic distortion field is reversed from row 1 to row 3 (compare corner A) while the orientation field is the same (compare corner C). **Bottom Row:** Reflection in horizontal.

It remains to show the equivariance of the cortical-map vector dynamics in equation 5.3 under this action:

$$\begin{aligned}
 \mathbf{F}[\mathbf{v}](x - \delta x) &= \mathbf{F}[\mathbf{v}(x - \delta x)] & (5.17) \\
 \begin{pmatrix} 1 & & & \\ & R_\psi & & \\ & & R_{2\psi} & \\ & & & 1 \end{pmatrix} \mathbf{F}[\mathbf{v}](R_{-\psi}x) &= \mathbf{F} \left[\begin{pmatrix} 1 & & & \\ & R_\psi & & \\ & & R_{2\psi} & \\ & & & 1 \end{pmatrix} \mathbf{v}(R_{-\psi}x) \right] \\
 \begin{pmatrix} 1 & & & \\ & S_1 & & \\ & & S_1 & \\ & & & 1 \end{pmatrix} \mathbf{F}[\mathbf{v}](S_1x) &= \mathbf{F} \left[\begin{pmatrix} 1 & & & \\ & S_1 & & \\ & & S_1 & \\ & & & 1 \end{pmatrix} \mathbf{v}(S_1x) \right]
 \end{aligned}$$

Translation invariance follows from the convolution structure of \mathbf{F} as it did for \mathbf{F}_0 :

$$\mathbf{F}[\mathbf{v}] = -\alpha\mathbf{v} + \lambda A * \mathbf{v} + \mathbf{K} * \mathbf{v}$$

Similarly, \mathbf{O}_2 invariance follows immediately for the two terms in \mathbf{F} that are multiples of the identity I_n ,

$$\begin{aligned}
 \mathcal{R}ot_\psi[-\alpha\mathbf{v} + \lambda A * \mathbf{v}] &= -\alpha\mathcal{R}ot_\psi[\mathbf{v}] + \lambda A * (\mathcal{R}ot_\psi[\mathbf{v}]) \\
 \mathcal{R}ef[-\alpha\mathbf{v} + \lambda A * \mathbf{v}] &= -\alpha\mathcal{R}ef[\mathbf{v}] + \lambda A * (\mathcal{R}ef[\mathbf{v}]),
 \end{aligned}$$

because the convolution kernel $A(x)$ is itself \mathbf{O}_2 invariant.

The \mathbf{O}_2 equivariance of the matrix-convolution operator \mathbf{K} poses the only diffi-

culty. For example, for $\mathcal{R}ot_\psi$ we must show:

$$\begin{aligned} & \begin{pmatrix} 1 & & & \\ & R_\psi & & \\ & & R_{2\psi} & \\ & & & 1 \end{pmatrix} \left[\int_{x'} \mathbf{K}((R_{-\psi}x) - x') \mathbf{v}(x') dx' \right] \\ &= \int_{x'} \mathbf{K}(x - x') \left[\begin{pmatrix} 1 & & & \\ & R_\psi & & \\ & & R_{2\psi} & \\ & & & 1 \end{pmatrix} \int_{x'} \mathbf{v}(R_{-\psi}x') \right] dx'. \end{aligned}$$

An analogous expression is required for $\mathcal{R}ef$.

I will break down the demonstration of equivariance according to a natural block structure for \mathbf{K} coinciding with the block-diagonalization of the group action 5.17. For example, the influence of retinotopic distortion s on the net fan-in deviation $\hat{\lambda}$ is given by the 1×2 matrix $K_{s \rightarrow \hat{\lambda}} = (K_{12}, K_{13})$. I will give examples showing the equivariance of several components of \mathbf{K} . (The complete list of formulae for the different components of \mathbf{K} are given in Tables 4.3, 4.4, 4.5 and 4.6.)

$$\mathbf{K} = \begin{pmatrix} K_{\hat{\lambda} \rightarrow \hat{\lambda}} & K_{s \rightarrow \hat{\lambda}} & K_{\chi \rightarrow \hat{\lambda}} & K_{\rho \rightarrow \hat{\lambda}} \\ K_{\hat{\lambda} \rightarrow s} & K_{s \rightarrow s} & K_{\chi \rightarrow s} & K_{\rho \rightarrow s} \\ K_{\hat{\lambda} \rightarrow \chi} & K_{s \rightarrow \chi} & K_{\chi \rightarrow \chi} & K_{\rho \rightarrow \chi} \\ K_{\hat{\lambda} \rightarrow \rho} & K_{s \rightarrow \rho} & K_{\chi \rightarrow \rho} & K_{\rho \rightarrow \rho} \end{pmatrix}$$

First consider the self-interaction terms $K_{\hat{\lambda} \rightarrow \hat{\lambda}}$, $K_{s \rightarrow s}$, $K_{\chi \rightarrow \chi}$ and $K_{\rho \rightarrow \rho}$. Two of these represent the self-interactions of the scalar fields $\hat{\lambda}$ and ρ , on which \mathbf{O}_2 acts trivially:

$$\begin{aligned} K_{\hat{\lambda} \rightarrow \hat{\lambda}} &= -\lambda_0 (K_\gamma G(x) + K_\lambda \delta(x)) \\ K_{\rho \rightarrow \rho} &= -K_\gamma \frac{\lambda_0}{2\sigma_0^2} G(x) \left(\frac{\|x\|^4}{16\mu^4} - 3\sigma_0^2 \frac{\|x\|^2}{4\mu^2} - \frac{\sigma_0^4}{2} \right) \end{aligned}$$

Recall that $G(x) = g(\frac{x}{\mu}, 2\sigma_0^2)$ is a circularly symmetric Gaussian, and $\delta(x)$ denotes

Dirac's delta-function. Both $K_{\hat{\lambda} \rightarrow \hat{\lambda}}$ and $K_{\rho \rightarrow \rho}$ are thus \mathbf{O}_2 -invariant, as required.

The vector self-interaction terms $K_{s \rightarrow s}$ and $K_{\chi \rightarrow \chi}$ are somewhat more complicated. Consider first $K_{s \rightarrow s}$:

$$\begin{aligned} K_{s \rightarrow s}(x) &= G(x) \left(c_1 I_2 + c_2 x x^{\text{tr}} \right) \\ c_1 &= -K_\gamma \frac{\lambda_0}{2} \\ c_2 &= \frac{K_\gamma \lambda_0}{4\mu^2 \sigma_0^2} \end{aligned}$$

To be shown:

$$R_\psi \int_{x'} K_{s \rightarrow s}((R_{-\psi}x) - x') s(x') dx' = \int_{x'} K_{s \rightarrow s} R_\psi s(R_{-\psi}) dx'.$$

$$\begin{aligned} & R_\psi \int x' K_{s \rightarrow s}((R_{-\psi}x) - x') s(x') dx' \\ &= R_\psi \int_{x'} K_{s \rightarrow s}(R_{-\psi}(x - x')) s(R_{-\psi}x') \frac{dx'}{|\det R_{-\psi}|} \\ &= R_\psi \int_{x'} G(R_{-\psi}(x - x')) \left(c_1 I_2 + c_2 R_{-\psi}(x - x')(x - x')^{\text{tr}} R_\psi \right) s(R_{-\psi}x') dx' \\ &= R_\psi \int_{x'} G(x - x') \left(c_1 R_{-\psi} I_2 R_\psi + c_2 R_{-\psi}(x - x')(x - x')^{\text{tr}} R_\psi \right) s(R_{-\psi}x') dx' \\ &= \int_{x'} G(x - x') \left(c_1 I_2 + c_2 (x - x')(x - x')^{\text{tr}} \right) R_\psi s(R_{-\psi}x') dx' \\ &= \int_{x'} K_{s \rightarrow s} R_\psi s(R_{-\psi}) dx' \end{aligned}$$

□

The demonstration for the reflection operator is identical: substitute S_1 for R_ψ throughout.

The self-interaction kernel for χ is

$$\begin{aligned}
& K_{\chi \rightarrow \chi}(x) \\
&= G(x) \left(c_1 I_2 + c_2 \|x\|^2 I_2 + c_3 \begin{pmatrix} (x^{\text{tr}} S_1 x)^2 & (x^{\text{tr}} S_1 x)(x^{\text{tr}} S_2 x) \\ (x^{\text{tr}} S_1 x)(x^{\text{tr}} S_2 x) & (x^{\text{tr}} S_1 x)^2 \end{pmatrix} \right) \\
&= G(x) \left(c_1 I_2 + c_2 \|x\|^2 I_2 + c_3 \begin{bmatrix} x^{\text{tr}} S_1 x \\ x^{\text{tr}} S_2 x \end{bmatrix} \begin{bmatrix} x^{\text{tr}} S_1 x & x^{\text{tr}} S_2 x \end{bmatrix} \right) \\
c_1 &= -K_\gamma \frac{\lambda_0}{4} \\
c_2 &= -K_\gamma \frac{\lambda_0}{8\mu^2 \sigma_0^2} \\
c_3 &= -K_\gamma \frac{\lambda_0}{64\mu^4 \sigma_0^4}.
\end{aligned}$$

Recall that $S_2 = \begin{pmatrix} 0 & 1 \\ 1 & 0 \end{pmatrix}$.

To be shown:

$$R_{2\psi} \int_{x'} K_{\chi \rightarrow \chi}((R_{-\psi} x) - x') s(x') dx' = \int_{x'} K_{\chi \rightarrow \chi} R_{2\psi} s(R_{-\psi}) dx'.$$

We will need the following identity, which shows how rotating the x -coordinates

by ψ “rotates” the orientation coupling matrix by 2ψ :

$$\begin{aligned}
\begin{bmatrix} (R_{-\psi}x)^{\text{tr}} S_1(R_{-\psi}x) \\ (R_{-\psi}x)^{\text{tr}} S_2(R_{-\psi}x) \end{bmatrix} &= \begin{bmatrix} x^{\text{tr}} R_{\psi} S_1 R_{-\psi} x \\ x^{\text{tr}} R_{\psi} S_2 R_{-\psi} x \end{bmatrix} \\
&= \begin{bmatrix} x^{\text{tr}} \begin{pmatrix} \cos 2\psi & \sin 2\psi \\ \sin 2\psi & -\cos 2\psi \end{pmatrix} x \\ x^{\text{tr}} \begin{pmatrix} -\sin 2\psi & \cos 2\psi \\ \cos 2\psi & \sin 2\psi \end{pmatrix} x \end{bmatrix} \\
&= \begin{bmatrix} \cos 2\psi \left(x^{\text{tr}} S_1 x \right) + \sin 2\psi \left(x^{\text{tr}} S_2 x \right) \\ -\sin 2\psi \left(x^{\text{tr}} S_1 x \right) + \cos 2\psi \left(x^{\text{tr}} S_2 x \right) \end{bmatrix} \\
&= R_{-2\psi} \begin{bmatrix} x^{\text{tr}} S_1 x \\ x^{\text{tr}} S_2 x \end{bmatrix} \tag{5.18}
\end{aligned}$$

Using the identity 5.18 for the equality $* =$ below, we now can show equivariance:

$$\begin{aligned}
& R_{2\psi} \int_{x'} K_{\chi \rightarrow \chi}((R_{-\psi}x) - x') \chi(x') dx' \\
&= R_{2\psi} \int_{x'} K_{\chi \rightarrow \chi}(R_{-\psi}(x - x')) \chi(R_{\psi}x') \frac{dx'}{|\det R_{-\psi}|} \\
&= R_{2\psi} \int_{x'} G(R_{-\psi}(x - x')) (c_1 I_2 + c_2 \|R_{-\psi}(x - x')\|^2 I_2 \\
&\quad + c_3 \begin{bmatrix} (R_{-\psi}(x - x'))^{\text{tr}} S_1(R_{-\psi}(x - x')) \\ (R_{-\psi}(x - x'))^{\text{tr}} S_2(R_{-\psi}(x - x')) \end{bmatrix} \left[\text{Trans. of same} \right] \chi(R_{\psi}x') dx' \\
&* = R_{2\psi} \int_{x'} G(x - x') (c_1 I_2 + c_2 \|x - x'\|^2 I_2 \\
&\quad + c_3 R_{-2\psi} \begin{bmatrix} (x - x')^{\text{tr}} S_1(x - x') \\ (x - x')^{\text{tr}} S_2(x - x') \end{bmatrix} \left[\text{Trans. of same} \right] R_{2\psi} \chi(R_{\psi}x') dx' \\
&= \int_{x'} G(x - x') (c_1 I_2 + c_2 \|x - x'\|^2 I_2 \\
&\quad + c_3 \begin{bmatrix} (x - x')^{\text{tr}} S_1(x - x') \\ (x - x')^{\text{tr}} S_2(x - x') \end{bmatrix} \left[\text{Transpose of same} \right] R_{2\psi} \chi(R_{\psi}x') dx' \\
&= \int_{x'} K_{\chi \rightarrow \chi}(x - x') R_{2\psi} \chi(R_{-\psi}x') dx'
\end{aligned}$$

□

Equivariance of the cross-feature interactions, e.g. $K_{s \rightarrow \chi}$, may be shown using similar identities to 5.18.

5.2 Restriction to Plane-Periodic Solutions

The \mathbf{E}_2 -equivariance of the synaptic-weight dynamical system 5.1 and the steady state 5.2, which is inherited by the linear feature-map dynamical system 5.3 and its steady state $\mathbf{v} \equiv \mathbf{0}$, has significant consequences for the structure of patterns that emerge at a bifurcation. When the homogenous steady state of a Γ -equivariant dynamical system $\dot{\mathbf{v}} = \mathbf{F}[\mathbf{v}]$ loses stability, branching solutions to $\mathbf{dF}[\mathbf{v}] = \mathbf{0}$ that lie in fixed-

point subspaces of isotropy subgroups of Γ may be expected to occur generically, provided that¹

1. the nullspace $\ker \mathbf{dF}$ is finite dimensional;
2. the intersection of $\ker \mathbf{dF}$ with a given fixed-point subspace is one-dimensional.

The second requirement picks out those patterns with the symmetry of the *axial subgroups* of Γ . If the isotropy subgroup² under which a pattern is invariant picks out a one-dimensional subspace then the pattern is uniquely identified up to scalar multiplication. In this way the different axial subgroups classify the bifurcating patterns.

The first requirement is violated *a priori* because of rotational invariance: if for some nonzero $\mathbf{v}(x)$, $\mathbf{dF}[\mathbf{v}](x) = 0$, then for any angle ψ , $\mathbf{dF}[\mathbf{v}](\mathcal{R}ot_{-\psi}x) = 0$ as well. Therefore the kernel of \mathbf{dF} is infinite-dimensional. To overcome this difficulty I restrict attention to patterns that are periodic on a planar lattice, in the hopes that these solutions will give insight to the structure of the more irregular arrangements seen *in vivo*.

I will consider solutions periodic on either the square or hexagonal lattice, i.e.

$$\mathbf{v}(x) = \mathbf{v}(x + \ell_1) = \mathbf{v}(x + \ell_2) \quad (5.19)$$

where for the square lattice

$$\ell_1 = 2\pi \begin{bmatrix} 1 \\ 0 \end{bmatrix} \quad (5.20)$$

$$\ell_2 = 2\pi \begin{bmatrix} 0 \\ 1 \end{bmatrix} \quad (5.21)$$

¹I implicitly assume that the synaptic-weight dynamical system determines a nonlinear dynamical system for the feature-map vector \mathbf{v} . One should expect that this nonlinear system would preserve the equivariance of equation 5.1, in which case the analysis of this Chapter would apply to the full system. I have only derived the first-order terms of this dynamical system, so for the dynamical system 5.3 it happens that $\mathbf{dF} \equiv \mathbf{F}$.

²For group theoretic terminology, see Appendix A.3.

while for the hexagonal lattice

$$\ell_1 = \frac{4\pi}{\sqrt{3}} \begin{bmatrix} \sqrt{3}/2 \\ 1/2 \end{bmatrix} \quad (5.22)$$

$$\ell_2 = \frac{4\pi}{\sqrt{3}} \begin{bmatrix} 0 \\ 1 \end{bmatrix}. \quad (5.23)$$

I implicitly adjust the length scale in the problem so that the critical wavelength matches the lattice vector lengths. This scaling allows me to represent the critical-wave vectors for these lattices as unit vectors k_i :

$$\text{(square lattice)} \quad (5.24)$$

$$k_1 = \begin{bmatrix} 1 \\ 0 \end{bmatrix}$$

$$k_2 = \begin{bmatrix} 0 \\ 1 \end{bmatrix}$$

$$\text{(hexagonal lattice)} \quad (5.25)$$

$$k_1 = \begin{bmatrix} 1 \\ 0 \end{bmatrix} \quad (5.26)$$

$$k_2 = \begin{bmatrix} -1/2 \\ \sqrt{3}/2 \end{bmatrix}$$

$$k_3 = -(k_1 + k_2) = \begin{bmatrix} -1/2 \\ -\sqrt{3}/2 \end{bmatrix}.$$

The space of lattice-periodic solutions no longer has the full \mathbf{E}_2 symmetry, but rather that of a subgroup of \mathbf{E}_2 . $\Gamma_{\text{sq}} = T^2 \rtimes D_4$ acts on V_{sq} , the space of solutions on the square lattice, and $\Gamma_{\text{hex}} = T^2 \rtimes D_6$ acts on V_{sq} , the hexagonal-lattice solutions. T^2 is the two-dimensional torus of translations modulo the lattice and D_{2n} is the dihedral group with a $2n^{\text{th}}$ -order rotation, the holohedry of the lattice. At the bifurcation point the solutions will be linear combinations of plane waves $\cos k_i x$ and $\sin k_i x$. For each of six components of the feature-map vector $\mathbf{v}(x)$, there will be

n distinct directions on the D_{2n} lattice, so $V_{\text{sq}} \approx \mathbb{R}^{24}$ and $V_{\text{hex}} \approx \mathbb{R}^{36}$. Thus the requirement for a finite-dimensional kernel is satisfied.

By choosing the kernel to contain only functions periodic on a particular lattice, I restrict the space of possible solutions to \mathbb{R}^{24} or \mathbb{R}^{36} for the square or the hexagonal lattice, respectively. The action of Γ_{lat} on the solution space V_{lat} splits it into smaller invariant subspaces on each of which the group acts *irreducibly*. These *irreducible representations*³ fall into a small number of possible types. The subspaces corresponding to a given irrep together constitute an isotypic component of the solution space, and bifurcating solutions will be restricted to lie within a given isotypic component. In particular, components of the feature-map vector (such as orientation and retinotopy) can only interact in the formation of bifurcating patterns if they occur in the same isotypic component. *Because the symmetry structure of the cortical-map vector is independent of the details of the developmental model, the restrictions on coupling across different isotypic components hold in any model that correctly incorporates the cortical-map symmetries.* The structure imposed on solutions by symmetry helps classify the possible kinds of interactions that might be produced in different models.

5.3 Pattern Formation on a Square Lattice

First I consider the action of Γ_{sq} on V_{sq} . We may write a periodic cortical map on the square lattice as

$$\mathbf{v}(x) = \left\{ \mathbf{z}_1 e^{ik_1 x} + \mathbf{z}_2 e^{ik_2 x} + \text{complex conjugate} \mid \mathbf{z}_1, \mathbf{z}_2 \in \mathbb{C}^6 \right\}. \quad (5.27)$$

This “naive” coordinate system will shortly be replaced with a *symmetry-adapted basis* for V_{sq} in which the isotypic decomposition is made explicit. In the naive coordinate system, the action of Γ_{sq} on V_{sq} is given by Tables 5.3 and 5.3, which I constructed according to the \mathbf{E}_2 -action given in equations 5.14–5.16. I denote rotation by $\pi/2$ by ξ , the reflection in the k_1 -axis by κ , and translation by an element of \mathcal{T} by $\mathcal{T}_{[\alpha_1, \alpha_2]}$, where $0 \leq \alpha_i < 2\pi$.

³Abbreviated, *irreps*.

$$\begin{array}{l}
\mathbf{1}v(x) = \\
\begin{bmatrix} z_1^1 \\ z_1^2 \\ z_1^3 \\ z_1^4 \\ z_1^5 \\ z_1^6 \end{bmatrix} e^{ik_1x} + \begin{bmatrix} z_2^1 \\ z_2^2 \\ z_2^3 \\ z_2^4 \\ z_2^5 \\ z_2^6 \end{bmatrix} e^{ik_2x} + \text{c.c.} \\
\kappa v(x) = \\
\begin{bmatrix} z_1^1 \\ z_1^2 \\ -z_1^3 \\ z_1^4 \\ -z_1^5 \\ z_1^6 \end{bmatrix} e^{ik_1x} + \begin{bmatrix} \bar{z}_2^1 \\ \bar{z}_2^2 \\ -\bar{z}_2^3 \\ \bar{z}_2^4 \\ -\bar{z}_2^5 \\ \bar{z}_2^6 \end{bmatrix} e^{ik_2x} + \text{c.c.} \\
\xi v(x) = \\
\begin{bmatrix} \bar{z}_2^1 \\ -\bar{z}_2^3 \\ \bar{z}_2^2 \\ -\bar{z}_2^4 \\ -\bar{z}_2^5 \\ \bar{z}_2^6 \end{bmatrix} e^{ik_1x} + \begin{bmatrix} z_1^1 \\ -z_1^3 \\ z_1^2 \\ -z_1^4 \\ -z_1^5 \\ z_1^6 \end{bmatrix} e^{ik_2x} + \text{c.c.} \\
\kappa\xi v(x) = \\
\begin{bmatrix} \bar{z}_2^1 \\ -\bar{z}_2^3 \\ -\bar{z}_2^2 \\ -\bar{z}_2^4 \\ \bar{z}_2^5 \\ \bar{z}_2^6 \end{bmatrix} e^{ik_1x} + \begin{bmatrix} \bar{z}_1^1 \\ -\bar{z}_1^3 \\ -\bar{z}_1^2 \\ -\bar{z}_1^4 \\ \bar{z}_1^5 \\ \bar{z}_1^6 \end{bmatrix} e^{ik_2x} + \text{c.c.} \\
\xi^2 v(x) = \\
\begin{bmatrix} \bar{z}_1^1 \\ -\bar{z}_1^2 \\ -\bar{z}_1^3 \\ \bar{z}_1^4 \\ \bar{z}_1^5 \\ \bar{z}_1^6 \end{bmatrix} e^{ik_1x} + \begin{bmatrix} \bar{z}_2^1 \\ -\bar{z}_2^2 \\ -\bar{z}_2^3 \\ \bar{z}_2^4 \\ \bar{z}_2^5 \\ \bar{z}_2^6 \end{bmatrix} e^{ik_2x} + \text{c.c.} \\
\kappa\xi^2 v(x) = \\
\begin{bmatrix} \bar{z}_1^1 \\ -\bar{z}_1^2 \\ \bar{z}_1^3 \\ \bar{z}_1^4 \\ -\bar{z}_1^5 \\ \bar{z}_1^6 \end{bmatrix} e^{ik_1x} + \begin{bmatrix} z_2^1 \\ -z_2^2 \\ z_2^3 \\ z_2^4 \\ -z_2^5 \\ z_2^6 \end{bmatrix} e^{ik_2x} + \text{c.c.} \\
\xi^3 v(x) = \\
\begin{bmatrix} z_2^1 \\ z_2^3 \\ -z_2^2 \\ -z_2^4 \\ -z_2^5 \\ z_2^6 \end{bmatrix} e^{ik_1x} + \begin{bmatrix} \bar{z}_1^1 \\ \bar{z}_1^3 \\ -\bar{z}_1^2 \\ -\bar{z}_1^4 \\ -\bar{z}_1^5 \\ \bar{z}_1^6 \end{bmatrix} e^{ik_2x} + \text{c.c.} \\
\kappa\xi^3 v(x) = \\
\begin{bmatrix} z_2^1 \\ z_2^3 \\ z_2^2 \\ -z_2^4 \\ z_2^5 \\ z_2^6 \end{bmatrix} e^{ik_1x} + \begin{bmatrix} z_1^1 \\ z_1^3 \\ z_1^2 \\ -z_1^4 \\ z_1^5 \\ z_1^6 \end{bmatrix} e^{ik_2x} + \text{c.c.}
\end{array}$$

Table 5.2: Action of rotation and reflection (\mathbf{O}_2) elements of Γ_{sq} on V_{sq} .

$$\mathcal{T}_{[\alpha_1, \alpha_2]} v(x) = e^{-i\alpha_1} \begin{bmatrix} z_1^1 \\ z_1^2 \\ z_1^3 \\ z_1^4 \\ z_1^5 \\ z_1^6 \end{bmatrix} e^{ik_1 x} + e^{-i\alpha_2} \begin{bmatrix} z_2^1 \\ z_2^2 \\ z_2^3 \\ z_2^4 \\ z_2^5 \\ z_2^6 \end{bmatrix} e^{ik_2 x} + \text{c.c.}$$

Table 5.3: Action of translation elements of Γ_{sq} on V_{sq} .

5.3.1 Irreducible Representations

The action of Γ_{sq} splits V_{sq} into six four-dimensional invariant subspaces. For example, the subspace of patterns in which only the net fan-in deviates from uniformity, corresponding to $\{z_i^j = 0 | i \in \{1, 2\}, j \neq 1\}$ (abbr. $z_i^1 \neq 0$), forms a four (real)-dimensional subspace. Similarly the receptive field-width deviations form a subspace, $z_i^6 \neq 0$. By inspection of Tables 5.3 and 5.3, there are two invariant subspaces corresponding respectively to the first and second component of the orientation vector, namely $z_i^4 \neq 0$ and $z_i^5 \neq 0$. The retinotopic deviation patterns also occupy two four-dimensional invariant subspaces. One contains “compression waves” of the form $z_1^2, z_2^3 \neq 0$ and the other contains “transverse waves” of the form $z_1^3, z_2^2 \neq 0$. Figure 5.2 illustrates these retinotopic distortion patterns.

Because Γ_{sq} contains translations and reflections, none of the four-dimensional subspaces just described can themselves contain any proper invariant subspaces—they are irreducible. The group action on the i^{th} four-dimensional subspace V_i forms an irreducible representation, i.e. a map from group elements to the 4×4 matrices acting on the coordinates of the subspace, $\rho_i : \gamma \in \Gamma_{\text{sq}} \rightarrow GL_4(V_i)$. Two irreps ρ_i, ρ_j are *equivalent* if there is a coordinate transformation between them, that is, a nonsingular matrix M such that for all group elements γ ,

$$M\rho_i(\gamma) = \rho_j(\gamma)M.$$

For example, the irreducible representation defined by the action of Γ_{sq} on the mass

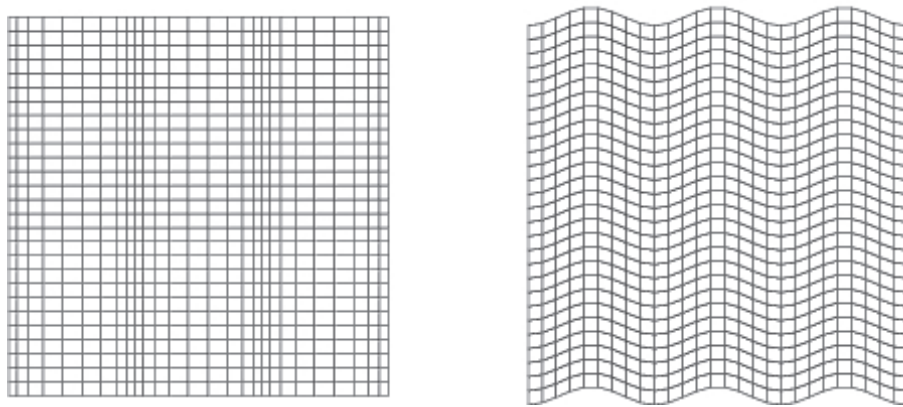


Figure 5.2: Splitting the retinotopic distortion subspace.

Left: An element of the compression-wave subspace. This pattern represents $z_1^2 = 1$ and all other $z_i^j = 0$. It may also be written $s(x) = k_1 \sin(k_1 x)$.

Right: An element of the transverse-wave subspace. This pattern represents $z_1^3 = 1$ and all other $z_i^j = 0$. It may also be written $s(x) = k_2 \cos(k_1 x)$.

subspace is exactly the same as that defined by the group's action on the subspace of receptive field width deviations $\rho(x)$ ⁴ Hence these two four-dimensional irreducible representations are equivalent, with $M = I_4$.

The equivalence or inequivalence of two irreducible representations may be calculated using orthogonality of group characters. The calculations are straightforward with the assistance of MATLAB's symbolic mathematics toolbox (see for example `irrepcalc1.m` and `irrepcalc3.m` in Appendix E). To give an example I will ask whether the mass irrep and the first orientation irrep are equivalent.

1	z_1	z_2
ξ	\bar{z}_2	z_1
κ	z_1	\bar{z}_2
$[\alpha_1, \alpha_2]$	$e^{-i\alpha_1} z_1$	$e^{-i\alpha_2} z_2$

Mass representation

1	z_1	z_2
ξ	$-\bar{z}_2$	$-z_1$
κ	z_1	\bar{z}_2
$[\alpha_1, \alpha_2]$	$e^{-i\alpha_1} z_1$	$e^{-i\alpha_2} z_2$

First orientation rep.

Table 5.4: Action of the Group Generators on $V_j, j = 1, 4$.

Writing $z_1^j = a_1 + ib_1, z_2^j = a_2 + ib_2$ and ordering coordinates $[a_1, b_1, a_2, b_2]^{\text{tr}}$ on V_j , I derive two representations of Γ_{sq} in 4×4 matrices (see table 5.4). (The mass irrep corresponds to $j = 1$ and the first orientation irrep to $j = 4$.)

$\rho_M(\xi)$	$\rho_M(\kappa)$
$\begin{pmatrix} & 1 & & \\ & & 1 & \\ 1 & & & \\ & -1 & & \end{pmatrix}$	$\begin{pmatrix} 1 & & & \\ & 1 & & \\ & & 1 & \\ & & & -1 \end{pmatrix}$
$\rho_M([\alpha_1, \alpha_2])$	
$\begin{pmatrix} \cos(\alpha_1) & \sin(\alpha_1) & & \\ -\sin(\alpha_1) & \cos(\alpha_1) & & \\ & & \cos(\alpha_2) & \sin(\alpha_2) \\ & & -\sin(\alpha_2) & \cos(\alpha_2) \end{pmatrix}$	

Table 5.5: Mass Representation: 4×4 Matrices.

⁴The customary use of $\rho(\gamma)$ to denote a group representation should not be confused with the receptive-field-width-deviation map component $\rho(x)$, and should be clear from context.

$\rho_{O1}(\xi)$	$\rho_{O1}(\kappa)$
$\begin{pmatrix} & -1 & & \\ -1 & & 1 & \\ & -1 & & \end{pmatrix}$	$\begin{pmatrix} 1 & & & \\ & 1 & & \\ & & 1 & \\ & & & -1 \end{pmatrix}$
$\rho_{O1}([\alpha_1, \alpha_2])$	
$\begin{pmatrix} \cos(\alpha_1) & \sin(\alpha_1) & & \\ -\sin(\alpha_1) & \cos(\alpha_1) & & \\ & & \cos(\alpha_2) & \sin(\alpha_2) \\ & & -\sin(\alpha_2) & \cos(\alpha_2) \end{pmatrix}$	

Table 5.6: First Orientation Representation: 4×4 Matrices.

Absolute Irreducibility

Both of these representations are absolutely irreducible, meaning that any matrix M that commutes with $\rho_j(\gamma)$ (fix either $j = M$ or $j = O1$) for all $\gamma \in \Gamma_{\text{sq}}$ must be a real scalar multiple of the identity. To see this, suppose a matrix M commutes with $\rho_M(\kappa)$ and $\rho_M(\kappa\xi^2) = \text{diag}(1, -1, 1, 1)$. Then M must have the form

$$M = \begin{pmatrix} m_{11} & & m_{13} & \\ & m_{22} & & \\ m_{31} & & m_{33} & \\ & & & m_{44} \end{pmatrix}. \quad (5.28)$$

If, in addition, M commutes with $\rho_M([\alpha_1, \alpha_2])$ then $m_{11} = m_{22}, m_{33} = m_{44}$ and $m_{13} = m_{31} = 0$, so $M = \text{diag}(m_{11}, m_{11}, m_{33}, m_{33})$.

Note that $\rho_M(\kappa) = \rho_{O1}(\kappa), \rho_M(\kappa\xi^2) = \rho_{O1}(\kappa\xi^2)$ and $\rho_M([\alpha_1, \alpha_2]) = \rho_{O1}([\alpha_1, \alpha_2])$. Up to this point the demonstration of absolute irreducibility is the same for both representations. Note also that if there were a coordinate transformation A under which the two representations were equivalent, then we would have $A\rho_M(\gamma) = \rho_{O1}(\gamma)A$ and A would have to assume the form $A = \text{diag}(a_{11}, a_{11}, a_{33}, a_{33})$ as well.

Finally, consideration of $M\rho_M(\xi) - \rho_M(\xi)M$ and $M\rho_{O1}(\xi) - \rho_{O1}(\xi)M$ shows that in either case, M must be a multiple of the identity matrix (see Table 5.7).

$M\rho_M(\xi) - \rho_M(\xi)M$	$M\rho_{O1}(\xi) - \rho_{O1}(\xi)M$
$(m_{11} - m_{33}) \begin{pmatrix} & & 1 \\ & -1 & \\ & & 1 \end{pmatrix}$	$(m_{11} - m_{33}) \begin{pmatrix} & & -1 \\ & 1 & \\ & & 1 \end{pmatrix}$

Table 5.7: Absolute Irreducibility of ρ_M and ρ_{O1} , Respectively.

Equivalence via Characters

The matrices in tables 5.5 and 5.6 generate real orthonormal representations of a compact Lie group. Equivalence between such representations may be determined by comparing their character functions χ_j :

$$\chi_j(\gamma) = \text{Tr}(\rho_j(\gamma)). \quad (5.29)$$

Characters of inequivalent irreducible representations are orthogonal under the Haar measure of the group:

$$\chi_i \cdot \chi_j = \langle \chi_i(\gamma) \bar{\chi}_j(\gamma) \rangle_{\Gamma} = \frac{\int_{\Gamma} \chi_i(\gamma) \bar{\chi}_j(\gamma) d\gamma}{\int_{\Gamma} d\gamma} = \begin{cases} 0 & \rho_i \not\sim \rho_j \\ 1 & \rho_i \sim \rho_j \end{cases} \quad (5.30)$$

Γ_{sq} is the semi-direct product of \mathbf{T}^2 with D_4 , hence every $\gamma \in \Gamma_{\text{sq}}$ may be represented as a rotation or flip followed by a translation:

$$\Gamma_{\text{sq}} = \{[\alpha_1, \alpha_2] \cdot \sigma \mid 0 \leq \alpha_1, \alpha_2 < 2\pi, \sigma \in D_4\} \quad (5.31)$$

The Haar measure of a function $f(\gamma)$ on Γ_{sq} is given by

$$\langle f \rangle_{\Gamma_{\text{sq}}} = \frac{1}{4\pi^2} \int_{[\alpha_1, \alpha_2]} \frac{1}{8} \sum_{k=0}^3 \left\{ f([\alpha_1, \alpha_2] \cdot \xi^k) + f([\alpha_1, \alpha_2] \cdot \kappa \cdot \xi^k) \right\} d\alpha_1 d\alpha_2. \quad (5.32)$$

The computation of χ_M and χ_{O1} are straightforward using tables 5.5 and 5.6 and MATLAB's symbolic toolbox (see for example `irrepcalc1.m` and `irrepcalc3.m` in Appendix E). The character functions are identical for the two representations and

γ	$\chi(\gamma)$
t	$2 \cos(\alpha_1) + 2 \cos(\alpha_2)$
$t\xi$	0
$t\xi^2$	0
$t\xi^3$	0
$t\kappa$	$2 \cos(\alpha_1)$
$t\kappa\xi$	0
$t\kappa\xi^2$	$2 \cos(\alpha_2)$
$t\kappa\xi^3$	0

Table 5.8: The Character Function for the Representations. $t = [\alpha_1, \alpha_2]$

are given in table 5.8. Note that $\chi(\gamma)$ is normalized, i.e. $\chi \cdot \bar{\chi} \equiv 1$, indicating again that the representations are irreducible. Because they have the same character, they must be equivalent.⁵

Repeating this calculation for different pairs of irreducible representations, I find that V_{sq} splits into two isotypic components. The mass irrep is equivalent to the first (compression-wave) retinotopy irrep which is equivalent to the first orientation irrep. These are all equivalent to the irrep on the receptive field-width subspace as well. I will call this irrep “even” because it is equivalent to the even irrep studied in related work by Bressloff *et al.* [7, 8]. The second (transverse-wave) retinotopy irrep and the second orientation irrep are equivalent and together form the *odd* isotypic component.

5.3.2 Symmetry-Adapted Basis Vectors

Within each irreducible subspace of an isotypic component of V_{sq} , it is possible to choose coordinates such that the action of Γ_{sq} acts in exactly the same way on each set of basis vectors. Such a basis for the isotypic component is called *symmetry-adapted*⁶, and facilitates the search for bifurcating solutions.

To construct a symmetry-adapted basis for the even component of V_{sq} , I begin with an arbitrary choice of vectors from one of the irreps and determine how Γ_{sq}

⁵Same character implies equivalence for finite groups but not in general for infinite groups. However the theorem still holds for unitary representations of compact groups. See for example [57].

⁶See [26].

permutes them. Choosing from the mass irrep four orthogonal vectors given by $\cos k_i x$ and $\sin k_i x$ for $i = 1, 2$, I find from Table 5.3:

$$\begin{aligned} \xi & : \cos k_1 x \rightarrow \cos k_2 x \rightarrow \cos k_1 x \\ & \quad \sin k_1 x \rightarrow \sin k_2 x \rightarrow -\sin k_1 x \\ \kappa & : \cos k_1 x \rightarrow \cos k_1 x \\ & \quad \cos k_2 x \rightarrow \cos k_2 x \\ & \quad \sin k_1 x \rightarrow \sin k_1 x \\ & \quad \sin k_2 x \rightarrow -\sin k_2 x. \end{aligned}$$

Therefore in the ordered basis

$$\begin{bmatrix} \cos k_1 x \\ \cos k_2 x \\ \sin k_1 x \\ \sin k_2 x \end{bmatrix},$$

the action of the holohedry D_4 is generated by the representing matrices

$$\begin{aligned} \rho_{ES}(\xi) &= \left(\begin{array}{c|c} +1 & \\ \hline +1 & \\ \hline & -1 \\ & +1 \end{array} \right) \\ \rho_{ES}(\kappa) &= \left(\begin{array}{c|c} +1 & \\ \hline & +1 \\ \hline & +1 \\ & -1 \end{array} \right). \end{aligned} \tag{5.33}$$

Considering the group action on a retinotopic-deviation compression wave or an even-irrep orientation wave, it is straightforward to work out basis vectors for these irreps for which the representing matrices are the same as in equation 5.34. They are summarized in Table 5.9. Figure 5.3 shows the patterns in the first row of the table, from which the rows are generated in identical fashion by rotation, translation and/or

Net Fan-in Mass Deviation $\lambda(x)$	Retinotopic Compression Wave $s(x)$	Even Orientation Pattern $\chi(x)$	Receptive Field Width Deviation $\rho(x)$
$\cos k_1 x$	$k_1 \sin k_1 x$	$k_1 \cos k_1 x$	$\cos k_1 x$
$\cos k_2 x$	$k_2 \sin k_2 x$	$-k_1 \cos k_2 x$	$\cos k_2 x$
$\sin k_1 x$	$-k_1 \cos k_1 x$	$k_1 \sin k_1 x$	$\sin k_1 x$
$\sin k_2 x$	$-k_2 \cos k_2 x$	$-k_1 \sin k_2 x$	$\sin k_2 x$

Table 5.9: Symmetry-adapted basis vectors, square lattice even irrep. When ordered as in this Table, the basis vectors within each irrep permute in identical fashion under the action of Γ_{sq} .

Retinotopic Transverse Wave $s(x)$	Odd Orientation Pattern $\chi(x)$
$-k_2 \cos k_1 x$	$k_2 \sin k_1 x$
$k_1 \cos k_2 x$	$-k_2 \sin k_2 x$
$k_2 \sin k_1 x$	$k_2 \cos k_1 x$
$-k_1 \sin k_2 x$	$-k_2 \cos k_2 x$

Table 5.10: Symmetry-adapted basis vectors, square lattice odd irrep.

reflection.

Proceeding similarly, I calculate the symmetry-adapted basis for the odd isotypic subspace on the square lattice, given in Table 5.10 and Figure 5.4. In this basis, the action of the rotation and reflection element are, respectively:

$$\rho_{OS}(\xi) = \left(\begin{array}{c|c} -1 & \\ \hline +1 & \\ \hline & +1 \\ & +1 \end{array} \right) \quad (5.34)$$

$$\rho_{OS}(\kappa) = \left(\begin{array}{c|c} -1 & \\ \hline +1 & \\ \hline & -1 \\ & -1 \end{array} \right).$$

The advantage of adapting one's basis for a vector space to the symmetry of a

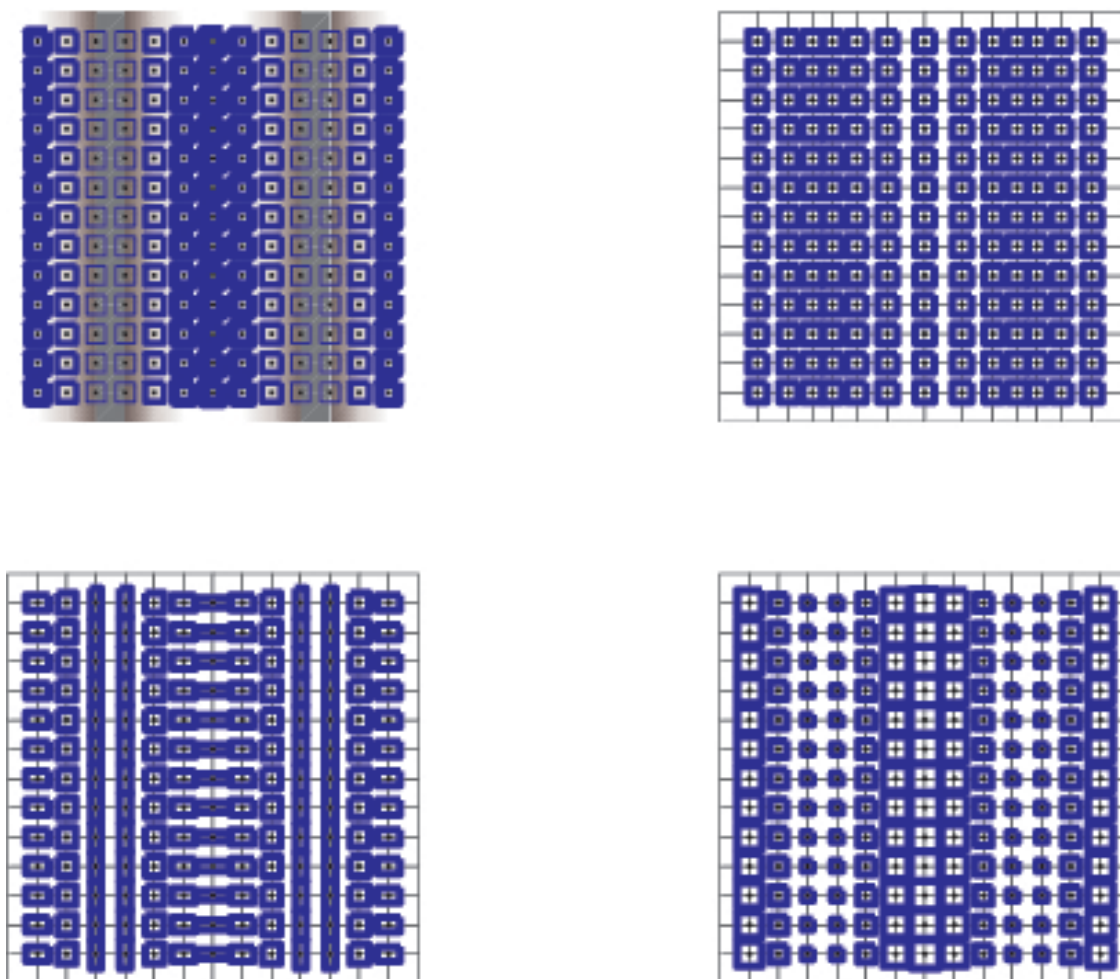


Figure 5.3: Symmetry-adapted basis vectors, square lattice even irrep. The brightness of the background and the thickness of the line elements both reflect the net input mass, which deviates from uniformity only in the top-left frame. The centers of the squares, marked by small dots, reflect the retinotopic spacing, which deviates from uniformity only in the top-right frame. The elongation of the rectangles reflects orientation preference (elongated receptive-field shape), and deviates from uniformity only in the bottom-left frame. The area of the boxes reflects the receptive-field widths, which deviate from uniformity only in the bottom-right frame.

Top Left: Mass irrep.

Top Right: Retinotopic compression wave irrep.

Bottom Left: Even orientation irrep.

Bottom Right: Receptive-field-width irrep.

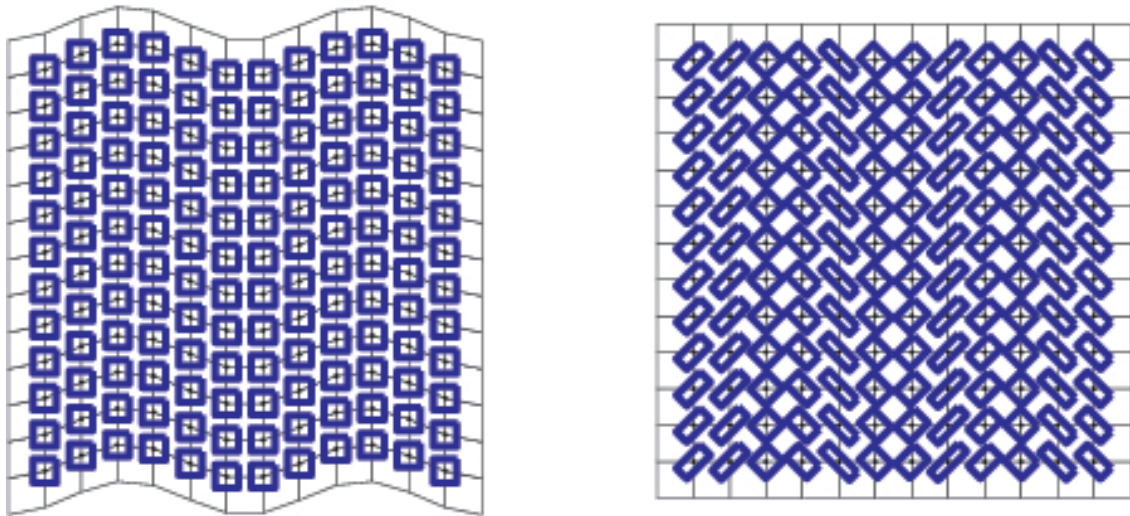


Figure 5.4: Symmetry-adapted basis vectors, square lattice odd irrep. Taken from the top row of Table 5.10.

Left: Retinotopic transverse-wave irrep.

Right: Odd orientation irrep.

group acting on the space is the following: any linear operator that commutes with the group action on the space will have a block-diagonal form in the symmetry-adapted basis. If there are c_j copies of the j^{th} irrep in the j^{th} isotypic component, and the j^{th} irrep has dimension n_j , then the matrix will have n_j identical blocks of size $c_j \times c_j$ along the diagonal. Because the linearized dynamics \mathbf{dF} has the symmetry of Γ_{sq} , it commutes with the representation of Γ_{sq} on V_{sq} . In the basis given in Tables 5.9 and 5.10, \mathbf{dF} takes the form:

$$\mathbf{dF}|_{(\text{sym. ad. basis})} = \left(\begin{array}{ccc|ccc} M_+ & & & & & \\ & M_+ & & & & \\ & & M_+ & & & \\ & & & M_+ & & \\ \hline & & & & m_- & \\ & & & & & m_- \\ & & & & & & m_- \\ & & & & & & & m_- \end{array} \right) \quad (5.35)$$

where M_+ is a four-by-four matrix and m_- is a two-by-two matrix.

Generically, the kernel of \mathbf{dF} will itself be an irreducible subspace of V_{sq} . According to the Equivariant Branching Lemma [30], there will be bifurcating solution branches with the symmetry of isotropy subgroups the fixed-point subspaces of which are one-dimensional. Therefore we seek bifurcating solutions in subspaces with one-dimensional intersections with $\ker \mathbf{dF}$. Finding the kernel of \mathbf{dF} *a priori* requires solving a degenerate eigenvalue problem for the 24×24 matrix \mathbf{dF} in arbitrary coordinates. In the form 5.35 however, we confront either a four-by-four or a two-by-two eigenvalue problem, depending on whether the kernel lies in the even (M_+) or odd (m_-) subspace.

5.3.3 Axial Subgroups

The axial subgroups of Γ_{sq} classify the expected bifurcating solution branches, or *planforms*, appearing when the homogeneous state $\mathbf{v} \equiv \mathbf{0}$ becomes unstable. The

axial subgroups for the even and odd irreps on the square lattice (and also on the hexagonal and rhombic lattices) have been derived elsewhere—see for example [19]. On the square lattice there are four possibilities: *Even Rolls*, which are single waves such as those shown in Figure 5.3, *Even Squares*, which are sums of Even Rolls in two orthogonal directions with equal coefficients, *Odd Rolls*, pictured in Figure 5.4, and *Odd Squares*, which are equal-coefficient sums of Odd Rolls.

The kernel of \mathbf{dF} on the square lattice will contain combinations of a given kind of planform drawn from the different irreducible subspaces in a given isotypic component. For example, a bifurcating planform could be a combination of Odd Squares in both orientation and retinotopy simultaneously, or instead a combination of Even Rolls from the mass irrep, the width irrep and the even retinotopy and orientation irreps. The signs of the coefficients with which the components from different subspaces are combined determine whether the different cortical-map features are *correlated* or *anti-correlated*. For example, if a pattern combining components of the even irreps had increased fan-in mass positively correlated with increased receptive-field width, this relation would be manifest in the two components having the same sign in the zero eigenvector of $\mathbf{dF}|_{(\text{sym. ad. basis})}$. Different models for cortical-map development cannot produce different couplings between irreps than those allowed by symmetry, but they could yield different pairwise correlations between features that are coupled. Generically one would not expect to find features sharing an equivalent irrep to be uncoupled in any model.

The possible models of cortical-map development may therefore be classified by the correlations they predict between cortical-map components. Within the odd irrep, which combines two subspaces (retinotopic transverse waves and orientation zig-zag pattern), there are two possibilities: either the two components are correlated or anti-correlated. Within the even irrep the possible pairwise correlations between components allow eight types of models. Using \approx to denote positive correlation and

$\not\approx$ to denote negative correlation, we have the following possibilities:

1. $m \approx s_e \approx \chi_e \approx \rho$
2. $m \not\approx s_e \approx \chi_e \approx \rho$
3. $s_e \not\approx \chi_e \approx \rho \approx m$
4. $\chi_e \not\approx \rho \approx m \approx s_e$
5. $\rho \not\approx m \approx s_e \approx \chi_e$
6. $m \approx s_e \not\approx \chi_e \approx \rho$
7. $m \approx \chi_e \not\approx s_e \approx \rho$
8. $m \approx \rho \not\approx s_e \approx \chi_e$

Figure 5.5 shows a sample Even Square pattern combining components from the four even irreps. The correlations are chosen so that the pattern approximately preserves uniform geniculate fan-out $\Upsilon(r)$.

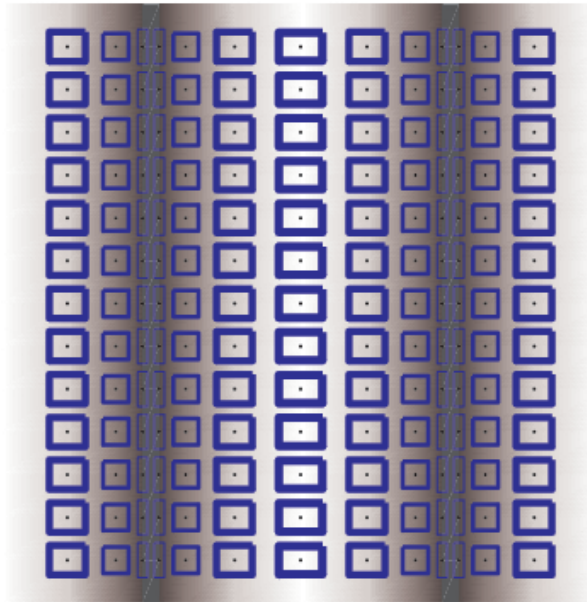


Figure 5.5: An Even Square planform. Positive or negative correlations were chosen between components of the mass, retinotopic compression, even orientation and width irreps so as to approximately preserve a uniform geniculate fan-out $\Upsilon(r)$.

5.4 Numerical Isolation of a Bifurcating Planform on the Square Lattice

In Chapter 4, I derived a detailed set of linear interactions between different components of the cortical-map vector, based approximately on realistic values of parameters such as receptive field spread and distance of lateral cortical interactions. The interactions also depended on parameters that could naturally vary during development, such as the strength of the attraction to the target for net-fan K_λ and fan-out K_γ , the rate of spontaneous decay of synaptic weight α and the strength of the lateral cortical center-surround interaction λ . By increasing the weight-decay coefficient α it is always possible to find a region in parameter space in which all patterns decay to homogeneous state $\mathbf{v}(x) \equiv \mathbf{0}$. One can then search for values of $K_\lambda, K_\gamma, \alpha$ and λ at which a steady-state bifurcation occurs⁷.

The transformation of the dynamics into the frequency domain converts the matrix convolution equation

$$\mathbf{F}[\mathbf{v}] = -\alpha\mathbf{v} + A * \mathbf{v} + \mathbf{K} * \mathbf{v}$$

into a separate matrix multiplication at each wave-vector k :

$$(\mathbf{F}[\tilde{\mathbf{v}}])(k) = -\alpha\tilde{\mathbf{v}}(k) + \tilde{A}(k)\tilde{\mathbf{v}}(k) + \tilde{\mathbf{K}}(k)\tilde{\mathbf{v}}(k).$$

The dynamics \mathbf{F} is thereby block-diagonalized into 5×5 blocks⁸ each containing a combination of M_+ and m_- in an arbitrary basis. For each 5×5 block, I solved the eigenvalue problem numerically. The block with the largest eigenvalue (real part) was recorded for each value of $K_\lambda, K_\gamma, \alpha$ and/or λ . (See the MATLAB script `ctxpat1.m`.

⁷One can also find Hopf bifurcations from the steady state. Because cortical maps are themselves static patterns, oscillatory pattern formation (Turing-Hopf Bifurcations) were not of interest for this study.

⁸This frequency-diagonalization of \mathbf{dF} would contain 6×6 blocks for a six-dimensional cortical map vector. For numerical simulation I simply eliminated the sixth dimension, representing receptive-field width, because the critical parameter values proved easier to isolate that way. The approximations made to arrive at the cortical-map dynamics are most severe for this map component, which is directly affected by the hard $w(x, r) \geq 0$ cutoff (see for example the discussion accompanying Figure 4.1).

in Appendix E.) Once I isolated a zero-crossing of the spectrum, I recorded the critical block and its eigenvector, the cortical eigenmode. Using a 32×32 grid for the components of $\mathbf{v}(x)$ and the different convolution kernels, I found a pair of critical wave vectors at coordinates $[3, 31]$ and $[31, 3]$, corresponding to vectors $k_c = \begin{bmatrix} 2 \\ -2 \end{bmatrix}$ and $-k_c = \begin{bmatrix} -2 \\ 2 \end{bmatrix}$ relative to the origin $[1, 1]$. The critical eigenvector for this wave vector is:

$$\begin{array}{c} \text{Critical coordinates} \end{array} \quad \begin{array}{cc} [3, 31] & [31, 3] \end{array}$$

$$\begin{bmatrix} m(x) \\ s_1(x) \\ s_2(x) \\ \chi_1(x) \\ \chi_2(x) \end{bmatrix} \begin{bmatrix} 0 \\ 0.3037 - 0.1973i \\ 0.3037 - 0.1973i \\ -0.4680 - 0.7202i \\ 0 \end{bmatrix} + \text{c.c.} \quad \begin{bmatrix} 0 \\ 0.3518 - 0.0862i \\ 0.3518 - 0.0862i \\ 0.2044 + 0.8342i \\ 0 \end{bmatrix} + \text{c.c.}$$

Both of these cortical-map vectors have the form

$$\mathbf{v}(x) = \begin{bmatrix} 0 \\ \begin{bmatrix} 1 \\ 1 \end{bmatrix} a_s \cos \left(\begin{bmatrix} -2 \\ 2 \end{bmatrix} \cdot (x - x_0) \right) \\ \begin{bmatrix} 1 \\ 0 \end{bmatrix} a_\chi \sin \left(\begin{bmatrix} -2 \\ 2 \end{bmatrix} \cdot x\theta \right) \end{bmatrix}$$

for the values

$$\begin{aligned} a_s &= 0.3622 \\ a_\chi &= 0.8589 \\ \theta &= \begin{cases} -0.5761, [3, 31] \\ -0.2403, [31, 3] \end{cases} \end{aligned}$$

After a rotation by $\pi/4$, they may be recognized as instances of the odd roll pattern coupling orientation and retinotopic distortion.

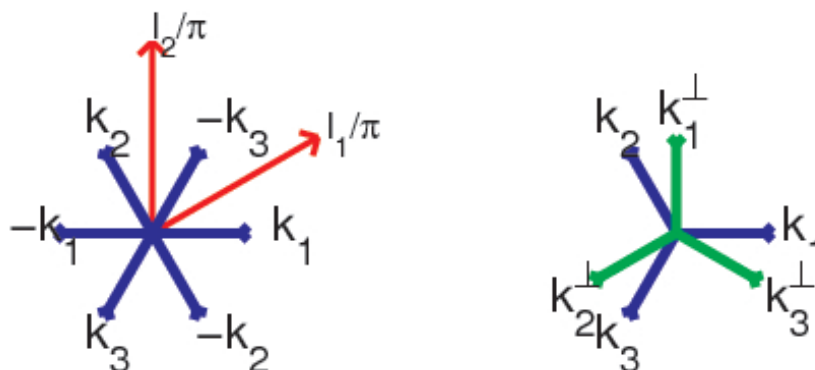


Figure 5.6: Lattice vectors and wave vectors for the hexagonal lattice, as defined in equations 5.22 and 5.25.

Left: Wave vectors in six directions, and the two spatial vectors generating the lattice: $\ell_i \cdot k_j = 2\pi\delta_{ij}$ for $i, j \in \{1, 2\}$.

Right: Orthogonal wave vectors k_i^\perp , each rotated by $+\pi/2$ from k_i .

5.5 Pattern Formation on a Hexagonal Lattice

I arrived at the isotopic decomposition of the cortical-map vector space on the square lattice through a rather indirect set of calculations. With the benefit of hindsight, it is straightforward to adapt the square-lattice construction to the hexagonal lattice and write down its irreducible representations directly. The same even and odd roll patterns such as the retinotopic compression and transverse waves provide the building blocks of the symmetry-adapted basis for V_{hex} . The axial subgroups of the even irrep are well known from classical studies of pattern formation in convective fluid flow [7, 8, 10]; axials for the odd irrep are studied in [7, 8]. Because the axial planforms on the hexagonal lattice can form orientation singularities of unit topological charge ($\pm\pi$), the hex lattice provides the most promising scenario for understanding the formation of the orientation map.

Recall that the hexagonal lattice has lattice vectors ℓ_1 and ℓ_2 and wave vectors as shown in Figure 5.6. The symmetry-adapted basis for the even and odd hexagonal representations are given in Tables 5.11 and 5.12, respectively. As in the square lattice case, the elements of the lattice are plane waves rotated by the lattice angles, in this case by $\pi/3$ (taking k_1x to $-k_3x$) and by $2\pi/3$ (taking k_1x to k_2x). In these

coordinates the action of the $\pi/3$ -rotation ξ and the reflection κ are given by:

$$\begin{aligned} \rho_{EH}(\xi) &= \left(\begin{array}{cc|cc} & & & \\ & & +1 & \\ \hline +1 & & & \\ & +1 & & \\ \hline & & +1 & -1 \\ & & & +1 \\ & & & +1 \end{array} \right) \\ \rho_{EH}(\kappa) &= \left(\begin{array}{cc|cc} & & & \\ & & +1 & \\ \hline +1 & & & \\ & +1 & & \\ \hline & & +1 & -1 \\ & & & -1 \\ & & & -1 \end{array} \right) \end{aligned} \quad (5.36)$$

for the even hexagonal irrep. For the odd hexagonal irrep they are given by:

$$\begin{aligned} \rho_{OH}(\xi) &= \left(\begin{array}{cc|cc} & & & \\ & & +1 & \\ \hline +1 & & & \\ & +1 & & \\ \hline & & +1 & -1 \\ & & & +1 \\ & & & +1 \end{array} \right) \\ \rho_{OH}(\kappa) &= \left(\begin{array}{cc|cc} & & & \\ & & -1 & \\ \hline -1 & & & \\ & -1 & & \\ \hline & & -1 & +1 \\ & & & +1 \\ & & & +1 \end{array} \right). \end{aligned} \quad (5.37)$$

For purposes of illustration I will show pictures of the odd planforms occurring on the hexagonal lattice. In square lattice simulations (see section 5.4), it is the odd ir-

Net Fan-in Mass Deviation $\lambda(x)$	Retinotopic Compression Wave $s(x)$	Even Orientation Pattern $\chi(x)$	Receptive Field Width Deviation $\rho(x)$
$\cos k_1 x$	$k_1 \sin k_1 x$	$k_1 \cos k_1 x$	$\cos k_1 x$
$\cos k_3 x$	$k_3 \sin k_3 x$	$k_2 \cos k_3 x$	$\cos k_3 x$
$\cos k_2 x$	$k_2 \sin k_2 x$	$k_3 \cos k_2 x$	$\cos k_2 x$
$\sin k_1 x$	$k_1 \cos k_1 x$	$k_1 \sin k_1 x$	$\sin k_1 x$
$-\sin k_3 x$	$-k_3 \cos k_3 x$	$-k_2 \sin k_3 x$	$-\sin k_3 x$
$\sin k_2 x$	$k_2 \cos k_2 x$	$k_3 \sin k_2 x$	$\sin k_2 x$

Table 5.11: Symmetry-adapted basis vectors, hexagonal lattice even irrep.

Retinotopic Transverse Wave $s(x)$	Odd Orientation Pattern $\chi(x)$
$k_1^\perp \sin k_1 x$	$k_1^\perp \cos k_1 x$
$k_3^\perp \sin k_3 x$	$k_2^\perp \cos k_3 x$
$k_2^\perp \sin k_2 x$	$k_3^\perp \cos k_2 x$
$k_1^\perp \cos k_1 x$	$k_1^\perp \sin k_1 x$
$-k_3^\perp \cos k_3 x$	$-k_2^\perp \sin k_3 x$
$k_2^\perp \cos k_2 x$	$k_3^\perp \sin k_2 x$

Table 5.12: Symmetry-adapted basis vectors, hexagonal lattice odd irrep. As in the square lattice, the retinotopic distortion vector k_i^\perp lies orthogonal to the direction of the wave vector k_i . The orthogonal vector k_i^\perp is k_i rotated by $+\pi/2$.

Name	Representative Function	Isotropy Group
Even	Representative from Mass Irrep	
Even Rolls	$\cos k_1 x$	$\mathbf{O}_2 \times \mathbf{Z}_2(\kappa)$
Even Hexagons+	$\cos k_1 x + \cos k_2 x + \cos k_3 x$	$\mathbf{D}_6(\xi, \kappa)$
Even Hexagons-	$-\cos k_1 x - \cos k_2 x - \cos k_3 x$	$\mathbf{D}_6(\xi, \kappa)$
Odd	Representative from Orientation Irrep	
Odd Rolls	$k_1^\perp \cos k_1 x$	$\mathbf{O}_2 \times \mathbf{Z}_4(\xi^3 \kappa \mathcal{T}_{[\frac{1}{2}, 0]})$
Odd Triangles	$k_1^\perp \sin k_1 x - k_2^\perp \sin k_3 x + k_3^\perp \sin k_2 x$	$\mathbf{D}_3(\kappa \xi, \xi^2)$
Odd Hexagons	$k_1^\perp \cos k_1 x + k_2^\perp \cos k_3 x + k_3^\perp \cos k_2 x$	$\mathbf{Z}_6(\xi)$
Odd Rectangles	$k_2^\perp \cos k_3 x - k_3^\perp \cos k_2 x$	$\mathbf{D}_2(\kappa, \xi^3)$

Table 5.13: Axial planforms on the hexagonal lattice. Each planform corresponds to a one-dimensional fixed-point subspace of an isotropy subgroup of Γ_{hex} , up to conjugacy. The nomenclature has been adapted from [8].

rep that appears in the monocular model. Figure 5.7 shows the Odd Rolls, Triangles, Hexagons and Rectangles planforms. All planforms except the rolls show singularities in the orientation field $\phi(x)$. In the hexagonal pattern, both *double* and *single* singularities appear. The double singularities have net orientation-change of $+2\pi$ when traversed counter-clockwise, and the single singularities have a net orientation-change of $-\pi$. Because double singularities are never observed in orientation maps, the Odd Hexagons planform is not a plausible model for orientation-map formation. The Odd Triangles and Odd Rectangles planforms have only $\pm\pi$ singularities. The triangles planform also exhibits *fractures*, *i.e.* line boundaries across which the preferred orientation jumps by $\pi/2$. The triangles planform has only $-\pi$ singularities, while the rectangles planform has equal numbers of $+\pi$ and $-\pi$ singularities.

The occurrence of orientation and retinotopy together in the odd irrep provides a natural explanation for recent observations linking together local distortions in the retinotopic map and rapid changes in the orientation map. Contrary to classical predictions of self-organizing map models, Das and Gilbert found that larger-than-typical shifts in orientation and retinotopy, relative to uniformly spaced cortical locations, tended to be *positively* correlated [18]. If there were no bias in their experiment for a particular relation between the direction of the cortical track chosen and the local orientation preference, then the observation of larger retinotopic shifts should reflect *lower magnification*, or larger retinal areas per unit cortical area, in the regions where orientation preference is shifting more rapidly. In the Odd Rectangles planform the retinal area per cortical area and the orientation gradient $|\nabla\phi(x)|$ have a positive correlation coefficient⁹ of 0.15. The correlation coefficient is the same regardless of whether the coefficients of the odd orientation and retinotopy planforms in linear combination are positive or negative. In the Odd Triangles planform, which exhibits both orientation singularities and orientation fractures as regions of rapid orientation change, the correlation coefficient of area and $|\nabla\phi(x)|$ is 0.40—again positive. It is not possible to make any claim about the stability of these planforms without analysis of a higher-order dynamics for $\mathbf{v}(x)$. Nevertheless the agreement of

⁹The correlation coefficient of area and $|\nabla\phi(x)|$ is the covariance normalized by the variances, and lies within ± 1 .

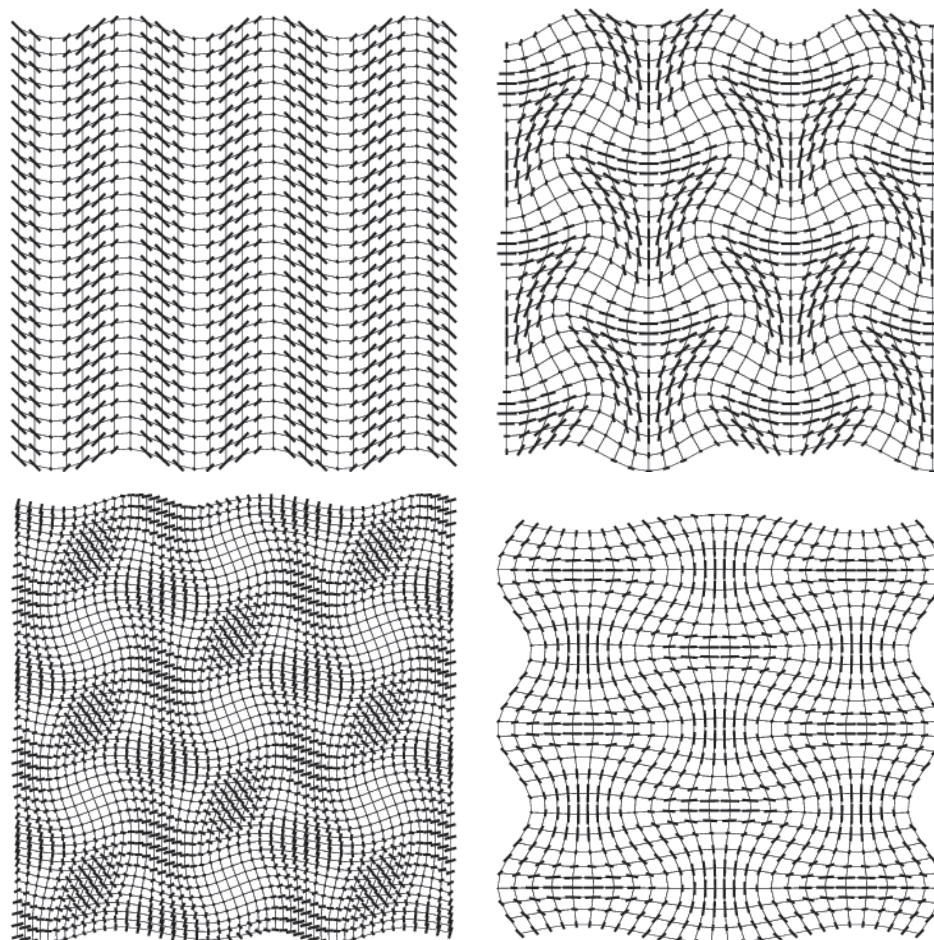


Figure 5.7: Odd axial planforms on the hexagonal lattice.

Top Left: Odd Rolls.

Top Right: Odd Triangles. Each singularity (center of a triangle) is surrounded by a fracture boundary, across which the orientation changes by $\pi/2$.

Bottom Left: Odd Hexagons. Note the combination of single and double singularities. The large low-orientation-preference region at the center of the image is a double singularity.

Bottom Right: Odd Rectangles. The $+$ and $-$ singularities form alternating columns. The $-$ singularities lie in North-South striped regions that also contain horizontal and vertical orientations; the $+$ singularities lie in North-South stripes that also contain oblique orientations.

the correlation of retinotopic and orientation shifts arising from planforms derived from axial superpositions of odd roll patterns—which in turn are those appearing in numerical evaluation of a realistic interaction kernel—indicates that this approach to cortical-map formation may indeed be on the right track.

CHAPTER 6

SUMMARY AND CONCLUSION

I model the inter-related cortical feature maps as resulting from a spontaneous symmetry-breaking process in which a uniform, isotropic geniculo-cortical architecture loses stability under the influence of lateral cortical competition and correlation-based weight modification. The cortical-map features jointly comprise a vector derived from various moments of the receptive field profiles. The center-surround lateral architecture influences all cortical-map vectors in the same way, providing a common wavelength for pattern formation in the different features. The geometrical nature of the features — total input weight, center-of-mass, covariance matrix — mean that departures from uniformity in the lower moments influence the subsequent formation of patterns in the higher moments. Conversely, smooth nonlinear constraints on the total synaptic weight projecting from geniculate loci determine additional influences of each feature on the others. The entire feature-development dynamics may be captured, to first order, in a linear integro-differential equation that possesses the symmetries of the Euclidean planar motions under a novel group action. The analysis of these symmetries leads to the identification of certain patterns of interaction between the features, and the prediction of e.g. the correlation of orientation preference with retinotopic shear.

By representing the cortical-map features as moments of the receptive fields I obtain in a completely natural way a derivation of a *vector model* for map development. This vector model is in the same family as the XY and Ising models familiar from the physics of magnetic spin lattices. In particular for the orientation map there is a direct connection to the XY model with a mixed ferro-antiferromagnetic Hamiltonian. Dynamical Monte Carlo techniques for simulating the finite temperature Gibbs ensemble of such a system connects these models to statistical measures of disorder in the architecture of visual cortex.

6.1 Predictions

Section 3.3 gives the prediction, based on the feedforward Hebbian model of orientation-map development and the simple geometrical model of receptive fields, that within a hypercolumn the direction of local stretching in the retinotopic map should be correlated with the direction of orientation preference. Symmetry forces the coupling of orientation and retinotopy patterns found in the same isotopic component of the cortical-map space. Moreover, in planforms that reproduce appropriate patterns of orientation singularities I find significant correlation between local variations in magnification and the orientation preference map that could be tested with data such as that reported by Das and Gilbert [18].

6.2 Discussion

6.2.1 Noise in Cortical Maps

Matching Monte Carlo simulations of the XY model with data from Maldonado and Gray [49], I find that the orientation map lies on the threshold of an order-disorder transition. The degree of disorder of a given cortical-map feature could reflect its functional significance. For example, although rats possess orientation-tuned cells in visual cortex, orientation is not topographically organized (and the rat is not as highly visual an animal as a cat or primate). But whatever biological mechanism tunes the degree of disorder in a cortical feature-map remains unknown.

6.2.2 Alternative Models for Cortical Feature-Map Development

I have worked throughout from the simplifying assumption that response properties of cortical neurons are shaped by the architecture of feedforward geniculo-cortical connections, while the lateral connections within the cortex that provide the basis for the symmetry-breaking pattern formation are themselves isotropic. One entirely different approach to understanding cortical-map formation begins from a uniform feedforward architecture and studies the formation of receptive field properties via

anisotropies in the lateral connections [67]. Experiments by Fitzpatrick and Bosking, and also Blasdel, have shown long-range anisotropic connections in V1 in ferrets and monkeys respectively. These connections run for several hypercolumns in distance and connect patches of cells preferring similar orientations. Moreover the connections run along a direction in the cortex which when translated under the inverse retino-cortical map to visual field coordinates lies parallel to the common preferred orientation of the connected iso-orientation patches. Using a one-dimensional model of this kind, for example, Ernst *et al* were able to obtain the clustering of receptive-field properties observed by Das and Gilbert [23]. One approach to understanding the development of these anisotropic connections would be to study symmetry breaking from an initially isotropic lateral architecture, which should be possible with the tools developed here for pattern formation in the cortical-map vectors.

Another major question not addressed here is the role of feedback in the development both of cortical response properties and the pattern formation process for cortical maps. V1 receives massive feedback from higher visual areas whose anatomical organization and functional significance is not yet well understood. And V1 sends a massive feedback to the LGN – four times the number of fibers the LGN receives from the retina – the role of which is again poorly understood. Murphy *et al* have found that feedback from V1 to the LGN clusters in elongated regions the orientation of which falls with probability better than chance within $\pm\pi/8$ of either the orientation preferred by the cortical cell or that orthogonal to it [58], leading to the possibility that more complicated mechanisms will be necessary to understand realistic cortical-map development.

Alternative models for cortical-map development would still possess Euclidean symmetry, with the usual rotation action for retinotopy and a double rotation action for orientation. The coupling of the isotropic orientation and retinotopy components forced by symmetry will persist even if there is no feedforward determination of orientation tuning. Hence the tools developed here, the isotropic decomposition and symmetry-adapted basis for the space of cortical maps, will apply to models with different developmental mechanisms.

6.2.3 Ocular Dominance and the Orientation Map

Ocular dominance stripes appear result from another pattern-formation process on the same length scale as the orientation map modeled here. Hence one would expect a symmetry analysis to provide an explanation of the appearance of ocular dominance stripes and their coupling to the orientation map. It is well established that the centers of pinwheel orientation singularities have a tendency to be located near the centers of ocular dominance regions (see Figure 6.1).

A binocular model for cortical maps can possess a new symmetry beyond those in the monocular model: ι , the exchange operation between the eyes. The action of the exchange will lead to a tensor product of the irreducible representations in the monocular case with \mathbb{Z}_2 . This new space, twice as large, will split into odd and even components according to whether the exchange acts as ± 1 . Each quantity in the monocular model leads to two in the binocular model: one for the mean and one for the difference. Retinotopy gives mean retinotopy between the two eyes (even under ι) and retinotopic disparity (odd under ι). Orientation gives mean orientation preference (even) and orientation disparity (odd). Orientation disparity has not been commonly investigated in the biological literature; the odd quantities can only be meaningfully measured in cells strongly driven by both eyes.

The ι -even and ι -odd quantities derived from the net input mass are the total input mass $m_1(x) + m_2(x)$ and the difference $-1 \leq \frac{m_1(x) - m_2(x)}{m_1(x) + m_2(x)} \leq 1$, which is the ocular dominance variable. Whereas the ι -even quantities such as mean orientation and retinotopy occupy one set of irreducible representations, the ι -odd quantities — including O.D. — will occupy inequivalent irreducible representations. *Therefore in a single-bifurcation pattern-formation model, O.D. cannot couple to the mean orientation preference.* However, it is likely that the coupling between O.D. and orientation may be understood in terms of a secondary bifurcation which further breaks the lattice symmetry (see Figure 6.2). I leave a rigorous treatment of secondary bifurcation scenarios, as well as a full nonlinear stability analysis of branching planforms, to future work.

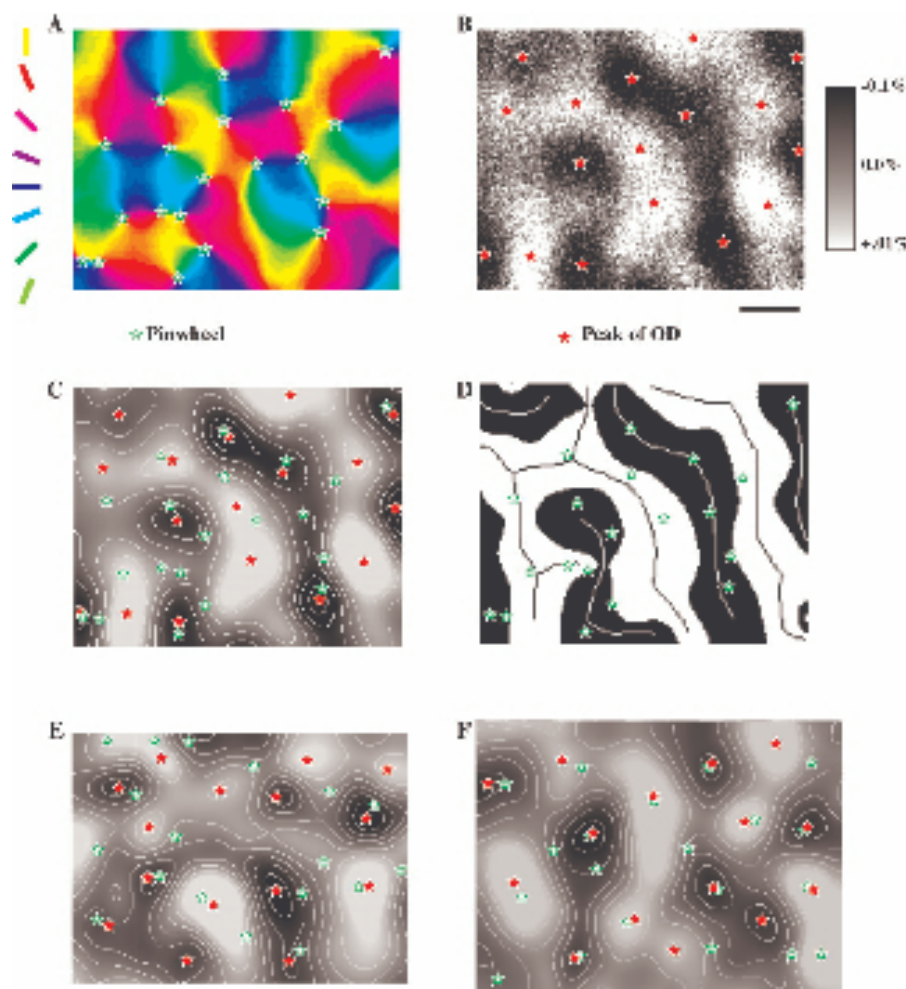


Figure 6.1: Correlation of ocular dominance and orientation maps. A: Orientation preference map obtained by optical imaging. Orientation singularities marked with green stars. B: Ocular dominance map. Extrema of the OD map marked with red stars. C: OD map with both markers superimposed, illustrating better-than-chance coordination of singularities with OD extrema. D: Stick-figure spines of OD regions with orientation singularity markers superimposed. There is a strong correlation of orientation singularities with the centers of OD regions. E,F: Same format as C, data from different animals. [17]

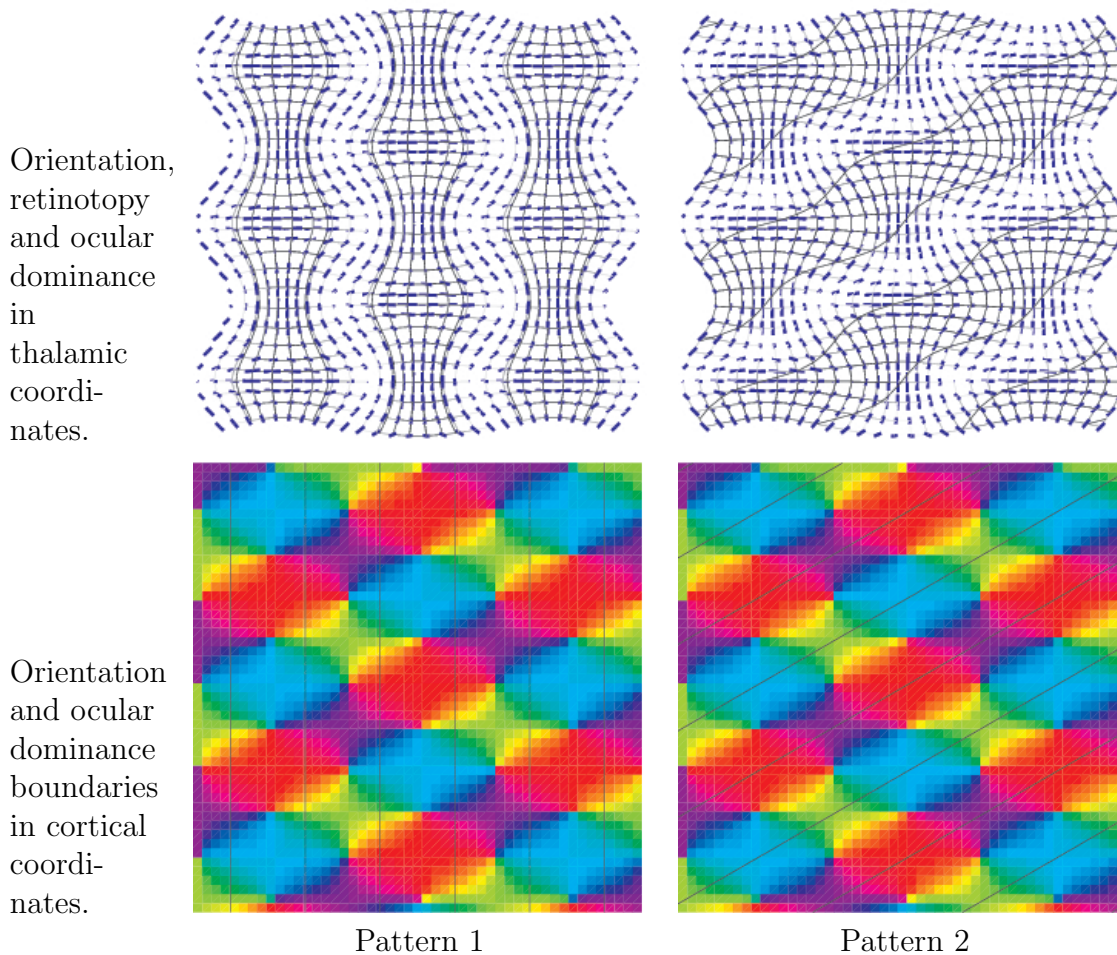


Figure 6.2: Ocular dominance and orientation patterns. Secondary bifurcations from a monocular steady-state pattern of orientation singularities to a binocular state with lower symmetry provides a possible mechanism for coupling orientation and ocular dominance columns. This monocular orientation pattern, from the Odd Rectangles planform on the hexagonal cortical lattice is assumed to be identical for both eyes (see section 5.5). It has the symmetry group $\Sigma = \mathbf{D}_2(\kappa, \xi^3) \times \mathbb{Z}_2(\iota)$. The branching of a nonuniform ocular-dominance pattern results in a binocular pattern with the symmetry of a subgroup of Σ .

Left: Orientation and ocular-dominance pattern with the symmetry group $\mathbf{D}_2(\kappa, \xi^3\iota)$.

Right: Orientation and ocular-dominance pattern with the symmetry group $\mathbb{Z}_2(\xi^3\iota)$.

APPENDIX A: QUADRATIC FORMS

The covariance matrices that characterize the feed-forward receptive fields in the synaptic model, and other matrix quantities arising in the reduction to the feature model, have geometric properties which are captured by the geometry of quadratic forms. Therefore it will be useful to review their properties and establish some notation.

A.1 Degenerate Quadratic Forms

Given a pair of vectors u, v , their *outer product* uv^{tr} is the matrix $(uv^{\text{tr}})_{ij} = u_i v_j$.¹

The outer product of a planar vector $u = \begin{pmatrix} u_1 \\ u_2 \end{pmatrix} = |u| \begin{pmatrix} \cos \theta \\ \sin \theta \end{pmatrix}$ with itself is thus the symmetric matrix

$$uu^{\text{tr}} = \begin{pmatrix} u_1^2 & u_1 u_2 \\ u_1 u_2 & u_2^2 \end{pmatrix} \quad (\text{A.1})$$

$$= \frac{1}{2} \begin{pmatrix} u_1^2 + u_2^2 & \\ & u_1^2 + u_2^2 \end{pmatrix} + \frac{|u|^2}{2} \begin{pmatrix} \frac{u_1^2 - u_2^2}{|u|^2} & \frac{2u_1 u_2}{|u|^2} \\ \frac{2u_1 u_2}{|u|^2} & -\frac{(u_1^2 - u_2^2)}{|u|^2} \end{pmatrix} \quad (\text{A.2})$$

$$= \frac{|u|^2}{2} \left\{ I_2 + \begin{pmatrix} \cos^2 \theta - \sin^2 \theta & 2 \cos \theta \sin \theta \\ 2 \cos \theta \sin \theta & -(\cos^2 \theta - \sin^2 \theta) \end{pmatrix} \right\} \quad (\text{A.3})$$

$$= \frac{|u|^2}{2} \{ I_2 + \Phi_2(\theta) \}, \quad (\text{A.4})$$

where I define

$$\Phi_2(\theta) := \begin{pmatrix} \cos 2\theta & \sin 2\theta \\ \sin 2\theta & -\cos 2\theta \end{pmatrix}. \quad (\text{A.5})$$

¹I denote the *transpose* of a matrix or vector by the ^{tr} superscript.

I have split uu^{tr} into a multiple of the identity and a traceless part; any traceless 2x2 symmetric matrix A can be written $(\det A)\Phi_2(\theta)$ for some θ . In this case $\theta = \arctan(u_2/u_1)$, which is the angle in the plane made by the vector u (up to $\pm\pi$). The quadratic form uu^{tr} is *degenerate* because the matrix is singular.

A.2 Nondegenerate Quadratic Forms

Suppose $A = \begin{pmatrix} a & b \\ b & c \end{pmatrix}$ is a covariance matrix with $a > c > 0$ and $\det A \geq 0$. Then the ellipse given by $u^{\text{tr}}Au = r^2$ has its major axis oriented along the direction

$$\tan 2\phi = \frac{2b}{a - c}$$

and its minor axis along $\phi + \frac{\pi}{2}$; its area is proportional to the product of the eigenvalues of A :

$$\text{area} = \pi r^2 \lambda_1 \lambda_2 = \pi r^2 \det A;$$

and its eccentricity is given by

$$e = \sqrt{1 - \left(\frac{\lambda_2}{\lambda_1}\right)}.$$

These standard results may be obtained these by decomposing A into a product of two rotations and an anisotropic expansion. Writing α^2 for the ratio of the larger

eigenvalue to the smaller, $\alpha := \sqrt{\lambda_1/\lambda_2}$, gives:

$$A = (\det A)^{\frac{1}{2}} \text{Rot}_\phi \Lambda \text{Rot}_{-\phi} \quad (\text{A.6})$$

$$= \sqrt{\lambda_1 \lambda_2} \begin{pmatrix} \cos \phi & -\sin \phi \\ \sin \phi & \cos \phi \end{pmatrix} \begin{pmatrix} \alpha & \\ & \frac{1}{\alpha} \end{pmatrix} \begin{pmatrix} \cos \phi & \sin \phi \\ -\sin \phi & \cos \phi \end{pmatrix} \quad (\text{A.7})$$

$$= \sqrt{\lambda_1 \lambda_2} \begin{pmatrix} \alpha \cos^2 \phi + \frac{1}{\alpha} \sin^2 \phi & \left(\alpha - \frac{1}{\alpha}\right) \sin \phi \cos \phi \\ \left(\alpha - \frac{1}{\alpha}\right) \sin \phi \cos \phi & \frac{1}{\alpha} \cos^2 \phi + \alpha \sin^2 \phi \end{pmatrix} \quad (\text{A.8})$$

$$= \sqrt{\lambda_1 \lambda_2} \left(\alpha I_2 + \left(\alpha - \frac{1}{\alpha}\right) \begin{pmatrix} -\sin^2 \phi & \sin \phi \cos \phi \\ \sin \phi \cos \phi & -\cos^2 \phi \end{pmatrix} \right) \quad (\text{A.9})$$

$$= \frac{\sqrt{\lambda_1 \lambda_2}}{2} \left(\left(\alpha + \frac{1}{\alpha}\right) I_2 + \left(\alpha - \frac{1}{\alpha}\right) \Phi_2(\phi) \right) \quad (\text{A.10})$$

where Φ_2 is given by equation A.5. I must now cast α in terms of $\det A$ and $\text{Tr} A$.

The eigenvalues are given by

$$\lambda_{1,2} = \frac{1}{2} \left\{ \text{Tr} A \pm \sqrt{(\text{Tr} A)^2 - 4 \det A} \right\},$$

from which

$$\alpha = \sqrt{\frac{\lambda_1}{\lambda_2}} = \frac{\text{Tr} A + \sqrt{(\text{Tr} A)^2 - 4 \det A}}{2\sqrt{\det A}}$$

$$\frac{1}{\alpha} = \frac{\text{Tr} A - \sqrt{(\text{Tr} A)^2 - 4 \det A}}{2\sqrt{\det A}}.$$

Hence

$$\alpha + \frac{1}{\alpha} = \frac{\text{Tr} A}{\sqrt{\det A}} \quad (\text{A.11})$$

$$\alpha - \frac{1}{\alpha} = \frac{\sqrt{(\text{Tr} A)^2 - 4 \det A}}{\sqrt{\det A}}. \quad (\text{A.12})$$

I have decomposed A into trace and traceless parts given by:

$$A = \frac{\sqrt{\lambda_1 \lambda_2}}{2} \left(\left(\alpha + \frac{1}{\alpha} \right) I_2 + \left(\alpha - \frac{1}{\alpha} \right) \Phi_2(\phi) \right) \quad (\text{A.13})$$

$$= \frac{\sqrt{\det A}}{2} \left(\frac{\text{Tr} A}{\sqrt{\det A}} I_2 + \frac{\sqrt{(\text{Tr} A)^2 - 4 \det A}}{\sqrt{\det A}} \Phi_2(\phi) \right) \quad (\text{A.14})$$

$$= \frac{\text{Tr} A}{2} I_2 + \frac{\sqrt{(\text{Tr} A)^2 - 4 \det A}}{2} \Phi_2(\phi) \quad (\text{A.15})$$

$$= \frac{a+c}{2} I_2 + \frac{\sqrt{(a-c)^2 + 4b^2}}{2} \Phi_2(\phi) \quad (\text{A.16})$$

$$= \frac{a+c}{2} I_2 + \sqrt{\left(\frac{a-c}{2} \right)^2 + b^2} \begin{pmatrix} \frac{(a-c)/2}{\sqrt{(a-c)^2/4+b^2}} & \frac{b}{\sqrt{(a-c)^2/4+b^2}} \\ \frac{b}{\sqrt{(a-c)^2/4+b^2}} & -\frac{(a-c)/2}{\sqrt{(a-c)^2/4+b^2}} \end{pmatrix} \quad (\text{A.17})$$

$$= \frac{a+c}{2} I_2 + \begin{pmatrix} \frac{a-c}{2} & b \\ b & -\frac{a-c}{2} \end{pmatrix}; \quad (\text{A.18})$$

I can now identify the angle ϕ in the original decomposition as satisfying

$$\cos 2\phi = \frac{a-c}{\sqrt{(a-c)^2 + (2b)^2}} \quad (\text{A.19})$$

$$\sin 2\phi = \frac{2b}{\sqrt{(a-c)^2 + (2b)^2}}. \quad (\text{A.20})$$

This is the angle in the direction of the major axis in the plane of the ellipses associated with the quadratic form A . As a linear transformation, A takes the unit ball in \mathbf{R}^2 to an ellipse with area $2\pi \det A$. And the eccentricity is given by the deviation from unity of the ratio of the major and minor axes of the ellipse:

$$e = \sqrt{1 - \left(\frac{\lambda_2}{\lambda_1} \right)} = \sqrt{1 - \left(\frac{1}{\alpha} \right)^4}.$$

In the main text (Chapter 3) the quantity $q[A] = \sqrt{\text{Tr}^2 A - 4 \det A}$ becomes the magnitude of the orientation-tuning vector χ . For A a multiple of the identity matrix, $\text{Tr}^2 A = 4 \det A$ so $q[A] = 0$. As $\det A \rightarrow 0$, $q[A] \rightarrow \text{Tr} A$. Hence $0 \leq q[A] \leq \text{Tr} A$. The

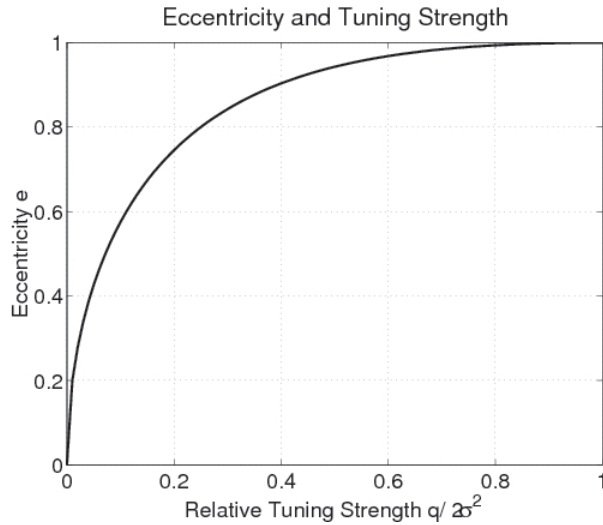


Figure A.3: Eccentricity and magnitude of orientation preference. The *relative* orientation-tuning strength refers to the ratio $q[Q^{-1}]/\text{Tr}Q^{-1}$, which lies between 0 and 1.

eccentricity e may be related to the relative orientation-tuning strength, $q[A]/\text{Tr}A$, as shown in figure A.3. It may also be represented as the ratio between the geometric and arithmetic means of the pair $(q[A], \text{Tr}A)$:

$$e = \frac{2\sqrt{\text{Tr}A/q[A]}}{1 + \text{Tr}A/q[A]} = \frac{\sqrt{q[A]\text{Tr}A}}{(q[A] + \text{Tr}A)/2}.$$

In considering the geometry of receptive fields we deal both with the covariance matrix Q and its inverse Q^{-1} , so we need to know how the two relate as quadratic forms. Let us rewrite A in terms of its trace, its orientation $\phi[A]$ and its “orientation magnitude” $q[A]$:

$$A = \frac{\text{Tr}A}{2}I_2 + \frac{q[A]}{2}\Phi_2(\phi[A])$$

Since $\Phi_2(\phi)^2 = I_2$ we see at once that

$$\begin{aligned} \left(\frac{\text{Tr}A}{2}I_2 + \frac{q[A]}{2}\Phi_2(\phi[A])\right) \left(\frac{\text{Tr}A}{2}I_2 - \frac{q[A]}{2}\Phi_2(\phi[A])\right) &= \frac{1}{4} \left((\text{Tr}A)^2 - q[A]^2\right) I_2 \\ &= \det A I_2, \end{aligned}$$

whence

$$A^{-1} = \frac{1}{\det A} \left(\frac{\text{Tr}A}{2} I_2 - \frac{q[A]}{2} \Phi_2(\phi[A]) \right).$$

Because $A^{-1} = \frac{1}{\det A} \begin{pmatrix} c & -b \\ -b & a \end{pmatrix}$, $\text{Tr}A^{-1} = \frac{\text{Tr}A}{\det A}$. Also, $\Phi_2(\phi - \frac{\pi}{2}) = -\Phi_2(\phi)$, so we can write

$$A^{-1} = \frac{\text{Tr}A^{-1}}{2} I_2 + \frac{q[A^{-1}]}{2} \Phi_2(\phi[A'])$$

where

$$\begin{aligned} \phi[A^{-1}] &= \phi[A] + \frac{\pi}{2} \\ q[A^{-1}] &= \frac{q[A]}{\det A}. \end{aligned}$$

Hence the level curve formed by $u^{\text{tr}} A^{-1} u = r^2$ forms an ellipse with major axis oriented orthogonal to that formed by A . Finally, because the eccentricity depends only on the ratio $(\text{Tr}A)^2 / \det A$ and because

$$\frac{(\text{Tr}A)^2}{\det A} = \frac{(\text{Tr}A^{-1})^2}{\det A^{-1}},$$

the ellipses formed by A and A^{-1} have the same eccentricity.

A.3 Measuring Anisotropy in a Map from $\mathbb{R}^2 \rightarrow \mathbb{R}^2$

The retinocortical map, which may be visualized using metabolic markers such as cytochrome oxidase immunoreactive stains or deoxyglucose autoradiograph techniques (see Figure 1.4), may be thought of as a map between open subsets of \mathbb{R}^2 . On the scale of a two- or three-mm-square region of cortical surface, the coarse topography has little enough curvature that it may be taken to be a linear map of retinotopic coordinates. On this scale we may approximate the cortical sheet as a plane with coordinates

$$\underline{x} := [x_1, x_2]^{\text{tr}} \in \mathcal{X}.$$

Similarly a small region of the LGN may be represented by its retinotopic coordinates

$$\underline{r} := [r_1, r_2]^{\text{tr}} \in \mathcal{R}.$$

The retinotopic map of the cortex, $\underline{R} : \mathcal{X} \rightarrow \mathcal{R}$ is smooth and 1 : 1 on this scale and so we can impose coordinate systems on \mathcal{X} and \mathcal{R} such that the Jacobian

$$\underline{J}(\underline{x}) := \nabla_{\underline{x}} \underline{R}(\underline{x}) = \begin{pmatrix} \frac{\partial R_1}{\partial x_1} & \frac{\partial R_1}{\partial x_2} \\ \frac{\partial R_2}{\partial x_1} & \frac{\partial R_2}{\partial x_2} \end{pmatrix}$$

has positive determinant everywhere. From \underline{J} I obtain the retino-cortical *magnification factor*

$$\mu(\underline{x}) := \sqrt{\det \underline{J}(\underline{x})}$$

and the *modulus of anisotropy*,²

$$\eta(\underline{x}) := \frac{\|\underline{J}\|_{\text{f}}^2}{2\mu^2} - 1.$$

For a map which is purely a rotation and a uniform expansion or contraction, i.e.

$$\begin{aligned} \underline{R}(\underline{x}) &= \underline{R}_0 + \underline{J}(\underline{x}) \cdot (\underline{x} - \underline{x}_0) \\ \underline{J} &= \mu \begin{pmatrix} \cos \theta & -\sin \theta \\ \sin \theta & \cos \theta \end{pmatrix} = \text{constant}, \end{aligned}$$

we have no anisotropy because $\|\underline{J}\|_{\text{f}}^2 = 2\mu^2$ and $\eta = 0$. On the other hand η will be positive if the map is sheared, for example, if

$$\underline{J} = \begin{pmatrix} 1 + \epsilon & 0 \\ 0 & 1 \end{pmatrix}$$

²The *Frobenius norm* of \underline{J} is $\|\underline{J}\|_{\text{f}} = \sqrt{\sum_{j,k=1}^2 J_{jk}^2}$.

then we obtain $\eta = \epsilon^2/2 + O(\epsilon^3)$. Shearing can also occur by adding an off-diagonal term: for

$$\underline{\underline{J}} = \begin{pmatrix} 1 & \epsilon \\ 0 & 1 \end{pmatrix}$$

we have $\eta = \epsilon^2/2$. $\underline{\underline{J}}$ takes the unit ball in \mathcal{X} to an ellipse in \mathcal{R} . The ratio of the principal axes of this ellipse gives the *shear* of the retinocortical map at \underline{x} . The principal axes are the maximum and minimum values taken by $\|\underline{\underline{J}}\underline{x}\|/\|\underline{x}\|$. Since $\|\underline{\underline{J}}\underline{x}\|^2 = \underline{x}^{\text{tr}} \underline{\underline{J}}^{\text{tr}} \underline{\underline{J}} \underline{x}$ we can find these values as the roots of the eigenvalues of $\underline{\underline{M}} := \underline{\underline{J}}^{\text{tr}} \underline{\underline{J}}$, which is positive-definite symmetric matrix. These eigenvalues are

$$\lambda_{\pm} = \frac{1}{2} \left(\text{Tr} \underline{\underline{M}} \pm \sqrt{(\text{Tr} \underline{\underline{M}})^2 - 4 \det \underline{\underline{M}}} \right)$$

so their root-ratio is

$$\sqrt{\frac{\lambda_+}{\lambda_-}} = \left[\frac{(\text{Tr} \underline{\underline{M}} + \sqrt{(\text{Tr} \underline{\underline{M}})^2 - 4 \det \underline{\underline{M}}})^2}{4 \det \underline{\underline{M}}} \right]^{1/2}$$

Since $\text{Tr} \underline{\underline{M}} = \|\underline{\underline{J}}\|_{\text{f}}^2$ and $\det \underline{\underline{M}} = (\det \underline{\underline{J}})^2 = \mu^4$, the shear is given by

$$\sqrt{\frac{\lambda_+}{\lambda_-}} = \left[\frac{\|\underline{\underline{J}}\|_{\text{f}}^2}{2\mu^2} + \sqrt{\left\{ \frac{\|\underline{\underline{J}}\|_{\text{f}}^2}{2\mu^2} - 1 \right\}} \right]^{1/2} = \sqrt{1 + \eta + \sqrt{\eta}}$$

The eigenvectors of $\underline{\underline{M}}$ are

$$\begin{aligned} \underline{x}_+ &= \begin{pmatrix} 2M_{12} \\ M_{22} - M_{11} + \sqrt{(M_{22} - M_{11})^2 + 4M_{12}^2} \end{pmatrix} \\ \underline{x}_- &= \begin{pmatrix} M_{11} - M_{22} - \sqrt{(M_{11} - M_{22})^2 + 4M_{12}^2} \\ 2M_{12} \end{pmatrix} \end{aligned}$$

The direction in the \mathcal{X} -plane in which the rate of change of retinotopic position is greatest—the shear direction in \mathcal{X} —is given up to $\pm\pi$ by the direction of \underline{x}_+ . The

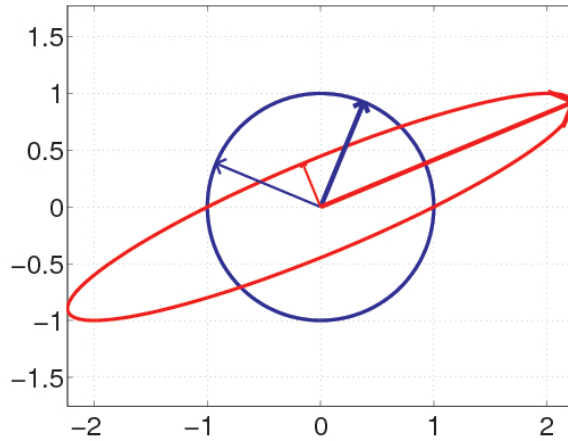


Figure A.4: Shear from the Singular Value Decomposition. The matrix $\underline{\underline{J}} = \begin{pmatrix} 1 & 2 \\ 0 & 1 \end{pmatrix}$ may be decomposed as $\underline{\underline{J}} \left(\begin{bmatrix} | \\ \underline{v}_1 \\ | \end{bmatrix} \begin{bmatrix} | \\ \underline{v}_2 \\ | \end{bmatrix} \right) = \left(\begin{bmatrix} | \\ \underline{u}_1 \\ | \end{bmatrix} \begin{bmatrix} | \\ \underline{u}_2 \\ | \end{bmatrix} \right) \begin{pmatrix} \sigma_1 & \\ & \sigma_2 \end{pmatrix}$, where $\underline{u}_i, \underline{v}_i$ are unit vectors. Heavy arrows indicate \underline{v}_1 (blue) and \underline{u}_1 (red), light arrows indicate \underline{v}_2 (blue) and \underline{u}_2 (red).

direction in the \mathcal{R} -plane corresponding to this maximum rate of displacement—the shear direction in \mathcal{R} —is given up to $\pm\pi$ by the direction of $\underline{\underline{J}}\underline{x}_+$. The shear is derived from the singular value decomposition³ of $\underline{\underline{J}}$ as follows: There exist orthonormal matrices $\underline{\underline{V}}$ and $\underline{\underline{U}}$ such that

$$\underline{\underline{JV}} = \underline{\underline{U}} \begin{pmatrix} \sigma_1 & \\ & \sigma_2 \end{pmatrix}.$$

The singular values σ_i are the major and minor semiaxes of the ellipse in \mathcal{R} ; the columns of $\underline{\underline{V}}$ are parallel to the vectors \underline{x}_\pm , and the columns of $\underline{\underline{U}}$ are parallel to the vectors $\underline{\underline{J}}\underline{x}_\pm$. For an example, see Figure A.4.

On a sufficiently coarse scale, the curvature of the cortical surface and of the complex logarithmic map invalidate the affine linear description of the mapping.

³See Trefethen and Bau, [76].

APPENDIX B: GUASSIAN IDENTITIES

The following identities are included for reference. They are used at various points throughout the text. Let $u = \begin{pmatrix} u_1 \\ u_2 \end{pmatrix}$ and $v = \begin{pmatrix} v_1 \\ v_2 \end{pmatrix}$ denote vectors in the plane, and let σ be a positive real number. Define

$$g(u, \sigma) := \frac{1}{2\pi\sigma^2} \exp\left(-\frac{|u|^2}{2\sigma^2}\right)$$

The following identities follow:

$$\int_{\mathbb{R}^2} g(u, \sigma) du = 1 \tag{B.21}$$

$$\int_{\mathbb{R}^2} ug(u - v, \sigma) du = v \tag{B.22}$$

$$\int_{\mathbb{R}^2} |u|^2 g(u, \sigma) du = \sigma^2 \tag{B.23}$$

$$\int_{\mathbb{R}^2} g(u - v, \sigma_u)g(v, \sigma_v) dv = g\left(u, \sqrt{\sigma_u^2 + \sigma_v^2}\right) \tag{B.24}$$

$$g(u, \sigma_1)g(u, \sigma_2) = \frac{g\left(u, \sigma_1\sigma_2/\sqrt{\sigma_1^2 + \sigma_2^2}\right)}{2\pi(\sigma_1^2 + \sigma_2^2)} \tag{B.25}$$

$$g(u - v, \sigma)g(u' - v, \sigma) = g(u - u', 2\sigma)g\left(\frac{u + u'}{2} - v, \frac{\sigma}{2}\right) \tag{B.26}$$

Let two quadratic forms (see Appendix 6.2.3) P and Q be given by

$$\begin{aligned} P &= \frac{\text{Tr}P}{2}I_2 + \frac{q[P]}{2}\Phi_2(\phi[P]) \\ Q &= \frac{\text{Tr}Q}{2}I_2 + \frac{q[Q]}{2}\Phi_2(\phi[Q]). \end{aligned}$$

In analogy with the notation $g(u, \sigma^2)$ given above, define

$$g(u, Q) = \frac{1}{2\pi\sqrt{\det Q}} \exp\left(-\frac{1}{2}u^{\text{tr}} Q^{-1}u\right) \quad (\text{B.27})$$

Then the convolution of two such Gaussians is again a Gaussian

$$\int_{u \in \mathbb{R}^2} g(u - u', P)g(u', Q) du' = g(u, C) \quad (\text{B.28})$$

where $\text{Tr}C = \text{Tr}P + \text{Tr}Q$. Also, if we write in vector form

$$\begin{aligned} \chi[P] &= q[P] \begin{pmatrix} \cos 2\phi[P] \\ \sin 2\phi[P] \end{pmatrix} \\ \chi[Q] &= q[Q] \begin{pmatrix} \cos 2\phi[Q] \\ \sin 2\phi[Q] \end{pmatrix} \\ \chi[C] &= q[C] \begin{pmatrix} \cos 2\phi[C] \\ \sin 2\phi[C] \end{pmatrix}, \end{aligned}$$

then

$$\chi[C] = \chi[P] + \chi[Q]. \quad (\text{B.29})$$

The effect of a shift in the location of the center by order ϵ is given by the Taylor series:

$$g(u + \epsilon v, \sigma) = g(u, \sigma) \left(1 - \epsilon \frac{v \cdot u}{\sigma^2} + \frac{\epsilon^2}{2\sigma^4} v \cdot \left[\begin{pmatrix} u_1^2 - \sigma^2 & u_1 u_2 \\ u_1 u_2 & u_2^2 - \sigma^2 \end{pmatrix} v \right] + O(\epsilon^3) \right). \quad (\text{B.30})$$

Further Gaussian Identities

Let $g(u, \sigma^2)$ denote a Gaussian in the plane with width σ :

$$g(u, \sigma^2) := \frac{1}{2\pi\sigma^2} \exp\left[-\frac{\|u\|^2}{2\sigma^2}\right].$$

The following are used in section 4.3.

$f(u)$	$\int_{u \in \mathbb{R}^2} f(u)g(u + v, \sigma^2/2) du$
1	1
u_j	$-v_j$
$u_1 u_2$	$v_1 v_2$
u_i^2	$v_i^2 + \sigma^2/2$
$\ u\ ^2$	$\ v\ ^2 + \sigma^2$
u_j^3	$-v_j(v_j^2 + 3\sigma^2/2)$
$u_i^2 u_j, i \neq j$	$-(v_i^2 + \sigma^2/2)v_j$
u_i^4	$v_i^4 + 3\sigma^2 v_i^2 + 3\sigma^4/4$
$u_i^3 u_j, i \neq j$	$v_i v_j (v_i^2 + 3\sigma^2/2)$
$u_1^2 u_2^2$	$v_1^2 v_2^2 + \ v\ ^2 \sigma^2/2 + \sigma^4/4$
$\ u\ ^4$	$\ v\ ^4 + 4\sigma^2 \ v\ ^2 + 2\sigma^4$

Fourier Transform

If $g(u, \sigma^2) = \exp\left[-\frac{u^2}{2\sigma^2}\right] / \sqrt{2\pi\sigma^2}$, $u \in \mathbb{R}$, then the Fourier transform of g is given by:

$$\begin{aligned}\tilde{g}(\omega) &:= \frac{1}{\sqrt{2\pi}} \int_{-\infty}^{\infty} g(u, \sigma^2) e^{i\omega u} du \\ &= \frac{\sigma \exp\left[-\frac{\sigma^2\omega^2}{2}\right]}{\sqrt{2\pi\sigma^2}} \\ &= \frac{1}{\sigma} g(\omega, \sigma^{-2}).\end{aligned}$$

APPENDIX C: STATISTICS FOR ANGULAR VARIABLES

Optical images generated by Blasdel and others necessarily represent orientation-tuned neural activity as population averages. The smoothing algorithms and optical resolution of the apparatus combine between tens and hundreds of cells' responses in each pixel of the orientation-preference map. The vector representation of orientation tuning implicitly assumes the responses of individual units (cells or neighborhoods of cells) to be unimodal functions of angle. That is, the orientation-tuning *vector* may be thought of as a cosinusoid with a phase representing the preferred orientation and an amplitude representing the strength of the preference. In the differential-imaging techniques the orientation-tuning vector has one component representing the magnitude of the signal difference for horizontal *vs.* vertical stimuli while the other represents right- *vs.* left-handed obliques.

Interpreting these images requires an ansatz about the nature of the underlying units. For example, the magnitude of the orientation-tuning vector passes smoothly through zero at the “centers” of the “singularities” in the angle map. One may conjecture that decreased magnitude represents weaker orientation tuning of individual cells on the one hand, or alternatively that they reflect a more widely scattered mixture of cells whose individual tuning strengths are constant.

To grasp quantitatively the trade-off between heterogeneity of the local orientation population *vs.* decrease in individual cell tuning strengths it is useful to analyze rules for summing cosines. Suppose that the locally averaged tuning generating a given pixel in the orientation map were a linear combination of the responses of individual tuning curves, each given as a cosine with a phase and amplitude. The sum of n cosines with arbitrary phases and amplitudes is again a cosine:

$$\sum_k a_k \cos(\theta - \delta_k) = a \cos(\theta - \delta) \tag{C.31}$$

where

$$\begin{aligned} a^2 &= 2 \sum_j \sum_k a_j a_k \cos(\delta_j - \delta_k) - \sum_k a_k^2 \\ a \cos(\delta) &= \sum_k a_k \cos(\delta_k) \\ a \sin(\delta) &= \sum_k a_k \sin(\delta_k) \end{aligned}$$

We may also use a continuum version of this identity when we have a distribution of phases $\rho(\psi)$:

$$\begin{aligned} \int_{\psi=0}^{2\pi} \rho(\psi) \cos(\theta - \psi) d\psi &= a \cos(\theta - \delta) \\ a^2 &= \int_{\psi} \int_{\psi'} \rho(\psi) \rho(\psi') \cos(\psi - \psi') d\psi d\psi' \quad (\text{C.32}) \end{aligned}$$

The mean of the distribution $\rho(\theta)$ is of course what determines δ . When considering the orientation map it is natural to assume that the magnitudes and phases $a(x), \delta(x)$ characterizing the population distribution vary smoothly as functions of position.

As a special case, let us calculate the magnitude of the response a as a function of the variance of a local distribution of phases when the local magnitudes a_k are constant. The local distribution will be a probability density function for an angular (i.e. periodic or pseudoscalar) variable. The question arises which family of distributions is most appropriate for representing such angular data and their moments. The common practice in biology of replacing circular distributions with Gaussians clipped at $\pm\pi$ from the mean is unfortunately rather Procrustean. Several alternatives to this approach exist, including the wrapped Gaussian g_w

$$g_w(\theta; \theta_0, \sigma_w) = \frac{1}{\sigma_w \sqrt{2\pi}} \sum_{k=-\infty}^{\infty} \exp\left(-\frac{(\theta - \theta_0 + 2\pi k)^2}{2\sigma_w^2}\right), 0 < \theta \leq 2\pi \quad (\text{C.33})$$

and the von Mises distribution g_M

$$g_M(\theta; \theta_0, \kappa) = \frac{1}{2\pi I_0(\kappa)} \exp(\kappa \cos(\theta - \theta_0)). \quad (\text{C.34})$$

The normalization factor $I_0(\kappa)$ is the zeroth-order modified Bessel function of the first kind,

$$I_0(\kappa) = \sum_{r=0}^{\infty} \frac{1}{r!^2} \left(\frac{\kappa}{2}\right)^{2r}. \quad (\text{C.35})$$

These two distributions are very similar, becoming identical for very narrow distributions ($\sigma_w \rightarrow 0$, $\kappa \rightarrow \infty$), or very broad ($\sigma_w \gg 2\pi$, $0 \leq \kappa \ll 2\pi$), because $e^{-\frac{1}{2}\sigma_w^2} \approx I_1(\kappa)/I_0(\kappa)$ as $\kappa \rightarrow \infty$ for an appropriate $\sigma_w(\kappa)$. The von Mises distribution arises as the conditional distribution (in angle) of a bivariate normal distribution (centered on the unit circle); it is the unique distribution for a given mean and circular variance that maximizes the entropy $\int_{\theta} g(\theta) \log(g(\theta)) d\theta$.⁴ The wrapped Gaussian distribution arises as a limiting sum of independent identically distributed distributions and as the probability density function of a particle undergoing a symmetric random walk on the circle. Each is easier to use in different contexts and they are close enough numerically to use interchangeably for many purposes.

The norm a of the resultant sum is simple to calculate when the phases obey the von Mises distribution with concentration parameter κ and mean ψ_0 :

$$\begin{aligned} a(\kappa) &= \left(\frac{1}{2\pi I_0(\kappa)} \right)^2 \int_{\psi} \int_{\psi'} \exp(\kappa \cos(\psi - \psi_0)) \exp(\kappa \cos(\psi' - \psi_0)) \cos(\psi - \psi') d\psi d\psi' \\ &= \left(\frac{I_1(\kappa)}{I_0(\kappa)} \right)^2 \end{aligned}$$

$I_1(\kappa)$ is the first-order modified Bessel function of the first kind. In general the p -th order function is given by

$$I_p(\kappa) = \sum_{r=0}^{\infty} \{\Gamma(p+r+1)\Gamma(r+1)\}^{-1} \left(\frac{\kappa}{2}\right)^{2r+p}.$$

⁴Reference: *Statistics of Directional Data*, by Mardia [50]. See section 3.4.9.

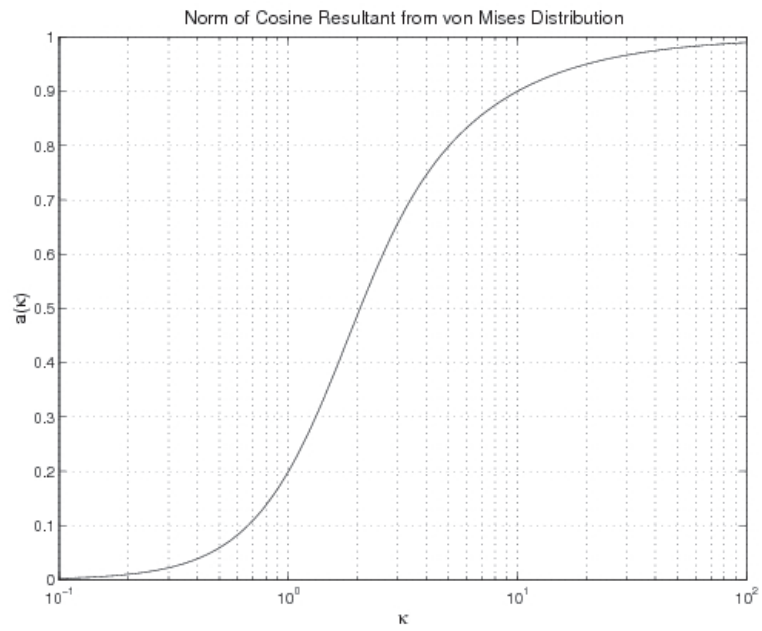


Figure C.5: Resultant sum of von Mises functions. The magnitude of the cosine resulting from a sum of cosines with phases distributed according to the von Mises distribution with concentration parameter κ .

See Figure C.5.

APPENDIX D: EQUIVARIANT BIFURCATION THEORY

D.4 Introduction

Bifurcations from steady states in systems which possess the symmetry of a group provide problems of enduring interest for dynamical systems theory. Typically, symmetries in a dynamical system force degeneracy of the critical eigenvalues at a bifurcation, rendering the standard bifurcation tools such as normal forms and Lyapunov-Schmidt reduction difficult to apply.

Nevertheless, exploration of such systems has yielded fascinating and beautiful results. In the Bénard problem, for example, E_2 invariance allows one to predict D_2 , D_3 , D_4 and D_6 invariant solutions of the Boussinesq equations. [12, 64]. Recently, group-theoretic tools have provided a wealth of techniques for the analysis of equivariant bifurcations. In this Appendix I review developments in equivariant bifurcation theory, including the so-called “symmetry - adapted basis” methods of Fässler - Stiefel, Werner, and Golubitsky - Stewart - Schaeffer [27, 30, 80, 81], and give examples of applications.

D.5 Equivariant Bifurcation Problems

I consider a dynamical system

$$\frac{dx}{dt} = G(x, \mu)$$

wherein $x \in V$ moves in a finite-dimensional vector space, $\mu \in \mathbb{R}$, and $G : V \times \mathbb{R} \Rightarrow V$ is C^∞ . I assume that for any μ , there exists a fixed point $x_0(\mu)$:

$$G(x_0(\mu), \mu) = 0$$

which is invariant under the action of a Lie group Γ .

The system is *equivariant* with respect to a representation ρ of Γ , $\rho : \Gamma \rightarrow \text{GL}(V)$, if for all x , μ , and $\gamma \in \Gamma$,

$$G(\rho_\gamma x, \mu) = \rho_\gamma G(x, \mu).$$

Without loss of generality I will consider only unitary representations. By way of abbreviation I will use γ in place of ρ_γ , when the intended representation is unambiguous.

Differentiating the equivariance condition gives us the immediate consequence: for all γ in Γ ,

$$J\gamma = \gamma J$$

where $J(x, \mu) = \frac{\partial G(x, \mu)}{\partial x}$ is the $n \times n$ Jacobian of G . Because J commutes with the representation, eigenvalues of J will occur in multiplets (as described below) resulting in degenerate bifurcations.

As another immediate consequence of equivariance, we can see that if x is any solution of $G(x, \mu) = 0$ then for any γ , $G(\gamma x, \mu) = 0$. One solution x will give rise to a family of conjugate solutions $\{\gamma x | \gamma \in \Gamma\}$; hence bifurcating solution branches often occur in multiplets as well.

Given any $x \in V$ I define Σ_x to be the subgroup of Γ under which x is preserved:

$$\Sigma_x := \{\sigma \in \Gamma | \sigma x = x\}.$$

A subgroup of Γ arising in this way is known as an *isotropy subgroup*.

With any subgroup Σ of Γ I associate its fixed-point space:

$$\text{Fix}(\Sigma) := \{x \in V | \sigma x = x\}$$

which is a subspace of V . It is a theorem due to Van der Bauwhede (see [30]) that generically, it is in the one-dimensional fixed-point subspaces of isotropy subgroups that one expects to find bifurcations from a Γ -invariant steady-state. This principle is known as *minimal symmetry breakdown*.

D.6 Representation Theory and Isotypic Decomposition

The requirement that a matrix A commute with the matrices ρ_γ representing a group Γ imposes restrictions on the possible form of A . In particular, a basis for V may be found in which all such matrices have a specified block-diagonal form, the blocks corresponding to the decomposition of ρ as a direct sum of irreducible representations θ_i of Γ . Knowledge of this structure allows us to determine which isotropy subgroups may have branching solutions at a bifurcation point.

A representation ρ of Γ acts *irreducibly* on the space V if V admits no nontrivial proper invariant subspaces under Γ . Each irreducible representation ρ_i of Γ possesses a distinct *character*

$$\chi_i(\gamma) := \text{trace}(\rho_i(\gamma))$$

which is orthogonal to the characters of nonisomorphic representations in the sense that

$$\langle \chi_i | \chi_j \rangle := \int_{\Gamma} \chi_i(\gamma^{-1}) \chi_j(\gamma) d\gamma = \delta_{ij}.$$

When Γ is finite, $\int_{\Gamma} d\gamma$ is to be understood as $\frac{1}{|\Gamma|} \sum_{\gamma \in \Gamma}$. Because the character is constant within conjugacy classes of Γ and distinct between them, the number of different characters and hence the number of nonisomorphic irreducible representations just equals the number of conjugacy classes of elements of Γ (provided this number is finite).

The set of all matrices

$$\mathcal{C}(\theta) := \{ \mathcal{A} \in \mathcal{M} \mid \theta_\gamma \mathcal{A} = \mathcal{A} \theta_\gamma, \forall \gamma \in - \}$$

is an associative algebra over \mathbb{R} , isomorphic to either \mathbb{R} , \mathbb{C} , or \mathbb{H} , when θ is an irreducible representation of Γ . An irreducible representation is of *real*, *complex*, or *quaternionic* type, accordingly. In applications irreducible representations of quaternionic type do not commonly arise.

If V is a finite-dimensional space, then any representation $\rho : \Gamma \rightarrow \text{GL}(V)$ may be

decomposed by virtue of the orthogonality relations:

$$\rho = c_1\rho_1 \oplus c_2\rho_2 \oplus \dots \oplus c_m\rho_m$$

where $c_k = \frac{\langle \rho_k | \rho \rangle}{d_k}$. Here c_k represents the multiplicity with which ρ_k appears in ρ ; $d_k = 2$ if ρ_k is a real representation of complex type, otherwise $d_k = 1$. For example, the regular representation of a finite group of order $|\Gamma|$ with m distinct irreducible representations, $\rho_{\text{reg}} : \Gamma \rightarrow \text{GL}(\mathbb{R}^{|\Gamma|})$, decomposes as

$$\rho_{\text{reg}} = n_1\rho_1 \oplus n_2\rho_2 \oplus \dots \oplus n_m\rho_m$$

where n_j is the dimension of the j^{th} representation of Γ . Each irreducible representation appears with multiplicity c_j equal to its dimension n_j , whence

$$\dim(V) = |\Gamma| = \sum_{j=1}^m n_j^2.$$

Corresponding to the decomposition of ρ there is a canonical decomposition of V ,

$$V = V_1 \oplus V_2 \oplus \dots \oplus V_m$$

with each V_k invariant under ρ , and $\dim(V_k) = c_k n_k$. The linear transformation of V which projects onto the subspace V_k is given by

$$P^{(k)} = \frac{n_k}{|\Gamma|} \int_{\Gamma} \chi_k(\gamma^{-1}) \rho_k(\gamma) d\gamma.$$

The V_k can be further decomposed, although no longer in a unique way, to

$$V_k = \bigoplus_{j=1}^{c_k} V_{k,j}$$

where $n_k = \dim(\rho_k) = \dim(V_{k,j})$ for fixed k , and the basis vectors for each $V_{k,j}$ are especially chosen to reflect the symmetry of the problem.

Beginning with a basis for V we may find basis vectors $\vec{b}_{k,j,i}, i = 1, \dots, n_k$ for $V_{k,j}$ as follows: One vector, $\vec{b}_{k,j,1}$ for each $V_{k,j}, j = 1, \dots, c_j$ is chosen as an independent column from the rank- c_k matrix

$$P_1^{(k)} = n_k \int_{\Gamma} d_{11}^{(k)}(\gamma^{-1}) \rho_k(\gamma) d\gamma$$

where $d_{\mu\nu}^{(k)}$ is the (μ, ν) -element, in the original basis, of the representation matrix for ρ_k .

The remaining basis vectors $\vec{b}_{k,j,i}, i = 2, \dots, n_k$ are determined as the images of $\vec{b}_{k,j,1}$ under the matrices

$$P_l^{(k)} = n_k \int_{\Gamma} d_{1l}^{(k)}(\gamma^{-1}) \rho_k(\gamma) d\gamma.$$

The basis $\{\vec{b}_{k,j,i}\}$ selected in this way has the property that ρ_k permutes the i^{th} basis vectors of each $V_{k,j}, j = 1, \dots, c_k$, in the same way; such a basis is called *symmetry adapted*, and greatly facilitates the computation of eigenvalues and bifurcation behavior of Γ -symmetric matrices⁵.

Written in the symmetry-adapted basis, every matrix in $\mathcal{C}(\rho)$ must be block-diagonal, with the following form:

- for each irreducible representation ρ_k of real type, appearing in ρ with multiplicity $c_k > 0$ and of dimension n_k , there are n_k identical $c_k \times c_k$ blocks A_k .
- for each irreducible representation ρ_k of complex type, appearing in ρ with multiplicity $c_k > 0$, and of (real) dimension n_k , there are $n_k/2$ identical $(2c_k) \times (2c_k)$ blocks A_k composed of

$$A_k = \begin{pmatrix} a_k & -b_k \\ b_k & a_k \end{pmatrix}$$

⁵The algorithm given is due to Fässler and Stiefel, see [27].

where a_k and b_k are $c_k \times c_k$ real matrices.

Each $V_{k,j}$ is invariant under A and the blocks A_k each act on the different $V_{k,j}$, $j = 1, \dots, c_k$, in the same way.

The eigenvalues of matrices in $\mathcal{C}(\rho)$ may be classified according to the isotypic subspaces V_k in which their eigenspaces lie. An eigenvalue λ of an A_i block will occur $\frac{n_i}{d_i}$ times in A ; if these are the only occurrences of λ it is called a Γ -simple eigenvalue of A . Just as the eigenvalues of arbitrary matrices are generically simple, the eigenvalues of arbitrary Γ -symmetric matrices are generically Γ -simple.

If, as μ crosses a critical value μ_0 , a Γ -simple eigenvalue λ of J of type ρ_k passes with nonzero speed through $\lambda = 0$, then $\ker(J(x_0, \mu_0))$ will be n_k -dimensional. Each A_k will have a simultaneous 0 eigenvalue and $\ker(J)$, which is a proper invariant subspace of V , will be isomorphic to any of the $V_{j,k}$. The equivariant branching lemma tells us to expect bifurcating branches at μ_0 with the symmetry of isotropy subgroups Σ for which $\ker(J) \cap \text{Fix}(\Sigma)$ is one-dimensional. Such subgroups are consequently known as the *bifurcation subgroups* for ρ_k .

Theorem D.1 (Equivariant Branching Lemma) *Let Γ be a Lie group acting irreducibly on V and let g be a Γ -equivariant bifurcation problem satisfying $|J(x_0(\mu), \mu)| = 0$ and $\frac{d|J|}{d\mu} \neq 0$. Let Σ be an isotropy subgroup of Γ satisfying*

$$\dim(\text{Fix}(\Sigma)) = 1.$$

Then there exists a unique smooth solution branch to $g = 0$ such that the isotropy subgroup of each solution is Σ .

Generically, Γ will act irreducibly on $\ker(J)$, so we expect Σ -symmetric bifurcation branches for bifurcation subgroups.

D.7 Symmetry-Adapted Basis Methods: Example

An idealized vibrating drumhead stretched across a square frame⁶ satisfies the equations

$$\Delta\phi + \lambda u = 0 \quad (\text{D.36})$$

$$\phi(x|_{\text{bdry}}) = 0 \quad (\text{D.37})$$

where $\phi(x)$ is the amplitude of vibrations at point x .

A coarse discretization of this system is given by considering the 3×3 lattice with basis vectors ϕ_1, \dots, ϕ_9 , as shown in figure D.6. The discretization of the Laplacian operator is the kernel M , given by the cross operator (see figure D.7).

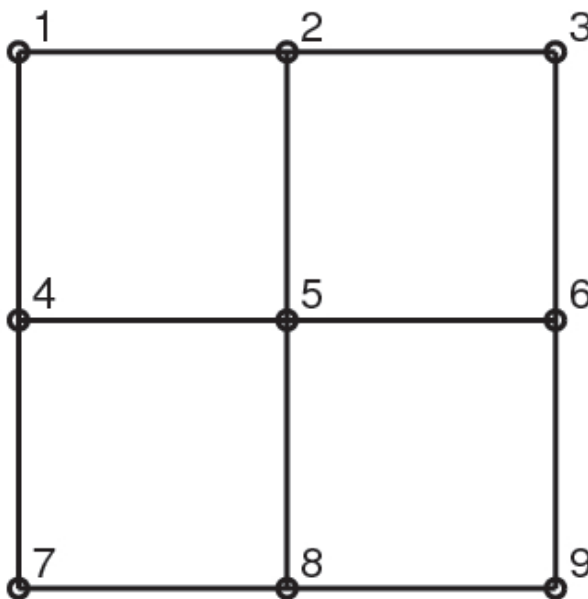


Figure D.6: 3×3 discretized membrane

In the standard basis M has the following matrix representation:

⁶Fässler and Stiefel consider this problem in [27].

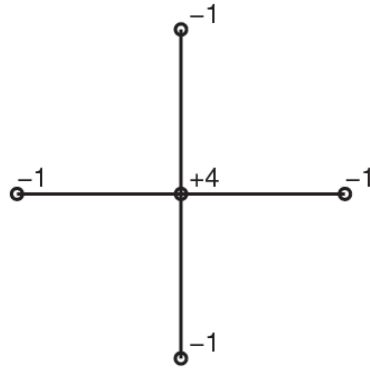


Figure D.7: Discrete Laplacian

$$M\phi = \begin{pmatrix} 4 & -1 & 0 & -1 & 0 & 0 & 0 & 0 & 0 \\ -1 & 4 & -1 & 0 & -1 & 0 & 0 & 0 & 0 \\ 0 & -1 & 4 & 0 & 0 & -1 & 0 & 0 & 0 \\ -1 & 0 & 0 & 4 & -1 & 0 & -1 & 0 & 0 \\ 0 & -1 & 0 & -1 & 4 & -1 & 0 & -1 & 0 \\ 0 & 0 & -1 & 0 & -1 & 4 & 0 & 0 & -1 \\ 0 & 0 & 0 & -1 & 0 & 0 & 4 & -1 & 0 \\ 0 & 0 & 0 & 0 & -1 & 0 & -1 & 4 & -1 \\ 0 & 0 & 0 & 0 & 0 & -1 & 0 & -1 & 4 \end{pmatrix} \begin{pmatrix} \phi_1 \\ \phi_2 \\ \vdots \\ \phi_9 \end{pmatrix}.$$

A priori, the eigenvalue problem for M appears cumbersome, but the D_4 -symmetry of the system allows for considerable simplification.

The projection formula given above yields a symmetry adapted basis:

$$\begin{aligned} x_1 &= \begin{pmatrix} \cdot & \cdot & \cdot \\ \cdot & 1 & \cdot \\ \cdot & \cdot & \cdot \end{pmatrix} & x_2 &= \begin{pmatrix} \cdot & 1 & \cdot \\ 1 & \cdot & 1 \\ \cdot & 1 & \cdot \end{pmatrix} & x_3 &= \begin{pmatrix} 1 & \cdot & 1 \\ \cdot & \cdot & \cdot \\ 1 & \cdot & 1 \end{pmatrix} \\ y &= \begin{pmatrix} \cdot & 1 & \cdot \\ -1 & \cdot & -1 \\ \cdot & 1 & \cdot \end{pmatrix} & z &= \begin{pmatrix} -1 & \cdot & 1 \\ \cdot & \cdot & \cdot \\ 1 & \cdot & -1 \end{pmatrix} \end{aligned}$$

$$\begin{array}{rcc}
 & \cdot & \cdot & \cdot & & -1 & \cdot & 1 \\
 u_1 = & -1 & \cdot & 1 & & u_2 = & \cdot & \cdot & \cdot \\
 & \cdot & \cdot & \cdot & & & -1 & \cdot & 1 \\
 \\
 & \cdot & 1 & \cdot & & 1 & \cdot & 1 \\
 v_1 = & \cdot & \cdot & \cdot & & v_2 = & \cdot & \cdot & \cdot \\
 & \cdot & -1 & \cdot & & & -1 & \cdot & -1
 \end{array}$$

The representation space \mathbb{R}^9 decomposes into invariant subspaces

$$V = \mathbb{R}^9 = V_1 \oplus V_2 \oplus V_3 \oplus V_4$$

$$\begin{array}{l}
 V_1 = \text{span}\{x_i\}_{i=1}^3 \\
 \text{with } V_2 = \text{span}\{y\} \\
 V_3 = \text{span}\{z\} \\
 V_4 = \text{span}\{u_1, u_2, v_1, v_2\}.
 \end{array}$$

D_4 is generated by two elements r and s , satisfying $r^4 = e, s^2 = e$, and $sr = r^{-1}s$. The decomposition of V corresponds to a decomposition of the representation $\rho : D_4 \rightarrow \text{GL}(\mathbb{R}^9)$

$$\rho = \rho_1 \oplus \rho_2 \oplus \rho_3 \oplus \rho_4.$$

In this decomposition, $\rho_1(r)$ and $\rho_1(s)$ act as $\begin{pmatrix} 1 & & \\ & 1 & \\ & & 1 \end{pmatrix}$ on V_1 ; $\rho_2(r)$ acts on V_2 as (-1) and $\rho_2(s)$ as (1) ; $\rho_3(r)$ acts on V_3 as (-1) and $\rho_3(s)$ also as (-1) . In the two-dimensional representation, $\rho_4(r)$ and $\rho_4(s)$ act on V_4 respectively as $I_2 \otimes$

$$\begin{pmatrix} \cos(\pi/2) & -\sin(\pi/2) \\ \sin(\pi/2) & \cos(\pi/2) \end{pmatrix} \text{ and } I_2 \otimes \begin{pmatrix} 1 & \\ & -1 \end{pmatrix}, \text{ or}$$

$$\rho_4(r) = \begin{pmatrix} 0 & 0 & -1 & 0 \\ 0 & 0 & 0 & -1 \\ 1 & 0 & 0 & 0 \\ 0 & 1 & 0 & 0 \end{pmatrix}$$

$$\rho_4(s) = \begin{pmatrix} 1 & & & \\ & 1 & & \\ & & -1 & \\ & & & -1 \end{pmatrix}.$$

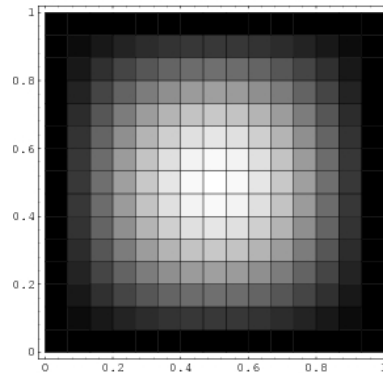
Within ρ_4 , D_4 acts on the paired vectors (u_1, v_1) and (u_2, v_2) in precisely the same fashion; also ρ_1 acts on each of $(x_i)_{i=1}^3$ in (trivially) like fashion. This coordination between the actions of the group on distinct sets of basis vectors is the essence of the symmetry adapted approach.

In the symmetry adapted basis, ordered as $\{x_1, x_2, x_3, y, z, u_1, u_2, v_1, v_2\}$, we find that M has been block-diagonalized:

$$M = \begin{pmatrix} A_1 & & & \\ & A_2 & & \\ & & A_3 & \\ & & & A_4 \end{pmatrix}$$

$$= \left(\begin{array}{c} \left(\begin{array}{ccc} 4 & -4 & 0 \\ -1 & 4 & -2 \\ 0 & -2 & 4 \end{array} \right) \\ (4) \\ (4) \\ \left(\begin{array}{cc} \left(\begin{array}{cc} 4 & -2 \\ -1 & 4 \end{array} \right) & \\ & \left(\begin{array}{cc} 4 & -2 \\ -1 & 4 \end{array} \right) \end{array} \right) \end{array} \right).$$

The eigenvalues and eigenfunctions of M may now be found easily. The first block has eigenvalues $\{4, 4 \pm 2\sqrt{2}\}$, the second and third both have $\{4\}$ and the last two blocks have eigenvalues $\{4 \pm \sqrt{2}\}$. The corresponding eigenvectors bear direct comparison to the analytical solutions $\sin(mx) \sin(ny)$ for the square drumhead. The lowest and highest frequency harmonics of the discretization, and their continuum counterparts, are shown for comparison.

Figure D.8: Lowest frequency; $\sin(\pi x) \sin(\pi y)$ 

Lowest frequency: $\nu = 4 - 2\sqrt{2}$

$$f_\nu = 2x_1 + \sqrt{2}x_2 + x_3$$

$$\begin{array}{ccc} 1 & \sqrt{2} & 1 \\ \sqrt{2} & 2 & \sqrt{2} \\ 1 & \sqrt{2} & 1 \end{array}$$

Highest frequency: $\nu = 4 + 2\sqrt{2}$

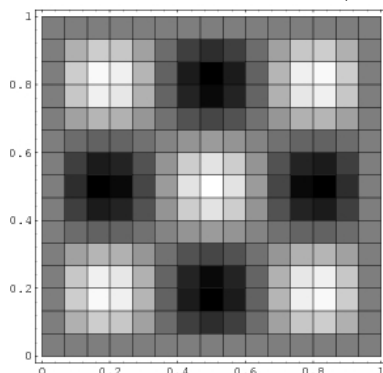
$$f_\nu = 2x_1 - \sqrt{2}x_2 + x_3$$

$$\begin{array}{ccc} 1 & -\sqrt{2} & 1 \\ -\sqrt{2} & 2 & -\sqrt{2} \\ 1 & -\sqrt{2} & 1 \end{array}$$

D.8 Spontaneous Symmetry Breaking in the n -Box Brusselator

The dynamical system

$$\frac{d}{dt} \begin{pmatrix} x \\ y \end{pmatrix} = f \begin{pmatrix} x \\ y \end{pmatrix} = \begin{pmatrix} a - (b+1)x + x^2y \\ bx - x^2y \end{pmatrix}$$

Figure D.9: Highest frequency; $\sin(3\pi x) \sin(3\pi y)$ 

models a chemical reaction-diffusion system, first developed in Brussels [62]. We imagine a ring of n identical, well-stirred reaction vessels, the common walls of which allow diffusion of the reacting species with coefficients $\frac{1}{\lambda^2}D_x, \frac{1}{\lambda^2}D_y$. The reaction equations for the n^{th} box become

$$\frac{dz_k}{dt} = g_k(\vec{z}) = f(z_k) + \frac{1}{\lambda} \begin{pmatrix} D_x & 0 \\ 0 & D_y \end{pmatrix} (z_{k-1} - 2z_k + z_{k+1})$$

where $z_k = (x_k, y_k)^{tr}$, $k = 1, \dots, n$; addition is taken modulo n .

The system has a D_n -symmetric steady state $z_k = \begin{pmatrix} a \\ b/a \end{pmatrix}$, $k = 1, \dots, n$, which is stable for sufficiently large coefficients of diffusion (small λ). To study bifurcations which break this symmetry we need to decompose the representation space $V = \mathbb{R}^{2n}$ via irreducible representations of D_n . The desired decomposition is

$$V = 2V_1^1 \oplus (2V_2^1) \oplus 2V_1^2 \oplus 2V_2^2 \oplus \dots \oplus 2V_l^2$$

If n is even, $l = \frac{n}{2} - 1$. If n is odd, $l = \frac{n-1}{2}$, and V_2^1 does not appear in the decomposition.

The one-dimensional irreducible representations are ρ_1^1 , the trivial representation, and $\rho_2^1 : r \rightarrow 1, \rho_2^1 : s \rightarrow -1$. When n is odd, ρ_2^1 does not appear.

The two-dimensional irreducible representations given by

$$\rho_k^2 : \begin{aligned} r &\rightarrow \begin{pmatrix} \cos 2\pi \frac{k}{n} & -\sin 2\pi \frac{k}{n} \\ \sin 2\pi \frac{k}{n} & \cos 2\pi \frac{k}{n} \end{pmatrix} \\ s &\rightarrow \begin{pmatrix} 1 & 0 \\ 0 & -1 \end{pmatrix} \end{aligned}, k = 1, \dots, l.$$

The symmetry-adapting projection algorithm gives basis vectors:

$$v_{1,1}^1 = (1, 0, 1, 0, \dots, 1, 0)$$

$$v_{1,2}^1 = (0, 1, 0, 1, \dots, 0, 1)$$

for $V_{1,1}^1$ and $V_{1,2}^1$;

$$v_{2,1}^1 = (1, 0, -1, 0, \dots, -1, 0)$$

$$v_{2,2}^1 = (0, 1, 0, -1, \dots, 0, -1)$$

and $V_{2,1}^1$ and $V_{2,2}^1$, (these are the one-dimensional representations); and

$$v_{k,1,1}^2 = (1, 0, \cos(2\pi \frac{k}{n}), 0, \dots, \cos(2\pi(n-1)\frac{k}{n}), 0)$$

$$v_{k,1,2}^2 = (0, 1, 0, \cos(2\pi \frac{k}{n}), \dots, 0, \cos(2\pi(n-1)\frac{k}{n}))$$

$$v_{k,2,1}^2 = (0, 0, \sin(2\pi \frac{k}{n}), 0, \dots, \sin(2\pi(n-1)\frac{k}{n}), 0)$$

$$v_{k,2,2}^2 = (0, 0, 0, \sin(2\pi \frac{k}{n}), \dots, 0, \sin(2\pi(n-1)\frac{k}{n}))$$

for $V_{k,1}^2$ and $V_{k,2}^2$.

For a concrete example, consider the 6-box Brusselator⁷. The basis vectors are

⁷Studied by Werner [80]

(suppressing the y -concentrations)

$$\begin{aligned}
 v_1^1 &= (1, 1, 1, 1, 1, 1) \\
 v_2^1 &= (1, -1, 1, -1, 1, -1) \\
 v_{1,1}^2 &= (2, 1, -1, -2, -1, 1) \\
 v_{1,2}^2 &= (0, 1, 1, 0, -1, -1) \\
 v_{2,1}^2 &= (2, -1, -1, 2, -1, -1) \\
 v_{2,2}^2 &= (0, 1, -1, 0, 1, -1).
 \end{aligned}$$

With the basis ordered as above, the Jacobian of the system at the steady state becomes

$$J = \begin{pmatrix} A_1^1 & & & & & \\ & A_2^1 & & & & \\ & & A_1^2 & & & \\ & & & A_1^2 & & \\ & & & & A_2^2 & \\ & & & & & A_2^2 \end{pmatrix} \\
 = \begin{pmatrix} \begin{pmatrix} 3b+1 & a^2 \\ b & -a^2 \end{pmatrix} & & & & & \\ & A_1^1 - \frac{4}{\lambda^2}D & & & & \\ & & A_1^1 - \frac{1}{\lambda^2}D & & & \\ & & & A_1^1 - \frac{1}{\lambda^2}D & & \\ & & & & A_1^1 - \frac{3}{\lambda^2}D & \\ & & & & & A_1^1 - \frac{3}{\lambda^2}D \end{pmatrix}.$$

where $D = \begin{pmatrix} D_x & 0 \\ 0 & D_y \end{pmatrix}$. Each irreducible representation appearing is of real type, and each has multiplicity two, leading to the (2×2) blocks throughout. Blocks for A_1^2 and A_2^2 appear twice because the corresponding representations are two-dimensional.

When for example block A_1^2 develops a zero eigenvalue it is forced to be degenerate, but is still Γ -simple. The kernel of J will then lie in V_1^2 , and from the equivariant branching lemma we expect bifurcating solution branches with the symmetries of

subgroups whose fixed-point spaces' intersections with V_1^2 are one-dimensional. It is in the direction of the shared subspace that the bifurcating solution will grow.

Bases for the fixed point subspaces of the isotropy subgroups of D_6 (shown here for all isotropy subgroups up to conjugacy) can be made to coincide with the symmetry-adapted basis vectors found via the irreducible representations, as follows:

Basis vectors	v_1^1	v_2^1	$v_{1,1}^2$	$v_{1,2}^2$	$v_{2,1}^2$	$v_{2,2}^2$
Isotropy Subgroups						
D_6	✓					
$D_3(s, r^2)$	✓	✓				
$\mathbb{Z}_2 \oplus \mathbb{Z}_2(s, r^3)$	✓				✓	
$\mathbb{Z}_2(r^3)$	✓				✓	✓
$\mathbb{Z}_2(sr^3)$	✓			✓	✓	
$\mathbb{Z}_2(s)$	✓	✓	✓		✓	
$\mathbf{1}$	✓	✓	✓	✓	✓	✓

When 0 becomes a Γ -simple eigenvalue of A_1^2 , we expect bifurcating solution branches with the symmetries of the three subgroups conjugate to $\mathbb{Z}_2(s)$, and the three conjugate to $\mathbb{Z}_2(sr^3)$. When A_2^2 has a Γ -simple zero we expect these subgroups and also the three conjugates of $\mathbb{Z}_2 \oplus \mathbb{Z}_2(s, r^3)$, but not $\mathbb{Z}_2(r^3)$ (nor $\mathbf{1}$). When A_2^1 becomes singular we expect to find symmetry breaking from D_6 to the normal subgroup D_3 .

Detailed numerical calculations by Werner and others⁸ have confirmed these expectations for the case of the 6-box Brusselator.

⁸see [30, 80]

D.9 Spontaneous Symmetry Breaking in the Bénard Problem

The Boussinesq approximation for Rayleigh-Bénard convection yields the equations

$$\begin{aligned} \frac{1}{\rho} \left\{ \frac{\partial v}{\partial t} + (v \cdot \nabla)v \right\} &= -\nabla p + \theta \vec{g} + \Delta v \\ \operatorname{div}(v) &= 0 \\ \frac{\partial \theta}{\partial t} + (v \cdot \nabla)\theta &= Rv_3 + \Delta \theta \end{aligned}$$

where ρ and p represent the fluid density and pressure, respectively; $v \in \mathbb{R}^3$ is the fluid velocity, $x \in \mathbb{R}^3$ the position and $\theta \in \mathbb{R}$ the variation of temperature from a linear profile. The boundary conditions $\frac{\partial v_1}{\partial x_3} = \frac{\partial v_2}{\partial x_3} = v_3 = 0$ at $x_3 = 0, 1$ are assumed for analytical convenience.

This system is equivariant with respect to the action of $\Gamma = E_2 \oplus \mathbb{Z}_2$ given by

$$\begin{aligned} \sigma \in O(2) &: (v, \theta)(x) \rightarrow (\sigma v, \theta)(\sigma^{tr} x) \\ (t_1, t_2) \in T_2 &: (v, \theta)(x) \rightarrow (v, \theta)(x - (t_1, t_2, 0)) \\ \kappa \in \mathbb{Z}_2 &: (v, \theta)(x) \rightarrow (v, -\theta)(x_1, x_2, 1 - x_3). \end{aligned}$$

The trivial solution $v = 0, \theta = 0$ is clearly Γ -invariant.

The linearized response of the system to perturbations of $(v, \theta) = (0, 0)$ is given by

$$\begin{aligned} \Delta v - \nabla p + \theta \vec{g} &= 0 \\ \operatorname{div}(v) &= 0 \\ \Delta \theta + Rv_3 &= 0, \end{aligned}$$

and these equations inherit the system's equivariance under Γ . For sufficiently small Rayleigh number R , the trivial solution is stable to small perturbations. Solutions for v_k and θ of the form $e^{i(k_1 x_1 + k_2 x_2)} \sin(n\pi x_3)$ become critical at

$$R = \frac{(n^2 \pi^2 + |k|^2)^3}{|k|^2},$$

so we expect a bifurcation from the steady state at $R_c = \min_{|k|} \left\{ \frac{(\pi^2 + |k|^2)^3}{|k|^2} \right\}$. For a given $|k_c|$ we have an infinity of solutions becoming critical at once, each with a different orientation in the plane, and we cannot apply the usual Lyapunov-Schmidt reduction.

To make the problem more tractable, we restrict attention to solutions which are periodic on a lattice, that is functions $f(x_1, x_2)$ of the form $f(x) = f(x + e_1) = f(x + e_2)$, where e_1 and e_2 are two vectors spanning the plane. Motivated by the observation under selected experimental conditions of hexagonal planar patterns in the fluid, we choose e_1 and e_2 to span a lattice \mathcal{L} with D_6 -symmetry (see figure D.10):

$$\begin{aligned} e_1 &= c(1, 0) \\ e_2 &= c(-1/2, \sqrt{3}/2). \end{aligned}$$

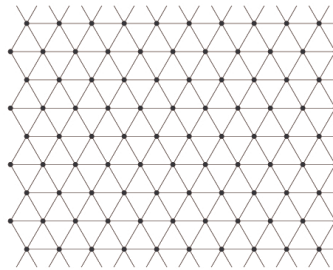


Figure D.10: Hexagonal Lattice \mathcal{L}

Any C^∞ function invariant under translations by e_1 and e_2 has an expansion in Fourier series

$$f(x_1, x_2) = \sum_{j \in \mathbb{Z}^2} c_j e^{i(j_1 \vec{k}_1 \cdot \vec{x} + j_2 \vec{k}_2 \cdot \vec{x})}$$

where $k_1 = \frac{4\pi}{c\sqrt{3}}(0, 1)$, $k_2 = \frac{4\pi}{c\sqrt{3}}(\frac{\sqrt{3}}{2}, \frac{1}{2})$; for real f , $c_j = \bar{c}_{-j}$. The natural action of T_2 on (x_1, x_2) induces an action on the Fourier components of f , taking $e^{i(j_1 \vec{k}_1 + j_2 \vec{k}_2) \cdot \vec{x}}$ to a complex multiple of itself. The orbits of D_6 are either six independent exponentials, if $j_1 \vec{k}_1 + j_2 \vec{k}_2$ is invariant under one of the reflections generating D_6 , or twelve exponentials if it is not. If $j_1 \vec{k}_1 + j_2 \vec{k}_2 = 0 \pmod{\mathcal{L}}$, the orbit is $\{1\}$. We arrive

therefore at families of irreducible representations of dimension either six or twelve. The *fundamental representation*, generated by $e^{i\vec{k}_1 \cdot \vec{x}}$, is given as

$$\sum_{j=1}^6 z_j e^{i\vec{k}_j \cdot \vec{x}}$$

$$z_j \in \mathbb{C}; \quad \bar{z}_1 = z_4, \quad \bar{z}_2 = z_5, \quad \bar{z}_3 = z_6 \\ \vec{k}_3 = -(\vec{k}_1 + \vec{k}_2), \quad \vec{k}_4 = -\vec{k}_1, \quad \vec{k}_5 = -\vec{k}_2, \quad \vec{k}_6 = -\vec{k}_3.$$

D_6 acts on $\{z_k\}_{k=1}^3$ as follows: D_3 permutes the coordinates (z_1, z_2, z_3) and $\mathbb{Z}_2(s)$ acts as complex conjugation. The action of a translation $\vec{p} \in T_2$ is

$$\vec{p} : (z_1, z_2, z_3) \rightarrow (e^{i\vec{k}_1 \cdot \vec{p}} z_1, e^{i\vec{k}_2 \cdot \vec{p}} z_2, e^{i\vec{k}_3 \cdot \vec{p}} z_3).$$

The isotropy subgroups with one dimensional fixed-point subspaces for Γ are calculated, up to conjugacy, to be:

$I_R \cong \mathbb{Z}_2^2 \oplus S^1$ generated by $(z_1, z_2, z_3) \rightarrow (z_1, z_3, z_2)$, $(z_1, z_2, z_3) \rightarrow (\bar{z}_1, \bar{z}_2, \bar{z}_3)$, and $(0, p_2) \in T_2$. *Rolls or Stripes*.

$I_H \cong D_6$ *Hexagons*.

$I_T \cong D_3$ *Triangles*.

$I_P \cong \mathbb{Z}_2^3$ generated by $(z_1, z_2, z_3) \rightarrow (\bar{z}_1, \bar{z}_2, \bar{z}_3)$, $(z_1, z_2, z_3) \rightarrow (z_2, z_1, z_3)$, and $(z_1, z_2, z_3) \rightarrow (z_1, z_2, -z_3)$. *Patchwork Quilt*.

The corresponding fixed-point spaces, shown in figure D.11, are:

$$\text{Fix}(I_R) = \mathbb{R}\{(1, 0, 0)\}$$

$$\text{Fix}(I_H) = \mathbb{R}\{(1, 1, 1)\}$$

$$\text{Fix}(I_T) = \mathbb{R}\{(i, i, i)\}$$

$$\text{Fix}(I_P) = \mathbb{R}\{(1, 1, 0)\}$$

Every bifurcation subgroup of $(T_2 \times D_6) \oplus \mathbb{Z}_2$ is conjugate to one of these.

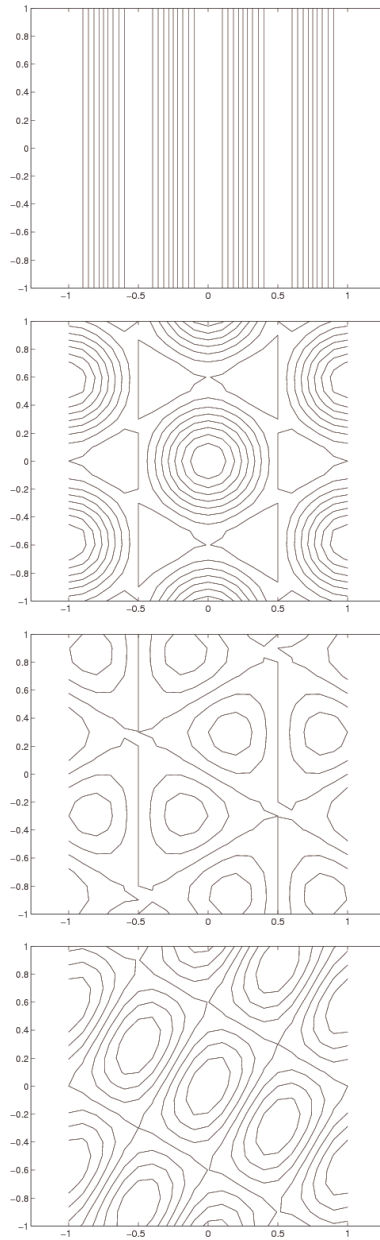


Figure D.11: Four planforms for bifurcation subgroups of $(T_2 \times D_6) \oplus \mathbb{Z}_2$: Rolls, Hexagons, Triangles, and Patchwork

APPENDIX E: MATLAB CODES

E.10 Simulated Annealing Codes

xyann1 (script) XY model heat-bath (annealing) simulation. Compares center-surround with pure Gaussian interaction kernel. Also compares same for Ising model.

xyann4 XY model heat-bath (annealing) simulation. Runs long-time average samples of steady states to evaluate orientation scatter as a function of temperature.

objfun2 Calculates XY objective function explicitly. Fairly slow.

The basic simulated annealing algorithm simulates a heat bath (Gibbs ensemble) by sampling a vector near the current vector, and selecting it with probability given by a sigmoid function of the energy increment or decrement it would cause. The effective step size in the random walk is controlled by the interaction of the "temperature", which determines the selectivity or slope of the sigmoid, and the sampling ensemble. If the sampling width is too large or too small compared to the size of features such as local minima on the energy landscape the random walk will proceed slowly, or become trapped. Similarly, if the "temperature" is too low the process will not escape local minima. In the center-surround XY model this means topological singularities will not approach each other and annihilate. If the "temperature" is too high then no organized pattern forms.

Generally the objective function or energy to be minimized is given as a quadratic function of the vector field, e.g.

$$H(\chi) = -\frac{1}{2} \sum_i \chi_i \cdot \sum_j A_{ij} \chi_j$$

(possibly with additional constraint terms). It is substantially more time-efficient to sample a neighborhood of each spin χ_i simultaneously and independently. Using some sampling function I generate a new χ'_i and compare it to the background field generated by the current χ_i

$$H(\chi' - \chi) = - \sum_i (\chi'_i - \chi_i) \cdot \sum_j A_{ij} \chi_j + O(|\chi_i|^2)$$

accurate to second order in $|\chi|$.⁹

xyann1

```

model = 'Ising';
    %'XY' -> planar XY model
    %'Ising' -> Ising model
kernel = 'dog';
    %'dog' -> difference of Gaussians.
    %'Jij' -> classical Ising interaction
    %'Gauss' -> a single Gaussian.

%%Parameters%%
gridsize = [100 100]; % 2 mm^2
sigp = 5; % 100 micron excitatory radius
sigm = 3*sigp; % 300 micron inhibitory radius

switch kernel
case 'Jij'
    K = [0 1 0; 1 0 1; 0 1 0];
case 'dog'
    K = kernel4(sigp,sigm,4*sigp,0);
case 'Gauss'
    K = kernel4(3,100,15,29);
end
%K = K/sum(abs(K(:))); % set maximal local energy change to 1.

```

⁹I am indebted to A. Dimitrov for originally pointing out this expedient to me.

```

%%Heat Bath parameters%%
sigphi = pi/10; % typical stepsize in sampling
beta = 1000;      % inverse temperature for Gibbs ensemble
%1000 for XY DOG, 100 for XY Jij;
%.1 for Ising -- DOG or , Gauss (or .01 for Jij?)

nits = 1000;      % total number of iterations
%snap = 10;      % snapshots per iteration
snap=10;        % use this for movie effect

switch model
case 'XY'

    %%Initial Conditions%%
    phi = pi*rand(gridsize);
    seephi(phi),drawnow

    for its = 1:nits
        %%Generate alternative angles%%
        phi0=phi;
        phi1 = mod(phi + sigphi*randn(gridsize),pi);    % random walk in phi
        % difference in energy function  $H = \sum_{ij} K_{ij} \cos(2(\phi_i - \phi_j))$ 
        dH = (cos(2*phi1)-cos(2*phi0)).*...
            conv2(cos(2*phi),-K,'same')/prod(size(K)) + ...
            (sin(2*phi1)-sin(2*phi0)).*...
            conv2(sin(2*phi),-K,'same')/prod(size(K));

        choice = rand(gridsize) < sigmoid(-2/beta,dH); % binary choice
        phi = phi1.*choice + phi0.*(1-choice);

    if ~rem(its,snap)
        seephi(phi),title(['Iteration ',num2str(its)])
        drawnow
    end
end
end

```

```

case 'Ising'

    %%%Initial Conditions%%
    z = round(rand(gridsize))*2 - 1; % +- 1
    seez(z),drawnow

    for its = 1:nits
        %%%Generate alternative angles%%
        z0=z;
        z1 = -z0; % flip spins
        % difference in energy function H = Kij cos(2(phi_i-phi_j))
        dH = (z1-z0).*conv2(z,-K,'same');
        choice = rand(gridsize) < sigmoid(-2/beta,dH); % binary choice
        z = z1.*choice + z0.*(1-choice);

        if ~rem(its,snap)
            seez(z),title(['Iteration ',num2str(its)])
            drawnow
        end
    end
end

end

```

xyann4

```

function [avephidiffs,ndiffs,locdiffs] = xyann4(fname,tol)

%function [avephidiffs,ndiffs,locdiffs] = xyann4(fname,tol)
%
% Simulate XY model with heat bath with difference-of-Gaussians
% interaction at different temperatures. Run at a given
% temp until the average change in the local statistics
% falls below tolerance TOL (e.g. 0.01) -- or reverses.
%
% Outputs:
% AVEPHIDIFFS is average absolute difference in neighboring
% angles -- the statistic reported in Maldonado & Gray Visual

```

```

% Neuroscience 1996.
% NNDIFFS is average angle difference between adjacent units,
% cos(2(phi1-phi2))
% LOCDIFFS is average angle difference with local field, cos(2(phi-philoc))
%
% FNAME is a filename to which to save data.
%
% Same setup as XYANN2, except statistics appropriate for
% exptl data comparisons.

if nargin < 2,
    tol = .01;          % one percent change in average difference to stop
end

%%% Set up the geometry & initial conditions %%%
ic = 'hot'; % initial conditions. 'cold' -> roll pattern. 'hot' -> random
gridsize = [100 100]; % size of spatial grid
maxits = 2000; % maximum number of iterations
sigp=4.718;sigm=3*sigp;% kernel widths -- gives 1mm stripes if each pix=50micr.
K = kernel3(sigp,sigm,ceil(4*sigp),0); % difference of Gaussians interaction
sigphi = pi/4; % typical stepsize in phi

switch ic
case 'cold' % low temp initial conds -> optimal roll pattern
    width = pi*sqrt(2/log(3))*sigp; % spatial period of roll pattern
    [x,y]=meshgrid(1:gridsize(2),1:gridsize(1)); % xy spatial grid
    phi0=pi*mod(y/width,1); % orientation roll pattern
case 'hot'
    phi0 = mod(pi*rand(gridsize),pi); % random -- high temp approx.
end

%%% Simmer at different temperatures beta and record statistical behavior %%%
nbeta = 9; minlogbeta = 2; maxlogbeta = 4;
betas = logspace(minlogbeta,maxlogbeta,nbeta);
for jbeta = 1:nbeta
    beta = betas(jbeta)
    [avephidifftemp,nndifftemp,locdifftemp,phi] = ...

```

```

    bake(phi0,beta,sigphi,maxits,K,gridsize,tol);
avephidiffs(jbeta,1:length(avephidifftemp)) = avephidifftemp;
nndiffs(jbeta,1:length(nndifftemp)) = nndifftemp;
locdiffs(jbeta,1:length(locdifftemp)) = locdifftemp;
phis(:,:,jbeta) = phi;

figure
plot(nndifftemp,'+'),hold on
plot(locdifftemp,'o'),plot(avephidifftemp,'*')
title(['Log10(\beta) = ',num2str(log10(beta))])
xlabel('Iteration')
axis([0 length(nndifftemp),0,2])

end

save(fname)

%%% FUNCTIONS %%%=====%%%

function [avephidiff,nndiff,locdiff,phi] = ...
    bake(phi0,beta,sigphi,maxits,K,gridsize,tol)

%%% Initialize %%%
its = 0;          % iteration number
% record average absolute difference between n.n. ala Maldonado+Gray
avephidiff = 0;
% record difference between nearest neighbors (ave. cos 2 phidiff)
nndiff = 0;
locdiff = 0;    % record difference between phi and local (K-averaged) phi
stopflag = 0;  % signals when stat'l steady state is approximately reached

%%% Iterate heat bath and calculate statistics %%%
while ((its+1) < maxits) & ~stopflag

    its = its + 1;
    %%% Choose new phi according to Boltzman Distribution %%%
    phi=phi0;

```

```

phi1 = mod(phi0 + sigphi*randn(gridsize),pi); % random walk in phi
% difference in energy function H = Kij cos(2(phi_i-phi_j))
dH = (cos(2*phi1)-cos(2*phi0)).*...
      conv2(cos(2*phi),-K,'same')/prod(size(K)) + ...
      (sin(2*phi1)-sin(2*phi0)).*...
      conv2(sin(2*phi),-K,'same')/prod(size(K));

choice = rand(gridsize) < sigmoid(-2/beta,dH); % binary choice
phi = phi1.*choice + phi0.*(1-choice);

[avephidiff(its), mndiff(its), locdiff(its)] = xystats(phi,K,gridsize);

% Continue until changes drop below tol -- and at least 200 its
if (its > 200) & ~rem(its-1,50) % check every 50 its after 200
    locdiffave1 = mean(locdiff(its + [-99:0])) % average last 250 mndiff
    locdiffave2 = mean(locdiff(its + [-199:-100])) % avg prior 100 mndiff
    % fractional decrease of tol.
    if ((locdiffave2-locdiffave1)/locdiffave2 < tol)...
        & (locdiffave1 < .5); % cool state
        stopflag = 1;
        %disp([locdiffave1,locdiffave2])
    end
end
phi0 = phi;

end % while ((its+1) < maxits) & ~stopflag

%%% Picture phi drawn from steady state distribution.
figure,seephi(phi),
title(['Typical \phi configuration at Log10(\beta) = ',num2str(log10(beta))])

%%%-----

function [avephidiff, mndiff, locdiff] = xystats(phi,K,gridsize)

%%% Find differences in neighboring angles as in Maldonado & Gray

```

```

% Find absolute angular differences and take population average
% phi difference -- horizontal neighbors
phidiffhor = conv2(phi,[1, -1],'valid');
phidiffhor = min(abs(phidiffhor),min(abs(phidiffhor+pi),abs(phidiffhor-pi)));
% phi difference -- vertical neighbors
phidiffver = conv2(phi,[1; -1],'valid');
phidiffver = min(abs(phidiffver),min(abs(phidiffver+pi),abs(phidiffver-pi)));
avephidiff = mean(phidiffhor(:)+phidiffver(:))/2;

%% Angle between neighboring orientations

% Population average of cos(2(phi1-phi2)) where phi1,phi2 are neighbors
phivec(:,:,1) = cos(2*phi);
phivec(:,:,2) = sin(2*phi);
nndiffhor = sum(phivec(1:(gridsize(1)-1),:,:).*phivec(2:gridsize(1),:,:),3);
nndiffver = sum(phivec(:,1:(gridsize(2)-1),:).*phivec(:,2:gridsize(2),:,:),3);
nndiff = mean(nndiffhor(:)+nndiffver(:))/2;

%% Angle between local field and phi

% Compute local field
phivecloc(:,:,1) = conv2(phivec(:,:,1),K,'same');
phivecloc(:,:,2) = conv2(phivec(:,:,2),K,'same');
qloc(:,:,1) = sqrt(sum(phivecloc.^2,3));
qloc(:,:,2) = qloc(:,:,1);

% Population average of cos(2(phi-philoc))
locdiff = 2*mean(phivec(:).*(phivecloc(:)./qloc(:)));

```

objfun2

```

function f = objfun2(x,K)

%function f = objfun2(x,K)
%
% An objective function to accompany ann5 (annealing program.)
% Calculates overlap (or "conflict") of orientation sensitive

```

```

% cells according to a convolution kernel K. The grid "x" is
% a square of orientation values scaled from 0 to pi.
% Returns a matrix the size of x.
% Uses zero-flux boundary conditions.
% Higher (positive) f represents less conflict or more overlap.

[rk ck] = size(K);
j = 1:rk;
k = 1:ck;
Kcent = [rk+1,ck+1]/2; % Assumes K has odd depth and breadth.

[rx cx] = size(x);
f = zeros(rx,cx);

pad1 = Kcent(1);
pad2 = Kcent(2);
x = addbdy(x,pad1,pad2); % Adds no-flux boundary to x.

for l1 = 1:rx
  for l2 = 1:cx

    f(l1,l2) = sum(sum( K .* ...
      cos(2*( ...
        x(l1+pad1, l2+pad2) ... % Center of kernel;
        - x(l1+j, l2+k) )) ... % outlying point.
      ));

  end % l2
end % l1

```

E.11 Visualization Codes

diffim Simulate physiology, optics and averaging of raw orientation distribution to generate optical image (Blasdel's method).

singplot2 Locate the singularities in an orientation map.

rect Draw an oriented box with given aspect ratio, area, position etc.

diffim

```
function [orients, prefstr] = diffim(x)

%function [orients, prefstr] = diffim(x)
%
%   Filter for "differential imaging" of annealed
%   orientation-preference data.
%   Input: GRIDSIZE x GRIDSIZE vector of preferred orientations
%   0 <= theta < pi.
%   Output: oplot of a subgrid of the values superimposed on
%   a colored background of averaged orientation responses.

[rx cx] = size(x);

hor = (cos(x)).^2 - (cos(x - pi/2)).^2;    % response to 0 - resp to pi/2
tilt = (cos(x+pi/4)).^2 - (cos(x-pi/4)).^2; % resp to -pi/4 - resp to pi/4

%   compress and smooth images -- average 8x8 region spaced every 4x4.
jmax = fix(rx/4)-1;
kmax = fix(cx/4)-1;
for j = 1:jmax, for k = 1:kmax
    horcomp(j,k) = sum2(hor(4*j-3:4*j+4,4*k-3:4*k+4));
    tiltcomp(j,k) = sum2(tilt(4*j-3:4*j+4,4*k-3:4*k+4));
end, end

figure(gcf+1);setfsz(600,600),pcolor(horcomp),colormap gray,axis('equal')
shading('interp'),
title('Preference for Horizontal Stimuli over Vertical')

figure(gcf+1);setfsz(600,600),pcolor(tiltcomp),colormap gray,axis('equal')
shading('interp'),
title('Preference for -Pi/4 Oblique Stimuli over +Pi/4')

% Plot orientation preferences (not strengths of preferences)
```

```

% as colorwheel plot, with oriented line segments overlain.

[xx yy] = meshgrid(1:jmax,1:kmax); % positions for line-segment plotting
points = length(xx(:));
a = zeros(4,points);
a(1,:) = xx(:)'+1/2;
a(2,:) = yy(:)'+1/2;
a(3,:) = atan2(tiltcomp(:),horcomp(:))'/2;
a(4,:) = sqrt(tiltcomp(:)'.^2 + horcomp(:)'.^2);

orients = reshape(a(3,:),size(xx));
prefstr = reshape(a(4,:),size(xx));

figure(gcf+1), setsize(800,800)
pcolor(orients), colormap hsv, axis('equal'), shading('flat')
hold on
oplot(a,.75)
title('Orientation Preference Based on Two-Component Differential Imaging')

figure(gcf+1), setsize(800,800)
pcolor(prefstr), colormap gray, axis('equal'), shading('flat')
title('Strength of Orientation Preferences')

```

singplot2

```

function sx = singplot2(x,period,plotflag)

%function sx = singplot2(x,period,plotflag)
%
% Let X be an RX x CX matrix of values of a PERIOD-periodic
% scalar (default period is 2*pi).
% SINGPLOT2 returns the closed integrals around the RX-1 x CX-1
% squares of size 2x2 ranging over X.

if nargin < 3, plotflag = 1; end
if nargin < 2, period = 2*pi; end

```

```

[rx cx] = size(x);

sx = zeros(rx-1,cx-1);

for j = 1:rx-1
    for k = 1:cx-1
        int = 0;
        int = delphi(x(j,k),    x(j+1,k),    period) + int;
        int = delphi(x(j+1,k),  x(j+1,k+1),  period) + int;
        int = delphi(x(j+1,k+1), x(j,k+1),  period) + int;
        int = delphi(x(j,k+1),  x(j,k),    period) + int;

        sx(j,k) = int;
    end
end

if plotflag == 1,
    figure(gcf+1), setfsize(800,800)
    pcolor(sx), colormap gray, axis('equal'), shading('interp'),
    caxis([-period, period])
end

```

MATLAB function `rect.m` creates an oriented box – a component of the graphics shown in chapter 5.

`rect`

```

function h=rect(x,y,theta,area,thick,aspect)

%function rect(x,y,theta,area,thick,aspect)
%
% Add a box (four line objects) to the current figure
% at position [X,Y], angle THETA,
% length sqrt(AREA*ASPECT), width sqrt(AREA/ASPECT).
% ASPECT should be >=1; default ASPECT=3.
% THICK (default 3) specifies the thickness of the
% line elements.

```

```

%
% Returns a vector of handles to the line elements.

if nargin < 6, aspect = 3; end
if nargin < 5, thick = 2; end
if nargin < 4, area = 1; end
if nargin < 3, theta = 0; aspect = 1; end % make a square box.

a = sqrt(area*aspect)/2;
b = sqrt(area/aspect)/2;
xa = a*cos(theta);
ya = a*sin(theta);
xb = -b*sin(theta);
yb = b*cos(theta);

xs = x + [xa+xb,-xa+xb,-xa-xb,xa-xb,xa+xb];
ys = y + [ya+yb,-ya+yb,-ya-yb,ya-yb,ya+yb];

h=line(xs,ys);
set(h,'LineWidth',thick)

```

E.12 Pattern Formation Analysis

irrepcalc1 Code for calculating equivalence of different irreducible representations.

irrepcalc3 Code for calculating projections onto isotypic subspaces.

ctxpat1 Searches for a bifurcation (zero eigenvalue) in the parameter space of the monocular model.

irrepcalc1

```

function irrepcalc1(i,j)

% Square Lattice
% Calculation to see if different Irreps from
% xy model are inequivalent or not

```

```

% Based on Schurr's lemma.
%
% choose i,j from 1,2,3,4,5.

% bases [cos(k1.x), sin(k1.x), cos(k2.x), sin(k2.x)]
% for +- permutation matrices

%%% five different 4x4 irreps
%% rotation by pi/2
a = zeros(4,4,5);
%% reflection in x-axis
b = zeros(4,4,5);

%%% First Irrep -- mass irrep

%% rotation by pi/2
a(1,3,1) = 1;
a(2,4,1) = 1;
a(3,1,1) = 1;
a(4,2,1) = -1;
% reflection in k1
b(:, :, 1)=eye(4,4);
b(4,4,1) = -1;

%%% Second Irrep -- "compression wave" retinotopy irrep

%% rotation by pi/2
a(1,3,2) = -1;
a(2,4,2) = 1;
a(3,1,2) = 1;
a(4,2,2) = 1;
% reflection in k1
b(:, :, 2)=eye(4,4);
b(3,3,2) = -1;

%%% Third Irrep -- "transverse wave" retinotopy irrep

```

```

%% rotation by pi/2
a(1,3,3) = 1;
a(2,4,3) = -1;
a(3,1,3) = -1;
a(4,2,3) = -1;
% reflection in k1
b(:, :, 3) = -eye(4, 4);
b(3, 3, 3) = 1;

%% Fourth Irrep -- Orientation (4)

%% rotation by pi/2
a(1,3,4) = -1;
a(2,4,4) = 1;
a(3,1,4) = -1;
a(4,2,4) = -1;
% reflection in k1
b(:, :, 4) = eye(4, 4);
b(4, 4, 4) = -1;

%% Fifth Irrep -- Orientation (5)

%% rotation by pi/2
a(1,3,5) = -1;
a(2,4,5) = 1;
a(3,1,5) = -1;
a(4,2,5) = -1;
% reflection in k1
b(:, :, 5) = -eye(4, 4);
b(4, 4, 5) = 1;

%% Choose which irreps to compare
if nargin < 2
    i=1;
    j=1;
end

```

```

a1 = squeeze(a(:,:,i))
b1 = squeeze(b(:,:,i))
a2 = squeeze(a(:,:,j))
b2 = squeeze(b(:,:,j))

tot = zeros(4,4);          % total
for k=0:3 % four rotations in D4
    tot = tot ...
        + a1^k*(a2^k)' ...
        + a1^k*b1*b2'*(a2)'^k; % note b2=b2'
end
tot = tot/8;              % normalize by number of elements in group

disp(['Inner Product of Irreps ',num2str(i),' and ',num2str(j),' is:'])
disp(tot)

%keyboard

syms alpha1 alpha2 real
t = [cos(alpha1),sin(alpha1),0,0;...
     -sin(alpha1),cos(alpha1),0,0;...
     0,0,cos(alpha2),sin(alpha2);...
     0,0,-sin(alpha2),cos(alpha2)];

%e.g.: finding the character function
disp(['Character Function for Irrep ',num2str(i)])
for k=0:3,[k,trace(t*a1^k)],end
for k=0:3,[k,trace(t*b1*a1^k)],end
%
disp(['Character Function for Irrep ',num2str(j)])
for k=0:3,[k,trace(t*a2^k)],end
for k=0:3,[k,trace(t*b2*a2^k)],end

keyboard

```

irrepcalc3

```
%Projection calculation onto isotypic subspaces for cortical map problem
%(square lattice actions).
```

```
opt = 1; % opt = +-1 for the two kinds of irreps
```

```
% bases [cos(k1.x), sin(k1.x), cos(k2.x), sin(k2.x)]
```

```
% for +- permutation matrices and rotation matrices
```

```
% Elements of the group  $T^2 \backslash \text{sdp } D_4$  are given as
```

```
% translation(alpha1,alpha2).\sigma where \sigma \in D_4.
```

```
% (alpha1,alpha2) is in  $[0,2\pi) \times [0,2\pi)$ .
```

```
syms alpha1 alpha2 real
```

```
% character of the irreducible
```

```
% representation is
```

```
%  $\chi(\gamma) =$ 
```

```
%  $2 \cos(\alpha_1) + 2 \cos(\alpha_2)$ , for  $t(\alpha_1, \alpha_2)$ ;
```

```
%  $+ - 2 \cos(\alpha_1)$ , for  $t(\alpha_1, \alpha_2) \cdot \kappa$ ;
```

```
%  $+ - 2 \cos(\alpha_2)$ , for  $t(\alpha_1, \alpha_2) \cdot \kappa \cdot \xi^2$ ;
```

```
% 0, otherwise.
```

```
% translation matrix in the above basis represented as
```

```
t = [cos(alpha1),sin(alpha1),0,0;...
      -sin(alpha1),cos(alpha1),0,0;...
      0,0,cos(alpha2),sin(alpha2);...
      0,0,-sin(alpha2),cos(alpha2)];
```

```
%%% five different 4x4 irreps in the above basis
```

```
%% rotation by pi/2
```

```
a = zeros(4,4,5);
```

```
%% reflection in x-axis
```

```
b = zeros(4,4,5);
```

```
%%% First Irrep -- mass irrep
```

```

%% rotation by pi/2
a(1,3,1) = 1;
a(2,4,1) = 1;
a(3,1,1) = 1;
a(4,2,1) = -1;
% reflection in k1
b(:, :, 1)=eye(4,4);
b(4,4,1) = -1;

%% Second Irrep -- "compression wave" retinotopy irrep

%% rotation by pi/2
a(1,3,2) = -1;
a(2,4,2) = 1;
a(3,1,2) = 1;
a(4,2,2) = 1;
% reflection in k1
b(:, :, 2)=eye(4,4);
b(3,3,2) = -1;

%% Third Irrep -- "transverse wave" retinotopy irrep

%% rotation by pi/2
a(1,3,3) = 1;
a(2,4,3) = -1;
a(3,1,3) = -1;
a(4,2,3) = -1;
% reflection in k1
b(:, :, 3)=-eye(4,4);
b(3,3,3) = 1;

%% Fourth Irrep -- Orientation (4)

%% rotation by pi/2
a(1,3,4) = -1;
a(2,4,4) = 1;

```

```

a(3,1,4) = -1;
a(4,2,4) = -1;
% reflection in k1
b(:, :, 4)=eye(4,4);
b(4,4,4) = -1;

%% Fifth Irrep -- Orientation (5)

%% rotation by pi/2
a(1,3,5) = -1;
a(2,4,5) = 1;
a(3,1,5) = -1;
a(4,2,5) = -1;
% reflection in k1
b(:, :, 5)=-eye(4,4);
b(4,4,5) = 1;

% Projections via characters:

for opt = -1:2:1
    disp(['Projections for type ', num2str(opt)])
    for i = 1:5

        disp(['Component number ', num2str(i)])
        a1 = squeeze(a(:, :, i));
        b1 = squeeze(b(:, :, i));

        int(...
            int(...
                simplify(...
                    (2*cos(alpha1)+2*cos(alpha2))*t+...
                    opt*(2*cos(alpha1)*t*b1+2*cos(alpha2)*t*b1*a1^2)),...
                alpha1,0,2*pi),...
            alpha2,0,2*pi)...
        *4/(8*4*sym(pi)^2)

    end
end

```

end

ctxpat1

```
function [vmax,dmax,a0grid,alphagrid,lammax,inds] = ctxpat1
```

```
%function [vmax,dmax,a0grid,alphagrid,lammax,inds] = ctxpat1
```

```
%
```

```
% Determine cortical pattern developing from  
% an instability in the six-dimensional xy model.
```

```
%
```

```
% The cortex vector is:
```

```
%
```

```
%      [(m-m0)/m0 ]      [ v(:, :, 1)   ]  
%      [s(:, :, 1) ]      [ v(:, :, 2)   ]  
% v =  [s(:, :, 2) ] =    [ v(:, :, 3)   ]  
%      [chi1(:, :, 1)]     [ v(:, :, 4)   ]  
%      [chi2(:, :, 2)]     [ v(:, :, 5)   ]  
%      [rh0              ]      [ v(:, :, 6)   ]
```

```
%
```

```
% The "dynamics" are given by
```

```
%
```

```
% (d/dt) u(:, :, j) = conv(u1, kj1, 'same') + ... + conv(u6, kj6, 'same')
```

```
%
```

```
% or, in the Fourier domain,
```

```
%
```

```
% (d/dt) U(:, :, j) = Kj1.*U(:, :, 1) + Kj2.*U(:, :, 2) + ... + Kj6.*U(:, :, 6)
```

```
%
```

```
% It's faster (by a factor of c. 100) to stay in the Fourier domain
```

```
% with occasional forays into position space for visualization and
```

```
% results.
```

```
%
```

```
% Capitalization conventions:
```

```
% U(:, :, j) = fft2(u(:, :, j))
```

```
% Kjk = fft2(kjk)
```

```
% etc.
```

```

% a menagerie of numerical convolution kernels
global AA Ax1 Ax2 Arr Ahv Aob
global GG Gx1 Gx2 G11 G22 G12 Grr Ghv Gob
global G111 G112 G122 G222 Ghv1 Ghv2 Gob1 Gob2 Grr1 Grr2
global Grrrr Grrhv Grrob Ghvhv Ghvob Gobob

%%% Geometry of simulation

n = 16;      % n x n cortical grid represents a 1x1 mm^2 region.
N = 2*n;    % N x N cortical grid total
mu = .5;    % retinocortical magnification factor dX/dR (mm CTX/mm LGN)

%Geniculate coordinates -- cortical given by dCTX = mu dLGN

% (2mm)^2 region of LGN
[x1,x2] = meshgrid(linspace(-1,1,N),linspace(-1,1,N));
r = sqrt(x1.^2+x2.^2);          % radial distance

%%% CONVOLUTION KERNELS %%%

% convolution kernels will be represented in Fourier space
% recall 1 mm^2 = n^2 units.

% nominal receptive field width -- 200 microns (in LGN)
sig = 0.2;
% correlation width in LGN -- sigr in paper -- 200 microns (in LGN)
sigG = 0.2;
% positive Mexican Hat width -- 100 microns (in LGN, under magnification)
sigp = 0.1;
% negative Mexican Hat width -- 300 microns (in LGN, under magnification)
sigm = 0.3;

%% try this..
%sigG = 0.05

% Difference of Gaussians and related kernels
A = (exp(-(r/(2*sigp)).^2)/(2*pi*sigp^2) ...

```

```

- exp(-(r/(2*sigm)).^2)/(2*pi*sigm^2));

AA = (1/n^2)*fft2(A);
Ax1 = (1/n^2)*fft2(A.*x1/mu);
Ax2 = (1/n^2)*fft2(A.*x2/mu);
Arr = (1/n^2)*fft2(A.*(r.^2)/mu^2);
% horizontal vs vertical kernel
Ahv = (1/n^2)*fft2(A.*(x1.^2 - x2.^2)/mu^2);
% +oblique vs -oblique kernel
Aob = (1/n^2)*fft2(A.*(2*x1.*x2)/mu^2);

% Gaussian LGN correlations and related kernels
G = exp(-(r/(2*mu*sqrt(2)*sigG)).^2)/(2*pi*(sqrt(2)*sigG)^2);

GG = (1/n^2)*fft2(G);
Gx1 = (1/n^2)*fft2(G.*x1/(2*mu));
Gx2 = (1/n^2)*fft2(G.*x2/(2*mu));
G11 = (1/n^2)*fft2(G.*x1.^2/((2*mu)^2));
G22 = (1/n^2)*fft2(G.*x2.^2/((2*mu)^2));
G12 = (1/n^2)*fft2(G.*x1.*x2/((2*mu)^2));
Grr = (1/n^2)*fft2(G.*(r.^2)/((2*mu)^2));
Ghv = (1/n^2)*fft2(G.*(x1.^2-x2.^2)/((2*mu)^2));
Gob = (1/n^2)*fft2(G.*(2*x1.*x2)/((2*mu)^2));
G111 = (1/n^2)*fft2(G.*(x1.^3)/((2*mu)^3));
G112 = (1/n^2)*fft2(G.*(x1.^2).*x2/((2*mu)^3));
G122 = (1/n^2)*fft2(G.*x1.*(x2.^2)/((2*mu)^3));
G222 = (1/n^2)*fft2(G.*(x2.^3)/((2*mu)^3));
Ghv1 = (1/n^2)*fft2(G.*(x1.^2-x2.^2).*x1/((2*mu)^3));
Ghv2 = (1/n^2)*fft2(G.*(x1.^2-x2.^2).*x2/((2*mu)^3));
Gob1 = (1/n^2)*fft2(G.*(2*x1.*x2).*x1/((2*mu)^3));
Gob2 = (1/n^2)*fft2(G.*(2*x1.*x2).*x2/((2*mu)^3));
Grr1 = (1/n^2)*fft2(G.*(r.^2).*x1/(2*mu)^3);
Grr2 = (1/n^2)*fft2(G.*(r.^2).*x2/(2*mu)^3);
Grrrr = (1/n^2)*fft2(G.*(r.^4)/((2*mu)^4));
Grrhv = (1/n^2)*fft2(G.*(r.^2).*x1.^2-x2.^2)/((2*mu)^4));
Grrob = (1/n^2)*fft2(G.*(r.^2).*x1.*x2)/((2*mu)^4));
Ghvhv = (1/n^2)*fft2(G.*(x1.^2-x2.^2).^2/((2*mu)^4));

```

```

Ghvob = (1/n^2)*fft2(G.*(x1.^2-x2.^2).*(2*x1.*x2)/((2*mu)^4));
Gobob = (1/n^2)*fft2(G.*(2*x1.*x2).^2/((2*mu)^4));

%keyboard

%%% Search iteratively through part of parameter space for bifurcation
%a00 = 3; a01 = 4; na0 = 25;
%alpha0 = 4; alpha1 = 5; nalpha = 20;
a00 = 1; a01 = 4; na0 = 16;
alpha0 = 1; alpha1 = 5; nalpha = 15;
a0s = linspace(a00,a01,na0);
alphas = linspace(alpha0,alpha1,nalpha);

ndim = 6; % dimensions of cortical map
ndim = 5; % dimensions of reduced cortical map, 5x5 system
lammax = zeros(nalpha,na0); % record eigenvalues of maximal modes
% record which modes were maximal (by indices within K)
inds = zeros(nalpha,na0,4);
vmax = zeros(nalpha,na0,ndim,ndim,ndim);
dmax = zeros(nalpha,na0,ndim,ndim,ndim);

for ja0 = 1:na0
    for jalpha = 1:nalpha

        %%% Interactions between different map components

        Kout = 1; % damping coefficient on fan-out
        Kin = 1; % damping coefficient on fan-in
        m0 = 1; % baseline fan-in weight
        %a0 = 4; % strength of intracortical interaction *
                % magnitude of LGN correlation fcn.
        %alpha = 4; % decay rate affecting all variables
        a0 = a0s(ja0);
        alpha = alphas(jalpha);

        K = Kinteract(alpha,a0,m0,Kin,Kout,sig,sigG);
        % study system without rho-interactions

```

```

%K(:,:,,6) = zeros(N,N,6,1);
%K(:,:,6,:) = zeros(N,N,1,6);
K = K(:,:,1:5,1:5);
[rs cs ndim1 ndim2] = size(K); ndim = ndim1;

% Want max and min of spectrum of K(k1,k2,1:ndim,1:ndim)
% for each wave vector index (k1,k2).

% Record all eigenvalues in rs x rc x ndim array
for k1 = 1:rs
    for k2 = 1:cs
        lambda(k1,k2,1:ndim) = eig(squeeze(K(k1,k2,:,:)));
        % alternative -- two largest real parts
        %lambda(k1,k2,1:2) = eigs(squeeze(K(k1,k2,:,:)),'LR',2);
    end
end
% Find the largest eigenvalue(s). (There should be pairs
% in orthogonal fourier vector directions, by D4 invariance.)
maxind = find(real(lambda(:)) == max(real(lambda(:))));
% k1max, k2max give the Fourier component
% jjmax gives which eigenvalue
[k1max, k2max, jjmax] = ind2sub([N,N,ndim],maxind);
modes = length(k1max);
for jmode = 1:modes
    [vmax(jalpha,ja0,:,: ,jmode),dmax(jalpha,ja0,:,: ,jmode)] = ...
    eig(squeeze(K(k1max(jmode),k2max(jmode),,:,:)));
end
%keyboard
inds(jalpha,ja0,1:length(maxind)) = maxind;
lammax(jalpha,ja0) = lambda(maxind(1));
[ja0,jalpha]
end
end

figure
[a0grid,alphagrid]=meshgrid(a0s,alphas);
%bifplot1(a0grid,alphagrid,lammax); axis equal,shading flat

```

```

%keyboard

%%=====%%
%%% SUBROUTINES
%%=====%%
function K = Kinteract(alpha,a0,m0,Kin,Kout,sig,sigG)

global AA Ax1 Ax2 Arr Ahv Aob
global GG Gx1 Gx2 G11 G22 G12 Grr Ghv Gob
global G111 G112 G122 G222 Ghv1 Ghv2 Gob1 Gob2 Grr1 Grr2
global Grrrr Grrhv Grrob Ghvhv Ghvob Gobob

% Interaction Parameters
% correlation width in LGN -- 200 microns (in LGN)
if nargin < 7, sigG = 0.2; end
% nominal receptive field width -- 200 microns (in LGN)
if nargin < 6, sig = 0.2; end
if nargin < 5, Kout = 1; end          % damping coefficient on fan-out
if nargin < 4, Kin = 1; end         % damping coefficient on fan-in
if nargin < 3, m0 = 1; end          % baseline fan-in weight
if nargin < 2, a0 = 4; end          % strength of intracortical interaction *
                                     % magnitude of LGN correlation fcn.
if nargin < 1, alpha = 4; end       % decay rate affecting all variables

% Influence of all variables on the first variable
%(Fan-in deviation / base fan-in)
K11 = m0*(-Kin - Kout*GG)+ a0*AA - alpha;
K12 = -m0*Kout*Gx1/sig^2;
K13 = -m0*Kout*Gx2/sig^2;
K14 = -m0*Kout*Ghv/(4*sig^4);
K15 = -m0*Kout*Gob/(4*sig^4);
K16 = -m0*Kout*(Grr+GG*sig^2/2)/(2*sig^4);

% Influence of all variables on the second and third variables
% s(:, :, 1) and s(:, :, 2) -- retinotopic deviation vector

```

```

K21 = -a0*Ax1 - Kout*m0*Gx1;
K31 = -a0*Ax2 - Kout*m0*Gx2;

K22 = a0*AA - alpha - Kout*m0*(sig^2*GG/2 - G11)/sig^2;
K32 =          - Kout*m0*G12/sig^2;

K23 =          - Kout*m0*G12/sig^2;
K33 = a0*AA - alpha - Kout*m0*(sig^2*GG/2 - G22)/sig^2;

K24 = -Kout*m0*(sig^2*(+Gx1) - (G111 - G122))/(4*sig^4);
K34 = -Kout*m0*(sig^2*(-Gx2) - (G112 - G222))/(4*sig^4);

K25 = -Kout*m0*(sig^2*Gx2 - 2*G112)/(4*sig^4);
K35 = -Kout*m0*(sig^2*Gx1 - 2*G122)/(4*sig^4);

K26 = -Kout*m0*(2*sig^2*Gx1 - Grr1)/(2*sig^4);
K36 = -Kout*m0*(2*sig^2*Gx2 - Grr2)/(2*sig^4);

% Influence of all variables on the fourth and fifth variables
% chi(:, :, 1) and chi(:, :, 2) -- orientation tuning vector

K41 = a0*Ahv - Kout*m0*Ghv;
K51 = a0*Aob - Kout*m0*Gob;

K42 = +2*a0*Ax1 - Kout*m0*(Ghv1 - Gx1*sig^2)/sig^2;
K52 = +2*a0*Ax2 - Kout*m0*(Gob1 - Gx2*sig^2)/sig^2;
%
K43 = -2*a0*Ax2 - Kout*m0*(Ghv2 + Gx2*sig^2)/sig^2;
K53 = +2*a0*Ax1 - Kout*m0*(Gob2 - Gx1*sig^2)/sig^2;
%K42 = -2*a0*Ax1 - Kout*m0*(Ghv1 - Gx1*sig^2)/sig^2;
%K52 = -2*a0*Ax2 - Kout*m0*(Gob1 - Gx2*sig^2)/sig^2;
%??
%K43 = +2*a0*Ax2 - Kout*m0*(Ghv2 + Gx2*sig^2)/sig^2;
%K53 = -2*a0*Ax1 - Kout*m0*(Gob2 - Gx1*sig^2)/sig^2;

K44 = a0*AA - alpha - Kout*m0*(Ghvhv - Grr*2*sig^2 + GG*sig^4)/(4*sig^4);
K54 =          - Kout*m0*(Ghvob)/(4*sig^4);

```

```

K45 = -Kout*m0*(Ghvob)/(4*sig^4);
K55 = a0*AA - alpha - Kout*m0*(Gobob - Grr*2*sig^2 + GG*sig^4)/(4*sig^4);

K46 = -Kout*m0*(Grrhv - (3*sig^2)*Ghv)/(2*sig^4);
K56 = -Kout*m0*(Grrob - (3*sig^2)*Gob)/(2*sig^4);

% Influence of all variables on the sixth variable (rho) --
% receptive field width deviation

K61 = a0*Arr + AA*sigG^2 - Kout*m0*Grr;
K62 = 2*a0*Ax1 - Kout*m0*(G111+G122-sig^2*Gx1)/sig^2;
K63 = 2*a0*Ax2 - Kout*m0*(G112+G222-sig^2*Gx2)/sig^2;
K64 = -Kout*m0*(Grrhv-Ghv*2*sig^2)/(4*sig^4);
K65 = -Kout*m0*(Grrob-Gob*2*sig^2)/(4*sig^4);
K66 = a0*AA - alpha - Kout*m0*(Grrrr - Grr*3*sig^2 - GG*sig^4/2)/(2*sig^4);

%keyboard

%%% Identify eigenvalue with largest real part.
[rs cs] = size(K11); % size of spatial grid = size of fourier grid
ndim = 6; % number of dimensions (variables).

K = zeros(rs,cs,ndim,ndim);

K(:,:,1,1) = K11; K(:,:,1,2) = K12; K(:,:,1,3) = K13;
K(:,:,1,4) = K14; K(:,:,1,5) = K15; K(:,:,1,6) = K16;

K(:,:,2,1) = K21; K(:,:,2,2) = K22; K(:,:,2,3) = K23;
K(:,:,2,4) = K24; K(:,:,2,5) = K25; K(:,:,2,6) = K26;

K(:,:,3,1) = K31; K(:,:,3,2) = K32; K(:,:,3,3) = K33;
K(:,:,3,4) = K34; K(:,:,3,5) = K35; K(:,:,3,6) = K36;

K(:,:,4,1) = K41; K(:,:,4,2) = K42; K(:,:,4,3) = K43;
K(:,:,4,4) = K44; K(:,:,4,5) = K45; K(:,:,4,6) = K46;

```

```
K(:, :, 5, 1) = K51; K(:, :, 5, 2) = K52; K(:, :, 5, 3) = K53;
    K(:, :, 5, 4) = K54;    K(:, :, 5, 5) = K55; K(:, :, 5, 6) = K56;
```

```
K(:, :, 6, 1) = K61; K(:, :, 6, 2) = K62; K(:, :, 6, 3) = K63;
    K(:, :, 6, 4) = K64;    K(:, :, 6, 5) = K65; K(:, :, 6, 6) = K66;
```

```
%%=====%%
```

```
function bifplot1(a,b,lam,ind1,ind2,ind3,ind4)
```

```
%function bifplot1(a,b,lam,ind1,ind2,ind3,ind4)
```

```
%
```

```
% Given an array of eigenvalues LAM sampled at
% different values of two parameters A and B,
% and up to four (optional) binary indicator array
% IND1..IND4: plot eigenvalues identifying
% complex numbers with a color space; also draw
% lines indicating boundary between real an complex,
% negative vs positive real part, and regions where
% INDS take on different values.
```

```
%
```

```
[r,c]=size(a);
```

```
maxeigsize = max(abs(lam(:).*real(lam(:)>0))); % largest + eigenvalue
```

```
%maxeigsize = max(abs(lam(:))); % largest magnitude
```

```
ncolor = 256; % size of hue-saturated colormap
```

```
cmap = hsv(ncolor); % hue-saturated colormap
```

```
for jb = 1:(r-1)
```

```
    for ja = 1:(c-1)
```

```
        theta = angle(lam(jb,ja));
```

```
        rho = abs(lam(jb,ja));
```

```
        %plotcolor = cmap(mod(floor(ncolor*theta/(2*pi))+ncolor/2,ncolor)... + 1) ...
```

```
        % * rho/maxeigsize;
```

```
        plotclr = cmap(mod(floor(ncolor*theta/(2*pi))+ncolor/2,ncolor) + 1,:) ...
```

```
        * rho/maxeigsize;
```

```
        patch(a(jb,ja)+(a(1,2)-a(1,1))*[0 1 1 0 0],...
```

```

        b(jb,ja)+(b(2,1)-b(1,1))*[0 0 1 1 0],...
        ...%plotcolor);
    plotclr);
    hold on
end
end
%caxis([1, ncolor]), colorbar
%colorbar
axis equal,%shading flat

[c1,h1]=contour(a,b,real(lam)>0,1);
set(plot(c1(1,2:length(c1)),c1(2,2:length(c1)),'w'),'LineWidth',5)
hold on

[c2,h2]=contour(a,b,imag(lam)==0,1);
set(plot(c2(1,2:length(c2)),c2(2,2:length(c2)),'w'),'LineWidth',5)
hold on

if nargin > 3
    [c3,h3]=contour(a,b,ind1,1);
    % plot(c3(1,2:length(c3)),c3(2,2:length(c3)),'k')
    hold on
end

if nargin > 4
    [c4,h4]=contour(a,b,ind2,1);
    % plot(c4(1,2:length(c4)),c4(2,2:length(c4)),'k')
    hold on
end

if nargin > 5
    [c5,h5]=contour(a,b,ind3,1);
    % plot(c5(1,2:length(c5)),c5(2,2:length(c5)),'k')
    hold on
end

if nargin > 6

```

```

[c6,h6]=contour(a,b,ind4,1);
% plot(c6(1,2:length(c6)),c6(2,2:length(c6)),'k')
hold on
end

```

E.13 General Utilities

addbdy Adds a boundary to a matrix – for zero-flux boundary conditions.

kernel4 Generates difference-of-Gaussians convolution kernel with specified + and - widths.

kernel5 Generates difference-of-Gaussians convolution kernel with specified + and - widths and a given L2 norm.

nowave Generates a grid of orientations in a roll-pattern with a proscribed amount of noise.

addbdy

```

function mout = addbdy(m,r1,c1,r2,c2)

%function mout = addbdy(m,r1,c1,r2,c2)
%
% Adds a boundary to matrix M equal to the adjacent
% row or column, of thickness r1 before the first row,
% r2 after the last row, c1 before the first column,
% and c2 after the last column.
% By default, r2 := r1 and c2 := c1.
% Default thickness is one.
%
% Example:
% a = [1 2 3; 4 5 6; 7 8 9];
% addbdy(a,0,1,2,3)
%
%      1      1      2      3      3      3      3

```

```

%   4   4   5   6   6   6   6
%   7   7   8   9   9   9   9
%   7   7   8   9   9   9   9
%   7   7   8   9   9   9   9
%
% Useful for setting up zero-flux boundary conditions!
% See also ADDBDYP (periodic), SUBBDY, PAD, and CLIP.

[rm cm] = size(m);

if nargin < 3, r1 = 1; c1 = 1; end
if nargin < 5, r2 = r1; c2 = c1; end

mout = zeros(rm+r1+r2,cm+c1+c2);

% middle

mout(r1+1 : r1+rm,      c1+1 : c1+cm) = m;

% sides

mout(1 : r1,           c1+1 : c1+cm) = ones(r1,1)*m(1,:);
mout(r1+rm+1 : r1+r2+rm, c1+1 : c1+cm) = ones(r2,1)*m(rm,:);
mout(r1+1 : r1+rm,     1 : c1) = m(:,1)*ones(1,c1);
mout(r1+1 : r1+rm,     c1+cm+1 : c1+c2+cm) = m(:,cm)*ones(1,c2);

% corners

mout(1 : r1,          1 : c1) = m(1,1)*ones(r1,c1);
mout(1 : r1,          c1+cm+1 : c1+c2+cm) = m(1,cm)*ones(r1,c2);
mout(r1+rm+1 : r1+r2+rm, 1 : c1) = m(rm,1)*ones(r2,c1);
mout(r1+rm+1 : r1+r2+rm, c1+cm+1 : c1+c2+cm) = m(rm,cm)*ones(r2,c2);

kernel4

function K = kernel4(d1,d2,d3,bias)

```

```

%function K = kernel4(d1,d2,d3,bias)
%
% Discrete approximation of a 2-d difference of Gaussians.
% Returns an N x N matrix of weights. (N = 2*d3+1)
% D1 is approx. half-width of first gaussian, D2 of second.
% BIAS is the net integral of area under the weights; default = 0.
% UNLIKE KERNEL3, self interaction K(1+d3, 1+d3) is NOT set to zero.
% For a single gaussian set d2 = large and bias = 1.

if nargin < 4, bias = 0; end

n = 2*d3 + 1;
K = zeros(n);
j = 1:n; k = 1:n;
x = (j - d3 - 1)' * ones(1,n);
y = ones(n,1) * (k - d3 - 1);
dist = sqrt(x.^2 + y.^2);

K1(j,k) = gauss(dist, d1);
K2(j,k) = gauss(dist, d2);

%K1(d3+1,d3+1) = 0;           % these lines are the only difference
%K2(d3+1,d3+1) = 0;           % between KERNEL3 and KERNEL4

K2 = K2 * (sum(sum(K1)) - bias) / sum(sum(K2)) ;

K = K1 - K2;

% Bug: the range of DOGs with a given area is 2-dimensional.
% This program picks out a 1-par. family by holding the
% positive gaussian K1 fixed for any choice of BIAS.
% Don't know how much difference this makes.

```

kernel5

```

function K = kernel5(d1,d2,d3,bias)

%function K = kernel5(d1,d2,d3,bias)
%
% Discrete approximation of a 2-d difference of Gaussians.
% Returns an N x N matrix of weights. (N = 2*d3+1)
% D1 is approx. half-width of first gaussian, D2 of second.
% BIAS is the net integral of area under the weights; default = 0.
% UNLIKE KERNEL3, self interaction K(1+d3, 1+d3) is NOT set to zero.
% For a single gaussian set d2 = large and bias = 1.
%
% Same as KERNEL4, but generates K with fixed L2 norm sum2(K.^2) = 1.

if nargin < 4, bias = 0; end

n = 2*d3 + 1;          % pixel-size of the resulting kernel
K = zeros(n);
j = 1:n; k = j;
x = (j - d3 - 1)' * ones(1,n);
y = ones(n,1) * (k - d3 - 1);
dist = sqrt(x.^2 + y.^2);

K1 = gauss(dist, d1)/(d1*sqrt(pi/2));
    %K1=K1/sqrt(sum2(K1.^2)/n^2);
K2 = gauss(dist, d2)/(d2*sqrt(pi/2));
    %K2=K2/sqrt(sum2(K2.^2)/n^2);
% start with Gaussians of unit L2 norm.

%K1(d3+1,d3+1) = 0;          % these lines are the only difference
%K2(d3+1,d3+1) = 0;          % between KERNEL3 and KERNEL4

% Rescale to fit mean=bias and mean-square = norm 1:
% K = C1 K1 - C2 K2, Cj > 0.

k1 = sum2(K1);

```

```

k2 = sum2(K2);
k11 = sum2(K1.^2); % = 1
k12 = sum2(K1.*K2);
k22 = sum2(K2.^2); % = 1

% using the L2 norm leads to a quadratic equation for Cj with coefficients
% a,b,c.

a = k11*k2^2 - 2*k2*k12*k1 + k22*k1^2;
b = 2*bias*(k11*k2 - k12*k1);
c = k11*bias^2 - k1^2;
q = b^2 - 4*a*c;    if q < 0 , error('KERNEL5: BIAS too large!'), end

c2 = (-b + sqrt(q))/(2*a);
c1 = (c2*k2 + bias) / k1;

K = c1*K1 - c2*K2;

%=====

%visualization for debugging
if 0 % set to 1 to include this part
    clf
    plot(K(:,d3+1)),hold on,plot(c1*K1(:,d3+1),'g'),plot(-c2*K2(:,d3+1),'r')
    grid on

    [sum2(K),sum2(K.*K)]

    figure(gcf+1)
    [a1 a2]=meshgrid(0:.1:5.0,0:.1:5.0);
    [cs, h]=contour(0:.1:5.0,0:.1:5.0, ...
        a1.^2*k11-2*k12*a1.*a2+k22*a2.^2, ...
        [1 2 3 4 5]);

    clabel(cs,h,[1 2 3 4 5])
    view([0 90])
    grid on

```

```

hold on
plot(a1(1,:),(a1(1,:)*k1 - bias)/k2,'+')
xlabel('c1'),ylabel('c2')
%figure
%surf(a1.^2*k11-2*k12*a1.*a2+k22*a2.^2)
hold off
end

```

nowave

```

function x = nowave(noise,gridsize, k1, k2)

%function x = nowave(noise,gridsize, k1, k2)
%
% Generates X, a GRIDSIZExGRIDSIZE array of angles 0 <= X <= Pi
% on a wave with reciprocal vector [K1 K2] (gridsize ~ Pi spatial unit)
% with each point's angle perturbed with gaussian-wrapped noise
% of width NOISE.
%
% Defaults: NOISE = 0; GRIDSIZE = 50; [K1 K2] = [? 0].

k = 4;
if nargin == 3, k = k1; end
if nargin <3, k1 = k; k2 = 0; end
if nargin < 2, gridsize = 50; end
if nargin < 1, noise = 0; end

x = zeros(gridsize);

hgs = (gridsize - 1)/2; % half GRIDSIZE; offset by 1/2
[h v] = meshgrid(-hgs:hgs,-hgs:hgs); % Horizontal, Vertical

x = pi*(k1*h + k2*v)/gridsize;
dx = noise * randn(size(x));
x = x+dx;
x = mod(x,pi);

```

REFERENCES

- [1] Kurt Binder and Dieter W. Heermann. *Monte Carlo Simulation in Statistical Physics: An Introduction*, volume 80 of *Solid-State Sciences*. Springer Verlag, Heidelberg, third edition, 1997.
- [2] Gary Blasdel. Differential imaging of ocular dominance and orientation selectivity in monkey striate cortex. *The Journal of Neuroscience*, 12(8):3115–3138, August 1992.
- [3] Gary Blasdel. Orientation selectivity, preference, and continuity in monkey striate cortex. *The Journal of Neuroscience*, 12(8):3139–3161, August 1992.
- [4] Gary Blasdel and Darlene Campbell. Functional retinotopy of monkey visual cortex. In preparation, 2000.
- [5] G.G. Blasdel and G. Salama. Voltage sensitive dyes reveal a modular organization in monkey striate cortex. *Nature*, 321:579–585, 1986.
- [6] T. Bonhoeffer and A. Grinvald. Orientation columns in cat are organized in pinwheel-like patterns. *Nature*, 353:429–431, 1991.
- [7] Paul C. Bressloff, Jack D. Cowan, Martin Golubitsky, and Peter J. Thomas. Scalar and pseudoscalar bifurcations motivated by pattern formation on the visual cortex. *Nonlinearity*, 14:739–775, 2001.
- [8] Paul C. Bressloff, Jack D. Cowan, Martin Golubitsky, Peter J. Thomas, and Matthew C. Wiener. Geometric visual hallucinations, Euclidean symmetry, and the functional architecture of visual cortex. *Phil. Trans. Roy. Soc. Lond. B.*, 356:299–330, 2001.

- [9] Paul C. Bressloff, Jack D. Cowan, Martin Golubitsky, Peter J. Thomas, and Matthew C. Wiener. What geometric visual hallucinations tell us about the visual cortex. *Neural Computation*, 14(3):473–491, March 2002.
- [10] F. H. Busse. Non-linear properties of thermal convection. *Reports on Progress in Physics*, 41:1929–1967, 1978.
- [11] John Cardy. *Scaling and Renormalization in Statistical Physics*, volume 5 of *Cambridge Lecture Notes in Physics*. Cambridge University Press, 1996.
- [12] S. Chandrasekhar. *Hydrodynamic and Hydromagnetic Stability*. Oxford University Press, 1961.
- [13] Jack D. Cowan and Edward A. Friedman. Simple spin models for the development of ocular dominance columns and iso-orientation patches. In R. Lippmann, J. Moody, and D. Touretzky, editors, *Advances in Neural Information Processing Systems 3*, pages 26–31. Morgan Kaufmann, 1991.
- [14] Jack D. Cowan and Schmucl Winograd. *Reliable Computation in the Presence of Noise*. MIT Press, 1963.
- [15] J.D. Cowan. Some remarks on channel bandwidths for visual contrast detection. *Neurosci. Res. Program. Bull.*, 15:492–517, 1977.
- [16] Michael C. Crair, Deda C. Gillespie, and Michael P. Stryker. The role of visual experience in the development of columns in the cat visual cortex. *Science*, 279:566–570, 1998.
- [17] Michael C. Crair, Edward S. Ruthazer, Deda C. Gillespie, and Michael P. Stryker. Ocular dominance peaks at pinwheel center singularities of the orientation map in cat visual cortex. *J. Neurophys.*, 77:3381–3385, 1997.
- [18] A. Das and C. D. Gilbert. Distortions of visuotopic map match orientation singularities in primary visual cortex. *Nature*, 387:594–598, 1997.

- [19] Benoit Dionne and Martin Golubitsky. Planforms in two and three dimensions. *Z. Angew. Math. Phys.*, 43(1):36–62, 1992.
- [20] R. Durbin, R. Szeliski, and A. Yuille. An analysis of the elastic net approach to the traveling salesman problem. *Neural Computation*, 1(3):348–358, 1989.
- [21] Richard Durbin and David Willshaw. An analogue approach to the travelling salesman problem using an elastic net method. *Nature*, 326(6114):689–691, 16 April 1987.
- [22] G.B. Ermentrout and J.D. Cowan. A mathematical theory of visual hallucination patterns. *Biological Cybernetics*, 34:137–150, 1979.
- [23] Udo Ernst, Klaus Pawelzik, Misha Tsodyks, and Terrence J. Sejnowski. Relation between retinotopical and orientation maps in visual cortex. *Neural Computation*, 11(2):375–379, 15 February 1999.
- [24] E. Erwin and K.D. Miller. Modeling joint development of ocular dominance and orientation maps in primary visual cortex. In J.M. Bower, editor, *Computational Neuroscience: Trends in Research 1995*, pages 179–184. Academic Press, 1996.
- [25] E. Erwin, K. Obermayer, and K. Schulten. Models of orientation and ocular dominance columns in the visual cortex: A critical comparison. *Neural Computation*, 7(3):425–468, May 1995.
- [26] A. Fassler and E. Stiefel. *Group Theoretical Methods and Their Applications*. Birkhauser, Boston, Basel, Berlin, 1992. with English translation by Baoswan Dzung Wong.
- [27] Albert Fässler and Eduard Stiefel. *Group Theoretical Methods and Their Applications*. Birkhäuser, Boston, 1992. English translation by Baoswan Dzung Wong.
- [28] D. Ferster and K.D. Miller. Neural mechanisms of orientation selectivity in the visual cortex. *Annual Reviews of Neuroscience*, 23:441–471, 2000.

- [29] Charles D. Gilbert. Horizontal integration and cortical dynamics. *Neuron*, 9:1–13, July 1992.
- [30] Martin Golubitsky, Ian Stewart, and David G. Schaeffer. *Singularities and Groups in Bifurcation Theory*, volume II of *Applied Mathematical Sciences*. Springer-Verlag, New York, 1988.
- [31] A. F. Häussler and Christof von der Malsburg. Development of retinotopic projections: an analytical treatment. *J. Theoret. Neurobiol.*, 2:47–73, 1983.
- [32] D. O. Hebb. *The Organization of Behavior; A Neuropsychological Theory*. John Wiley & Sons, Inc., New York, 1949.
- [33] Sherwin E. Hua, Lina L. Massone, and James C. Houk. Model of topographic map development guided by a transiently expressed repulsion molecule. *NeuroReport*, 4(12):1319–1322, December 1993.
- [34] David H. Hubel and Torsten N. Wiesel. Receptive fields of single neurons in the cat's striate cortex. *J. Physiol.*, 148:574–591, 1959.
- [35] David H. Hubel and Torsten N. Wiesel. Receptive fields, binocular interaction, and functional architecture in the cat's visual cortex. *J. Physiol.*, 160:106–154, 1962.
- [36] David H. Hubel and Torsten N. Wiesel. Receptive fields and functional architecture of monkey striate cortex. *J. Physiol.*, pages 215–243, 1968.
- [37] David H. Hubel and Torsten N. Wiesel. Laminar and columnar distribution of geniculo-cortical fibers in the macaque monkey. *Journal of Comparative Neurology*, 146:421–450, 1972.
- [38] David H. Hubel and Torsten N. Wiesel. Sequence regularity and geometry of orientation columns in the monkey striate cortex. *Journal of Comparative Neurology*, 158(3):267–294, 1 December 1974.

- [39] David H. Hubel and Torsten N. Wiesel. Uniformity of monkey striate cortex: a parallel relationship between field size, scatter and magnification factor. *Journal of Comparative Neurology*, 158:295–306, 1974.
- [40] David H. Hubel, Torsten N. Wiesel, and Michael P. Stryker. Anatomical demonstration of orientation columns in macaque monkey. *Journal of Comparative Neurology*, 177:361–380, 1978.
- [41] Mark Hübener, Doron Shoham, Amiram Grinvald, and Tobias Bonhoeffer. Spatial relationships among three columnar systems in cat area 17. *J. Neurosci.*, 17(23):9270–84, 1997.
- [42] Eric R. Kandel, James H. Schwartz, and Thomas M. Jessell, editors. *Principles of Neural Science*. Elsevier, New York, third edition, 1991.
- [43] Teuvo Kohonen. Self-organized formation of topologically correct feature maps. *Biological Cybernetics*, 43:59–69, 1982.
- [44] Teuvo Kohonen. *Self Organizing Maps*. Springer, 1995.
- [45] J. M. Kosterlitz and D. J. Thouless. *Progress in Low Temperature Physics*, volume VII B, chapter 5: Two-dimensional Physics, pages 373–433. North-Holland, 1978.
- [46] Juan K. Lin, David G. Grier, and Jack D. Cowan. Faithful representation of separable distributions. *Neural Computation*, 9(6):1305 – 1320, August 15 1997.
- [47] Jennifer S. Lund, 1999. Personal Communication.
- [48] Pedro E. Maldonado, Imke Gödecke, Charles M. Gray, and Tobias Bonhoeffer. Orientation selectivity in pinwheel centers in cat striate cortex. *Science*, 276:1551–1555, 6 June 1997.
- [49] Pedro E. Maldonado and Charles M. Gray. Heterogeneity in local distributions of orientation-selective neurons in the cat primary visual cortex. *Visual Neuroscience*, 13:509–516, 1996.

- [50] K. V. Mardia. *Statistics of Directional Data*. Probability and Mathematical Statistics. Academic Press, New York, 1972.
- [51] N. D. Mermin and H. Wagner. Absence of Ferromagnetism or Antiferromagnetism in One- or Two-Dimensional Isotropic Heisenberg Models. *Physical Review Letters*, 17(22):1133–1136, 1966.
- [52] K.D. Miller. Derivation of Hebbian equations from a nonlinear model. *Neural Computation*, 2:319–331, 1990.
- [53] K.D. Miller. Development of orientation columns via competition between on- and off-center inputs. *NeuroReport*, 3:73–76, 1992.
- [54] K.D. Miller. *Models of Neural Networks III*, chapter Receptive Fields and Maps in the Visual Cortex: Models of Ocular Dominance and Orientation Columns, pages 55–78. Springer-Verlag, NY, 1996.
- [55] K.D. Miller, E. Erwin, and A. Kayser. Is the development of orientation selectivity instructed by activity? *Journal of Neurobiology*, 41:44–57, 1999.
- [56] K.D. Miller and M.P. Stryker. *Connectionist Modeling and Brain Function: The Developing Interface*, chapter The Development of Ocular Dominance Columns: Mechanisms and Models, pages 255–305. MIT Press, 1990.
- [57] Willard Miller, Jr. *Symmetry Groups and their Applications*, volume 50 of *Pure and Applied Mathematics*. Academic Press, New York and London, 1972.
- [58] Penelope C. Murphy, Simon G. Duckett, and Adam M. Sillito. Feedback connections to the lateral geniculate nucleus and cortical response properties. *Science*, 286(5444):1552–1554, 19 November 1999.
- [59] James D. Murray. *Mathematical Biology*. Biomathematics Texts. Springer-Verlag, 1993.
- [60] Klaus Obermayer and Gary Blasdel. Geometry of orientation and ocular dominance columns in monkey striate cortex. *The Journal of Neuroscience*, 13:4114–4129, 1993.

- [61] Giorio Parisi. *Statistical Field Theory*, volume 66 of *Frontiers in Physics*. Addison-Wesley, 1988.
- [62] I. Prigogine and Lefever R. Stability and self-organization in open systems. in *Membranes, Dissipative Structures, and Evolution*. Wiley, 1974. Nicolis and Lefever, editors.
- [63] H. Ritter and K. Schulten. On the stationary state of Kohonen's self-organizing sensory mapping. *Biological Cybernetics*, 54:99–106, 1986.
- [64] D. H. Sattinger. *Group Theoretic Methods in Bifurcation Theory*. University of Chicago Department of Mathematics Lecture Notes in Mathematics, 1978.
- [65] E. Schwartz. Spatial mapping in the primate sensory projection: analytic structure and relevance to projection. *Biological Cybernetics*, 25:181–194, 1977.
- [66] Amir Shmuel and Amiram Grinvald. Functional organization for direction of motion and its relationship to orientation maps in cat area 18. *J. Neurosci.*, 16(21):6945–64, 1996.
- [67] Harel Z. Shouval, David H. Goldberg, Judson P. Jones, Martin Beckerman, and Leon N. Cooper. Structured long-range connections can provide a scaffold for orientation maps. *J. Neurosci.*, 20(3):1119–1128, Feb. 1 2000.
- [68] N. V. Swindale. A model for the formation of ocular dominance stripes. *Proceedings of the Royal Society of London B*, 208:243–264, 1980.
- [69] N. V. Swindale. Patches in monkey visual cortex. *Nature*, 293:509–510, 1981.
- [70] N. V. Swindale. A model for the formation of orientation columns. *Proceedings of the Royal Society of London B*, 1982.
- [71] N. V. Swindale. Coverage and the design of striate cortex. *Biological Cybernetics*, 65:415–424, 1991.
- [72] N. V. Swindale. The development of topography in the visual cortex: a review of models. *Network: Computation in Neural Systems*, 7(2):161–247, May 1996.

- [73] N. V. Swindale, Matsubara J. A., and Cynader M. S. Surface organization of orientation and direction selectivity in cat area 18. *J. Neuroscience*, 1987.
- [74] N.V. Swindale. A model for the coordinated development of columnar systems in primate striate cortex. *Biological Cybernetics*, 66:217–230, 1992.
- [75] Roger B. H. Tootell, Eugene Switkes, Martin S. Silverman, and Susan L. Hamilton. Functional Anatomy of Macaque Striate Cortex. II. Retinotopic Organization. *The Journal of Neuroscience*, 8(5):1531–1568, May 1988.
- [76] Lloyd N. Trefethen and David Bau, III. *Numerical Linear Algebra*. Society for Industrial and Applied Mathematics, Philadelphia, 1997.
- [77] Alan M. Turing. The chemical basis of morphogenesis. *Phil. Trans. Roy. Soc. Lond*, B237:37–72, 1952.
- [78] Christof von der Malsburg and David J. Willshaw. How to label nerve cells so that they can interconnect in an ordered fashion. *Proceedings of the National Academy of Sciences*, 74(11):5176–5178, November 1977.
- [79] Cornelius Weber, Helge Ritter, Jack D. Cowan, and Klaus Obermayer. Development and regeneration of the retinotectal map in goldfish: a computational study. *Phil. Trans. R. Soc. Lond. B*, 352:1603–1623, 1997.
- [80] B. Werner. Computational methods for bifurcation problems with symmetries and applications to steady states of n-box reaction-diffusion models. in *Numerical Analysis 1987*, D.F. Griffiths, G.A. Watson (eds.), pages 279-293; Pitman, 1988.
- [81] B. Werner. Eigenvalue problems with the symmetry of a group and bifurcations. in *Continuation and Bifurcations: Numerical Techniques and Applications*, D. Roose et al. (eds.), pages 71-88, 1990.
- [82] Virginia A. Whitelaw and Jack D. Cowan. Specificity and plasticity of retinotectal connections: A computational model. *Journal of Neuroscience*, 1(12):1369–1387, December 1981.

- [83] David J. Willshaw and Christof von der Malsburg. A marker induction mechanism for the establishment of ordered neural mappings: its application to the retinotectal problem. *Philos. Trans. R. Soc. London, Ser. B*, 287:203–243, 1979.
- [84] Hugh R. Wilson and Jack D. Cowan. Excitatory and inhibitory interactions in localized populations of model neurons. *Biophysical Journal*, 12:1–24, 1972.
- [85] Hugh R. Wilson and Jack D. Cowan. A mathematical theory of the functional dynamics of cortical and thalamic nervous tissue. *Kybernetik*, 13(2):55–80, Sept 1973.
- [86] S. Wimbauer, O.G. Wensich, K.D. Miller, and J.L. van Hemmen. Development of spatiotemporal receptive fields of simple cells: I. model formulation. *Biological Cybernetics*, 77:453–461, 1997.
- [87] S. Wimbauer, O.G. Wensich, J.L. van Hemmen, and K.D. Miller. Development of spatiotemporal receptive fields of simple cells: II. simulation and analysis. *Biological Cybernetics*, 77:463–477, 1997.